Ph.D. thesis

A Coupled CFD-DEM Model for Sand Production in Oil Wells

by: Natalia Climent Pera

Supervised by:

Dr. Marcos Arroyo Álvarez de Toledo

Prof. Antonio Gens Solé

Barcelona, September 2016

UNIVERSITAT POLITÈCNICA DE CATALUNYA BARCELONATECH

Abstract

During the oil recovery a hole is drilled, the sandstone is left unsupported next to the cavity and disloged sand grains can enter the oil recovery system. This process is called sand production and several problems may arise due to that process, as clogging up of the well or damage to the well equipment. The study of sand production process is of paramout importance for safe and economical hydrocarbon production.

The majority of numerical models to predict sand production that have been used to date are continuum-based. However, a continuum approach cannot easily capture important features of the sanding problem, such as erosion, and it requires the formulation recognized as a difficult task because of the large number of interactions and non-lineaities intrinsic to the problem. On the other hand, discrete-element based approaches allow a simpler formulation of the problem and a better understanding of some of its features. Discrete Element Methods (DEM) describe more naturally the disaggregation and erosion of sand particles and the fluid-solid interaction.

In this research rock behavior has been represented in DEM using the parallel-bond model (PBM) because it mimics the effect of cement between particles. The study has involved the calibration of the DEM rock model agains real data. Moreover, limitations of the DEM model have been explored and sensitivity analyses examining the effects of the local damping have been performed.

The main aim of this research is to improve the understanding of sand production based on a Computational Fluid Dynamics (CFD) -DEM coupling model. CFD-DEM is frequently used for process and chemical engineering problems (Zhu et al., 2007). To simulate the interaction of the particles with the fluid, the solid DEM model is coupled with a fluid model (CFD). A validation of the CFD-DEM model has been carried out in this thesis by performing single particle simulations and analyses of permeability tests. Simulations of sand production using a homogeneous sandstone analogue and, finally, the simulation of sand production under realistic conditions are presented.

Acknowledgments

First of all, I would like to express my sincere thanks to my supervisors, Dr Marcos Arroyo and Professor Antonio Gens for their support and guidance throughout this research and giving me the trust to develop my ideas. I have learnt a lot from them.

I also would like to thank Dr Catherine O'Sullivan and her research team for her help and guidance during my stay at Imperial College London.

I would also thank all my PhD fellows for their support and help during all these years. I also would like to thank Joanna Butlanska for sparing the time to discuss the issues related to the PFC^{3D} software with me at the beginning of my research.

This research was partly funded by the Ministry of Education studentship through research grant BIA2008-06537. This funding is grateful acknowledged.

I would also thank IESL company for providing the perforation test results for this research and for their help and technical guidance.

I would like to express my thanks to Jason Furtney from Itasca for his help and guidance discussing the issues related to the CCFD add-on software.

I would like thank especially to my parents and my sister for their emotional support and for helping me believe in myself. Also thanks to my new born nephew who made me smile the last months during the writing of the thesis.

And a very big thank you to all my friends, mates, partners and special people around me who helped me remind me who I am and what I really love during a hard period of my life the last two years of my PhD.

Contents

List of Figures

List of Tables

Chapter 1 – Introduction

1.1. Background

The Thesis presents a study of the phenomenon of sand production by means of coupled CFD-DEM analyses. CFD refers to Computational Fluid Dynamics and DEM stands for Discrete Element Method. Sand production is the erosion of formation sand during drilling and during the process of oil recovery. In order to recover the hydrocarbon, a well needs to be drilled to the depth of the reservoir. As the sandstone is left unsupported next to the cavity, sand grains can be dislodged and enter the oil recovery system. In addition, the rock around the wellbore is weakened due to the stress concentrations around the cavity. The weakened and decohesioned sandstone may be eroded away by the produced fluid.

Even though sand production can have a beneficial effect on hydrocarbon production, several problems may also arise; these include clogging up of the well, damage to the well equipment, well instability due to the loss of material and damage to the formation. Consequently, the study of the sand production process and the development of methods to control sanding are of paramount importance for safe and economical hydrocarbon production.

Sand production is a coupled fluid-solid process that primarily involves two mechanisms: mechanical instabilities that lead to localized plastic behaviour and failure of the rock around the cavity, and the subsequent transport of sand particles due to the fluid drag forces. The sandstone rock initially fails close to the cavity and the failed material is then eroded by the flowing fluid. These two mechanisms are coupled, since stress concentrations around the eroded cavity lead to increased damage, which in turn, increases the amount of cohesionless material that can be dislodged.

Methods commonly used to predict sand production can be classified into four categories: empirical methods, laboratory methods, theoretical models and numerical methods. Different methodologies are commonly used at the same time and they

complement each other. While both experimental and analytical models of the sand production problem play an important role, the development of numerical models is essential for realistic predictions (Rahmati et al., 2013).

The vast majority of the numerical models that have been used to date are continuum-based. However, a continuum approach cannot easily capture important features of the sanding problem, such as erosion and localized failure. Moreover, using a continuum model requires the formulation of several constitutive relations and it is generally recognised that such a formulation is a difficult task, because of the large number of interactions and non-linearities intrinsic to the problem.

These difficulties have encouraged the use of discrete-element based approaches, which, by redefining the solid physics at the micro-scale, allow a simpler formulation of the problem and a better understanding of some of its features. The disaggregation and the erosion of sand particles are more naturally described with DEM methods. However, even where DEM is used a number of constitutive choices remain, such as the solid-solid contact law and the fluid-solid interaction.

DEM was proposed originally by Cundall & Strack (1979) and is widely used to model soils and rocks, including sandstone (e.g. Potyondy & Cundall, 2004; Cheung et al., 2013). DEM involves micromechanical quantities that cannot be easily obtained from experimental tests but it is able capture the particle-scale interactions. The variables obtained using DEM are discrete variables such as forces, particle displacements, stresses on particles or particle velocities. Model boundaries are defined by introducing wall elements, to which displacement rates can be imposed. In DEM the parameters to be calibrated depends on the contact model adopted.

The large majority of the DEM sand production studies (e.g. Dorfmann et al., 1997; O'Connor et al., 1997; Cook et al., 2004; Marrion & Woods, 2009; Quadros et al., 2010; Boutt et al., 2011) have been performed using 2D discrete models; these certainly offer qualitative insight, but they produce results which are difficult to relate quantitatively to field or experimental observations. Other studies have used 3D particles, but have focused on small scale phenomena involving only a few particles (Grof et al., 2009) or

have radically simplified some aspect of the problem, such as the flow pattern (Cheung, 2010) or the boundary conditions (Zhou et al., 2011).

In general, particles in granular materials are surrounded by fluid, as it is the case of sand production process. To simulate this interaction at the soil particle scale, the solid DEM model must be coupled with a fluid model; several fluid-coupling techniques are available (Zhu et al., 2007). The method used in this thesis uses mesoscopic coupling and it is known as CFD-DEM (Zhu et al., 2007). CFD-DEM was pioneered by Tsuji et al. (1993) to simulate the formation of bubbles in gas-fluidized granular beds. It is now frequently used for process and chemical engineering problems (Zhu et al., 2007).

1.2. Scope and objectives

The main aim of this research is to improve the understanding of sand production based on a CFD-DEM coupling model. To represent rock behaviour in DEM the parallel-bond model has been used because it mimics the effect of cement between particles. However, the calibration of this model is a complicated process because of the number of micro parameters involved. Moreover, in the case of this thesis, the mechanical model is only a part of a more complex model that also includes solid-fluid interaction, leading to some restrictions and limitations. Because for sand production simulation, the fluid-solid interaction is a paramount of importance, the resulting coupled modelling approach must be carefully verified.

The objectives of the research reported in this Thesis are:

1. To review the methods that have been used to simulate sand production process.
2. To review the current available fluid-solid coupling techniques used in DEM in order to develop an appropriate model to study the sand production process.

3. To test the CFD-DEM model and to identify its limitations.
4. To develop and calibrate a DEM parallel-bond model for rock and sandstone suitable for performing sand production simulations.
5. To develop a 3D CFD-DEM model of for sand production simulation.

1.3. Thesis layout

This thesis has been divided into ten chapters.

The current chapter, Chapter 1, provides the background and the objectives of this research.

Chapter 2 reviews some basic soil and rock mechanics concepts relevant for the sand production problem. Some basic characteristics of the soil as a material are presented in Section 2.2. A simple theory of elasticity is described in Section 2.3 whereas Section 2.4 introduces the poroelasticity theory commonly used in petroleum rock mechanics. Failure mechanics are introduced in Section 2.5, necessary to adequately understand some of the main mechanisms involved in sand production process.

The sand production problem is defined in Chapter 3. Oil wells properties are introduced in Section 3.2. In Sections 3.3 and 3.4 the sand production problem and the mechanisms of sand production are described whereas the prediction methods for sand production are reviewed in Section 3.5. Section 3.6 presents an analytical model for the sand production problem.

In Chapter 4 the DEM method is described. The equations and basic theory of this method are presented in Section 4.2. Sections 4.3 and 4.4 describe the inter-particle contact models employed, including the parallel-bond model. The damping force is introduced in Section 4.5 and the DEM boundary conditions used in this thesis are described in Section 4.6. An overview of some applications of DEM to soil mechanics is

presented in Section 4.7 and Section 4.8 explains the representations of DEM output using ParaView.

An application of the parallel-bond model to represent rock behaviour using DEM together with its calibration is presented in Chapter 5. Section 5.2 contains a review of published use of the parallel bond model to represent rock behaviour. An introduction of the parallel-bond model to represent sand production problems is described in Section 5.3. Finally, Section 5.4 presents the datasets that were selected for calibration, the generation of the specimen tested and the calibration of the model.

The CFD-DEM coupled model is introduced in Chapter 6. First of all, some concepts of fluid dynamics and computational fluid dynamics are recalled in Section 6.2. Section 6.3 explains the basics of particle-fluid interaction and the different numerical approaches available for studying this interaction, with particular emphasis in CFD-DEM (Section 6.3.2). Previous examples of sand production studies and other applications using CFD-DEM are presented in Sections 6.4 and 6.5. Finally, Section 6.6 describes the representations of CFD output.

In Chapter 7 the modelling approach CFD-DEM is tested in simpler cases to allow a clearer understanding of some aspects affecting fluid-particle interaction. In Section 7.2 simulations involving a single particle are performed to examine the effect of fluid forces, the damping force and the fluid viscosity. In Section 7.3 an evaluation of the method is performed using a permeameter test as a benchmark.

Coupled CFD-DEM simulations of sand production for a discrete analogue of ideal sandstone are presented in Chapter 8. A first simulation of dry perforation is presented and discussed in Section 8.2. In Section 8.3 fluid is introduced in the model under hydrostatic initial conditions whereas simulations with an imposed fluid velocity are presented in Section 8.4. The effect of numerical damping is explored in Section 8.5. Section 8.6 presents some comparisons with available published results (Cheung, 2010).

Chapter 9 contains the results of analyses using the discrete analogues of sandstone calibrated in Chapter 5. In Section 9.2 the data of the different oil fields are introduced. Section 9.3 presents preliminary sand production estimates using empirical approaches

and an analytical solution. The geometry, the fluid, the scaling and the adjustments required are discussed in Sections 9.4 and 9.5. In Section 9.6 the simulation set-up is described and the results of the simulations are presented in Section 9.7.

Chapter 10 summarises and concludes the main findings of this research and proposes some suggestions for future work on these topics.

Chapter 2 - Basic soil mechanics concepts for sand production problems

2.1. Introduction

Sand production process in oil wells is a geomechanical problem where rocks are transformed into soils. Oil reservoirs are composed by sedimentary rocks that discompose to sand grains (soils) during the oil recovery process. For this reason, this chapter recalls some basic soil and rock mechanics concepts relevant for the sand production problem described in Chapter 3. First of all, in Section 2.2, some basic characteristics of soil as a material are exposed. After that, in Section 2.3 the theory of elasticity as a first and simple way to describe materials is explained in order to introduce the poroelasticity theory. This theory is commonly used in petroleum rock mechanics is exposed in Section 2.4. Finally, Section 2.5 is an introduction of failure mechanics to understand some mechanisms that have to be taken into account in sand production process in oil wells.

2.2. Characteristics of soils

Soil is an uncemented or weakly cemented accumulation of mineral particles. Soil particles are frequently originated by the weathering of rocks. However, there are soils originated by other processes, as limestones which are formed by sedimentation of organic material in shallow marine waters. Each particle can be described as a single grain being in contact with other grains (Fig. 2.1). The space between grains contains fluid (water, other liquids, gas and/or air). When the space between grains is totally filled by water or a liquid the soil is said to be saturated; otherwise the soil is unsaturated. The structure of the soil may be loose, medium or dense depending on the way in which the

particles are packed together. On the other hand, when particles and grains are strongly cemented together it is considered to be a rock.

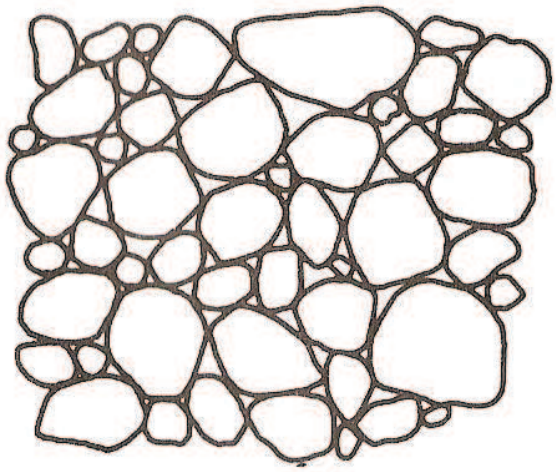

Fig. 2.1. Grain assemblage (Craig, 1992)

Fig. 2.2 shows the size ranges for soils proposed in British Standards. Fine or fine-grained soils are those composed mainly by clay and silt size particles, and coarse-grained soils are those whose properties are influenced mainly by sand and gravel particles.

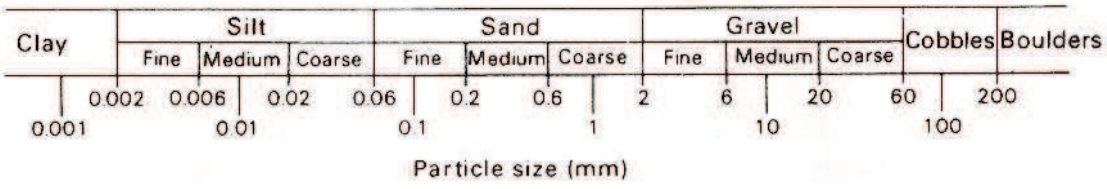

Fig. 2.2. Particle size ranges in British Standards (Craig, 1992)

2.2.1. Particle size distribution

The particle size distribution (PSD) represents the percentage by weight of particles smaller (or bigger) than the size given by the abscissa. Therefore, there are two ways to

represent the particle distribution. In soil mechanics practice is customary to use the one that represents the percentage of smaller particles. On the other hand in petroleum engineering (e.g. Nouri et al., 2006; Fattahpour et al., 2012) the other representation is commonly employed. Fig. 2.3 exemplifies these two representations using data from a material later introduced (Chapter 5): when the percentage of smaller particles is represented, the plotted line has an S-shape; otherwise, the plotted line has an inverted shape. The size of the particles is represented in a logarithmic scale.

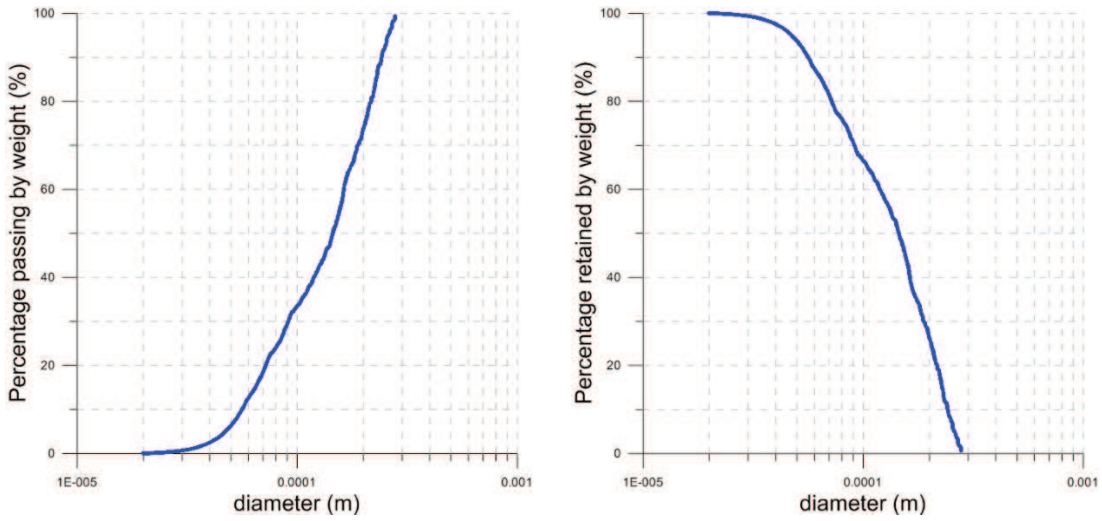

(a) (b)

Fig. 2.3. FIELD1 (Sections 5.4.1 and 5.4.2) PSD. (a) Soil mechanics typical representation: weight percentage of particles smaller than the size particle in the abscissa; and (b) petroleum engineering typical representation: weight percentage of particles bigger than the size particle in the abscissa.

In this thesis we present all PSD data using the petroleum engineering convention of percentage retained by weight. Therefore, the effective size D_{10} is the size such that 10% of the particles are bigger than that size. The coefficient of uniformity (C_U), the sorting coefficient (S_c) and the coefficient of curvature (C_Z), are defined as follows

$$C_U = \frac{D_{40}}{D_{90}} \qquad \text{Eq. 2.1}$$

$$S_C = \frac{D_{10}}{D_{95}} \qquad \text{Eq. 2.2}$$

$$C_Z = \frac{D_{70}^2}{D_{40} D_{90}} \qquad \text{Eq. 2.3}$$

The higher the value of the coefficient of uniformity the larger the range of particle sizes in the soil.

2.2.2. Permeability

Water and other fluids may flow through the pores between the solid particles. The phreatic level is the level at which the pressure is atmospheric, below which the soil is assumed to be fully saturated.

The pore water may be static (the hydrostatic pressure depends on the depth below that level) or it may be seeping through the soil under hydraulic gradient. In one dimension, water flows through a fully saturated soil following Darcy's empirical law

$$u_f = \frac{q}{A} = K \nabla h \qquad \text{Eq. 2.4}$$

where q is the volume of water flowing per unit time, A is the cross-sectional area of soil corresponding to the flow q, K is the hydraulic conductivity, ∇h is the hydraulic gradient, and u_f is the discharge velocity. The units of the hydraulic conductivity are those of velocity (m/s).

A more fundamental concept than hydraulic conductivity is permeability. Hydraulic conductivity is related to permeability by the equation

$$K = \frac{\rho_f g}{\mu_f} k \qquad \text{Eq. 2.5}$$

where ρ_f is the density of the fluid, g is the acceleration of gravity, μ_f is the dynamic viscosity of the fluid and k (units m^2 or Darcy $1D \approx 10^{-12}\ m^2$) is the coefficient of permeability. The coefficient of permeability depends on the average size of the particles, the distribution of particle sizes, particle shape and soil structure. In general, the smaller the particles the smaller is the average size of the pores and the lower is the coefficient of permeability. The value of k for different types of soil are typically within the ranges shown in Fig. 2.4.

Rock Type	k (m^2)	k (Darcies)	K_h (m/s)	Reference
Coarse gravels	10^{-9}–10^{-8}	10^{3}–10^{4}	10^{-2}–10^{-1}	a
Sands, gravels	10^{-12}–10^{-9}	10^{0}–10^{3}	10^{-5}–10^{-2}	a
Fine sands, silts	10^{-16}–10^{-12}	10^{-4}–10^{0}	10^{-9}–10^{-5}	a
Clays, shales	10^{-23}–10^{-16}	10^{-11}–10^{-4}	10^{-16}–10^{-9}	a,b
Dolomites	10^{-12}–10^{-10}	10^{0}–10^{2}	10^{-5}–10^{-3}	a
Limestones	10^{-22}–10^{-12}	10^{-10}–10^{0}	10^{-15}–10^{-5}	a,b
Sandstones	10^{-17}–10^{-11}	10^{-5}–10^{1}	10^{-10}–10^{-4}	a,b
Granites, gneiss	10^{-20}–10^{-16}	10^{-8}–10^{-4}	10^{-13}–10^{-9}	a,b
Basalts	10^{-19}–10^{-13}	10^{-7}–10^{-1}	10^{-12}–10^{-6}	b

Fig. 2.4. Expected ranges of permeabilities and hydraulic conductivities of various rock types: a- de Marsily (1986); b- Guéguen and Palciauskas (Jaeger et al., 2007)

When permeability is deduced from reported values of hydraulic conductivity, it is always implicitly assumed that the fluid is water at $20^{\circ}C$, in which case $\rho_f = 998 kg/m^3$

and $\mu_f = 0.001$Pa·s (Jaeger et al., 2007). Conductivity of soils to other fluids - for instance oils such as those simulated in Chapter 9 - is related to permeability by the same equation, but different values of density and dynamic viscosity apply. The values of those properties for other fluids relevant in the sand production problem are presented in Section 3.2.3.

2.3. Elasticity

Elasticity is the ability of some materials to resist and recover from deformation produced by forces. The simplest type of response in rock mechanics is one in which there is a linear relation between the external forces and the corresponding deformations; this kind of response happens when changes in the forces are sufficiently small. The theory of elasticity is based on two concepts: stress and strain. The theory of elasticity described in the next sections is extracted from the presentations in Wang (2000), Jaeger et al. (2007) and Fjar et al. (2008).

The elastic theory for solid materials is not able to fully describe the behaviour of biphasic materials such as soils or rocks. The extension of elasticity to such materials is called poroelasticity and is described in the next section.

2.3.1. Stress and strain

2.3.1.1. Stress

The stress at a point is defined as the ratio of force divided by the area in the limit as the area ΔA_i goes to zero

$$\sigma_i = \lim_{\Delta A_i \to 0} \frac{\Delta F_i}{\Delta A_i} \qquad \text{Eq. 2.6}$$

The SI unit for stress is Pa (Pascal, N/m^2). In the petroleum industry, 'oilfield' units like psi (pounds per square inch) are commonly used (1 psi = 6894.76 N/m^2). The sign convention for the stress in rock mechanics states that compressive stresses are positive.

An area element has magnitude and direction defined by the outward normal to the surface. Because both force and area are vector quantities, stress is represented in six components of a symmetric second-rank tensor. The tensor components σ_{ij} of the applied stress on an elementary volume are shown in Fig. 2.5. The first subscript (*i*) identifies the axis normal or the actual surface, while the second subscript (*j*) identifies the direction of the force.

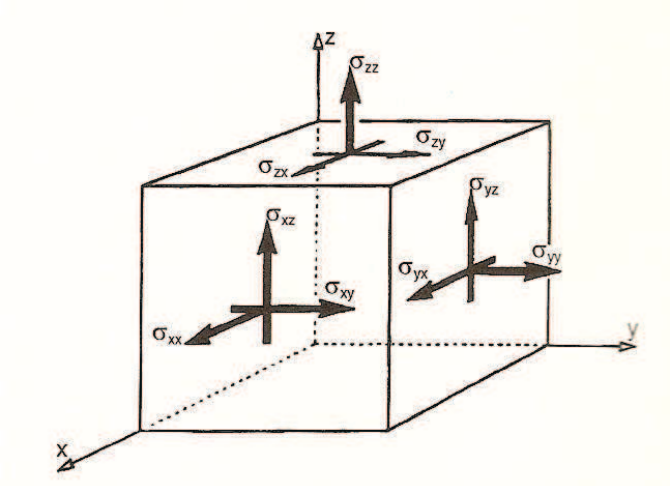

Fig. 2.5. Stress tensor. The first subscript refers to the direction of the normal to the plane, and the second subscript refers to the direction of the force. (Wang, 2000).

The stress components are total stresses. Normal stresses (σ_{xx}, σ_{yy} and σ_{zz}) are those for which the force is parallel to the normal to the face. The shear stresses (σ_{xy}, σ_{xz} and

σ_{yz}) are those for which the force is perpendicular to the normal to the face. Rotational equilibrium requires the stress tensor to be symmetric ($\sigma_{ij} = \sigma_{ji}$).

The stress tensor that represents the stress state at the point P is

$$\begin{pmatrix} \sigma_{xx} & \sigma_{xy} & \sigma_{xz} \\ \sigma_{xy} & \sigma_{yy} & \sigma_{yz} \\ \sigma_{xz} & \sigma_{yz} & \sigma_{zz} \end{pmatrix} \quad \text{Eq. 2.7}$$

The principal axes of stress are the directions for which the shear stress vanishes. If the coordinate system is oriented such that the x-axis parallel to the first, the y-axis parallel to the second, and the z-axis parallel to the third principal axis, the stress tensor has a particularly simple form

$$\begin{pmatrix} \sigma_1 & 0 & 0 \\ 0 & \sigma_2 & 0 \\ 0 & 0 & \sigma_3 \end{pmatrix} \quad \text{Eq. 2.8}$$

The solutions are conventionally organized such that $\sigma_1 \geq \sigma_2 \geq \sigma_3$.

Stress invariants are properties of the stress tensor that remain unchanged when changing to a rotated set of coordinate axes. Any combination of stress invariants will be a stress invariant as well. The simplest of these is the mean normal stress

$$\bar{\sigma} = \left(\sigma_{xx} + \sigma_{yy} + \sigma_{zz}\right)/3 \quad \text{Eq. 2.9}$$

When the coordinated system is reoriented such that the x-axis is parallel to the first principal stress, the y-axis parallel to the second principal stress and the z-axis parallel to the third principal stress, the stresses σ and τ can be plotted in a diagram obtaining circles called the Mohr's circles (where σ are the normal stresses σ_{ii} and τ the shear stresses σ_{ij}, where $i \neq j$). The basic features of the construction are shown in Fig. 2.6. In the direction in the yz-plane the stresses σ and τ are located on the small circle spanning from σ_3 to σ_2. In the direction in the xy-plane σ and τ are located on the circle spanning from σ_2 to σ_1; and, finally, in the direction in the xz-plane σ and τ are located on the large circle spanning from σ_3 to σ_1. For all other directions, σ and τ are located within the shaded areas.

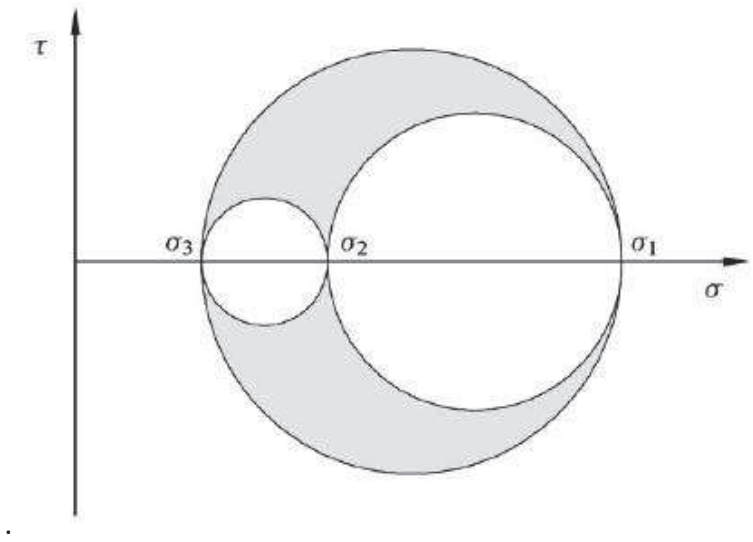

Fig. 2.6. Mohr's circles (Fjar et al., 2008).

2.3.1.2. Strain

After the action of an external force, the position of particles in a sample may change. If the new positions cannot be obtained simply by a rigid movement (translation and/or

rotation), the sample is said to be strained (the relative position of the particles are changed). Fig. 2.7 shows an example of a strained sample.

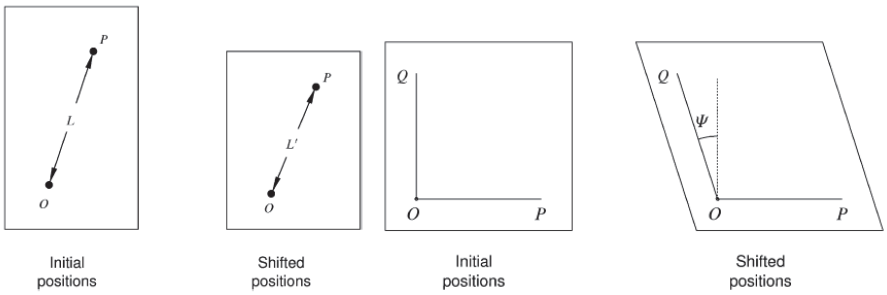

Fig. 2.7. Elongation (on the left) and shear deformation (on the right) (Fjar et al., 2008).

The definition of the strains is

$$\varepsilon_{xx} = \frac{\partial \delta_x}{\partial x} \qquad \text{Eq. 2.10}$$

$$\varepsilon_{yy} = \frac{\partial \delta_y}{\partial y} \qquad \text{Eq. 2.11}$$

$$\varepsilon_{zz} = \frac{\partial \delta_z}{\partial z} \qquad \text{Eq. 2.12}$$

$$\varepsilon_{xy} = \varepsilon_{yx} = \frac{1}{2}\left(\frac{\partial \delta_x}{\partial y} + \frac{\partial \delta_y}{\partial x}\right) \qquad \text{Eq. 2.13}$$

$$\varepsilon_{xz} = \varepsilon_{zx} = \frac{1}{2}\left(\frac{\partial \delta_x}{\partial z} + \frac{\partial \delta_z}{\partial x}\right) \qquad \text{Eq. 2.14}$$

$$\varepsilon_{yz} = \varepsilon_{zy} = \frac{1}{2}\left(\frac{\partial \delta_y}{\partial z} + \frac{\partial \delta_z}{\partial y}\right) \qquad \text{Eq. 2.15}$$

where δ_x is the displacement in the *x* direction, δ_y is the displacement in the *y* direction, and δ_z is the displacement in the *z* direction.

Extensional strains are taken as positive. We may organize the strains in a strain tensor

$$\vec{\vec{\varepsilon}} = \begin{pmatrix} \varepsilon_{xx} & \varepsilon_{xy} & \varepsilon_{xz} \\ \varepsilon_{xy} & \varepsilon_{yy} & \varepsilon_{yz} \\ \varepsilon_{xz} & \varepsilon_{yz} & \varepsilon_{zz} \end{pmatrix} \qquad \text{Eq. 2.16}$$

The trace of the strain tensor is called the volumetric strain (the relative decrease on volume).

The longitudinal strains (ε_{xx} , ε_{yy} and ε_{zz}) are the relative-length changes parallel to the coordinate axes (elongation, Fig. 2.6, left). Extensional strains are taken as positive. The shear strains ($\varepsilon_{ij}, i \neq j$) measure the change from a right angle of lines parallel to the coordinate axes (Fig. 2.6, right).

$$\varepsilon_{vol} = \varepsilon_{xx} + \varepsilon_{yy} + \varepsilon_{zz} \qquad \text{Eq. 2.17}$$

A general mathematical notation for strains is defined by

$$\varepsilon_{ij} = \frac{1}{2}\left(\frac{\partial \delta_i}{\partial x_j} + \frac{\partial \delta_j}{\partial x_i} \right) \qquad \text{Eq. 2.18}$$

The subscripts *i* and *j* may be any of the numbers 1, 2, 3, representing the x-, y-, and z-axis, respectively. $\delta_1 = \delta_x$, $\delta_2 = \delta_y$ and $\delta_3 = \delta_z$, while $x_1 = x$, $x_2 = y$, and $x_3 = z$.

2.3.2. Elastic moduli

In situations where there are linear relationships between applied stresses and resulting strains, the theory of linear elasticity is used. If the sample behaves linearly, there is a linear relationship between the applied stress in that direction (σ_{xx}) and the corresponding elongation (ε_{xx}). The relationship is known as the Hooke's law

$$\varepsilon_{xx} = \frac{\sigma_{xx}}{E} \qquad \text{Eq. 2.19}$$

The coefficient *E* is called Young's modulus or simply the E-modulus. It is a measure of the sample's resistance against being compressed by a uniaxial stress ($\sigma_{xx} \neq 0$, $\sigma_{yy} = \sigma_{zz} = \sigma_{xy} = \sigma_{xz} = \sigma_{yz} = 0$).

The ratio between the lateral elongation ($\varepsilon_{yy} = \varepsilon_{zz}$) and elongation in the direction of the applied stress is known as Poisson's ratio

$$\nu = -\frac{\varepsilon_{yy}}{\varepsilon_{xx}} \qquad \text{Eq. 2.20}$$

It is a measure of lateral expansion relative to the longitudinal contraction. These equations, which relate one component of stress or strain to another, are defined by a

specific state of stress, namely $\sigma_{xx} \neq 0$, $\sigma_{yy} = \sigma_{zz} = \sigma_{xy} = \sigma_{xz} = \sigma_{yz} = 0$ (uniaxial stress state). In general, each component of strain is a linear function of all components of stress.

Young's modulus and Poisson's ratio belong to a group of coefficients called elastic moduli. The elastic moduli are parameters that give the ratio of one of the stress components to one of the strain components.

Isotropic materials are materials whose response is independent of the orientation of the applied stress. For such materials the principal axes of stress and the principal axes of strain always coincide. For isotropic materials the general relations between stresses and strains may be written

$$\sigma_{xx} = (\lambda + 2G)\varepsilon_{xx} + \lambda\varepsilon_{yy} + \lambda\varepsilon_{zz} \quad \text{Eq. 2.21}$$

$$\sigma_{yy} = \lambda\varepsilon_{xx} + (\lambda + 2G)\varepsilon_{yy} + \lambda\varepsilon_{zz} \quad \text{Eq. 2.22}$$

$$\sigma_{zz} = \lambda\varepsilon_{xx} + \lambda\varepsilon_{yy} + (\lambda + 2G)\varepsilon_{zz} \quad \text{Eq. 2.23}$$

$$\sigma_{yz} = 2G\varepsilon_{yz} \quad \text{Eq. 2.24}$$

$$\sigma_{xz} = 2G\varepsilon_{xz} \quad \text{Eq. 2.25}$$

$$\sigma_{xy} = 2G\varepsilon_{xy} \quad \text{Eq. 2.26}$$

The coefficients λ and *G* are elastic moduli, known as Lamé's parameters. *G* is also known as the modulus of rigidity, or the shear modulus. *G* is a measure of the sample's resistance against shear deformation; it relates stresses to strains in a state of pure shear.

The bulk modulus *B* is another elastic modulus that measures the sample's resistance against hydrostatic compression. It is defined as the ratio of hydrostatic stress σ_p relative to the volumetric strain ε_{vol}. For a hydrostatic stress state we have $\sigma_p = \sigma_{xx} = \sigma_{yy} = \sigma_{zz}$ while $\sigma_{xy} = \sigma_{yz} = \sigma_{xz} = 0$.

$$B = \frac{\sigma_p}{\varepsilon_{vol}} = \lambda + \frac{2}{3}G \qquad \text{Eq. 2.27}$$

The inverse $1/B$ is known as the compressibility.

Then

$$E = \frac{\sigma_{xx}}{\varepsilon_{xx}} = G\frac{3\lambda + 2G}{\lambda + G} \qquad \text{Eq. 2.28}$$

$$\nu = -\frac{\varepsilon_{yy}}{\varepsilon_{xx}} = \frac{\lambda}{2(\lambda + G)} \qquad \text{Eq. 2.29}$$

The elastic moduli *E*, ν , λ , *G* and *B* are measured in the same units as stress. The stress-strain relations are the fundamental equations for description of isotropic, linear elastic materials.

The stress strain relations may be written on a more compact form using the notation introduced

$$\sigma_{ij} = \lambda\varepsilon_{vol}\delta_{ij} + 2G\varepsilon_{ij} \qquad \text{Eq. 2.30}$$

where δ_{ij} is the Kronecker symbol.

Energy considerations require that the following relations always hold. If they do not, one should suspect experimental errors or that the material is not isotropic (Mavko et al., 2003)

$$\lambda + \frac{2\mu}{3} \geq 0 \quad ; \quad \mu \geq 0 \qquad \text{Eq. 2.31}$$

or

$$-1 < \mu \leq 1/2 \quad ; \quad E \geq 0 \qquad \text{Eq. 2.32}$$

A particular type of idealized isotropic elastic material is the incompressible solid, which has $1/B = 0$ or $B \to \infty$. For such materials $\lambda \to \infty$, $E \to 3G$ and $\nu \to 1/2$ (Jaeger et al., 2007). A completely rigid material is not only incompressible but also has infinite values of *E* and *G*. The limiting case of a compressible fluid is that in which the shear modulus vanishes, but the bulk modulus remains finite: $G \to 0$, $\nu \to 1/2$, $E \to 0$ and $\lambda = B$.

2.4. Poroelasticity: Biot's theory and the effective stress concept

Soils are not solid materials, they can be visualized as a skeleton of solid particles enclosing voids which contain water, other liquids, gas, air, etc. Due to rearrangement of the particles the volume of the solid skeleton can change. The compressibility of the soil skeleton will depend on the structural arrangement of the solid particles.

The way soils behave depends also on the non-solid part of the materials. The mechanical and hydrological behaviour of soils is coupled. The void space plays an important role in soil mechanical behaviour as described in this section.

The general theory that accounts for this coupled hydromechanical behaviour is poroelasticity. This theory was put by Biot (1941) and, as cited by Jaeger et al. (2007), it was developed further by, among others, Verruijt (1969), Rice & Cleary (1976), and Detournay & Cheng (1993). In the next sections this theory is introduced following Wang (2000), Mavko et al. (2003), Jaeger et al. (2007) and Fjar et al. (2008).

2.4.1. Suspension of solid particles in a fluid

As a first approximation, a porous medium can be thought as a suspension of solid particles. Using this simplification, the solid and fluid parts are deformed independently of each other and the volumetric strain due to an external pressure σ_p is

$$\varepsilon_{vol} = \frac{\sigma_p}{B_{eff}} \qquad \text{Eq. 2.33}$$

where B_{eff} is the bulk modulus of the mixture (effective bulk modulus). The total deformation must, however, equal the sum of the deformations of each component, weighted by the volume portion of each component

$$\varepsilon_{vol} = \frac{V_s}{V_{tot}} \varepsilon_{vol,s} + \frac{V_f}{V_{tot}} \varepsilon_{vol,f} \qquad \text{Eq. 2.34}$$

where subscripts *s* and *f* are solid and fluid, respectively, and V_{tot} is the total volume. The porosity *n* is the volume occupied by the fluid relative to the total volume

$$n = \frac{V_f}{V_{tot}}$$ Eq. 2.35

And the void ratio

$$e = \frac{V_f}{V_s} = \frac{n}{1-n}$$ Eq. 2.36

The porosity is restricted to the range $0 \le n < 1$, whereas the void ratio can take on any positive value.

The strains $\varepsilon_{vol,s}$ and $\varepsilon_{vol,f}$ are given by the bulk moduli of the solid (B_s) and the fluid (B_f), respectively

$$\varepsilon_{vol} = (1-n)\frac{\sigma_p}{B_s} + n\frac{\sigma_p}{B_f}$$ Eq. 2.37

And the effective bulk modulus of the suspension is given by

$$\frac{1}{B_{eff}} = \frac{1-n}{B_s} + \frac{n}{B_f}$$ Eq. 2.38

(Fjar et al., 2008). This is called the Reuss bound which describes the effective moduli of a suspension of solid grains in a fluid (Mavko et al., 2003). This is a particular case of calculating the effective moduli of a mixture of different materials and phases.

This is an example of a particularly simple porous material. However, rocks consist of a solid framework and a pore fluid which cannot be treated independently and a generalization is taken into account in the next section.

2.4.2. Introduction to Biot's poroelastic theory

The medium considered in this section is isotropic, porous and permeable and it is divided in two components: a solid part and a fluid part. Displacements are denoted $\bar{\delta}_s$ (of the solid part) and $\bar{\delta}_f$ (of the fluid part). For a volume element attached to the solid framework, the strains are given as

$$\varepsilon_{vol} = \nabla \cdot \bar{\delta}_s \qquad \text{Eq. 2.39}$$

For the fluid part, a strain parameter ζ (increment of fluid content) which describes the volumetric deformation of the fluid relative to that of the solid is defined

$$\zeta = n\nabla \cdot \left(\bar{\delta}_s - \bar{\delta}_f\right) \qquad \text{Eq. 2.40}$$

Biot and Willis (1957), cited in Wang (2000). Where $\bar{\delta}_s$ and $\bar{\delta}_f$ are the average displacements of the fluid and solid, respectively. This equation carries the assumption

that the porosity is homogeneous (Wang, 2000) and represents continuity in a control volume (the volume of fluid entering the control volume is equal to the volume of fluid leaving the control volume).The stress tensor $\vec{\vec{\sigma}}$ represents the total external stress on a volume element, which balances this stress partly by stresses in the solid framework and partly by the pore pressure p_f. The pore pressure is the pressure of the fluid occupying the pore space.

The change in the mass of fluid contained into the control volume can be divided into two parts: the change of the pore volume (due to change in the external stresses and/or the pore pressure), and the compression/decompression of the fluid as the pore pressure changes

$$\zeta = -n\left(\frac{\Delta V_p}{V_p} + \frac{p_f}{B_f}\right) \qquad \text{Eq. 2.41}$$

where V_p is the pore volume and B_f is the bulk modulus of the pore fluid. The stress-strain relations for this two-phase system can be expressed

$$p_f = C_1 \varepsilon_{vol} - C_2 \zeta \qquad \text{Eq. 2.42}$$

$$\sigma_{ij} = \lambda \varepsilon_{vol} \delta_{ij} + 2G\varepsilon_{ij} - C\zeta\delta_{ij} \qquad \text{Eq. 2.43}$$

λ and G are the Lamé parameters of the porous material, while C_1 and C_2 are additional elastic moduli required to describe a two-phase medium.

Letting $\varepsilon_{vol} = 0$, it is found that

$$p_f = C_2 n \nabla \cdot \bar{\delta}_f \qquad \text{Eq. 2.44}$$

which shows that $C_2 n$ is a measure of how much the pore pressure increases as the amount of fluid in a volume element is increased. If the solid was completely rigid, we would thus have $C_2 n = B_f$, where $1/B_f$ is the fluid compressibility.

Summing equations gives

$$\bar{\sigma} = K\varepsilon_{vol} - C_1 \zeta \qquad \text{Eq. 2.45}$$

$B = \lambda + 2G/3$ is the bulk modulus of the porous rock in undrained condition (in a condition where the pore fluid is not allowed to escape, $\zeta = 0$).

Therefore

$$\frac{B}{B_s - B} = \frac{B_{fr}}{B_s - B_{fr}} + \frac{1}{n}\frac{B_f}{B_s - B_f} \qquad \text{Eq. 2.46}$$

where B_{fr} is called the bulk modulus of the framework or the frame modulus and B_s is the bulk modulus of the solid grains. B_s can be interpreted also as the unjacketed modulus (the modulus calculated under unjacketed conditions). Unjacketed conditions are the conditions where the differential pressure is held constant. That is, when a change in confining pressure produces an equal change in pore pressure.

Constant increment of fluid content means undrained conditions, constant pore pressure means drained conditions, constant stress means no external stress change, and constant strain means zero external displacement (Wang, 2000).

2.4.3. Effective stress

The effective stress is defined as

$$\sigma'_p = \sigma_p - \alpha p_f \qquad \text{Eq. 2.47}$$

This means that the total external stress σ_p is not carried only by the solid framework, which carries the part σ'_p, but also by the fluid, which carries the remaining part αp_f. The parameter α is called the Biot coefficient or the effective stress coefficient

$$\alpha = 1 - \frac{B_{fr}}{B_s} \qquad \text{Eq. 2.48}$$

α is restricted to the region $n < \alpha \leq 1$. In unconsolidated or weak rocks, α is close to 1, and sandstones have α values higher than 0.5 (Table 2.1). In general, the effective stress is defined by

$$\sigma'_{ij} = \sigma_{ij} - \delta_{ij} \alpha p_f \qquad \text{Eq. 2.49}$$

where δ_{ij} is the Kronecker symbol. Observe that only the normal effective stress depend on the pore pressure because shear stresses do not produce volumetric strains.

This idea is called the law of effective stress (Wang, 2000), first enunciated by Terzaghi, who introduced the same equation with $\alpha = 1$.

Table 2.1. Poroelastic moduli for different rock types (Wang, 2000).

Rock	**G (GPa)**	**ν**	**K (GPa)**	**α**	***n***	***k* (mD)**
Berea sandstone	6	0.2	8	0.79	0.19	190
Boise sandstone	4.2	0.15	4.6	0.85	0.26	800
Ohio sandstone	6.8	0.18	8.4	0.74	0.19	5.6
Pecos sandstone	5.9	0.16	6.7	0.83	0.2	0.8
Ruhr sandstone	13	0.12	1	0.65	0.02	0.2
Weber sandstone	12	0.15	13	0.64	0.06	1
Tennessee marble	24	0.25	40	0.19	0.02	0.0001
Charcoal granite	19	0.27	35	0.27	0.02	0.0001
Westerly granite	15	0.25	25	0.34	0.01	0.0004

2.5. Failure mechanics

When a rock specimen is subjected to large stresses it changes its shape permanently and sometimes it also fails apart. Failure is a complex process which is still not fully understood. However, it is useful to predict the conditions a rock is likely to fail, especially in petroleum related rock mechanics, as rock failure it is at the origin of severe problems such as borehole instability and solids production.

2.5.1. Strength

The strength is the stress level at which rock fails. The stress level depends on the type of test used to measure the strength, therefore rock strength is not given by a uniquely defined parameter, and there are different types of failure criteria that contain one or more parameters.

In general, the stresses at fracture can be expressed as a function between the principal stresses ($f(\sigma_1', \sigma_2', \sigma_3') = 0$). Different failure criteria have been used, as for example

· Coulomb failure criteria $|\tau| = S_0 + \mu\sigma'$ Eq. 2.50

· Mohr failure criteria $|\tau| = f'(\sigma')$ Eq. 2.51

· Griffith criterion $(\sigma_1' - \sigma_3')^2 = 8\sigma_T(\sigma_1' + \sigma_3')$ Eq. 2.52

Mogi (2007); where τ is the shear stress and σ_T is the tensile strength. There are other criteria as von Mises criteria, that contemplates the effect of σ_2' (Mogi, 2007).

The most important tests used to measure rock strength are the uniaxial and triaxial tests. The specimen in uniaxial and triaxial tests is usually a cylinder with length to diameter ratio 2:1 (Fig. 2.8). The stress is applied to the end faces of the cylinder, while confining fluid provides a stress to the axial perimeter. If the confining stress is zero, we have a uniaxial stress test. When test is performed with a non-zero confining pressure, a triaxial test is performed.

A typical result from a uniaxial test is shown in Fig. 2.9. The applied axial stress σ_{zz} is plotted as a function of the axial strain ε_{zz} of the sample. Several important concepts are defined in Fig. 2.9, as the elastic region and the uniaxial compressive strength. The

elastic region is the region where the rock deforms elastically, therefore if the stress is released the specimen returns to its original state. The uniaxial compressive strength is the peak stress. The triaxial is carried out keeping the confining pressure constant and increasing the axial load until the failure occurs. Results are usually different depending on the confining pressure (Fig. 2.10). The stress reaches a maximum, which is called uniaxial compressive strength when a uniaxial test is performed. The uniaxial compressive strength is a measure of the strength of the material.

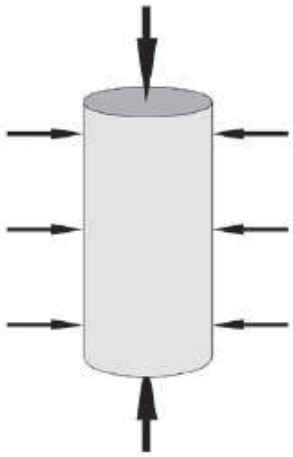

Fig. 2.8. Typical test specimen for uniaxial and triaxial test (Fjar et al., 2008).

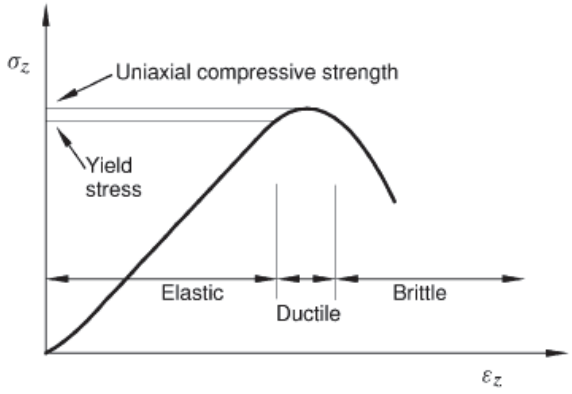

Fig. 2.9. Uniaxial compressive test result (Fjar et al., 2008).

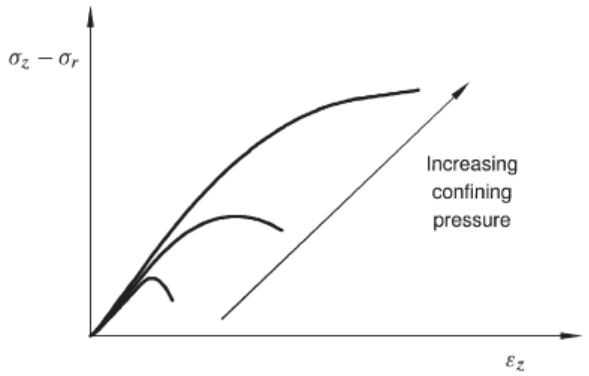

Fig. 2.10. Triaxial test results for different confining pressures (Fjar et al., 2008).

The shear failure, which is caused by excessive shear stress, is the most common failure mode observed in uniaxial and triaxial tests. On the other hand, tensile failure is caused by excessive tensile stress.

2.5.2. Failure

2.5.2.1. Tensile failure

A tensile failure occurs when the effective stress across a plane in the sample exceeds a critical limit (the tensile strength, T_0). A sample that suffers tensile failure typically splits along fracture planes (Fig. 2.11). The fracture planes often originate from pre-existing cracks, oriented more or less normal to the direction of the tensile stress.

The failure criterion specifies the stress condition for which tensile failure will occur and identifies the location of the failure surface in principal stress space

$$\sigma' = -T_0 \qquad \text{Eq. 2.53}$$

For isotropic rocks, the conditions for tensile failure will always be fulfilled first for the lower principal stress

$$\sigma_3' = -T_0 \qquad \text{Eq. 2.54}$$

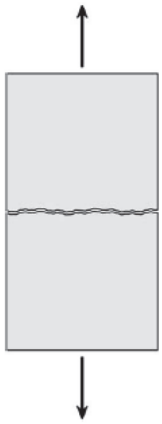

Fig. 2.11. Tensile failure (Fjar et al., 2008).

2.5.2.2. Shear failure

Shear failure occurs when shear stress along some plane in the sample is high enough. Sometimes a fault zone develops along the failure plane and the two sides of the plane move relative to each other in a frictional process (Fig. 2.12).

As introduced above, there are different kinds of failure criteria. The most used is the Mohr criteria, where the frictional force that acts against the relative movement of two bodies in contact depends on the force that presses the bodies together

$$\left|\tau_{max}\right| = f(\sigma') \qquad \text{Eq. 2.55}$$

where τ_{max} is the critical shear stress and σ' is the normal stress across the fracture plane. This assumption is called Mohr's hypothesis. Eq. 2.55 represents the failure surface in the $\tau - \sigma'$ plane that separates a 'safe region' from a 'failure region'. The line is sometimes referred to as the failure line or the failure envelop. An example is shown in Fig. 2.13, in which the three principal stresses and the Mohr's circles connecting them are also indicated. For a given set of principal stresses all possible combinations of τ and σ' lie within the area in between the three circles.

The criterion states that shear fracture takes place when the shear stress equals to the function of the normal effective stress. As it was introduced in Section 2.3.1, only stress states are permitted inside the Mohr's circle when no plane within the rock has a combination of τ and σ' that lies above the failure line (Fig. 2.13) it means that the stress state represents a safe situation. If σ_1' is increased the circle connecting σ_1' and σ_3' will expand, and eventually touch the failure line and the sample fails. Note that the value of the intermediate principal stress (σ_2') has no influence on this situation. Since σ_2' by definition lies within the range (σ_3', σ_1'), it does not affect the outermost of Mohr's circles, and hence it does not affect the failure. Thus, pure shear failure, as defined by Mohr's hypothesis, depends only on the minimum and maximum stresses and not on the intermediate stress. As it is explained above, there are other criteria where σ_2' affects the failure (e.g. the von Mises criteria, the Drucker-Prager criterion, the extended Griffith criterion, explained by Fjar et al., 2008).

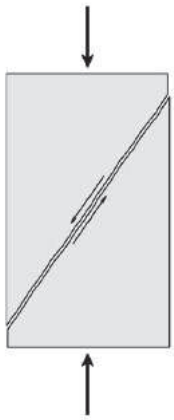

Fig. 2.12. Shear failure (Fjar et al., 2008).

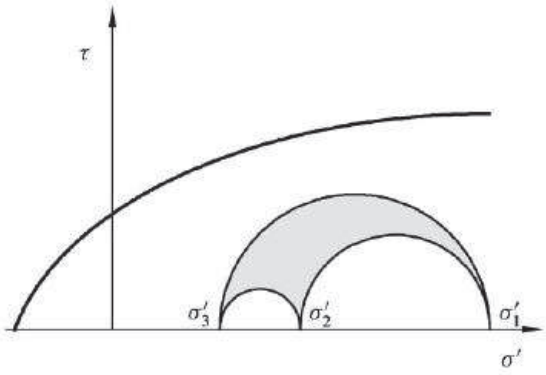

Fig. 2.13. Failure line and Mohr's circles (Fjar et al., 2008).

By choosing specific forms of the function $f(\sigma')$ various criteria for shear failure are obtained. A frequently used criterion is the Mohr-Coulomb criterion, which is based on the assumption that $f(\sigma')$ is a linear function of σ'

$$|\tau| = S_0 + \mu_{\text{int}}\sigma' \qquad \text{Eq. 2.56}$$

where S_0 is the inherent shear strength (also called cohesion or cohesive strength) of the material and μ_{int} is the coefficient of internal friction. The latter term is clearly chosen by analogy with sliding of a body on a surface and the equation was introduced by Cuolomb (1773) as cited in Mogi (2007). As explained above, failure will not occur on any plane for which $|\tau| < S_0 + \mu_{\text{int}}\sigma'$; circles that extend above the failure line have no meaning in this context, since, if the stresses are assumed to increase slowly starting from some 'safe' stress state that lies below the line, failure will occur as soon as the Mohr's circle first touches the line.

In Fig. 2.14 we have drawn the Mohr-Coulomb criterion, and a Mohr's circle that touches the failure line. The angle φ defined in the figure is called the angle of internal friction (or friction angle) and is related to the coefficient of internal friction by

$$\tan\varphi = \mu_{\text{int}} \qquad \text{Eq. 2.57}$$

The angle 2β gives the position of the point where the Mohr's circle touches the failure line. The shear stress at this point of contact is

$$|\tau| = \frac{1}{2}(\sigma_1' - \sigma_3')\sin(2\beta) \qquad \text{Eq. 2.58}$$

while the normal stress is

$$\sigma' = \frac{1}{2}(\sigma_1' + \sigma_3') + \frac{1}{2}(\sigma_1' - \sigma_3')\cos(2\beta) \qquad \text{Eq. 2.59}$$

β and φ are related by

$$\varphi + \frac{\pi}{2} = 2\beta \qquad \text{Eq. 2.60}$$

Since β is the angle for which the failure criterion is fulfilled, β gives the orientation of the failure plane.

The allowable range for φ is from 0° to 90° (in practice the range will be smaller, and centred around approximately 30°), and β may vary between 45° and 90°. One important point to note is that β is given solely by φ, which is a constant in the Mohr-Coulomb criterion. Thus the orientation of the failure plane is independent of the confining stress. This is a special feature for the Mohr-Coulomb criterion.

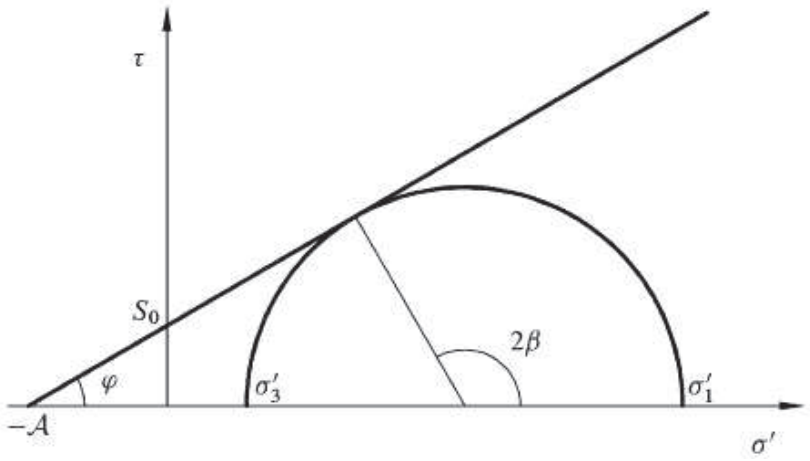

Fig. 2.14. Critical stress state (Fjar et al., 2008).

Mogi (2007) pointed out that the Coulomb fracture criterion appears to apply to fracture of many rocks, except for a low-pressure. Fig. 2.15 shows schematically the strength-pressure curves of various rocks, where it can be observed that the curves of some rocks are concave toward the pressure axis in a low-pressure region.

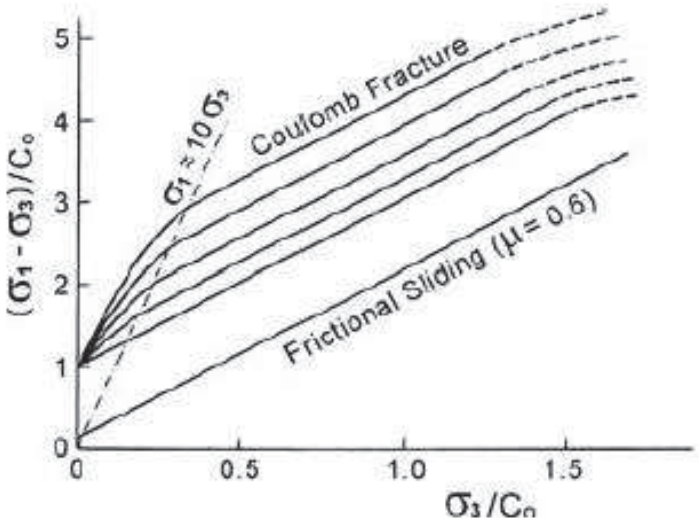

Fig. 2.15. Typical strength versus pressure curves of rocks between regions where Coulomb criterion holds and where it does not hold (Mogi, 2007).

2.6. Summary

In sand production process soil and rock are of interest. Oil reservoirs are sedimentary rocks that may discompose into soil (sands) during oil recovery. Soil and granular rock can be described as a group of grains in contact between them. The void space between grains contains liquid (normally water) and/or air. Particle may be of different sizes. Depending on the size of particles, the distribution of particle sizes, particle shape and soil structure, the ability of the fluid to flow through the particles may be different and it is measured with the coefficient of permeability.

As a first approximation, rocks are considered to behave elastically. The theory of elasticity is based on the concepts of stress and strain and considers a linear relation between them. The elastic moduli have been introduced, as the Young's modulus and the Poisson's ratio.

However, the behaviour of granular rocks and soils depends also on the non-solid part of the material, and the void spaced between grains must be considered. Biot's poroelastic theory has been introduced; this theory is an approach to study the mechanical properties of the media considering its porosity and permeability. In this

theory the concept of the effective stress plays a central and important role. The effective stress is the part of the total stress carried only by the solid framework; the rest of the total external stress is carried by the fluid.

The concept of failure has been also introduced. Rock fails when it is subjected to large stresses and its shape has permanent changes. The strength is a measure of the stress level at which the rock fails. It is usually measured in laboratory tests. The most common tests to measure the rock strength are the uniaxial and the triaxial tests. There is not a unique value for the strength because its value depends on the test being performed. Moreover, there are different kind of failures depending on the direction of the stress applied. The most common failure is the shear failure.

Chapter 3 - Sand production

3.1. Introduction

In this chapter, the sand production problem is defined and oil well conditions are described. The mechanisms of sand production and a description of the prediction methods for sand production are reviewed. Finally, an analytical model proposed by Risnes et al. (1982) is presented.

3.2. Oil wells

3.2.1. Sedimentary rocks

The regions where the hydrocarbons are found are called oil or gas reservoirs. Reservoirs are composed by sedimentary rocks within which the hydrocarbon can flow. Sedimentary rocks of most interest to the petroleum industry are sandstones, chalk, calcarenites and shales; these kinds of rocks are composed by assemblies of bonded particles. Even though the gross behaviour of the different reservoir rocks is similar, the main difference between these rocks is grain size, which affects petrophysical characteristics, such as permeability.

3.2.1.1. Sandstones

There are several processes involved in the formation of a sandstone: weathering, erosion and transportation, deposition and diagenesis process whereby sediments undergo physical and chemical processes as cementation (Cheung, 2010). Formation related properties, such as the PSD and arrangement of the grains as well as

cementation, have a significant impact on the porosity and the structure of the sandstone and this determines the behaviour of the material. Sandstone composition is shown in Fig. 3.1. Sandstones are composed by grains and a finer material (commonly consists of clay minerals or fine particles of quartz) between grains called matrix (Berg, 1986). Grains and matrix are deposited and altered by the physical effects of compaction and chemical changes. The most common mineral in sandstone is quartz, ranging from 65% to practically 100% (Fjar et al., 2008). After deposition and compaction cement appears between particles; the term cement refers to any material that is precipitated after the grains and the matrix have been deposited (Berg, 1986). Sand grains and cementation can be observed in an example of a sandstone in Fig. 3.2. Cementation helps to bind the particles together and the current understanding of cementation is that it increases the strength of a sandstone (Cheung, 2010). Grains of quartz are the major components of many sandstones and intergranular cements are commonly silica and carbonate (Berg, 1986).

Sandstone grain and pore sizes are tipically between 0.01 mm and 1 mm (Fjar et al., 2008); this gives permeabilities raging from microDarcy to several Darcies (where $1\mathrm{D} \approx 10^{-12}\,\mathrm{m}^2$), and makes sandstone more permeable than other sedimentary rocks. Porosities are between 0.1 and 0.4 (Berg, 1986). The porosity of a sandstone depends on the grain sizes, grain shapes, the packing of grains, the degree of cementation, the geological history and the depth at which the sandstone is located.

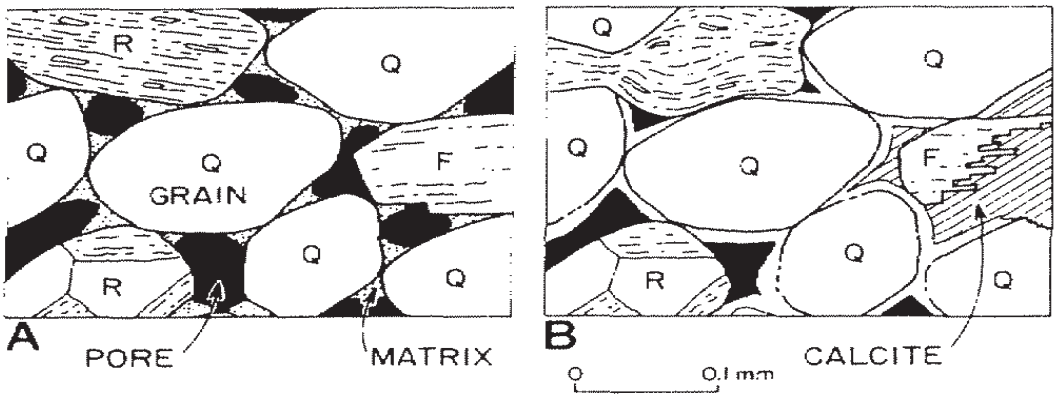

Fig. 3.1. Elements of sandstone: A) grains and matrix after deposition, and B) grains and matrix including silica and calcite as intergranular cement (Berg, 1986). Q = quartz, F = feldspar, R = rock fragments

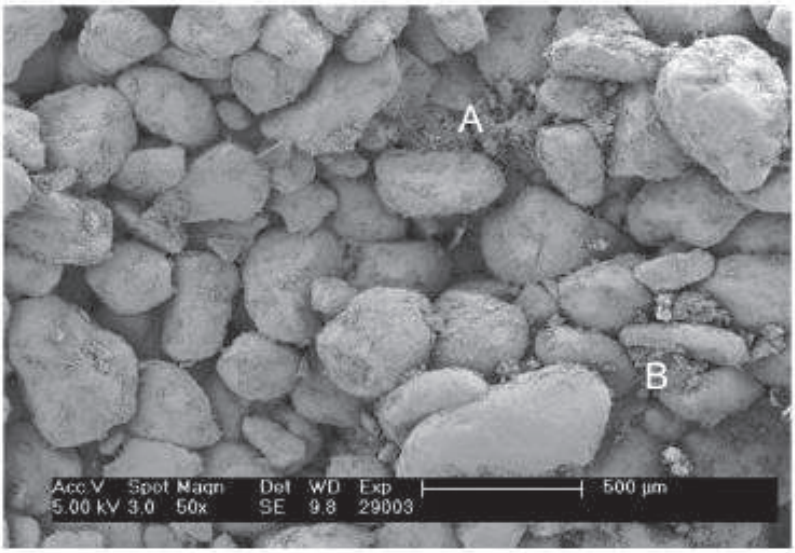

Fig. 3.2. SEM micrograph of Saltwash sandstone (Alvarado, 2007).

Sandstone behaviour above certain confining pressure requires a description based on plasticity theory. The failure envelope is usually nonlinear with a decreasing friction angle at high confining stresses. The friction angle may vary typically between 20° and 40° (Fjar et al., 2008). The stress threshold for grain crushing depends on particle size distribution and particle shape, and on the degree of cementation.

3.2.1.2. Other sedimentary rocks: chalk and shales

Chalks are composed by particles made of crushed organic marine skeletons. Chalks contain calcite, silica and clay minerals (Fjar et al., 2008). Permeabilities of chalk are between µD and mD (Fjar et al., 2008). Chalk porosity may vary depending on the confining pressure; it may be around 0.1 (in normally pressured areas) or it may be as high as 0.4 or 0.7 (Mavko et al., 2003; Fjar et al., 2008).

Shale is a sedimentary rock with a high clay mineral content. Shale porosity may vary the same as chalk porosity (from small porosities of 0.1 to up to 0.7). In addition, the clay minerals contain structurally bound water; it makes measuring and defining the elastic properties of the solid material difficult. Shale texture is strongly anisotropic (Fjar

et al., 2008). Shales have permeabilities between 10^{-3} μD and 10 μD (Reservoir Engineering notes, from Institute of Petroleum Engineering, Heriot-Watt University).

SEM images of chalk and shale are shown in Fig. 3.3 and Fig. 3.4.

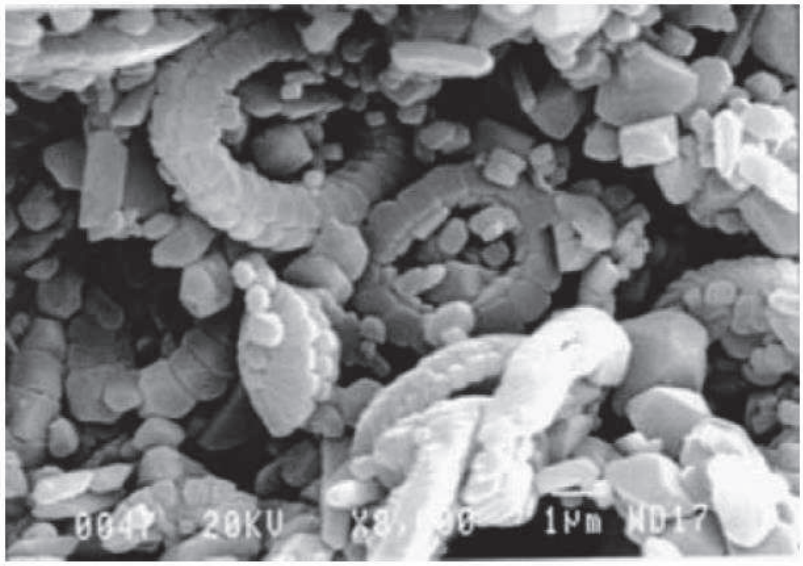

Fig. 3.3. SEM image of Liege outcrop chalk (Fjar et al., 2008).

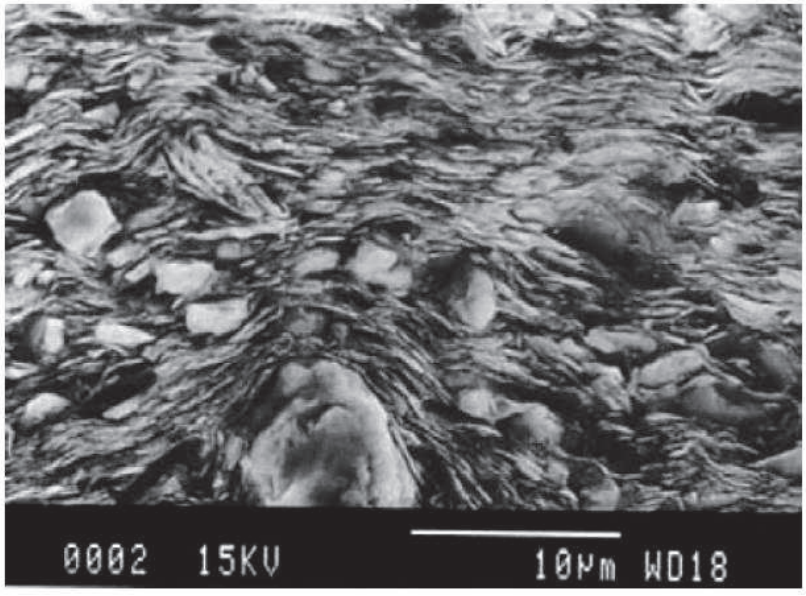

Fig. 3.4. SEM image of Kimmeridge shale (Fjar et al., 2008).

3.2.2. Oil well construction and oil recovery

The first step in the oil well construction is to drill a well to the depth of the reservoir by rotary drilling with the aid of drilling fluid. Fig. 3.5 shows schematic representations of the different ways to drill a well: depending on the exploratory environment different ways to drill a well can be used (vertical, horizontal, directional or multilateral). Oil well holes are usually between 200 and 300 mm in diameter (Cheung, 2010).

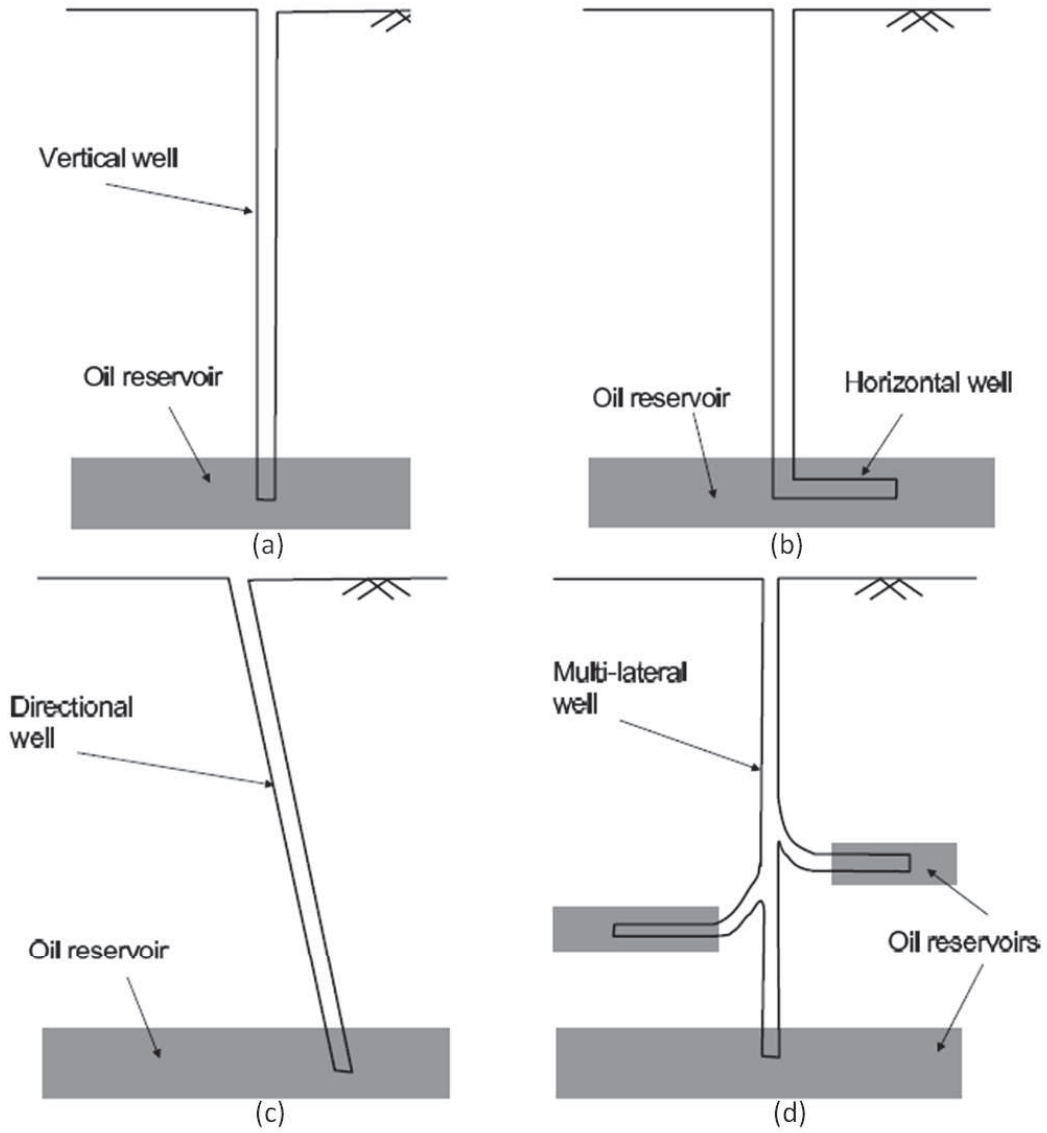

Fig. 3.5. Types of oil well (Cheung, 2010): (a) vertical well, (b) horizontal well, (c) directional well, and (d) multi-lateral well

After drilling, completion is performed: the well is prepared for the hydrocarbon production. In this process the sandstone around the hole can be left unsupported, as in the case of an open-hole completion (Fjar et al., 2008), when the formation is relatively strong and stable. The open-hole allows the hydrocarbons to flow freely into the well through the wellbore wall. The simplest open-hole technique is the natural (or barefoot) completion (Fig. 3.6.a), which do not involve specific equipment to prevent or reduce the consequences of solids production (Bellarby, 2009). Barefoot completions are common and find application in competent formations (especially naturally fractured limestones and dolomites) (Fjar et al., 2008; Bellarby, 2009). Pre-drilled or pre-slotted liners are also considered open-hole completion techniques (Bellarby, 2009); some purposes of these liners are to stop gross hole collapse, zonal isolation and deployment of intervention toolstrings. Pre-drilled and pre-slotted liners are not normally a form of sand control because slots are not usually small enough to stop sand (Bellarby, 2009). On the other hand, active solids control can be used in order to prevent solids from being released from the formation, or prevent produced solids from following the hydrocarbon flow to the surface. A gravel pack or screens can be placed which also may act as a filter for produced solids (Kuncoro et al., 2001; Fjar et al., 2008). Other methods for solids control include chemical consolidation, where the formation is strengthened by a resin injected into the rock (Kunkoro et al., 2001). Fig. 3.8 shows examples of sand control techniques.

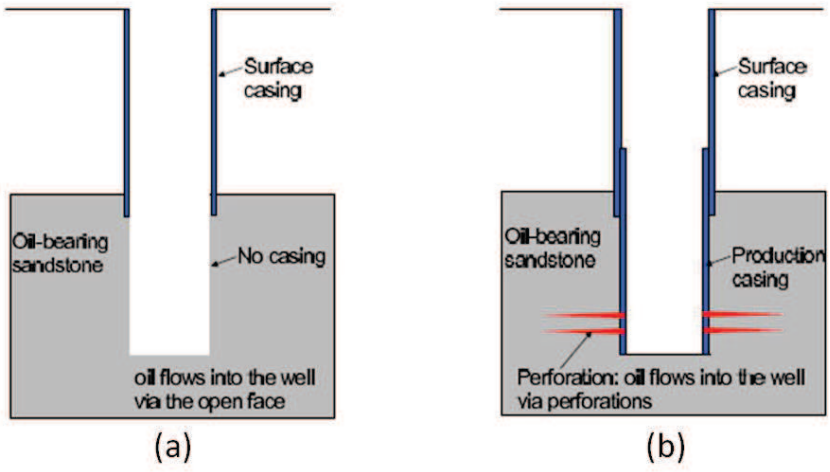

Fig. 3.6. (a) Open and (b) cased completions for oil wells (Cheung, 2010).

In weak formations in order to stabilize the borehole, instead of an open-hole completion, the hole can be supported by casing installed and cemented to the formation (Fig. 3.6.b). The casing is perforated in the reservoir zones, so that the hydrocarbons can flow into the formation (Fjar et al., 2008). A perforation typically generates a cylindrical hole (Fig. 3.7), which becomes conical when the maximum perforation length wants to be achieved (Bellarby, 2009). Typical perforations are 1-2 cm in diameter and 20-50 cm long (Papamichos, 2006; Fjar et al., 2008), or with smaller diameter (5-12 mm) when holes are penetrated deeper (Cheung, 2010). The size and shape of the perforations may vary considerably with the type of charge used, the formation properties, and the well pressure relative to the pore pressure in the formation at the time the perforation is created. Perforation have several advantages over the open hole completion, as the ability to shut-off water, gas or sand through relatively simple techniques, better oil productivity, suitability for fracture stimulation, etc (Bellarby, 2009).

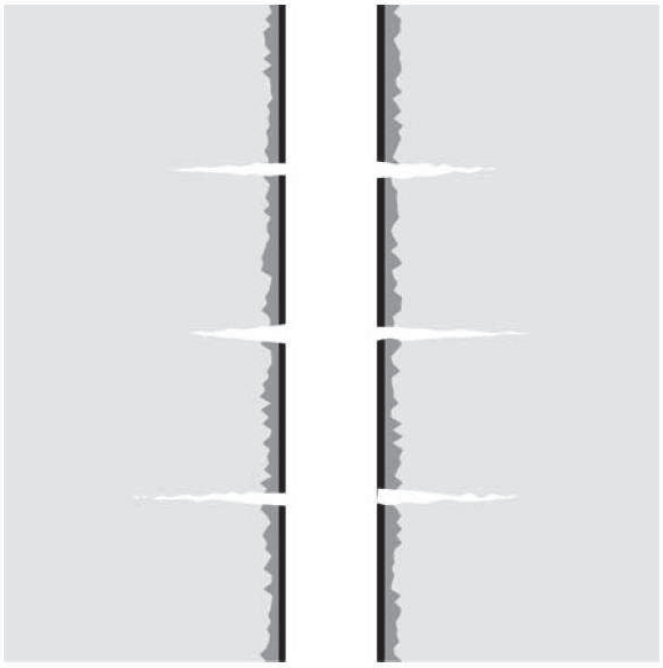

Fig. 3.7. Principle sketch of perforations through the casing and the cement (Fjar et al., 2008).

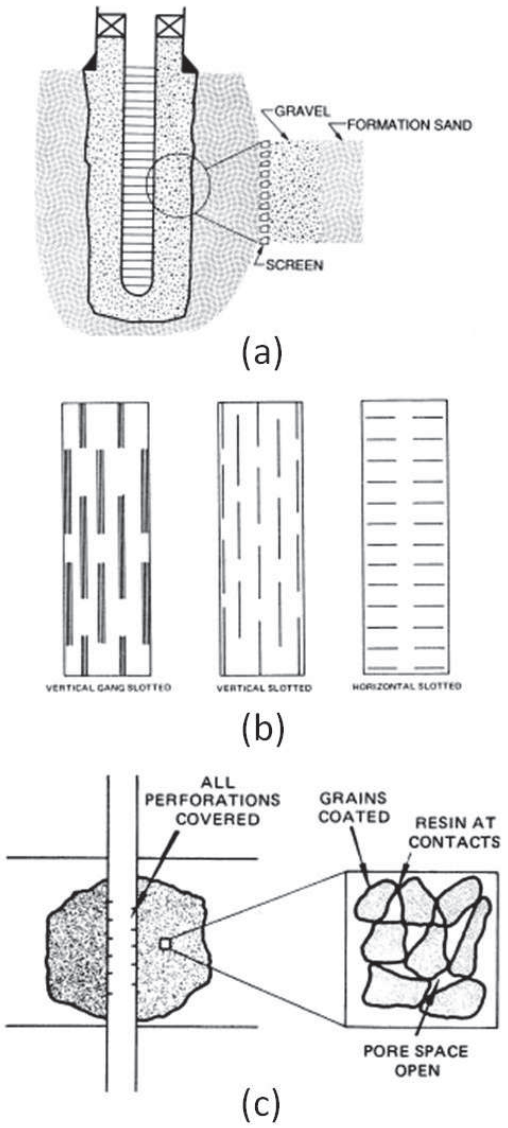

Fig. 3.8. Sand control methods (Penberthy & Shaughnessy, 1992): (a) Gravel packing, (b) screens, and (c) artificial cementation.

A third alternative for well completion is frac packing, where a fracture from the well into the formation is generated pumping a fluid at a high enough pressure down the wellbore than the rock will be broken in tension (Fjar et al., 2008). The fracture is filled with proppants to create a highly permeable slit in the formation, through which the hydrocarbons can be produced.

After completion, oil or gas can be recovered. There are different methods for hydrocarbon recovery, which can be classified as 'natural' or 'artificial' (Fjar et al., 2008;

Cheung, 2010). Natural recovery relies on the properties of the natural material and is difficult to control manually. The sources of energy come from the fluid pressure, the gas dissolved in the oil or under pressure, the mechanical properties of the rock or the gravity. On the other hand, 'artificial' methods include techniques to enhance oil recovery. Some examples of these methods are waterflooding, chemical flooding, thermal recovery and miscible recovery. The idea is to change some material properties such as the viscosity of the oil, the tension of water-oil interface, the relative permeability of the fluid or the pressure which drives oil to the surface. The rate of oil or gas recovery is easier to control when artificial method is used and the extraction rate of oil or gas can be incorporated as part of mitigation strategy of sanding.

3.2.3. Properties of reservoir fluids

Reservoir oil is a mixture of hydrocarbons which may exist in the solid, liquid or gaseous phases, depending on the conditions of temperature and pressure. Reservoir oil can vary from a light liquid with a viscosity similar to water (1 Pa·s) to a very viscous material (100 Pa·s). Even though water has been displaced by the influx of hydrocarbons, it is always present in the pore space of a reservoir.

Gas in the reservoir can be contained in the oil as a solution depending on the pressure of the fluid. When the liquid (oil) is saturated it cannot contain more gas into the solution, what means that there is gas in the solution and gas that is not contained into the oil (hence there are two phases: oil with dissolved gas and the gas that is not into the solution). When the reservoir oil is undersaturated it is capable of containing more gas and the reservoir is single phase. The bubble point is the pressure above which the fluid behavior in the reservoir is single phase and the oil is said to be undersaturated. As the reservoir pressure drops below bubble point, gas can be released and two phases appear, gas and oil. The bubble point depends on the temperature of the reservoir. The oil at surface conditions is termed stock tank oil and the gas produced solution gas.

The oil volume factor B_0 is the relationship between the volume of the oil and its dissolved gas at reservoir condition to the volume at stock tank conditions: volume in barrels (reservoir barrel, rb) occupied in the reservoir by one stock tank barrel (one stock tank barrel, stb) of oil plus its dissolved gas (dissolved gas contained in the produced oil). Values of oil volume factor typical range between 1 rb/stb for crude oil systems containing little or no solution gas to nearly 3 rb/stb for highly volatile oils. The total formation volume factor B_t or the two-phase volume factor is defined as the volume occupied in the reservoir by one stock tank barrel of oil plus the free gas that was originally dissolved in it. The volume of one UK barrel is 164 L, and the volume of one US barrel is 119 L.

The specific gravity of a liquid is the ratio of its density to that of water at the same temperature and pressure. It is sometimes measured at 60° and 1 atm. The petroleum industry uses another term called $^\circ$API gravity where

$$^\circ\text{API} = \frac{141.5}{\gamma_0} - 131.5 \qquad \text{Eq. 3.1}$$

where γ_0 is specific gravity at 60° and 1 atm. Values of the specific gravity of the oil range between 10 and 50 $^\circ$API, equivalent to γ_0 values between 1 and 0.8.

3.3. Sand production: problem definition

During the oil recovery, the rock around the wellbore is plastified, decohesioned and weakened due to the stress changes around the cavity (Papamichos, 2006). The weakened and decohesioned material may be eroded away by the produced fluid. Sand production is the erosion of the formation sand during this process. It often occurs in sandstone reservoirs. The sand production is usually given in petroleum engineering in

pounds per thousand barrels (pptb). This is the weight of the sand divided by the volume of the oil in one thousand barrels (volume of the sand production divided by 164 m^3 for UK barrels or divided by 119 m^3 for the US barrels). Table 3.1 gives examples of sand production values of two different field data. Veeken et al. (1991) reported that typical sand production levels (for a manageable regime and not chocking the field) are 2.1-210 pptb in oil producers.

Papamichos (2006) described three types of sand production depending on the sand production rate: the no sand regime, the manageable sand regime, and the catastrophic sand regime (when sand is produced at such a high rate that the well is chocked). It is important to predict both the onset of sand production and the moment when the catastrophic sand regime is initiated, because sometimes the manageable sand regime can be a good choice (as it is explained below).

On the other hand, Veeken et al. (1991) classified sand production types in three different kind of categories, depending on the frequency of the events: the transient sand production, the continuous sand production and the catastrophic sand production. Transient sand production refers to a sand produced concentration decreasing in time under constant well production conditions in these conditions the sand concentration, the cumulative sand volume and the decline period vary considerably. The continuous sand production occurs when the sand is produced constantly. Catastrophic sand production refers to events where a high rate sand influx causes the well suddenly choke and/or die. The continuous and catastrophic sand production cases are not so distant because catastrophic sand production could also be the result of a large continuous sand cut (Veeken et al., 1991).

Sand production increases the porosity close to the oil well; this can have a beneficial effect on the hydrocarbon production (Geilikman & Dusseault, 1997; Vaziri et al., 2002). However, several problems may arise due to sand production: clogging up of the well, damage of the well equipment (e.g. erosion of the production equipment), well instability due to the loss of material and damage of the formation, the necessity to handle large amounts of solids at the rig, etc (Fjar et al., 2008). Moreover, sand production will lead to a change in the geometry of the producing sand face.

Table 3.1. Examples of sand production.

Reference	Well	Average sand produced (pptb)	Maximum sand produced (pptb)	About the well
Veeken et al. (1991)		0-5	30	Light oil well
Palmer et al. (2003)	**A/3**	40	120	Unconsolidated sand reservoir
Bibobra et al. (2015)	**X17**	0.005	0.8	Fields in the Niger Delta oil province
Bibobra et al. (2015)	**WX4**	0.1083	35.46	Fields in the Niger Delta oil province
Bibobra et al. (2015)	**W5**	2.89	319.9	Fields in the Niger Delta oil province
Al-Awad and Al-Ahaidib (2005)	**51**	10	200	Medium oil from a weak sandstone formation
Al-Awad and Al-Ahaidib (2005)	**48**	10	60	Medium oil from a weak sandstone formation
Al-Awad and Al-Ahaidib (2005)	**20**	10	30	Medium oil from a weak sandstone formation
Al-Awad and Al-Ahaidib (2005)	**11**	10	20	Medium oil from a weak sandstone formation
Dickson (2014)	**A-64-D4**	33	40	Unconsolidated sandstone - Niger Delta wells
Dickson (2014)	**A-64-D2**	3	8	Unconsolidated sandstone - Niger Delta wells
Dickson (2014)	**A-65-D8**	2	2	Unconsolidated sandstone - Niger Delta wells

Consequently, studying the sand production process and developing methods to control sanding are of paramount importance for safe and economical hydrocarbon production. On the other hand, overestimating the risks of sand production could lead to installation of unnecessary sand control equipment with huge cost implications. For some sand regimes the sand may be produced at such a low rate that it is still acceptable from an operational point of view. Therefore, it is of interest to be able to predict not only the conditions for onset of sand production, but also the rate of sand production.

There are different parameters influencing sand production. These parameters can be grouped into three categories (Table 3.2): the physical properties of the reservoir formation and the fluid, the well installation and completion, and the petroleum recovery process (Veeken et al., 1991).

Cement bonding may have a significant impact on sand production. Strong bonding in the material 'delays' particle breakage and prevents significant particle movements. The cemented material may be located along the pore channels, what reduces both porosity and permeability.

There are different kinds of sand control strategies that can be incorporated in the design and installation of the perforations along which the oil flows into the well. Mechanical retention is a sand control mechanism that retains a certain portion of the formation material; horizontal well screens and gravel packs are the mechanical retention methods more used (Kuncoro et al., 2001). Plastic consolidation is also a sand control mechanism where the formation sand is cemented with some chemical injected to reduce the permeability around the wellbore (Kuncoro et al., 2001). Controlling oil recovery rate can also be considered part of the sand production control strategy. Finally, perforation design may be also an element to take into account in the sand control strategy (Bellarby, 2009; Cheung, 2010). Perforations reduce sanding potential because perforation diameters are smaller than a wellbore.

Table 3.2. Parameters influencing sand production (Veeken et al., 1991).

FORMATION Rock - Strength - Vertical and horizontal in-situ stresses (change during depletion) - Depth (influences strength, stresses and pressures) Reservoir - Far field pore pressure (changes during depletion) - Permeability - Fluid composition (gas, oil, water) - Drainage radius (maximum radius of fluid production) - Reservoir thickness - Heterogeneity
COMPLETION - Wellbore orientation, wellbore diameter - Completion type (openhole/perforated) - Perforation methods (height, size, density, phasing, under/overbalance) - Sand control (screen, gravel pack, chemical consolidation) - Completion fluids, stimulation (acid volume, acid type) - Size of tubulars (casing)
PRODUCTION - Flow rate - Drawdown pressure (difference between the average reservoir pressure and the wellbore flowing pressure) - Flow velocity - Damage (skin; variations in permeability in the critical near-wellbore region) - Bean-up*/shut-in policy (flow regulation processes that cause pore pressure fluctuations- Bean-up is a sequence of choke settings in the start-up of a well to apply stresses in the formation with the intention of strengthening the formation) - Artificial lift technique - Depletion - Water/gas coning - Cumulative sand volume

3.4. Mechanisms of sand production

Sand production process involves two mechanisms: localized plastification and failure of the rock around the cavity and the transportation of sand particles (erosion) due to the fluid drag (Papamichos, 2006). These two mechanisms are coupled to each other, since stress concentrations around the cavity lead to localized damage, which increases the amount of cohesionless material, and the decohesioned matrix of sand particles may be mobilized by the fluid flow. Moreover, the erosion of sand particles may reduce the strength and increase the instability around the cavity. Methods used to recover the reservoir oil, described in Section 3.2.2, affect sand production, as for example waterflooding; in this method water is pumped into the reservoir to 'push' the oil to flow, and is regarded as one of the causes of sand production.

To study experimentally the stress behaviour around the borehole and how it affects sand production process, modified thick wall cylinder (TWC) tests have been carried out by many researchers (e.g. Papamichos et al., 2001; Papamichos & Vardoulakis, 2005; Ispas et al., 2006). According to these tests, when the rock near the cavity reaches the peak strength, it yields and plastifies. Increasing external stress, localized failure occurs to the weakened material. Continued sand production depends on growth of the weakened zone, which requires increase of the external stress level (Tronvoll et al., 1997). Two different failure patterns are shown in Fig. 3.9, the lateral and the axial failure. Lateral failure occurs for high circumferential stress near the cavity, and axial failure occurs for high axial stress near the cavity. Lateral failure is in the form of breakouts or shear bands that run all along the length of the hole, and axial failure is in the form of shear bands toroidally shaped around the perimeter of the hole (Papamichos, 2006).

Erosion is the transport of sand particles through the rock matrix and it has been also proposed as another mechanism leading to sand production (Papamichos & Vardoulakis, 2005; Papamichos et al., 2001). Erosion occurs either when the drag force of the fluid is large enough to overcome the cohesive strength of the material and carry the particles away or when the drag force of the fluid is large enough to carry the

dislodged and weakened materials away with the flow. Finer particles (original depositional or created by particle breakage) can also be transported by the fluid. The erosion has the effect of reducing the strength and/or increasing the permeability of the rock at these sites. Tronvoll et al. (1997) observed experimentally that once sand production is triggered, it appears to depend on the fluid rate.

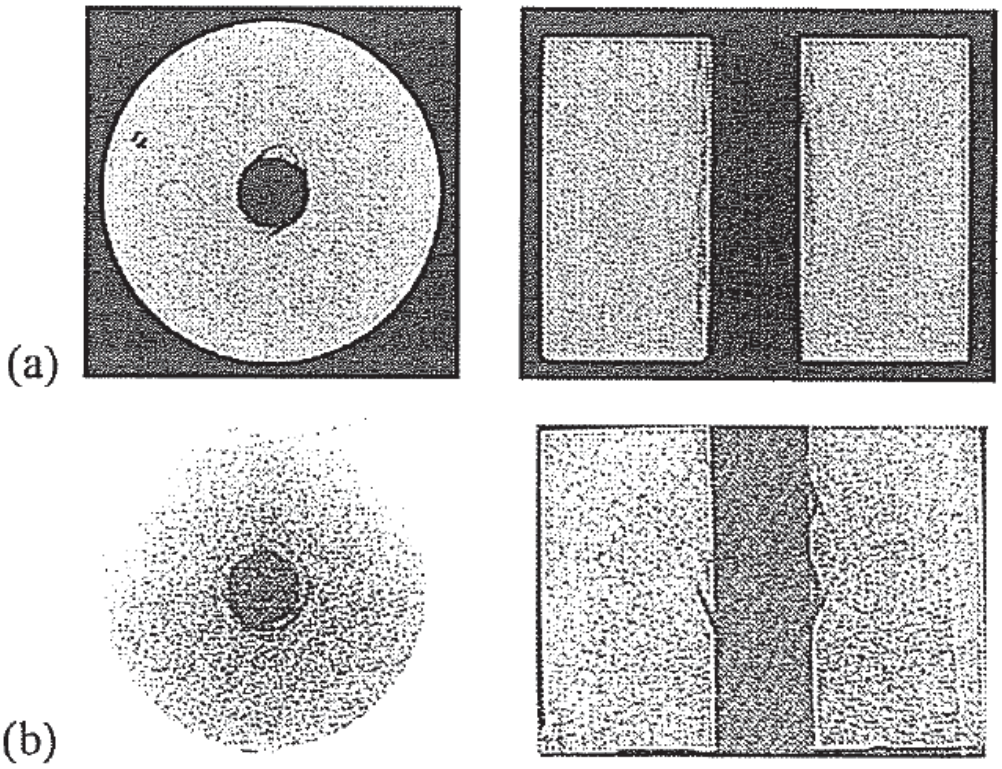

Fig. 3.9. CT (Computer tomography) scan sections normal and parallel to the hole axis showing cavity failure due to high (a) circumferential and (b) axial stress on Red Wildmoor sandstone (Papamichos, 2006)

A sequence of X-ray Computer Tomography (CT) scans of a specimen under compression and radial fluid flow towards the cavity is shown in Fig. 3.10. The material initially fails close to the cavity; with increasing stress more material fails and it is eroded and removed by the flowing fluid resulting in a larger cavity.

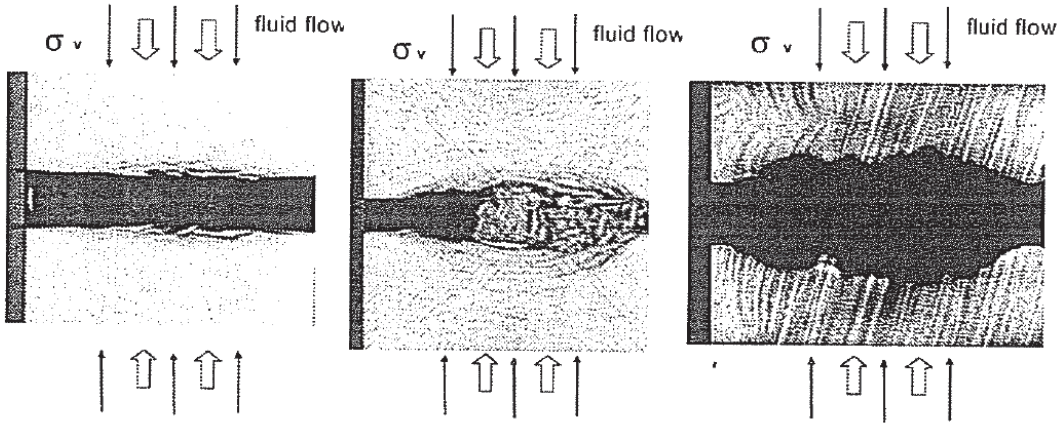

Fig. 3.10. Sequence (left to right) of perforation failure and sand erosion under external compression and fluid flow towards the cavity. X-ray CT scan sections along the hole axis of a hollow cylinder specimen tested in a laboratory (Papamichos, 2006)

3.5. Sand production prediction methods

Predictions for where and under which conditions sand production occurs, and also the sand production rate, are an important part of the study for an optimal well development, completion and exploitation strategy. To predict sand production there are different methods commonly used. These methods can be classified into four different categories: empirical methods, laboratory methods, theoretical modelling and numerical methods.

Field observations, laboratory experiments, theoretical modelling and numerical methods are highly complementary and should be combined to ensure a realistic and consistent approach to sand production prediction. Laboratory tests and theoretical modelling should be calibrated and validated using field data (Rahmati et al., 2013). Moreover, the extrapolation of laboratory tests to field conditions requires theoretical modelling and, on the other hand, theoretical modelling needs laboratory strength data as an input. Finally, theoretical models are calculated for each sand production problem using numerical methods.

3.5.1. Empirical methods

Empirical methods link several parameters from the field and monitoring data to predict sand production onset (Veeken et al., 1991). Correlations of the parameters listed in Table 3.2 are often dependent on the location, the well completion method and might vary from one oil-field to another. Normally, only a small selection of parameters is used due to the practical difficulties of monitoring and recording data of all the wells in a field (Veeken et al., 1991). These methods do not offer means to estimate the amount of sand production, therefore sand production is usually overestimated and lead to unnecessary sand controlling installation.

One method based on empirical correlations is establishing a critical depth. This criterion is based on the assumption that rock strength usually increases with depth. Below the critical depth sand control is not needed. The critical depth is established from field experience. This method is used in several deltaic environments (Veeken et al., 1991). Another example of an empirical criterion depending in only one parameter is to avoid porosities higher than 0.3 (Bellarby, 2009).

Another method based on empirical correlations specifies the maximum allowable drawdown for a vertically cased perforated well for sand free oil recovery (Vaziri et al., 2002). Drawdown is defined as the difference between the pore pressure far from the well and the well pressure. It is often convenient to use drawdown rather than well pressure to describe the pressure conditions in the well. The critical drawdown is the maximum drawdown value for which no sand is produced. The critical drawdown depends on the depth of the reservoir (Vaziri et al., 2002), therefore it is usually an empirical method depending on two parameters. Drawdown pressure and sonic transit time (the time sound travels across the reservoir per unit distance, obtained with borehole acoustic and wave propagation methods) can also be correlated (Veeken et al., 1991) as it is shown in Fig. 3.11.

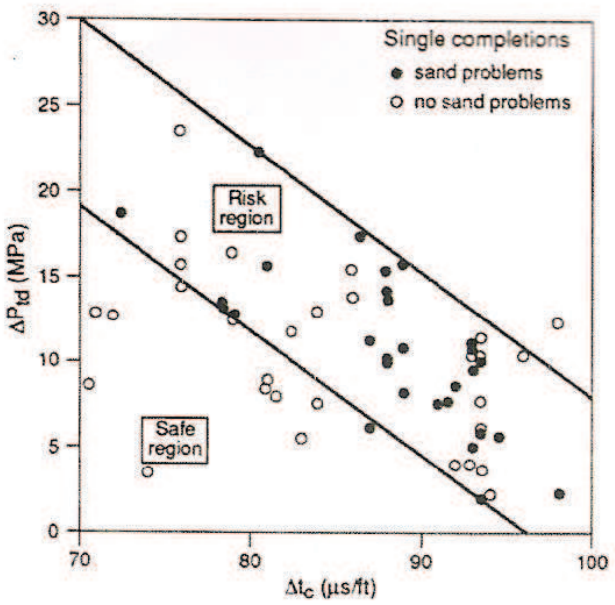

Fig. 3.11. Total drawdown (ΔP_{td}) versus transit time (Δt_c) for intervals with and without sand problems (Veeken et al., 1991)

Sand production can also be correlated with more than one parameter at the same time (e.g. depth, production rate, drawdown pressure, productivity index, shaliness, etc). For example, Palmer et al. (2003) developed an empirical model to predict the onset of sand production correlating the critical bottom hole flowing pressure (the fluid pressure at the bottom of the hole when the sand production starts), the reservoir pressure and the total principal major and minor stresses. In this model, the criterion for sanding is (Vaziri et al., 2002; Palmer et al., 2003)

$$CBHFP < \frac{3\sigma_1 - \sigma_3 - \sigma_Y}{2 - A_p} - P_r \frac{A_p}{2 - A_p} \qquad \text{Eq. 3.2}$$

where *CBHFP* is the critical bottomhole flowing pressure (the minimum fluid pressure at the bottom of the hole), P_r is the current average reservoir pressure, σ_1 and σ_3 are the total principal major and minor stresses, A_p is a poroelastic constant $A_p = \frac{1-2\nu}{1-\nu}\alpha$

(where ν is the Poisson's ratio, defined in Eq. 2.20, and α is the Biot coefficient, defined in Eq. 2.47) and σ_y is the formation strength near the opening

$$\sigma_y = 3.1 \cdot S_{TWC} \qquad \text{Eq. 3.3}$$

where S_{TWC} is the strength as determined in the thick-walled cylinder test. The factor 3.1 includes the scale transformation from TWC laboratory sample to field. TWC laboratory test is explained in next Section 3.5.2.

3.5.2. Laboratory methods

In-situ testing is a difficult task due to the costs involved in testing at reservoir depth. In order to observe and simulate sand production in a controlled environment, laboratory sand production experiments using modified TWC tests are carried out by many researchers (e.g. Veeken et al., 1991; Papamichos et al., 2001; Wu and Tan, 2002; Nouri et al., 2004, 2006; Ispas et al., 2006; Papamichos, 2006; Papamichos et al., 2010; Dresen et al., 2010; Fattahpour et al., 2012). This kind of testing gives insights into the sand production mechanisms and in the influence of the various field and operational parameters on sand production. However, these tests have some limitations, as it is easier to sample stronger rock than weak and uncemented rock. Moreover, Holt et al. (2000) and Alvarado (2007) highlighted that core samples from deep holes experience stress-release during sampling; this makes the experimental results gathered by testing these samples not an appropriate representation of the in-situ behaviour of the material and might provide a false representation of the likelihood of sand production.

Schematic examples of modified TWC tests are shown in Fig. 3.12. The outer diameter of the samples is usually up to 100 mm (larger than the usual TWC tests) and the size of the inner cavity is about 20-25 mm. The inner cavity can be drilled through all the sample

from one end to the other (Papamichos et al., 2001); however, to assess the end effects of a perforation, some researchers (e.g. Ispas et al., 2006) have carried out tests on samples where the inner cavities were drilled only one third to half way into the sample. In some tests, fluid flow is introduced into the sample in order to study its impact (e.g. Tronvoll, 1997; Papamichos et al., 2001; Papamichos, 2006; Ispas et al., 2006; Nouri et al., 2004, 2006; Fattahpour et al., 2012). The axial and confining stress can be controlled independently; therefore, samples can have anisotropic stress conditions (e.g. Nouri et al., 2004, 2006; Ispas et al., 2006; Papamichos et al., 2010). To provide a 3D view of the failure patterns, some researchers have used X ray CT scans (e.g. Ispas et al., 2006; Papamichos, 2006; Papamichos et al., 2010), as shown in Fig. 3.13.

Some examples of results obtained using TWC are summarized in Table 3.3.

Theoretical models (e.g. Risnes et al., 1982; Chen & Haberfield, 1999) and numerical analysis (e.g. Papamichos et al., 2001; Nouri et al., 2004, 2006) sometimes are used to better understand the problem and to evaluate the stresses distribution across the sample in laboratory tests. Moreover, the predictions of finite element modelling may be calibrated with strength data from TWC tests on material from the actual formation. On the other hand, theoretical sand prediction models can be validated against the laboratory observations and the laboratory sand production experiments can be used as a field sand production tool after translation of the test results to the field situation. Finally, TWC experimental results can be used to develop an analytical model (e.g. Papamichos et al., 2010).

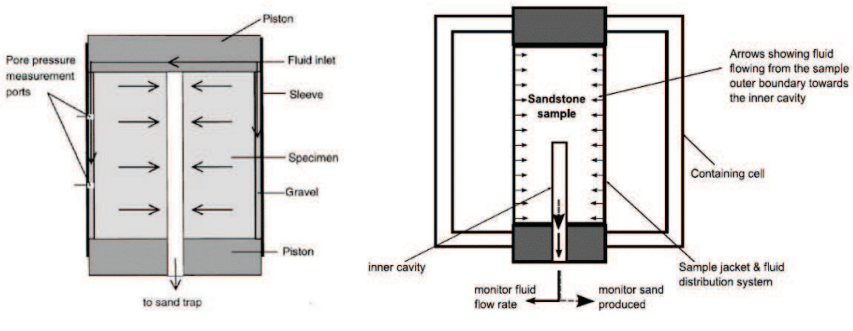

Fig. 3.12. Modified TWC tests for sand production research (Cheung, 2010): (a) Papamichos et al. (2001), and (b) Ispas et al. (2006).

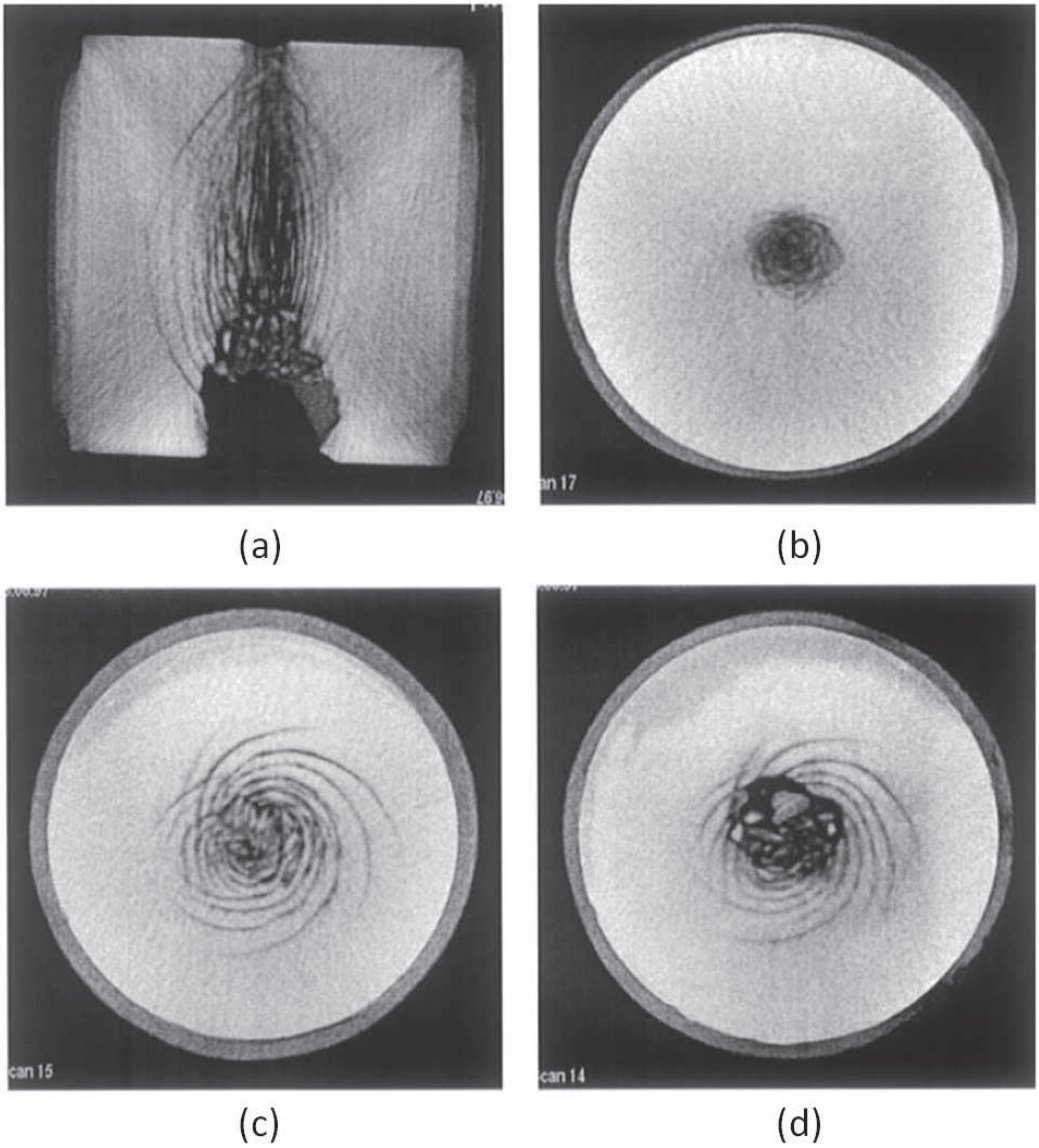

Fig. 3.13. X-ray CT scans of the testes specimen (Papamichos, 2001): (a) vertical cross section, and (b) upper, (c) middle, and (d) lower horizontal cross section.

Table 3.3. Laboratory tests results given in the literature.

	Laboratory results
Dresen et al. (2010)	The borehole breakouts initiated close to the borehole wall and formed a symmetric and planar structure. There was a critical isotropic stress required to initiate borehole breakouts. That critical isotropic stress decreases with increasing borehole radius and converges towards the uniaxial compressive strength.
Papamichos et al. (2010)	Under unequal lateral stress the hole strains in the major and minor lateral stress directions were different. An axial stress anisotropy had a significant effect on the borehole failure mode, with failures occurring in planes normal to the hole axis.
Papamichos (2006)	The cavity failure strength increased with decreasing the hole diameter. The size effect was also observed to depend on the sandstone class with the brittle sandstones exhibiting stronger size effect, the ductile milder size effect and the compactive practically none existent size effect.
Papamichos et al. (2001)	For low stress levels, it was osbserved that there was not a clear correlation of sand production wih fluid flow rates. As the external stress increased, the sand production rate increased with fluid flow rate. Above a critical fluid flow rate the sand production rate increased gradually with increasing fluid flow rate.

3.5.3. Theoretical modelling - Analytical methods

There are different kind of theoretical sand prediction tools depending on the sand failure mechanism considered in the formulation. These mechanisms responsible for sand production are: compressive failure, tensile failure and erosion (Veeken et al., 1991). Failures and erosion occurs near the cavity wall. Shear-compressive failure refers to excessive circumferential stress near the cavity which causes shear failure of the formation material. Tensile failure refers to a tensile radial stress exceeding the tensile failure envelope. Erosion occurs when the drag forces of the fluid flow exceed the apparent cohesion of the particles, and it is a special form of tensile failure.

Compressive failure modelling result is extremely sensitive to the choice of yield envelope and failure criterion (Veeken et al., 1991). One may choose between e.g. Drucker-Prager and Mohr-Coulomb yield envelopes and between failure criteria based on maximum plastic strain, maximum plastic zone size or maximum stress, etc. The material model needs to be validated against lab and field sand production data. Theoretical modelling of compressive failure is useful in qualitative terms. A reasonable consensus exists on how to model a tensile failure (Veeken et al., 1991). Tensile failure provides a reasonable description of laboratory sand production tests carried out using unconsolidated sand (cohesion corresponding to capillary forces) and weakly consolidated material (which experienced dilation). The combined use of compressive and tensile failure in the shape of a stability diagram has been introduced by Morita et al. (1989a,b). Finally, there is a class of sand production models based on erosional mechanisms (e.g. Vardoulakis et al., 1996; Geilikman & Dusseault, 1997). In these models fluid velocity becomes an important factor and the erosion mechanism is such that grains can pass through interconnected void spaces. Furthermore, matrix defects are considered as erosion starter points (Nouri et al., 2006).

Analytical methods are only suitable to predict the onset of sand production (Rahmati et al., 2013). Analytical methods have some limitations, as most of them are only valid under simplified geometrical and boundary conditions. Due to this limitation they are not valid in complicated field-scale problems (Rahmati et al., 2013).

3.5.4. Numerical methods

3.5.4.1. Continuum approaches

Continuum models are commonly used to simulate the behaviour of the soil. The two methods that are usually applied are the finite difference method (FDM) or the finite element method (FEM). Sand production is usually predicted with continuum fluid-mechanical coupled models, where the reservoir rock is treated as a continuum. Stress and strain can be calculated around the wellbore and the effect of fluid flow can be examined. The volume of sand particles produced can be estimated setting a sanding criterion. Therefore, using a continuum model the formulation of several constitutive relations is necessary: a stress-strain relation for the solid skeleton (constitutive model), a description of the fluid flow, a coupling between flow and skeleton variables (e.g. an effective stress definition) and a sanding criterion to identify the volume produced.

Near the wellbore strong deformations of the host formation, leading to complete disaggregation are characteristic, and elastic and elastic-plastic formulations that are typically used in many rock mechanics applications, cannot be used with confidence. Indeed, Rahmati et al. (2013) pointed out that the optimum constitutive models are those that are based on the critical state theory and use a combined isotropic and kinematic hardening model which allows capturing all kinds of failure (shear, tensile ad compressional).

For the fluid flow description, these models usually assume a Darcian flow (e.g. Papamichos & Vardoulakis, 2005). Despite the successes obtained (e.g. Papamichos & Vardoulakis, 2005; Nouri et al., 2006) it is recognized that solutions based on Darcy's formulation are not valid for the sand production problem, which requires a numerical approach that can handle flow regimes that range from creeping to high Reynolds types of flows near the wellbore.

A sanding criteria must also be used to simulate the mechanisms responsible for sand production (Rahmati et al., 2013). A realistic sanding criterion consists of a combination

of erosion criterion, tensile criterion and compression criterion, and must consider the effect of fluid flow in the eroded material (Rahmati et al., 2013). Finally, changes in boundary conditions should be considered because as sand is produced a sanded zone is formed around the borehole or the perforations (Rahmati et al., 2013).

Summarizing, it is fair to say that the formulation and verification of the constitutive relations required in a continuum model of the sanding problem remains a difficult task, because of the large number of interactions and non-linearities intrinsic to the problem.

3.5.4.2. Discrete element method

The difficulties presented by continuum approaches have encouraged the use of discrete-element based approaches, which by redefining the fluid and/or the solid physics at the micro-scale allow a simpler formulation of the problem and a better understanding of some of its features. For instance, the disaggregation of particles from the rock mass and its transport through the pore structure can be most naturally described in DEM models. DEM can model the effects of bonding, as well as the relative translation, sliding and rotation between the particles.

DEM can also be used to investigate the sanding problem under the influence of fluid flow. The fluid-solid coupling is a two stage modelling process. Firstly the fluid system is solved based on the problem geometry in the DEM model and the fluid boundary conditions. Subsequently, the forces on the individual particles exerted by the fluid are calculated and applied to the DEM particles as external forces. Finally, depending on the type of the coupled DEM-fluid approach, different types of fluid flows can be used, including flows at high Reynolds numbers.

Even using DEM a number of constitutive (solid-solid contact law; fluid-solid interaction) and numerical choices (e.g. 2D vs 3D) remain and, therefore, a variety of sand production models of the problem have been proposed with different focus and features (e.g. Dorfmann et al., 1997; Quadros et al., 2010; Boutt et al., 2011). Cheung (2010) performed three-dimensional simulations coupling DEM with fluid flow to model

sand production. A detailed discussion of this work is postponed until Chapter 6, after the fundamentals of DEM and coupled fluid-DEM models have been presented.

Although DEM-based methods are recognized as useful tools to understand the mechanism of sanding, they also suffer from several shortcomings (Rahmati et al., 2013). First, they are computationally costly and therefore the size of problems that can be practically computed is limited. Furthermore, in most models the micro properties cannot be determined by direct measurements but need to be calibrated instead on macro responses, by reproducing separate laboratory tests. This is frequently a slow and difficult process.

3.6. Stresses around a wellbore – Risnes solution

Despite the limitations indicated before for their application in practical problems, analytical methods remain interesting because they offer a benchmark against which more advanced numerical methods can be validated. With this purpose in mind we expose here one of the better known analytical solutions, that due to a Norwegian team lead by the late R. Risnes.

Risnes et al. (1982) obtained stress distributions around a wellbore or cavity applying theories of elasticity and plasticity, assuming the problem to be axi-symmetric and that the reservoir material is elastic perfectly plastic with a Mohr-Coulomb failure criterion. The fluid flow through the material was assumed Darcyan. Moreover, the flow is assumed stationary and constant pore pressure conditions are supposed to apply. The geometry is shown in Fig. 3.14. The material adjacent to the cavity, bounded by radius R_c behaves plastically and the material outside this zone is assumed to behave elastically.

Risnes et al. (1982) derived analytical expressions to estimate the radial, circumferential and vertical stress in the material as a function of the radial distance from the centre of the cavity. The solution assumed the existence of an inner plastic zone, closer to the cavity, and an outer elastic zone. The limit between the two zones is the plastic radius or the plastic boundary. That is a common assumption in cavity expansion theory (e.g.

Yu & Houlsby, 1991; Yu, 1992; Yu & Rowe, 1999). The material is supposed initially elastic, and after initial yielding at the cavity wall a plastic zone within the region between the inner wall and the plastic radius forms (Yu, 1992).

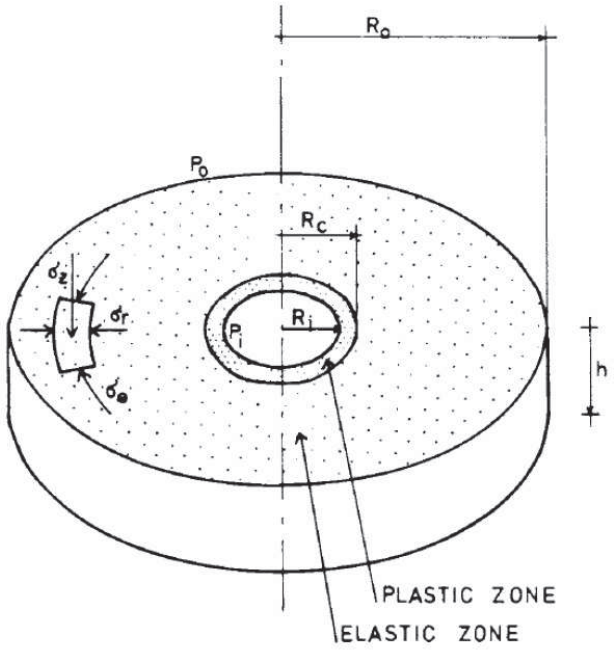

Fig. 3.14. Geometry considered by Risnes et al. (1982)

Expressions for the stresses in both zones were proposed. They are not unique, but dependent on the relative magnitudes of radial, circumferential and vertical stresses at the plastic boundary. A Poisson's ratio limit was found: for Poisson's ratio greater than the limit value, the circumferential stress is the greatest at the elastic/plastic boundary, while the vertical stress is greatest for smaller values. The Poisson's ratio limit value is given by the following expression:

$$\nu' = \frac{\left(\tan^2\phi + 1\right)\sigma_{zo} - \left[\tan^2\phi(2\alpha - 1) + 1\right]P_o - 2S_o\tan\phi}{\left(3\tan^2\phi + 1\right)\sigma_{zo} - \left[\tan^2\phi(4\alpha - 1) + 1\right]P_o - 2S_o\tan\phi} \qquad \text{Eq. 3.4}$$

where ϕ is the passive failure angle of the material ($\phi = 45^\circ + \varphi/2$, where φ is the internal friction angle), σ_{zo} is the vertical stress at the outer boundary, α is the Biot coefficient, P_o is the fluid pressure at the outer cylindrical boundary and S_o is the cohesive strength. Fig. 3.15, Fig. 3.16 and Fig. 3.17 show the dependence of the Poisson's ratio limit on the fluid pressure for different parameters.

It can be observed that the Poisson's ratio limit increase when the friction angle decrease. The Poisson's ratio limit for friction angles greater than 40° and smaller than 30° are unrealistic values for rocks (e.g. Section 5.4.1, Table 5.3). In that cases the Poisson's ratio value increases when the pore pressure increases and these limits are greater than the typical values for rocks (e.g. Table 5.3). For friction angles between 30° and 40° the Poisson's ratio limit has a value around the typical range for rocks (between 0 and 0.3, e.g. Table 5.3) and a special care should be taken because the relative order of the principal stresses will depend on the pore pressure value. In Fig. 3.16 and Fig. 3.17 it is shown that the dependency of the Poisson's ratio limit always decrease when the pore pressure increases. Poisson's ratio limit value only increases with the pore pressure when the friction angle is greater.

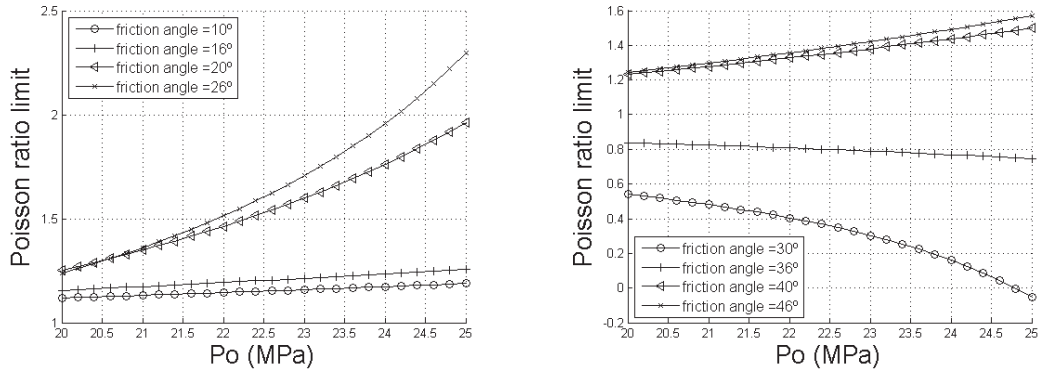

Fig. 3.15. Poisson's ratio limit versus pore pressure at the outer cylindrical boundary (P_o) for different values of friction angle φ, $\alpha = 1.0$, S_0 = 35 MPa and $\sigma_{zo} = 50\text{MPa}$.

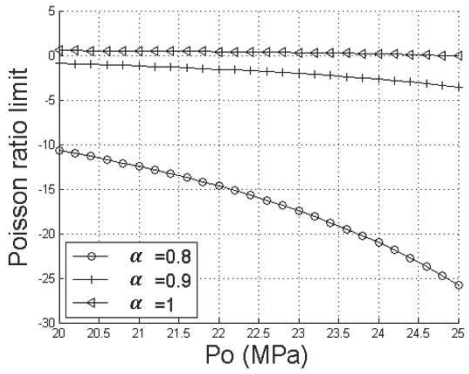

Fig. 3.16. Poisson's ratio limit versus pore pressure at the outer cylindrical boundary (P_o) for different values of α, $\varphi = 30^\circ$, S_0 = 35 MPa and $\sigma_{zo} = 50\text{MPa}$.

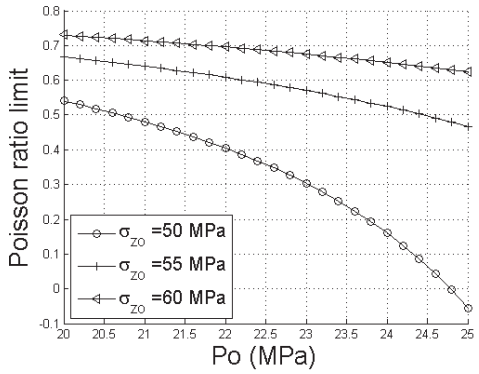

Fig. 3.17. Poisson's ratio limit versus pore pressure at the outer cylindrical boundary (P_o) for different values of σ_{zo}, $\varphi = 30^\circ$, $\alpha = 1.0$, S_0 = 35 MPa.

When the circumferential stress is the greatest at the elastic/plastic boundary, radial and circumferential stresses within the plastic zone can be determined as follows

$$\sigma_r = P_i + \frac{\mu_f q}{2\pi h k_c}\ln\frac{r}{R_i} - \frac{1}{W}\left(2S_0\tan\phi - \frac{\mu_f q}{2\pi h k_c}\right) + 2\tan^2\phi\frac{A_1}{V}r^W \qquad \text{Eq. 3.5}$$

$$\sigma_\theta = P_i + \frac{\mu_f q}{2\pi h k_c}\ln\frac{r}{R_i} - \frac{1}{W}\left(2S_0\tan\phi - \tan^2\phi\frac{\mu_f q}{2\pi h k_c}\right) + 2\tan^4\phi\frac{A_1}{V}r^W \qquad \text{Eq. 3.6}$$

where σ_r and σ_θ are the radial and circumferential stresses for a given radial distance *r*, μ_f is the fluid viscosity, *q* is the fluid flow rate, k_c is the permeability of the material in the plastic zone, A_1 is an integration constant, and

$$W = \tan^2\phi - 1 \qquad \text{Eq. 3.7}$$

$$V = \tan^4\phi + 1 - \nu\left(\tan^2\phi + 1\right)^2 \qquad \text{Eq. 3.8}$$

Another possibility is that the circumferential and the vertical stresses remain equal. In that case, radial and circumferential stresses are determined as follows:

$$\sigma_r = P_i + \frac{\mu_f q}{2\pi h k_c}\ln\frac{r}{R_i} + \frac{1}{W}\left(2S_o\tan\phi - \frac{\mu_f q}{2\pi h k_c}\right)\cdot\left[\left(\frac{r}{R_i}\right)^W - 1\right] \qquad \text{Eq. 3.9}$$

$$\sigma_\theta = P_i + \frac{\mu_f q}{2\pi h k_c}\left(1 + \ln\frac{r}{R_i}\right) + \frac{1}{W}\left(2S_o\tan\phi - \frac{\mu_f q}{2\pi h k_c}\right)\left[(t+1)\left(\frac{r}{R_i}\right)^W - 1\right] \qquad \text{Eq. 3.10}$$

Finally, when the vertical stress is greater than the circumferential stress at the plastic/elastic boundary, the solution for the radial and circumferential stresses are

$$\sigma_r = \frac{\tan^2\phi - 1 + (1-2\nu)\alpha}{\tan^2\phi - 2\nu}P_o - \frac{1}{\tan^2\phi - 2\nu}2S_0\tan\phi + \\ + \frac{B_1}{V}\left[\gamma + \nu\left(\tan^2\phi + 1\right)\right]r^{\gamma-1} + \frac{B_2}{V}\left[\nu\left(\tan^2\phi + 1\right) - \gamma\right]r^{-\gamma-1} \qquad \text{Eq. 3.11}$$

$$\sigma_\theta = \frac{\tan^2\phi - 1 + (1-2\nu)\alpha}{\tan^2\phi - 2\nu} P_o - \frac{1}{\tan^2\phi - 2\nu} 2S_0 \tan\phi + \\ + \gamma \frac{B_1}{V}\left[\gamma + \nu\left(\tan^2\phi + 1\right)\right] r^{\gamma-1} - \gamma \frac{B_2}{V}\left[\nu\left(\tan^2\phi + 1\right) - \gamma\right] r^{-\gamma-1} \quad \text{Eq. 3.12}$$

Where B_1 and B_2 are integration constants and

$$\gamma^2 = \tan^4\phi - 2\nu\tan^2\phi + 1 \quad \text{Eq. 3.13}$$

The material ouside the plastic zone behaves elastically, and the same expression applies in all cases

$$\sigma_r = \sigma_{ro} + (\sigma_{ro} - \sigma_{ri}) \frac{R_i^2}{R_o^2 - R_i^2}\left[1 - \left(\frac{R_o}{r}\right)^2\right] - \\ - (P_o - P_i)\frac{1-2\nu}{2(1-\nu)}\alpha\left\{\frac{R_i^2}{R_o^2 - R_i^2}\left[1 - \left(\frac{R_o}{r}\right)^2\right] + \frac{\ln(R_o/r)}{\ln(R_o/R_i)}\right\} \quad \text{Eq. 3.14}$$

$$\sigma_\theta = \sigma_{ro} + (\sigma_{ro} - \sigma_{ri}) \frac{R_i^2}{R_o^2 - R_i^2}\left[1 + \left(\frac{R_o}{r}\right)^2\right] - \\ - (P_o - P_i)\frac{1-2\nu}{2(1-\nu)}\alpha\left\{\frac{R_i^2}{R_o^2 - R_i^2}\left[1 + \left(\frac{R_o}{r}\right)^2\right] + \frac{1}{\ln(R_o/R_i)}\left[\ln(R_o/r) - 1\right]\right\} \quad \text{Eq. 3.15}$$

where σ_{ro} is the radial stress at the outer boundary, σ_{ri} is the radial stress at the inner boundary and P_o is the fluid pressure at the outer boundary.

A MATLAB code was written to evaluate Risnes et al. (1982) solution. The code is explained in detail in Appendix A. Fig. 3.18 and Fig. 3.19 show the analytical representation for different material strength and radial fluid flow. The elastic/plastic boundary coincides with the maximum value (peak) of the circumferential stresses. The peak of the circumferential stress increases when the cohesive strength increases. The plastic region extent decreases as the cohesive strength increases and the fluid flow velocity decreases.

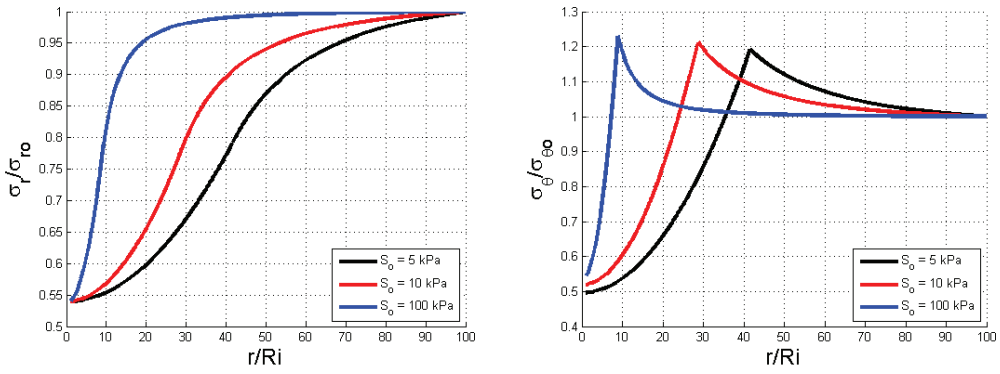

Fig. 3.18. Analytical solution: impact of material strength, Risnes et al. (1982). q = 0 cm^3/s; P_o = P_i (q = 0) = 32065 kPa; R_i = 0.1 m; R_o = 10.0 m; σ_{zo} = 65500 kPa; $\varphi = 30^\circ$; α = 1.0; and ν = 0.45.

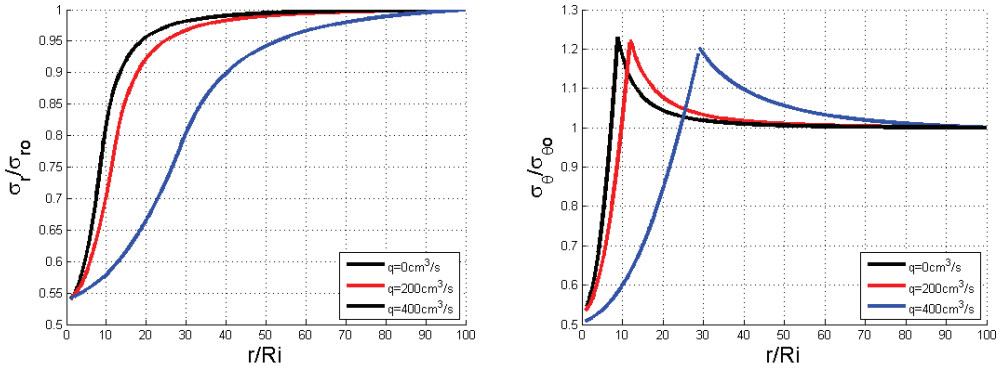

Fig. 3.19. Analytical solution: impact of the fluid flow rate, Risnes et al. (1982). P_o = P_i = 32065 kPa; R_i = 0.1 m; R_o = 10.0 m; σ_{zo} = 65500 kPa; $\varphi = 30^\circ$; S_o = 101.4 kPa; α = 1.0; and ν = 0.45.

3.7. Summary

Oil reservoirs are found in sedimentary rocks, which are composed by assemblies of bonded particles. Sedimentary rocks where sand production is more common are sandstones. Sandstones are more permeable than other sedimentary rocks.

Oil well construction starts with drilling. After the well is drilled, the next step is completion. In this process the sandstone around the hole can be left-unsupported or it can be supported by casing installed and cemented to the formation; the casing is perforated in the reservoir zones, so that the hydrocarbons can flow into the formation. Frac packing is another technique where a fracture is generated and then filled with proppants to create a highly permeable slit in the formation through which the hydrocarbons can be produced.

There are different methods for hydrocarbon recovery. Natural recovery relies on the fact that fluid flows from high to low pressure and according to the thermodynamic properties of the reservoir. On the other hand, 'artificial' methods include techniques to enhance oil recovery, such as waterflooding, chemical flooding, thermal recovery and miscible recovery.

Sand production is the erosion of formation sand during the drilling and the process of oil recovery. During the oil recovery, the rock around the wellbore is plastified, decohesioned and weakened due to stress concentrations around the cavity. Fluid flow transports the decohesioned material.

Even though sand production can have a beneficial effect on the hydrocarbon production, several problems may arise due to sand production. Studying the sand production process and controlling sanding are of paramount importance for safe and economical hydrocarbon production.

Sand production process involves two mechanisms: localized plastification and failure of the rock around the cavity and the erosion of sand particles due to the fluid flow. These two mechanisms are coupled to each other. Different failure patterns can be generated depending on the direction of the external stresses.

Methods commonly used to predict sand production can be classified in four categories: empirical methods, laboratory methods, theoretical models and numerical methods. Different methodologies are commonly used at the same time and they complement each other. Balance should be maintained between all sources of information.

Empirical methods link several parameters from the field and monitoring data to predict sand production onset. These correlations depend on the location, the well completion method and might vary from one oil-field to another. These methods do not offer means to estimate the amount of sand production and are typically over conservative.

Modified TWC tests are commonly used to simulate sand production in a controlled environment. It helps develop insights into the sand production mechanisms that are not possible to observe in-situ. Moreover, TWC tests are a useful method to calibrate the strength data for theoretical and numerical models.

Theoretical models use mathematical formulation to predict sand production. There are different formulations depending on the kind of failure taken into account: compressive failure, tensile failure and erosion. Continuum numerical models use these theoretical models to predict sand production. Using a continuum model the formulation of several relations is necessary and it is recognised that remains a difficult task, because of the large number of interactions and non-linearities intrinsic to the problem. These difficulties have encouraged the use of discrete-element based approaches, which by redefining the fluid and/or the solid physics at the micro-scale allow a simpler formulation of the problem and a better understanding of some of its features. The disgreggation and the erosion of sand particles are better described with DEM methods. Moreover, high Reynolds number types of fluid can be also represented.

Finally, an analytical solution for stresses around a wellbore have been presented in this chapter (Risnes et al., 1982). The material was assumed to behave elastic perfectly plastic and the Mohr-Coulomb failure criterion was applied. The numerical model presented later in this thesis will be validated using this analytical solution.

Chapter 4 - Discrete Element Method

4.1. Introduction

Models based on the discrete element method explicitly describe the interaction between particles. Because they seem well-adapted to its nature, they has been used in the recent years to simulate granular materials and soil. It is a useful tool when erosion takes an important role in the problem under study and/or when large deformations are present. Due to the importance of erosion in sand production process, DEM has been chosen as a basis for the simulations presented in this work.

In this chapter the equations and basic theory underlying DEM are presented in Section 4.2. The contact models between particles employed in this thesis are explained in Sections 4.3 and 4.4. Section 4.5 introduces the damping force and the boundary conditions used in this thesis are explained in Section 4.6. A brief overview of some applications of DEM to soil mechanics is presented in Section 4.7. Finally, representation of DEM output data with ParaView is presented in Section 4.8.

4.2. DEM fundamentals

DEM was proposed originally by Cundall & Strack (1979) to represent the macroscopic behaviour of particulate matter through the interactions between discrete individual particles that usually have simple geometries such as spheres in 3D or disks in 2D. These ideal particles are rigid but small overlaps are allowed at the contact points when a soft contact model is applied. Particles are allowed to lose contact if overlap between the particles no longer exists.

DEM provides micromechanical quantities and parameters that cannot be easily obtained from experimental tests and it can capture the particle-scale interactions

underlying the observed macro-scale behaviour of soils and other geomaterials (O'Sullivan, 2011). DEM simulations can provide dynamic information, such as trajectories and transient forces acting on individual particles, which are extremely difficult, if not impossible, to obtain by physical experimentation.

In this thesis, the three-dimensional DEM code, PFC^{3D} (Particle-Flow Code 3D), developed by Itasca Consulting Group, Inc., is used (Itasca, 2008a). This code is a simplified version of the general DEM, because of the restriction to spherical particles. Walls can be also defined to apply boundary conditions such as velocity or stresses, as explained in Section 4.6. The particle motion is described by Newton's second law and contact forces are used to model the interaction between particles and between particles and walls (Zhu et al., 2007; O'Sullivan, 2011).

The governing equations for translational and rotational motion of particle *of* mass *m* are

$$m\frac{dv}{dt} = \sum_j F_j^c + F^e + F^g \qquad \text{Eq. 4.1}$$

$$I\frac{d\omega}{dt} = \sum_j M_j \qquad \text{Eq. 4.2}$$

where *v* and ω are the translational and angular velocities of the particle, respectively, F_j^c and M_j are the contact force and torque acting on the particle by particle *j* or walls, F_j^e is the total external force acting on the particle by non-gravitational sources, and F_j^g is the gravitational force. The contact force between particles is described by the contact model used in each case. The contact models employed in this thesis are explained in Section 4.3.

The DEM calculation algorithm uses the central-difference time integration scheme (Itasca, 2008a). This is an explicit time integration method. The solution of the equations of motion will remain stable only if the timestep does not exceed a critical value (Itasca, 2008a). The approximation of the critical value for a particle as calculated by Itasca is

$$t_{crit} = \sqrt{m / \sum K_c} \qquad \text{Eq. 4.3}$$

where $\sum K_c$ is the stiffness (summing all the contributions of each contact of the particle, see Section 4.3.2.1) and *m* is the mass of the particle. The critical timestep of a system of particles is the minimum of all the critical timesteps calculated for each particle in the system. The actual time step used in any cycle is taken as a fraction of this estimated critical value.

Itasca (2008a) provides a detailed description of the distinct element calculation algorithm. The DEM calculation cycle in each calculation cycle is represented in Fig. 4.1. The flow chart summarises the DEM calculation sequence and each calculation cycle represents a computational time step. After the geometry is defined, the calculation is performed for a specified number of cycles. At the beginning of each time step the contact forces are calculated based on the magnitude of the overlap between the contacting particles, or between the contacting particles and walls, and the contact constitutive model used. Then the resultant force on each particle is determined by summing the contact forces and any externally applied forces on the particle. The particle acceleration is then determined by applying Newton's second law of motion. Finally, the incremental velocity and displacement of each particle are calculated by integration. Before the next calculation cycle the locations of all the particles are updated before the next calculation cycle begins.

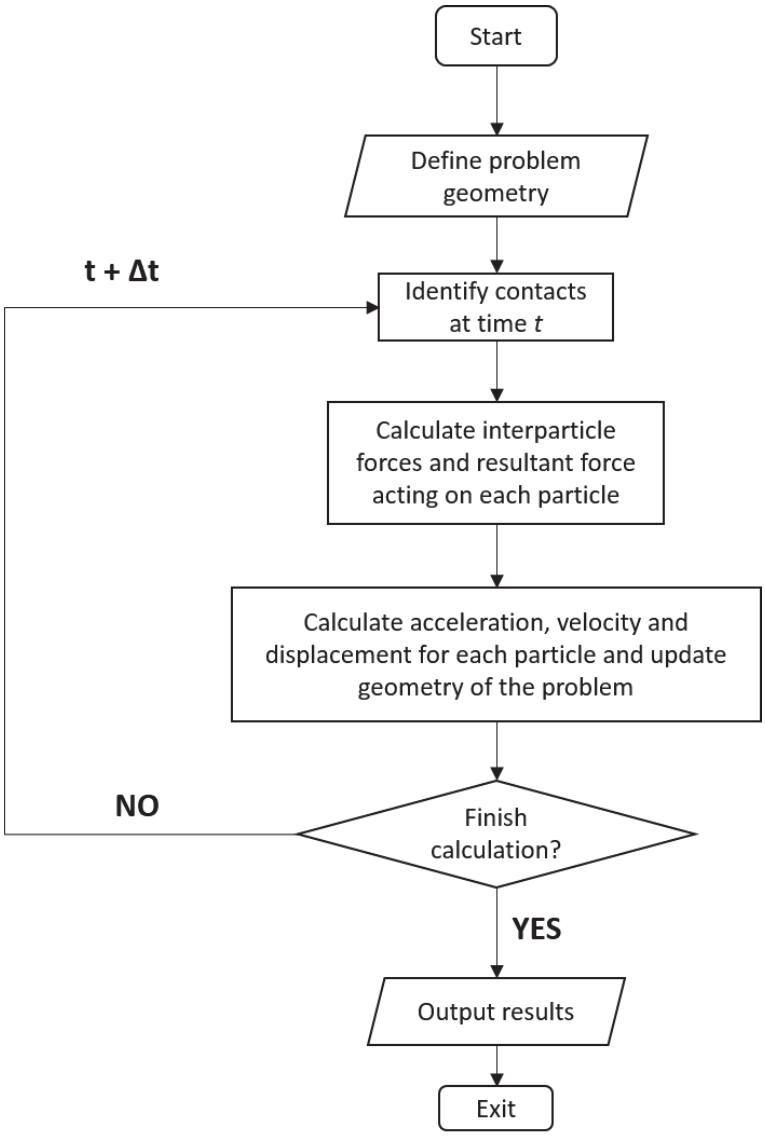

Fig. 4.1. DEM calculation flowchart in PFC[3D]

4.3. Contact models

Two types of DEMs related to contact forces have been employed: soft-particle and hard-particle approaches (Zhu et al., 2007). In the majority of the models presented in the geotechnical literature, as well as in the work presented in this thesis, a soft particle approach is adopted.

4.3.1. Hard-particle contact models

In hard particle models the interaction forces are assumed to be impulsive and hence the particles only exchange momentum by means of collisions (Hoomans et al., 1996; Zhu et al., 2007). A characteristic feature of a hard-sphere simulation is that a sequence of collisions is processed, one collision at time, assuming instantaneous collisions. Typically, hard-particle method is most useful in rapid granular flows. Hoomans et al. (1996) used this approach to simulate a two-dimensional gas-fluidised bed.

4.3.2. Soft-particle contact models

The soft-sphere method originally developed by Cundall & Strack (1979) was the first granular dynamics simulation technique published in the open literature. In such an approach, particles are permitted to suffer minute deformations (represented as overlaps between particles), and these deformations are used to calculate elastic, plastic and frictional forces between particles. A characteristic feature of the soft-sphere models is that they are capable of handling multiple and instantaneous particle contacts and the time step should be smaller than the duration of a contact (Zhu et al., 2007).

In general, the contact between two particles is not at a single point but on a finite area due to the overlap of the particles, which is equivalent to the contact of two rigid bodies allowed to overlap slightly in the DEM. The contact traction distribution over this area can be decomposed into a component in the contact plane (or tangential plane) and one normal to the plane, thus a contact force has two components: normal and tangential, as it is presented in Fig. 4.2 (Itasca, 2008a).

The approaches most commonly used in granular flows are the linear frictional model and the Hertz-Mindlin model.

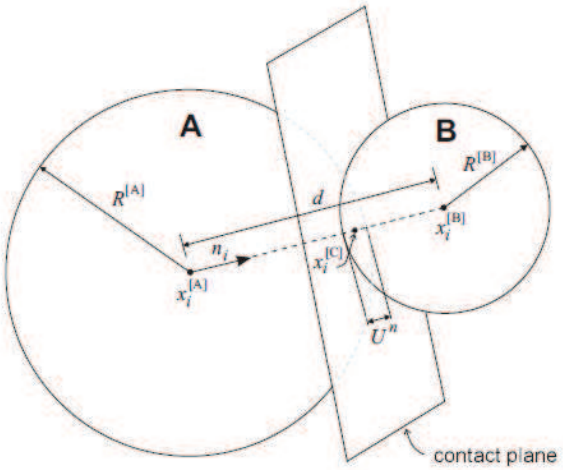

Fig. 4.2. Soft contact scheme (Itasca, 2008a).

4.3.2.1. Linear frictional contact model

The linear contact model was proposed by Cundall & Strack (1979). In this contact model, the load displacement relationship between two contacting bodies is represented by linear springs (Fig. 4.3).

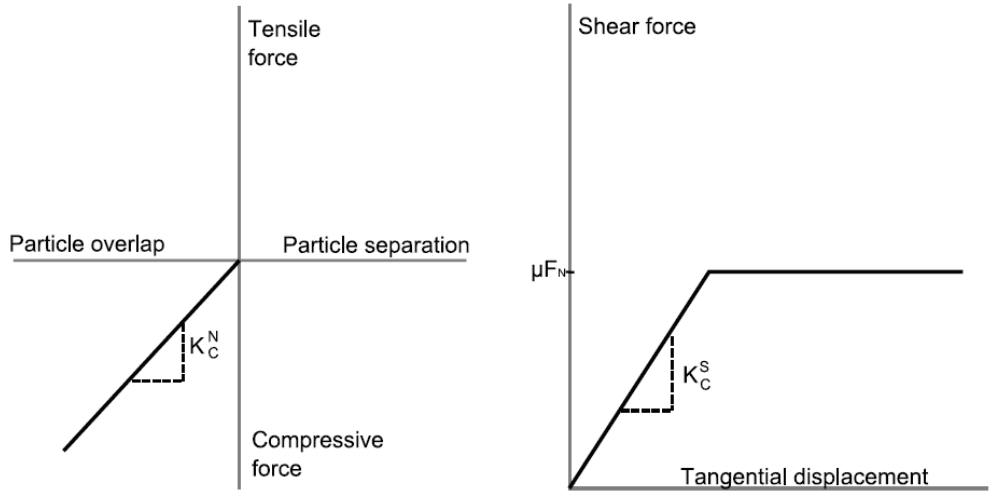

Figure 3.2: Linear frictional contact model.

Fig. 4.3. Linear frictional contact model (Cheung, 2010).

The three input parameters are the particle normal and shear stiffnesses, K_N and K_S, and the inter-particle friction coefficient μ_{DEM} (Cheung, 2010; O'Sullivan, 2011). The stiffness is constant for each particle. Normal and shear stiffnesses, K_c, between the contacting bodies (PA and PB) can be calculated from the particle normal or shear stiffness for each body, K_{PA} and K_{PB}, as follows

$$K_c = \frac{K_{PA} K_{PB}}{K_{PA} + K_{PB}} \qquad \text{Eq. 4.4}$$

The normal, F^N, and shear, F^S, contact forces are calculated as

$$F^N = K_c^N \Delta^N \qquad \text{Eq. 4.5}$$

$$F^S = -K_c^S \Delta^S \qquad \text{Eq. 4.6}$$

where Δ^N is the overlap, Δ^S is the relative displacement in the tangential direction, and K_c^N and K_c^S are the contact stiffnesses in the normal and shear directions respectively. The limiting value of the magnitude of F^S is equal to $\mu_{DEM} F^N$.

This approach is commonly used in fluidized beds numerical simulations (Tsuji et al., 1993; Xu & Yu, 1997; Xiong et al., 2005), and in other simulations as pipe or cone penetration (Jian et al., 2006; Butlanska et al., 2009; Climent et al., 2011).

4.3.2.2. Hertz-Mindlin contact model

The Hertz-Mindlin theory considers the variation of the contact area between two contacting particles as the normal contact force changes and the non-uniform distribution of the pressure at the contact (Cheung, 2010; O'Sullivan, 2011). The equivalent tangential contact stiffnesses, K_c^N and K_c^S, are calculated from the elastic properties of the contacting particle A and B using the equations:

$$K_c^N = \left(\frac{2\overline{G}\sqrt{2\overline{R}}}{2(1-\overline{\nu})} \right) \sqrt{\Delta^N} \qquad \text{Eq. 4.7}$$

$$K_c^S = \left(\frac{2\left(3\overline{R}\,\overline{G}^2(1-\overline{\nu})^{1/3}\right)}{2(1-\overline{\nu})} \right) \left| F^N \right|^{1/3} \qquad \text{Eq. 4.8}$$

where the sphere-sphere contact parameters, $\overline{R}$, $\overline{G}$ and $\overline{\nu}$, are given by

$$\overline{R} = \frac{2R_{PA}R_{PB}}{R_{PA}+R_{PB}} \qquad \text{Eq. 4.9}$$

$$\overline{G} = \frac{1}{2}\left(G_{PA}+G_{PB}\right) \qquad \text{Eq. 4.10}$$

$$\overline{\nu} = \frac{1}{2}\left(\nu_{PA}+\nu_{PB}\right) \qquad \text{Eq. 4.11}$$

Theoretically, the more complex nonlinear models as the Hertz-Mindlin approach should be more accurate than linear model. It was observed by Ciantia et al. (2015) that

for highly crushable materials such as petroleum coke the two contact models give very similar but when strong granular materials are considered, the linear contact model is not adequate. On the other hand, the numerical investigations conducted by Di Renzo & Di Maio (2004) of the collision of a single particle with a flat wall showed that the simple linear model sometimes gives better results, and an effort should be done on the choice of the correct parameters in the linear model.

4.4. Bonding: parallel-bond model

The Parallel-bond model (PBM), which is available in PFC^{3D} (Itasca, 2008a), is employed to numerically represent the mechanical effect of a cementing material deposited between particles. Several researchers pointed out that rock behaves like a cemented granular material in which cement may break (Potyondy & Cundall, 2004; Wang & Tonon, 2009a,b; Schöpfer et al., 2009; Cheung, 2010; O'Sullivan, 2011). The parallel-bond contact (PBC) transmits both forces and moments between particles which is a reasonable assumption of load transfer at contact where there is a finite amount of cementing material present; therefore it can mimic the mechanical behaviour corresponding with rock and sandstone. The mechanical representation of the cementing contact is, however, partial, since it does not include the mass or volume of the cemented material. The "parallel" in the name refers to the inclusion of a set of springs with constant normal and shear stiffnesses that work in parallel with other contact springs, typically the linear contact springs. The parallel-bonds can also sustain traction and shear. Both forces and moments can be transferred between the bonded particles and the bond restricts the particles from rotating.

The parameters required to define a parallel-bond are: the parallel-bond normal stiffness (K_{pb}^{N}, in Pa/m^3), the parallel-bond shear stiffness (K_{pb}^{S}, in Pa/m^3), the parallel-bond normal strength (S_{pb}^{N}, in Pa), the parallel-bond shear strength (S_{pb}^{S}, in Pa), and the degree of bonding (α_{bond}) (Potyondy & Cundall, 2004; Cheung, 2010; O'Sullivan, 2011).

When the forces acting on the parallel bond reach either of its strength limits the parallel bond is erased and cannot be reformed, even if the same contact appears again.

The bond can be thought to be a virtual cylinder linking the two spheres with radius R_{pb} which equals $\alpha_{bond} R_{\min}$, where R_{min} is the radius of the smaller of the two contacting particles (Fig. 4.4). Therefore, the degree of bonding, α_{bond}, defines the 'size' of the parallel-bond (Cheung, 2010; O'Sullivan, 2011). When the volume of cement deposited at the contact between two particles varies (varying the 'size' of the parallel-bond), the effective stiffness and the contact stress distribution will vary, as it is shown by the formulation below.

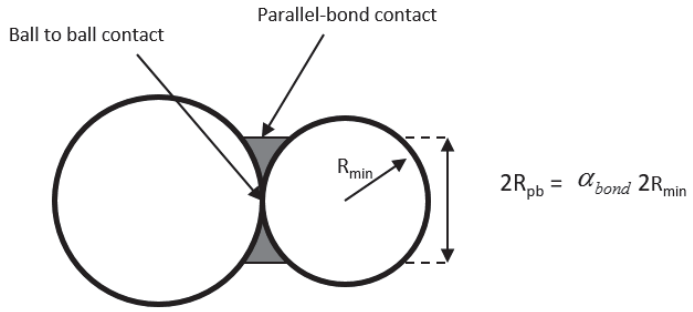

Fig. 4.4. Schematic illustration of the parallel-bond contact

The forces carried out by the parallel bond in the normal and shear directions (F_{pb}^{N} and F_{pb}^{S}) are given by

$$F_{pb}^{N} = K_{pb}^{N} A_{pb} \delta_{n} \qquad \text{Eq. 4.12}$$

$$F_{pb}^{S} = K_{pb}^{S} A_{pb} \sum \Delta\delta_{s} \quad \text{Eq. 4.13}$$

where δ_n is the contact normal displacement and $\sum \Delta\delta_S$ is the cumulative shear displacement. A_{pb} is the bond area, given by $A_{pb} = \pi R_{pb}^2$.

Two types of moment are transmitted by the parallel bond: a spin or twisting moment (M_{pb}^{spin}) and a bending moment (M_{pb}^{b}). The spin moment relates to a moment caused by relative rotation about the contact normal. The increments in moment (ΔM_{pb}^{spin} and ΔM_{pb}^{b}) caused by an incremental rotation of the particles are given by

$$\Delta M_{pb}^{spin} = K_{pb}^{S} I_{pb} \Delta\theta_{N} \quad \text{Eq. 4.14}$$

$$\Delta M_{pb}^{b} = K_{pb}^{N} I_{pb} \Delta\theta_{S} \quad \text{Eq. 4.15}$$

Where I_{pb} is the moment of inertia of the parallel bond and equals to $\frac{1}{4}\pi R_{pb}^{4}$. The cumulative rotation about the contact normal is given by $\sum \Delta\theta_n$, while the cumulative rotation orthogonal to the contact normal is given by $\sum \Delta\theta_s$. These angles are presented in Fig. 4.5.

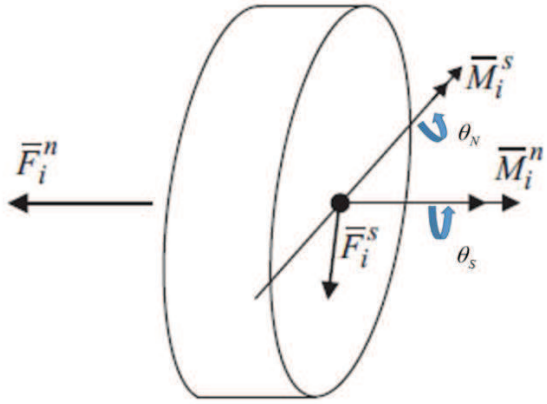

Fig. 4.5. Bond between two particles. M_i^s represents M_{pb}^{spin} and M_i^n represents M_{pb}^b.

Following Eq. 4.12 and Eq. 4.13 it should be noted that the input parameters K_{pb}^N and K_{pb}^S do not actually represent parallel-bond stiffness directly. The equivalent parallel-bond stiffness is obtained taking into account the parallel bond virtual radius, to obtain a total contact stiffness (Cheung, 2010) given by

$$K_{total} = K_c + K_{pb} A_{pb} \qquad \text{Eq. 4.16}$$

Where K_{total} is the total normal or shear stiffness and K_c is the particle-particle normal or shear contact stiffness.

A further aspect to be noted is that the PBC incorporates a modulus-stiffness scaling relation where the contact stiffness of each particle is made dependent on the particle radius (Potyondy & Cundall, 2004)

$$K_N = 4E_c R \qquad \text{Eq. 4.17}$$

$$K_N = \alpha_{ratio} K_s \qquad \text{Eq. 4.18}$$

where E_c is an effective particle stiffness, α_{ratio} is the ratio between the normal and the shear stiffnesses and R is the particle radius. Following Eq. 4.4, the stiffness of the contact can be expressed as

$$K_c^N = 2E_c \frac{R_{PA}R_{PB}}{R_{PA}+R_{PB}} \quad \text{Eq. 4.19}$$

$$K_c^N = \alpha_{ratio} K_c^S \quad \text{Eq. 4.20}$$

where R_{PA} and R_{PB} are the radius of the particles in contact. The same kind of formulation is applied for parallel-bond stiffnesses is

$$K_{pb}^N = \frac{E_{pb,c}}{R_{PA}+R_{PB}} \quad \text{Eq. 4.21}$$

$$K_{pb}^N = \alpha_{pb,ratio} K_{pb}^S \quad \text{Eq. 4.22}$$

where $E_{pb,c}$ is an effective PBC stiffness and $\alpha_{pb,ratio}$ is the ratio between the normal and the shear PBC stiffness. These formulations exhibit a minor size effect for the PFC^{3D} (Potyondy & Cundall, 2004) and, as it is further explained in Chapter 5, they contribute to make the model scale-independent.

The relative motion between the bonded particles generates a change in stresses and moments within the parallel-bond. Pure tensile or shear motions create a uniform distribution of tensile or shear (tangential) stress across the parallel-bond. The maximum tensile stress, $\sigma_{\max,pb}$, and shear stress, $\tau_{\max,pb}$ at a parallel-bond are calculated using:

$$\sigma_{\max,pb} = \frac{-F_{pb}^{N}}{A_{pb}} + \frac{\left|M_{i,pb}^{S}\right|}{I_{pb}} R_{pb} \qquad \text{Eq. 4.23}$$

$$\tau_{\max,pb} = \frac{\left|F_{pb}^{S}\right|}{A_{pb}} + \frac{\left|M_{pb}^{N}\right|}{J_{pb}} R_{pb} \qquad \text{Eq. 4.24}$$

where F_{pb}^{N} is the computed normal force at the parallel-bond (compression is positive) and F_{pb}^{S} is the computed shear force at the parallel-bond. M_{pb}^{N} and $M_{i,pb}^{S}$ are the computed moment components carried by the parallel-bond about the contact normal and any axis orthogonal to the contact in normal and shear directions respectively. A_{pb}, I_{pb} and J_{pb} are the area, the moment of inertia and the polar moment of inertia of the parallel-bond and are related to R_{pb}. Due to the reduced number of degrees of freedom in two-dimensional problems, the stresses developed at the parallel-bond can be calculated as follows:

$$\sigma_{\max,pb} = \frac{-F_{pb}^{N}}{A_{pb}} + \frac{\left|M_{i,pb}\right|}{I_{pb}} R_{pb} \qquad \text{Eq. 4.25}$$

$$\tau_{\max,pb} = \frac{\left|F_{pb}^{S}\right|}{A_{pb}} \qquad \text{Eq. 4.26}$$

The parallel-bond remains intact while the magnitudes of these maximum calculated and shear stresses are less than the tensile and shear parallel-bond strengths, S_{pb}^{N} and S_{pb}^{S}. A parallel-bond will break if $\alpha_{\max,pb}$ exceeds S_{pb}^{N} or if $\tau_{\max,pb}$ is greater than S_{pb}^{S}. Once

the parallel-bond is broken, it is irrecoverable. Particles that were in contact through a parallel bond can contact again after the bond is broken, but the contact model between them is the default one (linear, Hertzian, etc).

4.5. Damping

The aim of the damping in DEM is to account for energy dissipation in real situations that are not explicitly modelled via frictional contacts or bond breakages. The local damping used in PFC^{3D} is similar to that described in Cundall (1987). The following damping-force is added to the equations of motion

$$F^d = -\delta \left| F^{total} \right| \text{sign}(v) \qquad \text{Eq. 4.27}$$

where v is the particle velocity, and F^{total} is the resultant of other forces acting on a particle (contact forces, gravitational force and external forces). sign(v) is +1 when $v > 0$, -1 when $v < 0$, and 0 when $v = 0$. The damping force is controlled by the damping constant (δ). A commonly employed value of the damping constant to achieve quasi-static conditions is 0.7.

4.6. Boundary conditions: walls and servo-control

In DEM simulations, displacement and force boundary conditions are commonly used and they can be achieved by fixing or specifying the coordinates of selected particles, by applying displacements to selected particles or by applying a specified force to selected particles (an external force is added to the contact forces acting on the particle and the resultant force is then used to calculate the particle accelerations and incremental displacements). However, these force boundary conditions cannot easily be directly

used with systems that include thousands of particles as the system deforms. Consequently, algorithms to select boundary particles are needed. There are different kind of boundary conditions that can be applied in DEM, as periodic walls or membrane boundaries. In this thesis rigid walls are systematically used to apply boundary conditions.

The most widely employed boundary type is the rigid wall. These rigid boundaries are analytically described surfaces that can be planar or curved. Walls have no inertia and the contact force determined at particle-boundary contacts are used to update the particles coordinates only. While the force acting on the walls does not influence wall motion by default, the user can control the wall movement by explicitly specifying a relation between wall velocity and forces on walls. When the walls are moved, displacements and forces are applied to the assembly of particles through the walls via the wall-particle contacts. If a stress state is required a 'servo-controlled' algorithm can be developed to control the internal stresses by moving these boundaries. A value can be specified based on monitored forces or stresses (forces averaged per unit area or volume) within the particulate system or along the boundaries. The boundaries are then moved to cause a controlled change in the target stresses until the specified stress state is achieved.

Rigid walls can also be used to simulate inclusions or machinery interacting with the granular material. For example, Butlanska et al. (2009) and Climent et al. (2011) used rigid wall boundaries to represent cone penetration testing (Fig. 4.6).

Fig. 4.6. DEM boundaries in a cone penetration test (Butlanska et al., 2009).

4.7. Applications

DEM has been used to study particle-scale interactions, to perform laboratory experimental tests and to reproduce field problems. However, computational cost makes DEM difficult to apply for real scale problems. This is the reason why the most of the simulations are still performed for studying the micro-scale interaction and tests that can be reproduced at smaller scales (e.g. problems that can be scaled to reproduce the same experimental results).

As an example of a micro-scale study, sand crushing has been studied by several researchers. Lobo-Guerrero & Vallejo (2005) performed two DEM simulations of a pile in two dimensions (Fig. 4.7). Crushing was allowed during only one of the simulations and the results were compared with experimental data. They observed that particle crushing causes the production of particles of different sizes. Breakage and particle rearrangement were observed to induce stress relaxation, and caused the broken granular material to develop a lower resistance to pile penetration. Thornton & Liu (2004) and Golchert et al. (2004) also studied breakage performing 3D DEM simulations and they identified the physical processes that lead to breakage in agglomerates (Fig. 4.8). Ciantia et al. (2015) simulated oedometric compression tests in 3D using breakable particles. A multigenerational DEM approach was used with a procedure that established the relationship between the disappearing broken particle and the new generation of smaller particles. Upscaling was applied to manage the increasing number of particles during the simulations and several strategies were considered to alleviate the no conservation of mass.

Thornton & Antony (2000) presented results of 3D DEM simulations of axisymmetric compression and axisymmetric extension tests. Simulations were performed with a constant mean stress and other simulations with a constant volume. Thornton & Zhang (2010) explored general three-dimensional stress space an initially isotropically compressed system is subjected to radial deviatoric strain paths. Cui & O'Sullivan (2006) performed a series of DEM simulations to analyse the micromechanics of the direct

shear test in three dimensions. Cui et al. (2007) presented an insight into the micro-scale interactions experienced by particles during a triaxial test using DEM. In their approach they used circumferential periodic boundaries and a stress-controlled membrane and demonstrated that these periodic boundaries allowed material response to be captured accurately compared to circumferential rigid walls that show to be inappropriate.

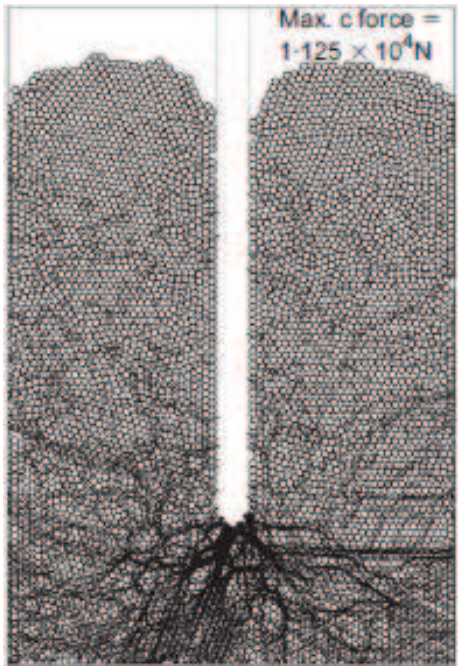

Fig. 4.7. Crushing study of a penetration test (Lobo-Guerrero & Vallejo, 2005).

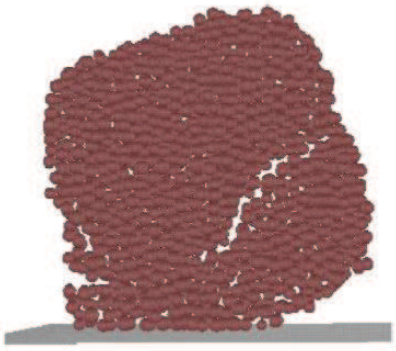

Fig. 4.8. Cuboidal agglomerate (Thornton and Liu, 2004).

Cone penetration test (CPT) studies are also performed using DEM. Jian et al. (2006) presented a 2D DEM study of CPT with the focus on the effect of soil-penetrometer interface friction and the penetration mechanism is continually investigated from viewpoints of deformation patterns, displacement paths, velocity fields, stress fields and stress paths. Butlanska et al. (2009) and Climent et al. (2011) examined the effect of symmetry performing CPT tests in 3D DEM with different sands.

Calvetti et al. (2004) performed 3D DEM simulations to reproduce experimental tests to understand the mechanism of pipe resistance. The model is shown in Fig. 4.9. Jenck et al. (2009) used a two-dimensional DEM model to investigate the mechanical behaviour of a platform over pile in soft soil. The results presented showed that the DEM is able to capture accurately the macro scale response of the platform over piles in soft soil by comparison to the experimental data obtained on the laboratory small scale model.

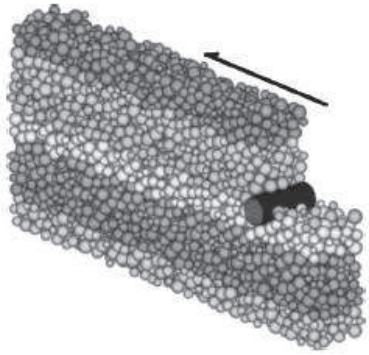

Fig. 4.9. Soil-pipe interaction simulation (Calvetti et al., 2004).

Langston et al. (1995, 1996) used 2D and 3D DEM model to simulate the filling and discharging of granular material from hoppers. Hopper discharge was also modelled by Cleary & Sawley (2002) using DEM in 2D and 3D for a wide selection of particle shapes to understand the effect that shape has on these flows (Fig. 4.10). Their work demonstrate that particle shape appears to be extremely important in hopper flows. Potapov & Campbell (1996) carried out large scale two-dimensional computer simulations of hopper flows. Li et al. (2004) studied the flow behaviour of particles and their arching and discharging in the hopper for different hopper openings using 2D and 3D DEM model.

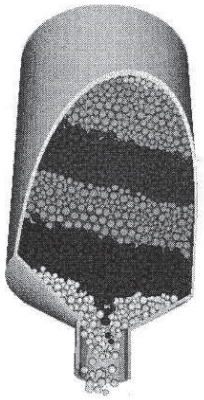

Fig. 4.10. Hopper discharge simulation (Cleary & Sawley, 2002).

4.8. Representing DEM results: simulation outputs

Using DEM the variables obtained are directly derived from the basic modelling units of the method (i.e., particles and contacts). The discrete variables obtained are contact forces, particle displacements, particle radii, stresses on particles, particle velocities, etc. In this thesis to represent these variables two different tools are used: MATLAB and ParaView.

MATLAB is used to map contact forces between particles. Contact forces are represented as lines tangential to surface where particles are in contact. The thickness of the line is proportional to the magnitude of the contact force (Fig. 4.11). The MATLAB script to map contact forces is in Appendix B.

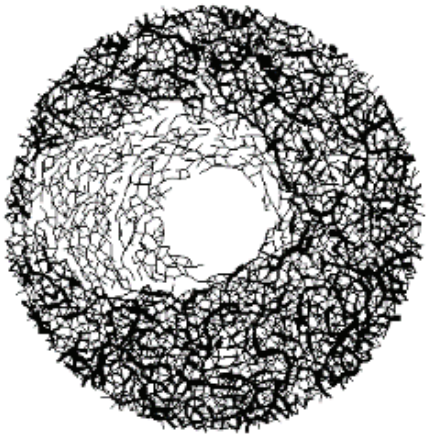

Fig. 4.11. Contact forces between particles.

ParaView is used to represent 3D visualizations of contact forces and particles. It is also used to represent the values obtained mapped with different colours on each particle or tube (a graph commonly used to represent contact forces, Fig. 4.18), as it is explained below. ParaView is an open-source application to visualize and analyse data. The data exploration can be done interactively in 2D or 3D and it has an intuitive user interface. The platforms supported by ParaView range from single-processor workstations to multiple-processor distributed-memory supercomputers or workstation clusters (Ahren et al., 2005). Techniques such as data streaming and parallelism can be used (Ahren et al., 2005), and it permits large datasets.

The ParaView project started in 2000 as a collaborative effort between Kitware Inc. and Los Alamos National Laboratory and its first public release was announced in 2002. To continue the development of the project, the project also has had the collaboration of Sandia National Laboratory, Advanced Simulation and Computing (ASC) and the Army Research Laboratory. Nowadays, the last version is ParaView 3.0. All the information about the project is provided in ParaView's website (http://www.paraview.org/).

ParaView builds the visualization of the data set on parallel and distributed Visualization Toolkit (VTK). VTK provides data representations for a variety of grid types (structured, unstructured, polygonal and image data) (Ahrens et al., 2005). The process of visualization takes raw data and converts it to a form that is viewable and

understandable. It usually takes scalars and vectors, and from them contours, isosurfaces, vector fields, streamlines, arrows (as in Fig. 4.17), cones and spheres (as in Fig. 4.13, Fig. 4.14, Fig. 4.15, Fig. 4.16and Fig. 4.17) are represented. The results can be coloured by any variable as a given scalar (as in Fig. 4.13, Fig. 4.14, Fig. 4.15, Fig. 4.16, Fig. 4.17 and Fig. 4.18), a vector magnitude or a vector component. Streamlines can be generated and displayed as points, lines, tubes (as in Fig. 4.18) and ribbons and can be processed by a magnitude. A sub-region of a dataset can be extracted by cutting or clipping specifying a plane (as in Fig. 4.15, Fig. 4.16, Fig. 4.17 and Fig. 4.18).

An example of a complex data representation is given in Fig. 4.12. Fig. 4.12 shows streamlines generated by ParaView using a dataset of airflow around a delta wing.

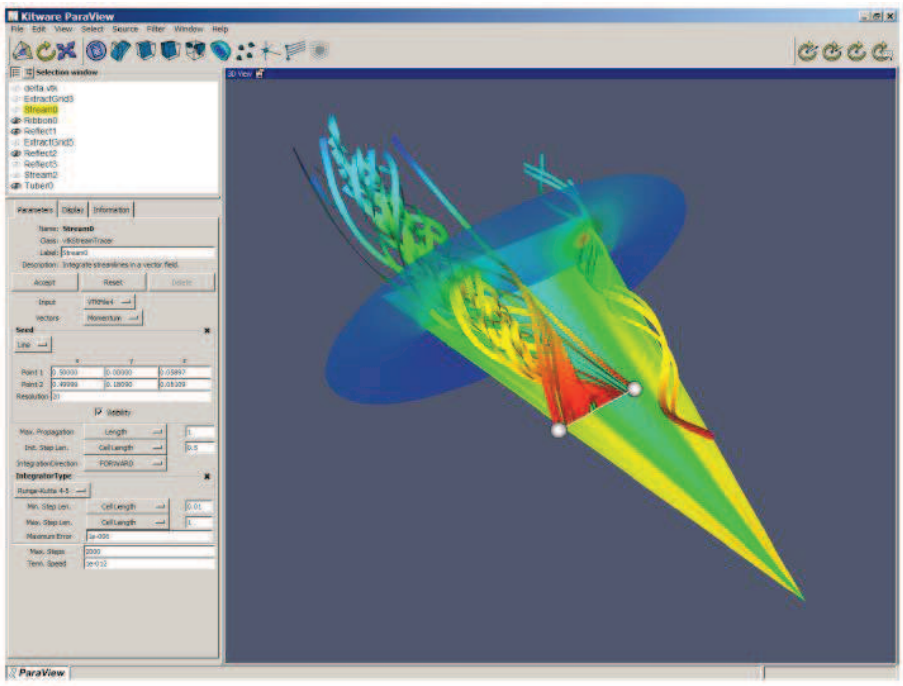

Fig. 4.12. The Delta Wing dataset in ParaView (Moreland, 2014).

Examples of outputs generated with Paraview are presented in Fig. 4.13, Fig. 4.14, Fig. 4.15, Fig. 4.16, Fig. 4.17 and Fig. 4.18. Fig. 4.13 represents a DEM sample with spheres in 3D. Each sphere is sized by the original diameter and coloured by the same magnitude. Fig. 4.14 is the same sample projected in the xy plane. Fig. 4.15 is the same

representation and orientation as Fig. 4.13 cut in the middle of the sample. Fig. 4.16 represents a smaller part of the same sample; particles are sized by the diameter and coloured by the mean normal stress on the particle. Fig. 4.17 is a zoom of Fig. 4.16 where arrows representing the velocity of each particle are represented; arrows are sized by the velocity magnitude. Finally, Fig. 4.18 is the same sample part as Fig. 4.16 where tubes represent the contact forces between particles; the size and the colour of the tubes are scaled by the magnitude of the contact force.

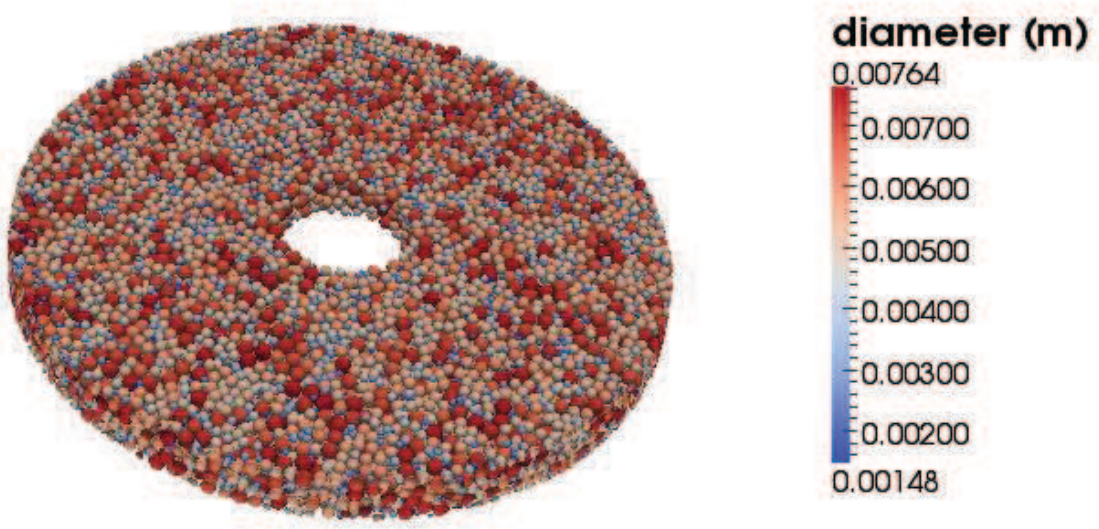

Fig. 4.13. 3D representation of spheres representing grains in DEM coloured and sized by the diameter

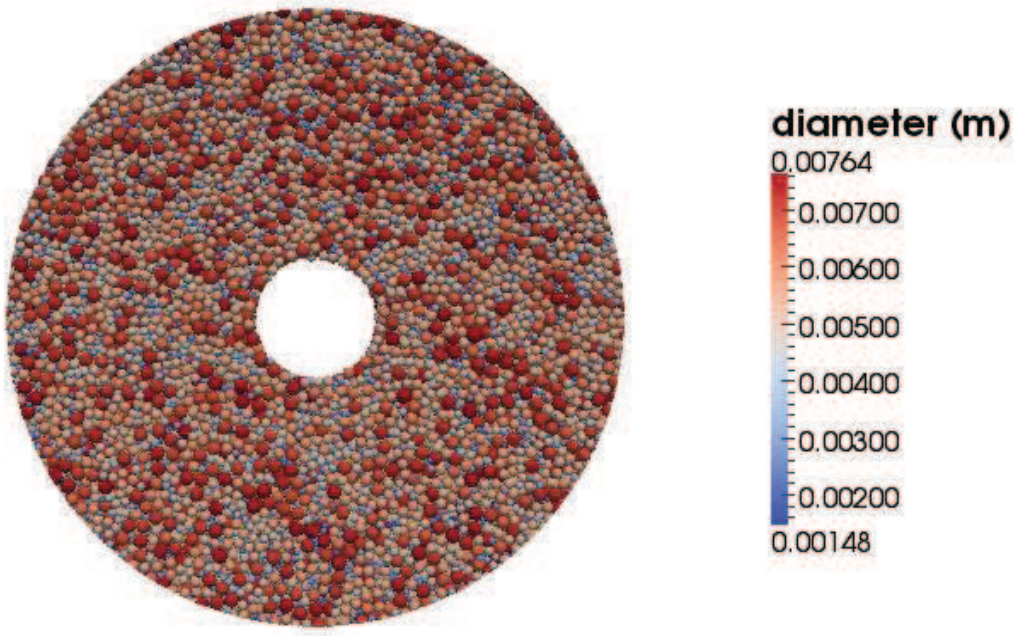

Fig. 4.14. Spheres representing grains in DEM coloured and sized by the diameter (plane xy)

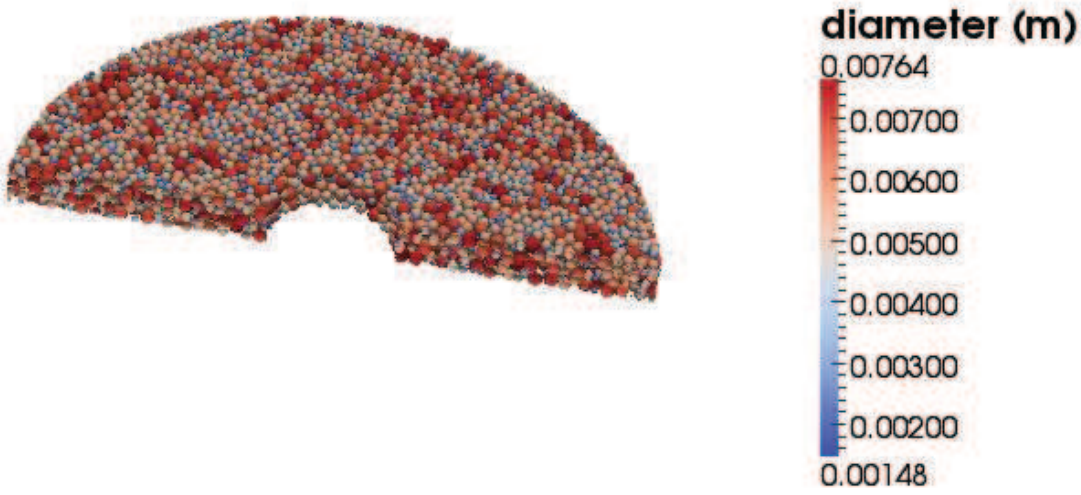

Fig. 4.15. Cutting of the 3D representation of spheres representing grains in DEM coloured and sized by the diameter

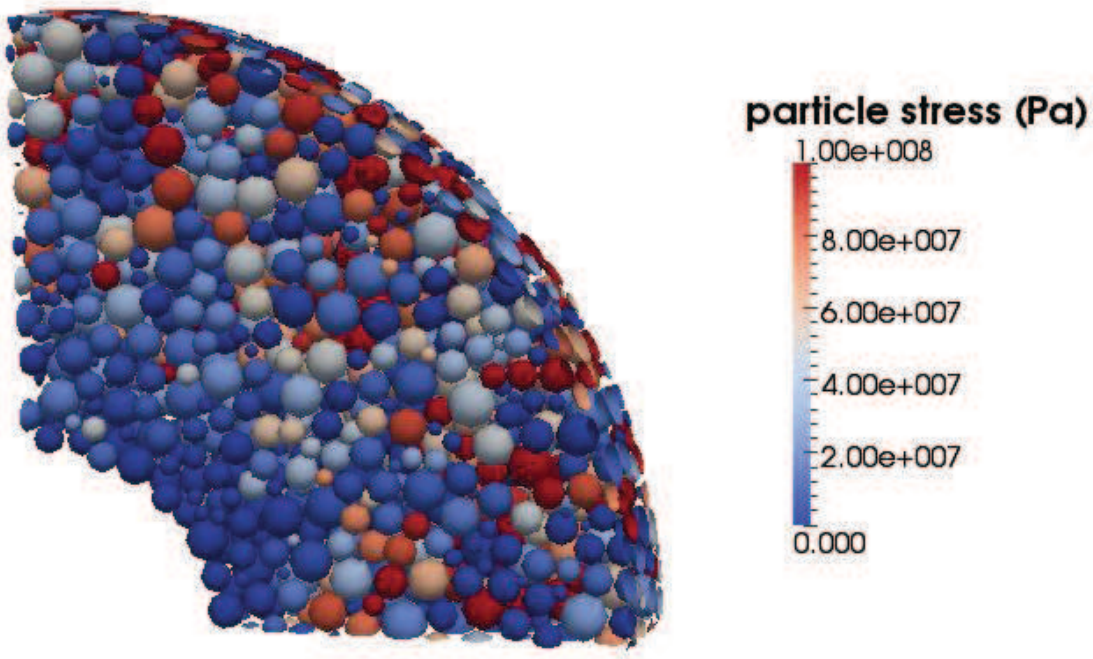

Fig. 4.16. 3D representation of spheres representing the grains in DEM coloured by the stress and sized by the diameter

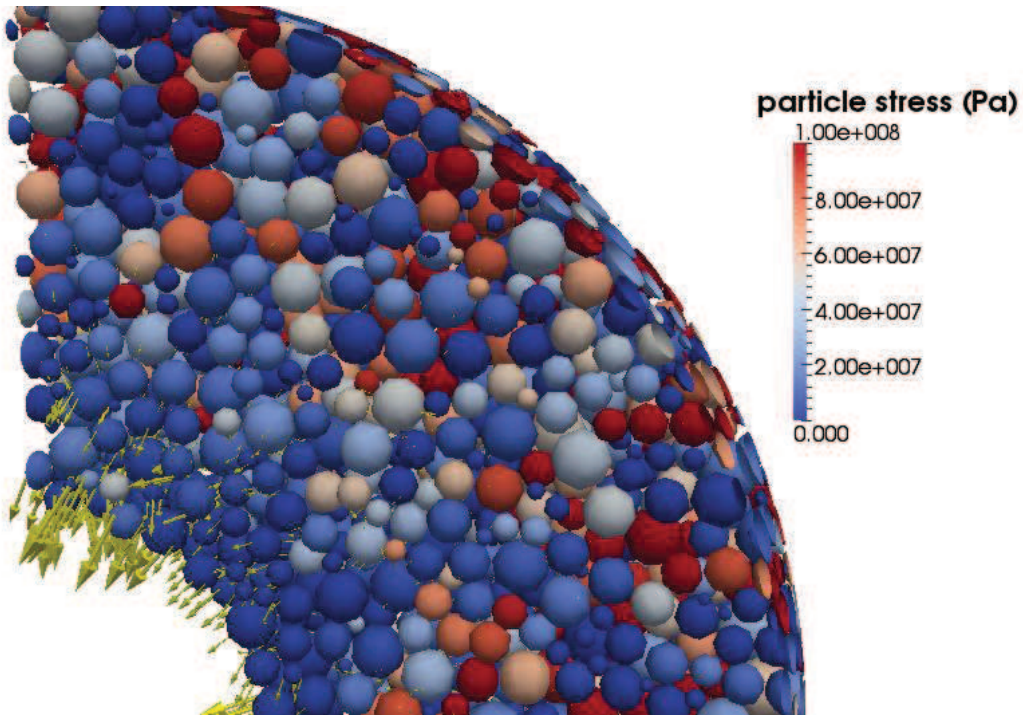

Fig. 4.17. 3D representation of spheres representing the grains in DEM coloured by the stress and sized by the diameter. Arrows in each particle representing the particle velocity, sized by the velocity magnitude.

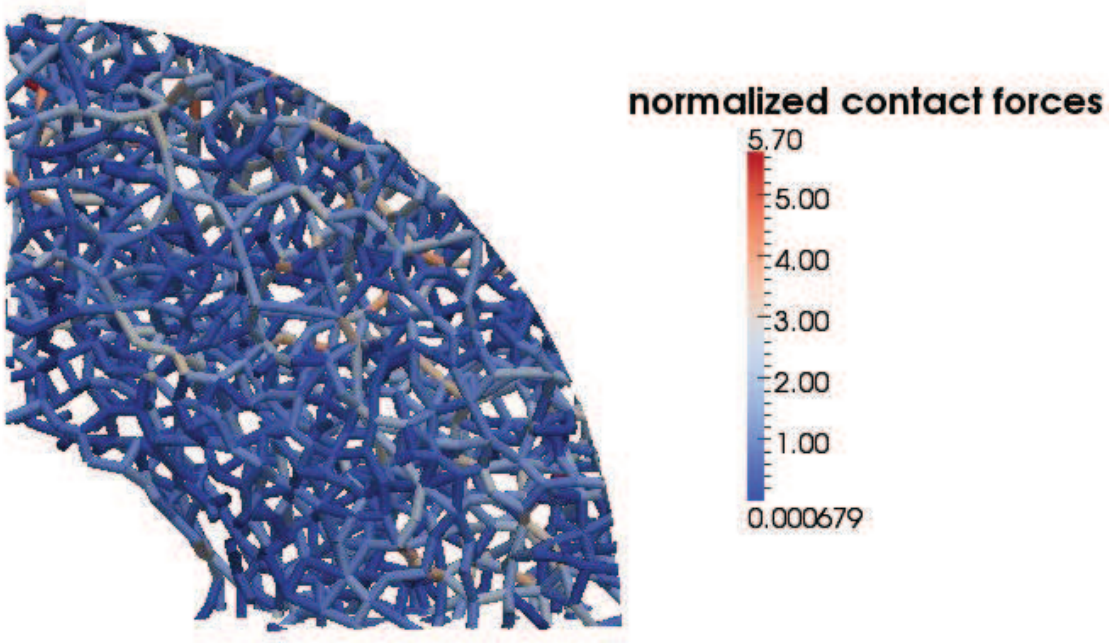

Fig. 4.18. Tubes representing the contact forces between particles coloured by the magnitude of the force (normalized by the mean contact force value)

ParaView can also be used to create animations by recording a series of keyframes. At each keyframe values for the properties of the readers, sources, and filters that make up the visualization pipeline are set, as well as the position and orientation of the camera.

The original data files have to be changed to a data file that ParaView can read. There are different kinds of ParaView data files depending on the data represented (discrete data, continuum fields, etc). Some MATLAB scripts to write these data files are in Appendix C.

The continuum field representation in ParaView is explained in Chapter 6.

4.9. Summary

DEM is a discrete modelling technique proposed originally by Cundall & Strack (1979) and commonly used to simulate granular materials. DEM provides micromechical

quantities that cannot be easily obtained from experimental tests and it can capture the particle-scale interactions. DEM can provide information as trajectories and forces acting on particles. The three-dimensional DEM code PFC^{3D} is used to perform all the simulations in this thesis.

In this thesis the linear contact model is used together with the PBM. The linear contact model was proposed by Cundall & Strack (1979). This contact model is a soft-sphere method used to calculate forces between particles where the particles are permitted to suffer minute deformations. The load displacement relationship between two contacting bodies is represented by linear springs. The three input parameters are the particle normal and shear stiffnesses, K_N and K_S, and the inter-particle friction coefficient μ. The parallel-bond model is available in PFC^{3D} (Itasca, 2008a). The parallel-bond can numerically represent cemented material deposited between particles. The parameters required to define a parallel-bond are: the parallel-bond normal stiffness (K_{pb}^{N}, in Pa/m), the parallel-bond shear stiffness (K_{pb}^{S}, in Pa/m), the parallel-bond normal strength (S_{pb}^{N}, in Pa), the parallel-bond shear strength (S_{pb}^{S}, in Pa) and the degree of bonding (α_{bond}). When the forces acting on the parallel bond reach either of its strength limits the parallel bond is erased and cannot be reformed, even if the same contact appears again.

Rigid boundaries are used as boundary conditions. These boundaries are described as surfaces that have no inertia and the contact force is used to update particle coordinates that are in contact with the walls. The movement of the wall can be explicitly specified, and a 'servo-controlled' algorithm can be used to control the internal stresses.

DEM has been used to study particle-scale interactions (e.g. Thornton & Liu, 2004; Golchert et al., 2004; Lobo-Guerrero & Vallejo, 2005), to perform laboratory experimental tests (e.g. Thornton & Antony, 2000; Cui & O'Sullivan, 2006; Cui et al., 2007; Thornton & Zhang, 2010) and to reproduce machinery as hoppers (Langston et al., 1994, 1995; Potapov & Campbell, 1996; Cleary & Sawley, 2002; Li et al., 2004).

The variables obtained using DEM are discrete variables as forces, particle displacements, particle radii, stresses on particles or particle velocities. MATLAB is used in this thesis to map contact forces, which are also represented with ParaView. ParaView

is a tool to represent 3D visualizations mapping value of interest on contacts (represented as a tube network) and particles. ParaView represents contours, isosurfaces, vector fields, streamlines, arrows, cones and spheres from scalars and vectors from simulated data.

Chapter 5 - Applications of the parallel-bond model to represent mechanical rock behaviour

5.1. Introduction

As stated in the previous chapter the PBM is frequently used to represent rock behaviour in DEM. This model mimics the effect of cement between particles and includes separate tensile and shearing failure modes. Despite being very frequently used there seems to lack a systematic approach to calibration, a complicated process because of the number of micro parameters involved. This is particularly problematic when, as it is the case here, the mechanical model is only a part of a more complex model that also includes solid-fluid interaction.

In this chapter we first review previous published usage of the PBM to represent rock behaviour is given in Section 5.2. After that, we introduce the parallel-bond model to represent sand production problems in Section 5.3. The datasets that were targeted for calibration, the specimen generation and the calibration are presented in Section 5.4.

5.2. Previous work on parallel-bond contact model calibration

In this thesis the contact models used are the linear friction model and the PBM presented in Chapter 4. As was explained in Section 4.4, rock behaves like a cemented granular material and DEM using the PBM can mimic the mechanical behaviour of rock in general and sandstone in particular.

As it was originally conceived (Potyondy & Cundall, 2004) a DEM model using the PBM did not aim to represent exactly the micro-structure of rock and the model parameters and, in particular, PBM micro-parameters needed calibration based on macro responses.

As explained in Chapter 4 the micro parameters to be calibrated are the contact parameters K_N, K_S, μ_{DEM}, and the cement parameters K_{pb}^N, K_{pb}^S, S_{pb}^N, S_{pb}^S, α_{bond} and λ. In a calibration process, values for these parameters should be chosen to represent a specific set of macro material properties of a given rock or sandstone.

Recall also from Chapter 4 that a radius dependence is inbuilt on the contact stiffness of the PBM and therefore

$$K_c^N = 2E_c \frac{R_{PA}R_{PB}}{R_{PA}+R_{PB}} \qquad \text{Eq. 5.1}$$

$$K_c^N = \alpha_{ratio} K_c^S \qquad \text{Eq. 5.2}$$

as well as

$$K_{pb}^N = \frac{E_{pb,c}}{R_{PA}+R_{PB}} \qquad \text{Eq. 5.3}$$

$$K_{pb}^N = \alpha_{pb,ratio} K_{pb}^S \qquad \text{Eq. 5.4}$$

Using this formulation the parameters calibrated are E_c, α_{ratio} and μ_{DEM}, and the cement parameters, $E_{pb,c}$, $\alpha_{pb,ratio}$, S_{pb}^N, S_{pb}^S α_{bond} and λ.

The calibration process is a typical inverse problem and is usually carried out by trial-and-error using laboratory test results, which are compared with simulation results. The most commonly macro properties used to calibrate these micro parameters have been the Young's modulus, the Poisson's ratio, the uniaxial compressive strength, the tensile

strength and the friction angle. Uniaxial compressive and tensile tests and triaxial tests are usually performed using DEM to achieve calibration (Potyondy & Cundall, 2004; Wang & Tonon, 2009a,b). However, one significant difficulty with this approach is that the micro parameters cannot be independently related to a specific macro property.

There are two types of micro parameters in the parallel bond contact model: deformability and strength parameters (Wang & Tonon, 2009a). Deformability parameters include normal and shear stiffnesses. These micro deformability parameters are sometimes calibrated to match the material macro deformability parameters, as Young's modulus and Poisson ratio (Potyondy & Cundall, 2004; Wang & Tonon, 2009a,b). Strength parameters include bond strengths, which are calibrated with macro parameters as the uniaxial compressive strength (Potyondy & Cundall, 2004; Wang & Tonon, 2009a,b).

However, that approach is somewhat naïve. The mechanical macroscopic properties (e.g. elasticity and strength) also depend on ensemble properties such as porosity, PSD and proportion of bonded contacts (Schöpfer et al., 2009). Low porosity leads to a greater coordination numbers (more particles in contact) increasing the Young's modulus and the strength. Moreover, the number of non-bonded contacts (controlled by the parameter λ) affects not only the strength, but also affects to the Young's modulus and the Poisson's ratio.

Schöpfer et al. (2009) studied the impact of porosity on Young's modulus. They found out that porosity had a strong impact on Young's modulus (Fig. 5.1). They also studied the impact of the shape of the PSD. Comparing the results between a uniform PSD (a PSD with a shape similar than the one presented in Fig. 5.12a) and a power law PSD (a PSD with a shape similar than the one presented in Fig. 5.12b), they found out that it also had an impact on the Young's modulus and Poisson's ratio (Fig. 5.2).

Ding et al. (2013) also studied the effect of the shape of the PSD on the uniaxial compressive strength and the Young's modulus. They concluded that when the ratio between the maximum particle diameter and the minimum particle diameter increases the uniaxial compressive strength and the Young's modulus that results in the calibrations decrease (Fig. 5.3).

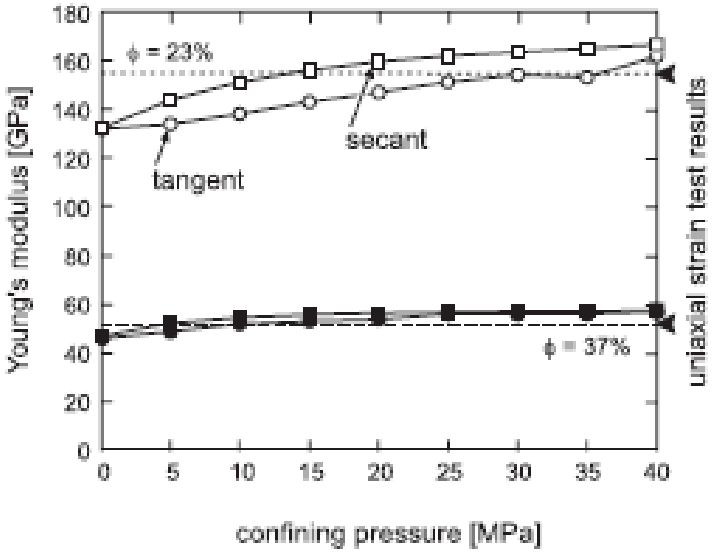

Fig. 5.1. Young's modulus vs. Confining pressure for different porosities ϕ (Schöpfer et al., 2009).

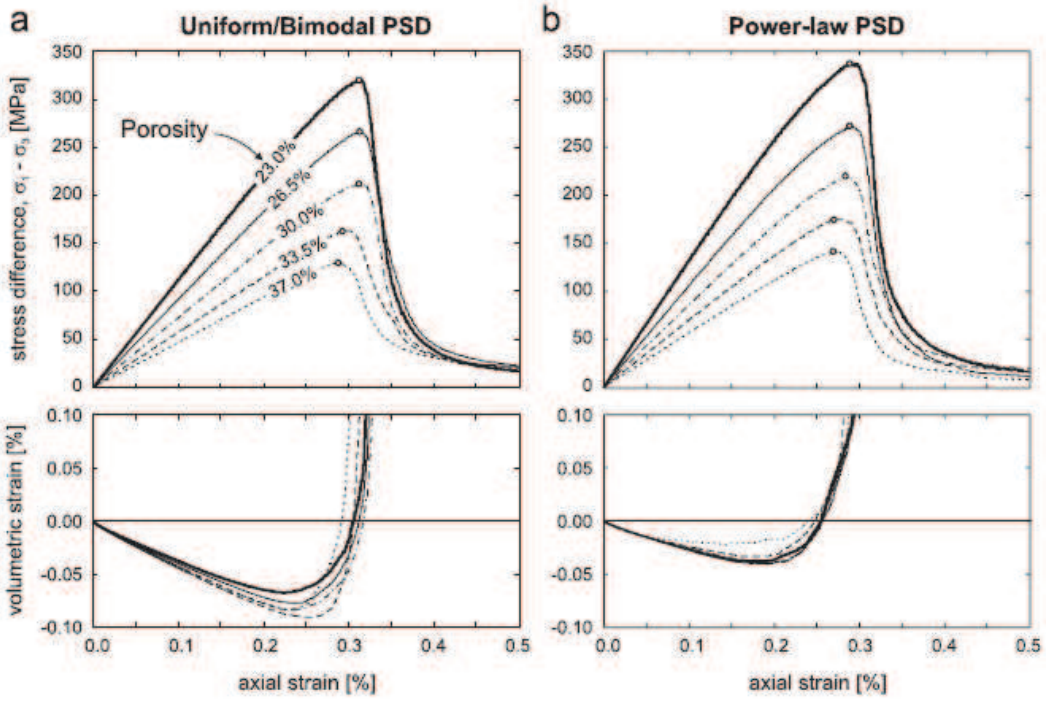

Fig. 5.2. Stress difference and volumetric strain curves obtained from unconfined compression tests on models with (a) uniform PSD and (b) power-law PSD (Schöpfer et al., 2009).

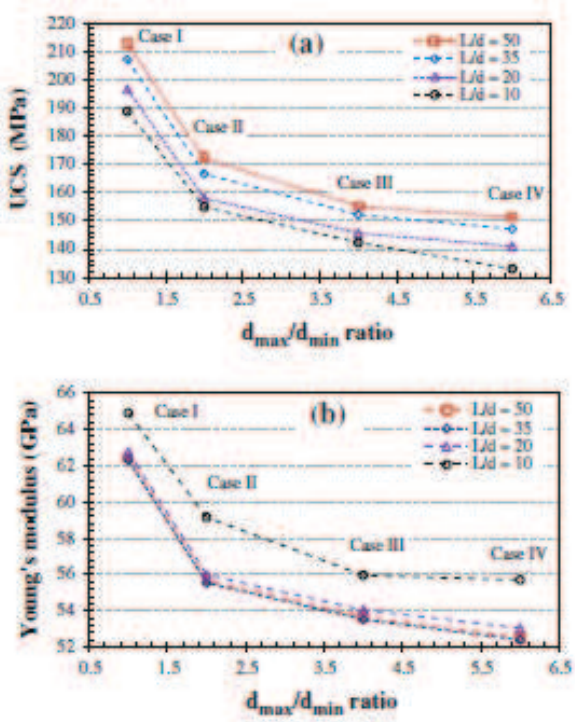

Fig. 5.3. Uniaxial compressive strength (UCS) and Young's modulus versus the ratio between the maximum and the minimum particle diameters for different cases (*l/L* is the ratio between the model size and the median particle diameter) (Ding et al., 2013).

For given ensemble properties, some sensitivity analyses have identified influences of micro-parameters in macro-responses as summarized in Table 5.1: Young's modulus seems to increase by increasing the percentage of bonded contacts (Schöpfer et al., 2009); it also depends on the particle stiffness (Schöpfer et al., 2009; Wang & Tonon, 2009a), the ratio between the normal stiffness and the shear stiffness K^S/K^N (Wang & Tonon, 2009a) and the bond strength (Schöpfer et al., 2009). Poisson's ratio seems to decrease when the percentage of bonded contacts increase (Schöpfer et al., 2009). Moreover, several researchers pointed out that Poisson's ratio does not depend on the normal stiffness but on the ratio between the normal and shear stiffnesses K^S/K^N (Cho et al., 2007; Wang & Tonon, 2009a,b). The axial compressive strength is increased by increasing the particle stiffness, increasing the bond strength and increasing the percentage of bonded contacts (Schöpfer et al., 2009). See Fig. 5.4.

Table 5.1. Observations on effects of PBM micro parameters on macro-response. + means that the macro-parameter increase when the micro parameter increase; - means that the macro-parameter decrease when the micro parameter increase; = means that there is no dependence.

	Proportion of bonded contacts	**Particle stiffness**	K^S/K^N	**Bond strength**
Young's modulus	+ (Schöpfer et al., 2009)	+ (Wang and Tonon, 2009a; Schöpfer et al., 2009)	+ (Wang and Tonon, 2009a)	+ (Schöpfer et al., 2009)
Poisson's ratio	- (Schöpfer et al., 2009)	= (Wang and Tonon, 2009a,b; Cho et al., 2007)	- (Wang and Tonon, 2009a,b; Cho et al., 2007)	
Axial compressive strength	+ (Schöpfer et al., 2009)	+ (Schöpfer et al., 2009)		+ (Schöpfer et al., 2009)

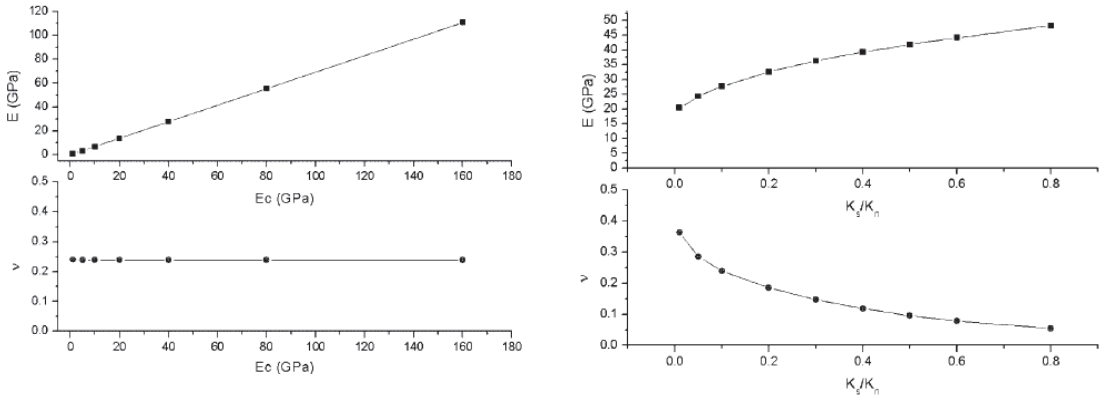

(a) (b)

Fig. 5.4. (a) Macro elastic properties versus stiffness (Wang & Tonon, 2009a) and (b) Macro properties versus K^S/K^N (Wang & Tonon, 2009a).

The effect of the parallel-bond strength on the macroscopic strength was also studied by Cheung (2010) performing triaxial simulations. The macro strength was represented by the peak stress during the triaxial simulations. As it can be observed in Fig. 5.5, the peak stress increases as the parallel-bond strength increases.

Cheung (2010) also studied the effect of the friction in the Young's modulus and the macroscopic strength. Cheung concluded that the general behaviour of the DEM parallel-bonded specimen becomes less sensitive to the inter-particle friction (μ_{DEM}) as

the degree of bonding (α_{bond}) increases. The degree of bonding (introduced in Section 4.4) defines de 'size' of the parallel-bond.

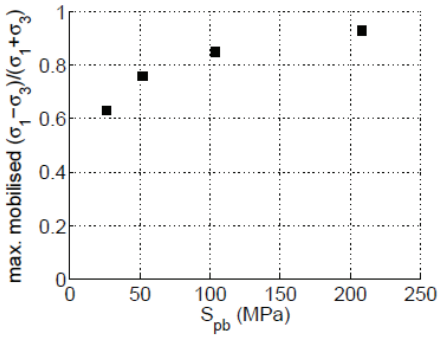

Fig. 5.5. Triaxial simulation: effect of S_{pb} on the peak mobilised stress ratio ($(\sigma_1-\sigma_3)/(\sigma_1+\sigma_3)$) (Cheung, 2010).

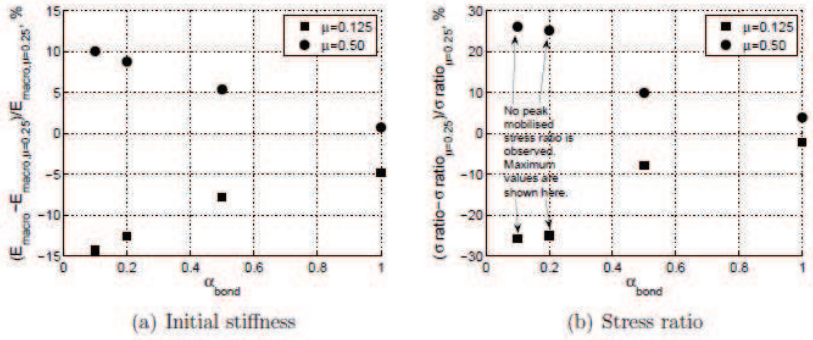

Fig. 5.6. Triaxial simulation: effect of the friction (μ_{DEM}) in the Young's modulus (E_{macro}) and peak stress response $(\sigma_{ratio}-\sigma_{ratio})/\sigma_{ratio}$ dependence on the degree of bonding (α_{bond}).

While the work just summarized offers some cues about the factors affecting the calibration of PBC model micro-parameters, a formal and systematic procedure for calibration is still missing. In this respect, it is also useful to consider the final result obtained by different researchers using this contact model. Results of calibrations performed by different researchers for different rocks are presented in Table 5.2. Some macro parameters of the corresponding target materials are presented in the same table.

Table 5.2. Calibrated PBM parameters and macro parameters obtained by different researchers for different materials. * randomly distributed between given numbers

Reference		***PBC micro parameters***									***Macro parameters***		
Authors	**Material**	E_c **(GPa)**	α_{ratio}	$E_{pb,c}$ **(GPa·m^{-1})**	$\alpha_{pb,ratio}$	μ	S_{pb}^{N} **(MPa)**	S_{pb}^{S} **(MPa)**	λ	α_{bond}	**Young's modulus (GPa)**	**Poisson's ratio**	**ucs (MPa)**
Cho et al. (2007)	Sulfaset	1.4	2.5	1.4	2.5	0.0	200	200	1	1	2.5		11.6
Potyondy & Cundall (2004)	Lac du Bonnet granite	72	2.5	72	2.5	0.5	157	63	1	1	69	0.26	200
Rahmati et al. (2013)	Castlegate sandstone	7	0.2	20	0.2	1.5	400	900	0.3	0-1*		0.2	22
Park & Min (2015)	Assan gneiss	72	0.2	72	0.2	0.8	143	143			73.5		183.8
Park & Min (2015)	Boryeong shale	38	0.3	38	0.3	0.8	75	75			42.1		89.2
Park & Min (2015)	Yeoncheon schist	53	0.8	53	0.8	0.8	80	80			42.1		89.2
Pierce et al. (2009)	Quartzite lithology	52.6	2.5	52.6	2.5	2.5	85	85			52	0.17	86
Cheung et al. (2013)	Castlegate sandstone	20	1	175	1.72	0.5	1250	1500	0.5	0.01-1.0*			
Cheung et al. (2013)	Saltwash sandstone	20	1	175	1	1.0	1000	1200	0.4	0.01-1.0*			
van Wyk et al. (2014)	Paarl granite	63	2.5	63	2.5	0.5	170.1	170.1		1	58.48	0.32	198.29
van Wyk et al. (2014)	Sandstone-2	30	2.5	30	2.5	0.5	174.3	174.3		1	28	0.29	173.7

5.3. Parallel-bond discrete models for the sand production problem

5.3.1. Role of ensemble properties

The sand production problem is, essentially, a problem of soil-fluid interaction. As will be illustrated in detail in subsequent chapters, such interaction is highly dependent on granular ensemble properties such as porosity and grain size distribution. Moreover, absolute grain size does also play a prominent role as fluid-grain interaction forces are grain size dependent.

The need to represent correctly solid-fluid interaction in the model is then a major consideration when selecting ensemble properties for the numerical model. Aspects such as porosity, grain-size distribution and grain size cannot be freely adjusted to match macro-scale mechanical properties.

Another aspect to be taken into account is that of practical computability. DEM models can be very greedy on computer resources and therefore computational constraints need to be also considered when designing the model. As will be exposed in the next sections this fact may also have consequences for the contact model formulation.

5.3.2. Numerical constraints

As explained in the previous chapter, DEM problems are dynamic and simulation is advanced on a stepwise manner. There are two different time-scales of interest. The first measures the duration of the physical problem being simulated; we can call it simulation time, represented as t. The second measures computation time, T, and is the actual time employed in computing the simulation.

Total computation time, T_{comp} required for given total simulation time t_{sim} is mediated by the ratio between the actual computation time step T_{cstep} and the represented simulation time-step t_{step}

$$T_{comp} = \frac{t_{sim}}{t_{step}} T_{cstep} = N_{step} T_{cstep} \qquad \text{Eq. 5.5}$$

As expressed, total computation time can also be obtained as the product of the total number of computational steps (N_{step}) and the time required to compute a single step, $T_{cstep.}$

The value of T_{cstep} depends on the hardware (e.g. memory of the computer), on the code efficiency and the problem complexity. The hardware available for running the simulations presented in this thesis was an Intel(R) Core(TM)2 Quad CPU Q8400 (2.67 GHz) processor, 4 GB of RAM, and Windows 7 Professional Operating System. The code used was PFC^{3D} (4.00-182, 64-bit) coupled with CCFD (first version), a fluid add on, as described in Chapter 6. PFC^{3D} can be extended and manipulated through added code in Fish or C++ but the core routines are not accessible to manipulation and, from the user viewpoint code efficiency can be taken as a given. In this thesis Fish was used for code extension and/or manipulation. It should be noted, however, that using C++ instead of Fish may reduce the computation time in problems with large number of particles or contacts (Itasca, 2008a). It also offers the possibility to perform efficient simulations in which PFC^{3D} variables must be manipulated and fed back to PFC^{3D}during cycling (e.g. coupled analysis).

The complexity of the simulation (Itasca, 2008a) depends on the number of particles and contacts in the model, but not only. During the simulation some problem-controlling parameters defined by the user may need to be evaluated at each step (i.e. the total force on a wall to simulate the servo-control). Also several output parameters chosen by the user can be written at a given number of steps (i.e. stresses for each particle). Obviously, complexity increases significantly when a parallel program is invoked at some given step interval as it happens when the CCFD add-on is used.

Therefore, only for given simulation conditions -i.e. hardware and code- and complexity, T_{cstep} can be roughly estimated as being proportional to the number of elements in the simulation, N_{el}. Moreover, such proportionality constant κ_{sim} needs to be determined empirically.

$$T_{comp} = \frac{t_{sim}}{t_{step}} T_{cstep} = \kappa_{sim} \frac{t_{sim}}{t_{step}} N_{el} \qquad \text{Eq. 5.6}$$

For the coupled CFD-DEM simulations presented in later chapters (Chapter 8 and Chapter 9) we have estimated that κ_{sim} is roughly $2\ \mu s/\text{particle}$. Once a model has been defined and κ_{sim} estimated, certain, desired values of t_{sim} and T_{comp} would impose a ratio between N_{el} and t_{step}. For instance, assuming a value of $\kappa_{sim} = 2\ \mu s/\text{particle}$, requesting a simulation time of 1 s within a computation time of 24 h, gives a ratio N_{el}/t_{step} of around $45 \cdot 10^9$ particles/s; if the computation time is extended to one month, that ratio would be around $2.5 \cdot 10^{12}$ particles/s. Fig. 5.7 represents, (for $\kappa_{sim} = 2\ \mu s/\text{particle}$) the effect of T_{comp}/t_{sim} on the relation between t_{step} and element number. It appears that time steps much below 10^{-8} s will result in either very small particle numbers or very long computational time.

As it is explained in Section 4.2, the DEM time step used in this model is the default time step calculated by PFC^{3D} (Itasca, 2008a). A critical time step is calculated for each particle following

$$t_{crit} = \sqrt{m / \sum K_c} \qquad \text{Eq. 5.7}$$

where *m* is the mass of the particle and $\sum K_c$ is the stiffness of the local particle contact network. The minimum critical time step for the entire system is used as simulation time step (tstep). After each DEM cycle, this minimum is recalculated. This value is dependent on the coordination number (the number of contacts) since

$$\sum K_c = \sum_{i=1}^{CN} K_{c,i} \qquad \text{Eq. 5.8}$$

where *CN* is the coordination number (the number of contacts of the particle) and $K_{c,I}$ is the stiffness of each one of the contacts. All other things equal, as the coordination number increases, K_c increases and the the critical time step decreases. The coordination number depends, in a first approximation, on the PSD -broadly decreasing with uniformity- and porosity -more porous materials have smaller coordination numbers.

Considering now individual contact stiffness (Eq. 5.1) we can see that the two other factors affecting the time step are effective stiffness E_c -it increases network stiffness and decreases time step- and contacting particle sizes.

All other things equal, the contact stiffness which gives the smallest critical time step is the contact between the largest particle and the smallest particle. To illustrate that, Fig. 5.8 represents the time step calculated for each one of the possible contacts for a given PSD, (assuming particle A has 10 contacts with particles of a given distribution fractile). A factor of 6 appears between the larger and smaller cases. Similar explorations for other cases of interest here (Fig. 5.9) reveal an influence on the time step of the same order of magnitude for coordination number and effective stiffness.

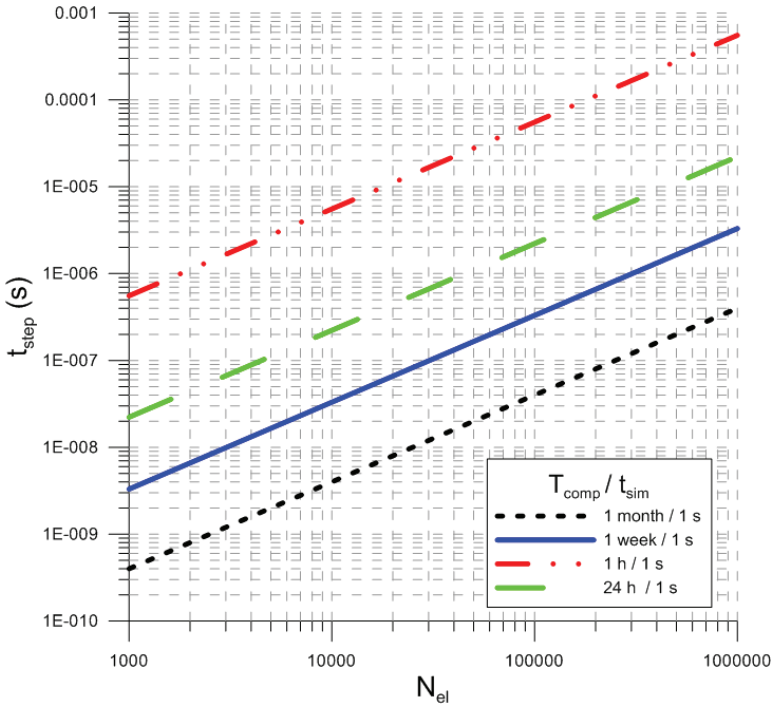

Fig. 5.7. Time step versus number of particles for different computational times and a simulation time of 1 s.

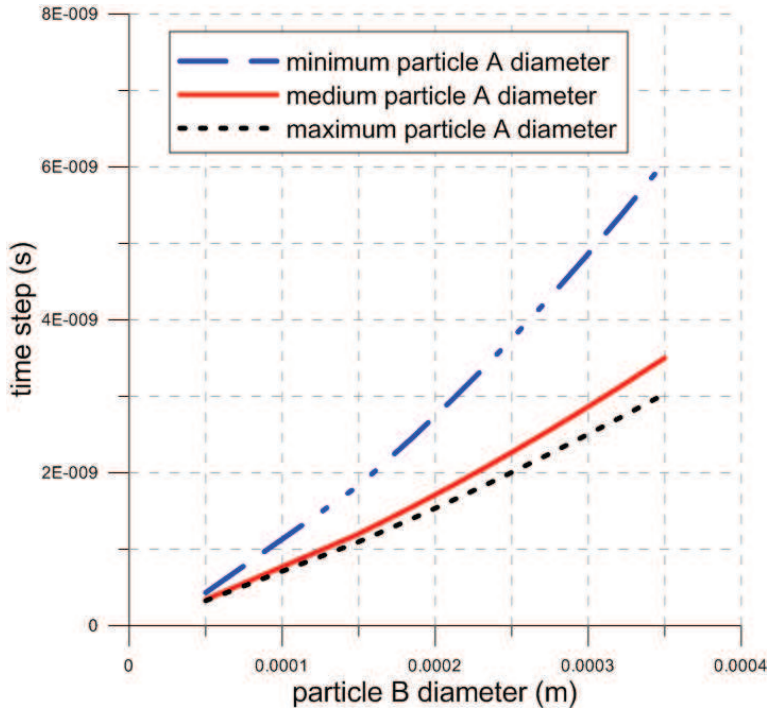

Fig. 5.8. Critical time estimates for FIELD3 (Section 5.4.1, Table 5.3). Particle A is the particle which the critical time is calculated from. Particle B is the particle that is in contact with particle A. Coordination number = 10.

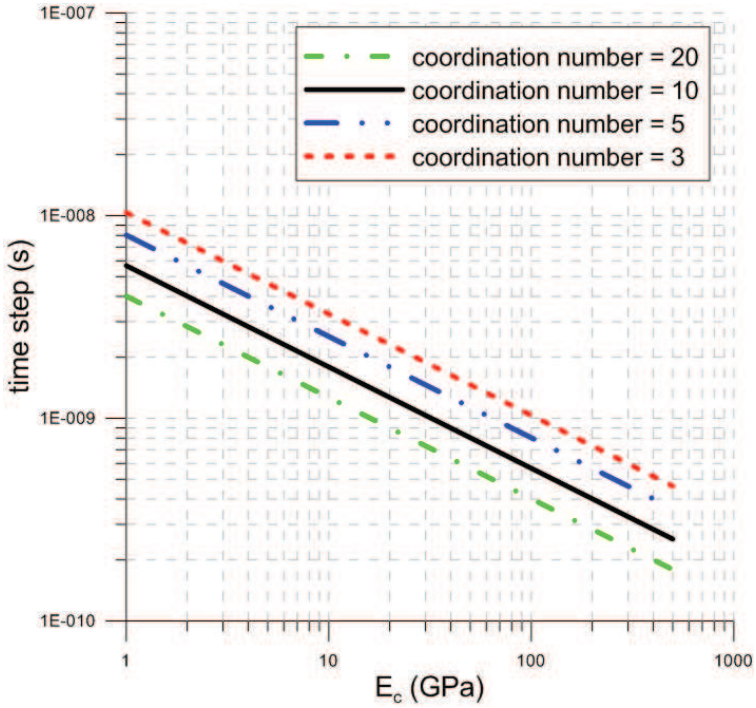

Fig. 5.9. Time step versus effective stiffness for different coordination numbers for the biggest particles of FIELD3 (Section 5.4.1, Table 5.3)

In summary, the maximum particle size in contact with the smallest particle (Fig. 5.8) present in a simulation controls the order of magnitude of the critical time step. Variations within that order of magnitude result from PSD, porosity and contact property characteristics. If the time step order of magnitude resulting from particle size is too small for computational purposes the only feasible alternative is scaling.

Indeed, one possibility to increase the value of the critical time step is by scaling up particle mass, which can be attained either by scaling density or scaling radius. The second route has the added advantage of diminishing computational load (via N_{el} reduction) if the external dimensions of the problem analyzed remain constant. This is the route that has been pursued here.

Following Eq. 5.7 and Eq. 4.4, it can be seen how scaling the particles by a factor of N scales the critical time step by the same factor

$$t_{crit,sc} = 0.8\sqrt{\frac{\rho_p 4\pi N^3 R_{PA,sc}^3}{3K_{c,sc}}} = 0.8\sqrt{\frac{\rho_p 4\pi N^3 R_{PA}^3}{3{\cdot}2E_c \dfrac{N^2 R_{PA}R_{PB}}{N(R_{PA}+R_{PB})}}} = \quad \text{Eq. 5.9}$$

$$= 0.8\sqrt{N^2 \frac{m}{K_c}} = Nt_{crit}\,(CN = 1)$$

where ρ_p is the density of the particle, R_{PA} is the radius of the particle, R_{PB} is the radius of the particle that is in contact, $R_{PA,sc}$ is the radius of the scaled particle and $K_{c,sc}$ is the stiffness of the contact of the scaled particle.

It is clear from the equation above that if a particular value of time step (say, 10^{-8} s) is targeted some iteration may be necessary to choose a scale factor *N,* since the unscaled reference value t_{crit} depends on factors such as effective stiffness and coordination number that are, respectively, calibration and model dependent. This procedure would be considered in Chapter 9 where sand production simulations with materials calibrated in Section 5.4 are carried out.

5.3.3. A scale-independent reduced PBC model

If the particles are scaled the contact model formulation should be such that the mechanical response remains invariant to scaling.

The formulation for contact stiffnesses presented in Chapter 4 is already scalable through the radius dependency inbuilt in the contact stiffness (Potyondy & Cundall, 2004; Gabrielli et al., 2009). Using these expressions the stiffness parameters calibrated are E_c, $E_{pb,c}$, α_{ratio} and $\alpha_{pb,ratio}$. The contact stiffnesses K_c^N, K_c^S, K_{pb}^N and K_{pb}^S are scale dependent, but the stiffness parameters calibrated are scale-independent.

The strength parameters of the PBC model can be made scale independent if particle rotation is prevented. When particle rotation is blocked, the rotation angles of the parallel-bond in Eq. 4.14 and Eq. 4.15 are

$$\theta_N = \Delta\theta_N = 0 \qquad \text{Eq. 5.10}$$

$$\theta_S = \Delta\theta_S = 0 \qquad \text{Eq. 5.11}$$

where these angles are described in Fig. 4.5. Spin and twisting moments of the parallel-bond (Eq. 4.14 and Eq. 4.15) become

$$\Delta M_{pb}^{spin} = M_{pb}^{spin} = 0 \qquad \text{Eq. 5.12}$$

$$\Delta M_{pb}^{b} = M_{pb}^{b} = 0 \qquad \text{Eq. 5.13}$$

The tensile and shear strengths of the parallel-bond (Eq. 4.23 and Eq. 4.24) become

$$\sigma_{\max,pb} = \frac{-F_{pb}^{N}}{A_{pb}} \qquad \text{Eq. 5.14}$$

$$\tau_{\max,pb} = \frac{\left|F_{pb}^{S}\right|}{A_{pb}} \qquad \text{Eq. 5.15}$$

where $A_{pb} = \pi R_{pb}^2$ and R_{pb} is the radius of the cylinder that represents the bond and it is proportional to the radii of the particles bonded (Section 4.4). When particle radii are increased by a factor of *N*, this area is related to the area before the scaling

$$A_{pb,sc} = \pi R_{pb,sc}^2 = \pi N^2 R_{pb}^2 = N^2 A_{pb} \qquad \text{Eq. 5.16}$$

where $A_{pb,sc}$ is the area of the scaled parallel-bond and $R_{pb,sc}$ is the radius of the scaled parallel-bond.

For the breakage limits, because of the no rotation condition it is enough to scale accordingly the strength limits

$$\sigma_{\lim,pb,sc} = \frac{\sigma_{\lim,pb}}{N^2} \qquad \text{Eq. 5.17}$$

$$\tau_{\lim,pb,sc} = \frac{\tau_{\lim,pb}}{N^2} \qquad \text{Eq. 5.18}$$

The failure criteria is then scale independent. That is for the tensile failure criterion

$$\sigma_{\max,pb,sc} = \frac{-F_{pb}^N}{A_{pb,sc}} = \frac{-F_{pb}^N}{N^2 A_{pb}} \le \sigma_{\lim,pb,sc} = \frac{\sigma_{\lim,pb}}{N^2} \qquad \text{Eq. 5.19}$$

$$\sigma_{\max,pb,sc} \le \sigma_{\lim,pb,sc} \Leftrightarrow \sigma_{\max,pb} \le \sigma_{\lim,pb} \qquad \text{Eq. 5.20}$$

And for the shear failure criterion

$$\tau_{\max,pb,sc} = \frac{\left|F_{pb}^{S}\right|}{A_{pb,sc}} = \frac{\left|F_{pb}^{S}\right|}{N^2 A_{pb}} \leq \tau_{\lim,pb,sc} = \frac{\tau_{\lim,pb}}{N^2} \qquad \text{Eq. 5.21}$$

$$\tau_{\max,pb,sc} \leq \tau_{\lim,pb,sc} \Leftrightarrow \tau_{\max,pb} \leq \tau_{\lim,pb} \qquad \text{Eq. 5.22}$$

which means that the bond strength parameters ($\sigma_{\lim,pb} = S_{pb}^{N}$ and $\tau_{\lim,pb} = S_{pb}^{S}$) are scale-independent i.e. they can be calibrated at a small scale and later applied at a larger scale.

The correctness of the scaling procedure proposed was verified experimentally. As an example, the result of an axial compressive test using the original PSD and one where particle size is scaled up by 300 (FIELD3 material in Table 5.3) is given in Fig. 5.10.

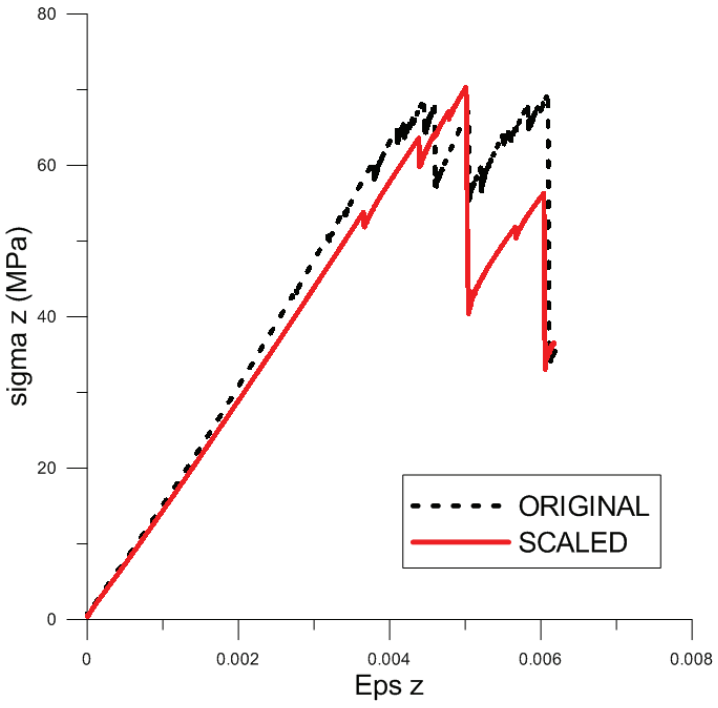

Fig. 5.10. Effect of scaling particle size (scale factor 300) on an axial compressive test of FIELD3.

5.4. Calibration

5.4.1. Target data

One of the objectives of this work was to simulate sand production in realistic scenarios. For this purpose later models are geared to reproduce the conditions prevailing at three different oil fields, whose data was provided by the field services company IESL. The rock mechanical data provided from those fields that was used in the calibration the PBM is presented in Table 5.3. The table also includes a reference to the appropriate sections and equations where these parameters are introduced within this thesis. The bulk density is the density of the solid framework. The dataset also included the PSD corresponding for each case, which are presented here in (Fig. 5.11).

These three cases present some significant differences that are considered of interest to explore their influences in sand production. For example, they cover a wide range of strengths, with FIELD3 being the strongest and FIELD1 the weakest. Comparing these values with the values presented in Section 3.2.1.1, it is observed that they are all inside the (admittedly wide) sandstone range (between 1 and 250 MPa). They also have significant differences in their PSD parameters, but their mean grain size is also well within that of sandstone (between 10 microns and 1000 microns, Section 3.2.1.1).

Table 5.3. Rock mechanical properties of the three different case studies (data provided by IESL). The sections and equations where this parameters are described are also shown in the table.

		FIELD1	FIELD2	FIELD3	Section	Equation
Rock mechanical properties	Young Modulus (GPa)	11,3	20,5	14,7	1.3.2	1.19
	Bulk density (gcm-3)	2,18	2,21	2,51		
	Porosity	0,27	0,25	0,23	1.4.1	1.34
	Friction angle (º)	27,4	34,6	47,45	1.5.2.2	1.62
	Biot's coefficient	0,9267	0,8689	0,7648	1.4.3	1.53
	Poisson Ratio	0,1126	0,1067	0,1717	1.3.2	1.20
	Reservoir permeability (mD)		200	181	1.5.1	1.5
	Uniaxial Compressive Strength (UCS) - Openhole strength (MPa)	3,2	11,7	70,2	4.5	
	Thick Walled Cylinder (TWC) strength - Cased and perforated strength) (MPa)	12,2	30,13	103,4	2,5,2	
Particle size distribution	D10 (microns)	150	431,02	322	1.2.1	
	D50 (microns)	120	227,36	231	1.2.1	
	D90 (microns)	100	30,41	148	1.2.1	
	Sorting Coefficient	2	14,17	2,8	1.2.1	1.2
	Uniformity Coefficient	1,4	8,4	1,7	1.2.1	1.1

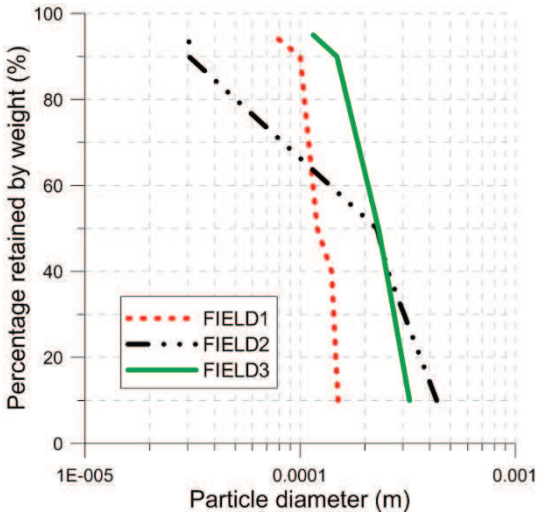

Fig. 5.11. PSDs of the three different case studies (data provided by IESL).

5.4.2. Specimen generation

Specimen formation follows a radius expansion method (REM), proposed by Itasca (2008a), in which small particles with linear contacts are seeded within frictionless walls and expanded to attain the target porosity and stress. Then the parallel bonds are installed.

The in-built particle generation procedure in PFC^{3D} is not able to match a PSD because the code only allows to generate particles with a uniform distribution between maximum and minimum particles diameters.

In order to match a PSD the grain size curve is divided in 10 parts (10% increments) and particles are generated in the range of those classes uniformly. Fig. 5.12 shows the PSD generated for the different materials presented in Section 5.4.1 and compared with the original curves.

It should be noted that the porosities obtained in the discrete analogues did not match those of the real materials. Generally speaking, porosities under 0.3 using REM generation are not attainable (Itasca, 2008a). The specimens were formed at the closest value to the physical porosity value that PFC^{3D} obtained, which varied slightly according to the PSD of each specimen.

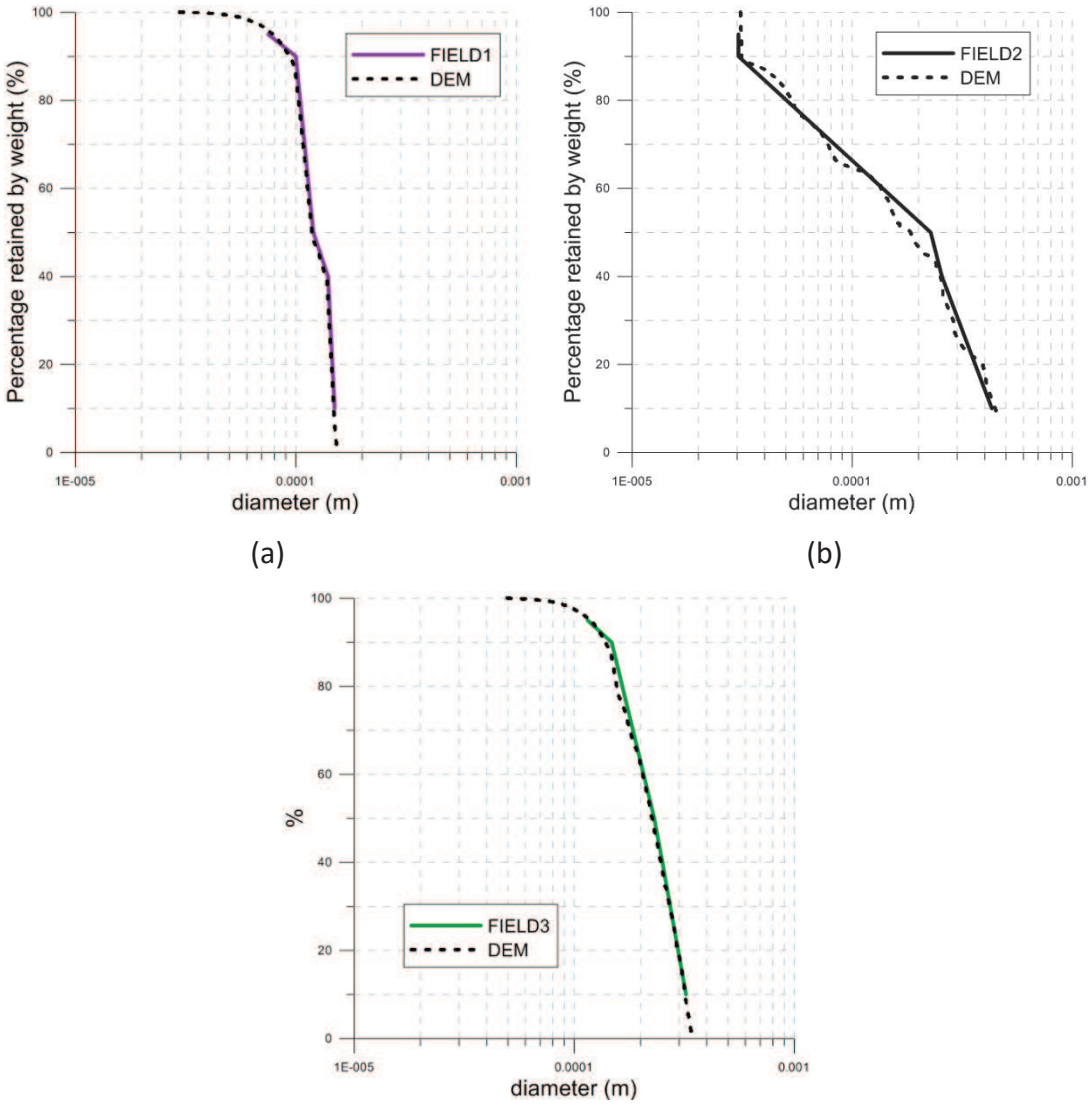

Fig. 5.12. PSDs (original compared with generated with DEM) of (a) FIELD1, (b) FIELD2, and (c) FIELD3.

Table 5.4 shows the different scale factors *N* and the porosity for each material.

Table 5.4. Porosities and scale factors of each specimen

	FIELD1	**FIELD2**	**FIELD3**
Porosity	0.41	0.37	0.38

5.4.3. Contact model calibration

The contact model between the particles has been calibrated to fit some macroscopic parameters provided beforehand (Table 5.3): the Young's modulus, the Poisson's ratio and the uniaxial compressive strength. To calibrate these parameters, different triaxial and axial compressive tests have been performed. Due to the difference between the number of macroscopic parameters (3) and the number of contact model parameters to calibrate (9), some extra simplifying hypothesis were required.

Although as explained in Section 5.2 porosity and PSD also have an effect on the macro mechanical behavior, they are taken as given in this problem. This has the advantage of simplifying the calibration procedure.

Particle rotation is prevented to mimic roughly the effect of nonspherical particle shapes. This limitation is frequently used in unbonded discrete models (e.g. Arroyo et al., 2011). It is key to achieve realistic macroscopic friction angles with spherical unbounded particles (Ting et al., 1989; Butlanska, 2014). This is a convenient feature in a problem were degraded rock plays a major role. Another reason to block rotation here was that it made much simpler the issue of model scalability, as it is explained previously in Section 5.3.3.

Following the same procedure as Potyondy & Cundall (2004), the grain and cement moduli and ratios of normal to shear stiffness are set equal to one another ($E_c = E_{c,pb}$, $\alpha_{ratio} = \alpha_{pb,ratio}$) and the moduli are chosen to match the Young's modulus and the ratios of normal to shear stiffness are chosen to match the Poisson's ratio. The cement strengths are set equal to one another $S_{pb}^{N} = S_{pb}^{S}$ to make both tensile and shear microfailures possible. The mean value of the cement strength is chosen to match the unconfined compressive strength, and $\alpha_{bond} = 1.0$ to make the choice of the inter-particle friction less influential in the results (Section 5.2). Finally, the particle-friction coefficient is chosen as $\mu_{DEM} = 0.5$.

After that, the only parameters left to be calibrated were E_c, the ratio α_{ratio}, S_{pb}^{N} and λ (the proportion of bonded contacts). The effective stiffness is calibrated comparing the Young's modulus resulted in the axial compressive test with the one given by the field data; the ratio between the normal and the shear stiffness is calibrated comparing the Poisson's ratio calculated from triaxial tests with the one given by the field data; and the bond strength and λ comparing the uniaxial compressive strength obtained in the axial compressive tests performed and the one given by the field data.

5.4.4. Modelling laboratory tests

5.4.4.1. Triaxial test

A cylindrical wall and two rectangular walls are first generated (Fig. 5.13). Particles are generated inside the walls and a confining pressure is first applied to all boundaries to reach an equilibrium state. The height to diameter ratio is 2:1. Then an axial displacement is applied incrementally while keeping the confining pressure constant on the cylindrical wall using a stress-controlled wall. The wall-particle friction is the same as the particle-particle friction. It is later explained (Chapter 7 and Chapter 8) that material damping has important effects on fluid-coupled simulations. Therefore, even for this mechanical-only simulations damping was set to 0 to use the same conditions that are prevailing in later fluid-coupling simulations.

If all grains were considered as in real triaxial tests the number of particles in a typical specimen (diameter between 10 mm and 50 mm, height between 20 mm and 100 mm) would be large (more than 200000 particles) and the computational cost high. Potyondy & Cundall (2004) considered the effects of the number of particles in DEM simulations of triaxial and Brazilian tests using the PBM. Their results indicated that the macro-properties obtained from a triaxial test simulation generally become less sensitive to the number of particles when there are more than 20 particles across the specimen width. The number of mean-sized particles across the specimen diameter has been always

maintained well above 20 in the DEM calibration tests performed in this thesis. Table 5.5 summarize the dimensions of the triaxial tests for each material and the ratio of the specimen diameter and the mean particle diameter (D50 defined and presented in Table 5.3).

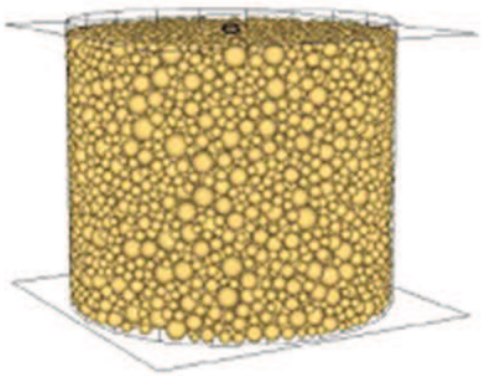

Fig. 5.13. DEM representation of a triaxial test

Table 5.5. Dimensions of the triaxial tests

	Specimen diameter (mm)	**Specimen height (mm)**	**Specimen diameter/ (D_{50})**
FIELD1	2.4	4.8	20
FIELD2	4.6	9.2	20.2
FIELD3	4.7	9.4	20.3

A typical result of a triaxial test is presented in Fig. 5.14. The elastic region is the region before the peak stress point. To calculate the Young's modulus and the Poisson's ratio, the values for the stress, axial strain and radial strain are taken when the stress value is the half of the peak stress value. The Poisson's ratio and the Young's modulus are calculated using the elastic region results as follows:

$$E = \frac{\sigma_z}{\varepsilon_z} \qquad \text{Eq. 5.23}$$

$$\nu = \frac{\varepsilon_r}{\varepsilon_z} \qquad \text{Eq. 5.24}$$

where *E* is the Young's modulus, ν is the Poisson's ratio, σ_z is the axial stress, ε_z is the axial stress and ε_r is the radial strain.

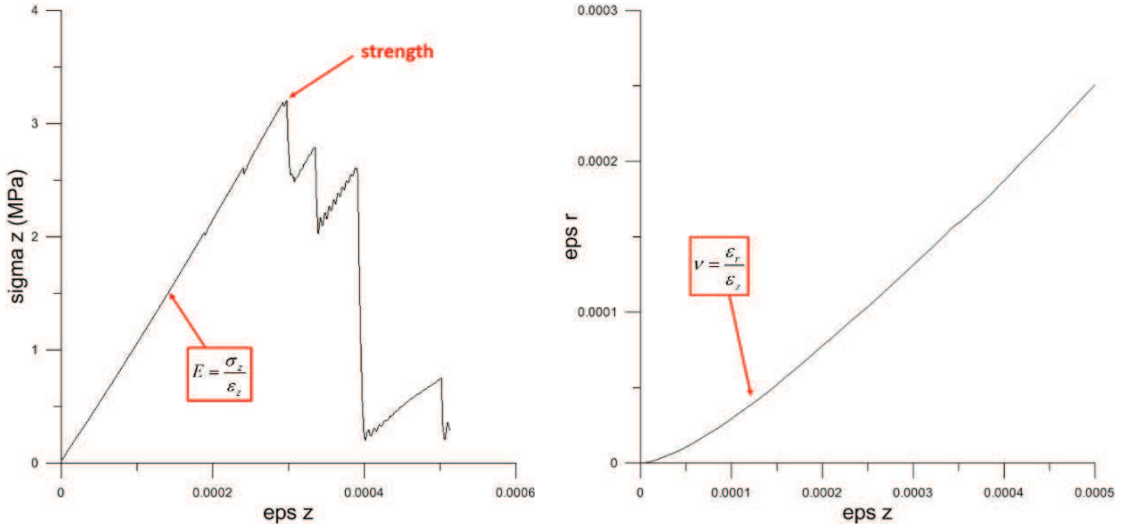

(a) (b)

Fig. 5.14. (a) Axial stress versus the axial strain, and (b) radial strain versus axial strain of a triaxial test DEM simulation.

5.4.4.2. Uniaxial compressive test

The procedure for the uniaxial compressive test simulation is similar than the one for triaxial test except that the lateral boundary is removed before the simulation. The axial stress is applied axially until the stress peak is reached. The shape of the stress-strain curve is similar than the one obtained for the triaxial test (Fig. 5.14). In this test only the

Young's modulus is calculated using the equation. The uniaxial compressive strength is the stress value at the peak (the strength, also indicated in Fig. 5.14).

The dimensions of the uniaxial compressive tests are the same as presented in Table 5.5 for triaxial tests.

Fig. 5.15 shows a generated sample before a test and at the end of the test.

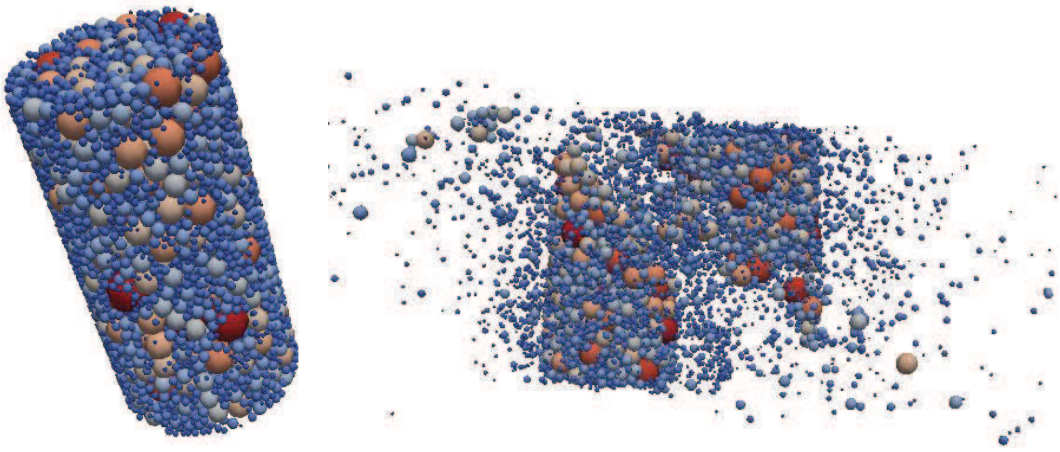

Fig. 5.15. Axial compressive test on a FIELD3 discrete analogue material. Before the simulation (left) and after the simulation (right). Colours represent the diameters of the particles.

5.4.5. Calibration results

Following the procedures explained, a calibration of the PBM for the 3 different materials presented in Section 5.4.1 has been performed.

The simulations performed to calibrate FIELD2 material are shown in Table 5.6. 'atc' represents the axial compressive tests and 'tri' the triaxial tests. E_c is the effective stiffness, *knks* is α_{ratio}, S is the parallel-bond strength, *lambda* is λ, and *ucs* is the uniaxial compressive strength. Table 5.7 shows the calibrated parameters for all the materials. First of all, axial compressive tests are performed changing the effective stiffness and the bond strength until the Young's modulus and the uniaxial compressive strength are achieved. After that, the same parameters are used for triaxial tests, where

the ratio between the normal and the shear stiffness and the effective stiffness are changed until the target Poisson's ratio is attained and the Young's modulus is maintained. An axial compressive test is again carried out. If the uniaxial compressive test does not equal the target one, the bond strength is again changed and uniaxial compressive tests are performed. All the procedure is repeated until the Young's modulus, the Poisson's ratio and the uniaxial compressive strength from the target data are achieved.

FIELD1 and FIELD3 materials calibrations are in Appendix E. For the FIELD1 needed a total of 18 axial compressive tests and 25 triaxial tests to adjust the calibration; FIELD2 needed 8 axial compressive tests and 7 triaxial tests; and FIELD3 is calibrated after a total of 31 axial compressive tests and 17 triaxial tests were simulated to adjust the calibration.

Table 5.6. Iterations to adjust FIELD2 macroscopic mechanical values.

	Ec (GPa)	knks	S (MPa)	lambda	Young Modulus (GPa)	ucs (MPa)	Poisson's ratio
act1	108	0,75	120	1	24,85	13,95	
act2	108	0,75	100	1	25,03	11,35	
act3	100	0,75	100	1	22,41	11,77	
act4	80	0,75	100	1	18,38	11,71	
act5	95	0,75	100	1	21,59	11,96	
act6	90	0,75	100	1	20,54	11,30	
act7	90	0,75	110	1	20,78	12,30	
tri7	90	0,75	110	1	17,13	10,27	0,0975
tri8	90	0,8	110	1	16,66	10,95	0,1119
tri9	100	0,8	110	1	18,44	10,70	0,1062
tri10	130	0,8	110	1	26,48	11,96	0,1179
tri11	110	0,8	110	1	20,10	11,46	0,1121
tri12	115	0,8	110	1	21,58	11,65	0,1150
tri13	112	0,8	110	1	20,72	10,90	0,1087
act13	112	0,8	110	1	24,66	11,78	

Table 5.7. Calibrated PBM micro parameters.

	E_c (GPa)	α_{ratio}	$E_{c,pb}$ (GPa)	$\alpha_{pb,ratio}$	S_{pb}^{N} (MPa)	S_{pb}^{S} (MPa)	λ
FIELD1	3.7	0.05	3.7	0.05	25	25	1
FIELD2	112	0.8	112	0.8	110	110	1
FIELD3	120	1.2	120	1.2	94	94	1

These calibrated parameters (Table 5.7) can be compared to other PBM parameters calibrated for other materials by different researchers (Table 5.2) FIELD1 has a normal stiffness below most values previously calibrated by other researchers. It is more similar than the Castlegate sandstone calibrated by Rahmati et al. (2013). The strength of that material is also very low, by comparison. The reason why of that low strength could be that FIELD1 sample has a higher porosity than the original material. As explained in Section 5.2 increasing the porosity could increase the uniaxial compressive strength having to decrease the strength of the PBM. On the other hand, stiffness of FIELD2 and FIELD3 are very high, of one order of magnitude higher than the ones calibrated by all the authors. Again, the porosity of the material during the calibration is higher than the original one. Due to that, as explained in Section 5.2, the Young's modulus could decrease having to increase the stiffness to increase the Young's modulus result in the simulations. Strengths of FIELD2 and FIELD3 have magnitudes similar than Sandstone-2, Paarl granite, Assan gneiss and Sulfaset.

Fig. 5.16 shows the ratio between the bond strength and the uniaxial compressive strength versus the ratio between the effective stiffness and the Young's modulus (E) for the three calibrations and some of the calibrations performed by other researchers (Table 5.2). It can be observed in Fig. 5.16 that FIELD 2 and FIELD3 have a ratio E_c/E much higher than the previously calibrated by other researchers. The reason of that difference could be the effect of the porosity explained above that increase the effective stiffness. Moreover, FIELD2 have a ratio S_N/ucs much higher than the most of the calibrated by other researchers. FIELD2 have a power-law PSD (Fig. 4.12b) and a ratio D_{max}/D_{min} (maximum and minimum particle diameters) very high (14-15) in comparison to FIELD1 and FIELD3. As it is explained in Section 5.2, as D_{min}/D_{max} increase the calibrated uniaxial compressive strength decreases (Fig. 5.3). FIELD1 calibration results are very similar than the ones presented by Cho et al. (2007) and the ratios E_c/E and S_N/ucs are also very similar.

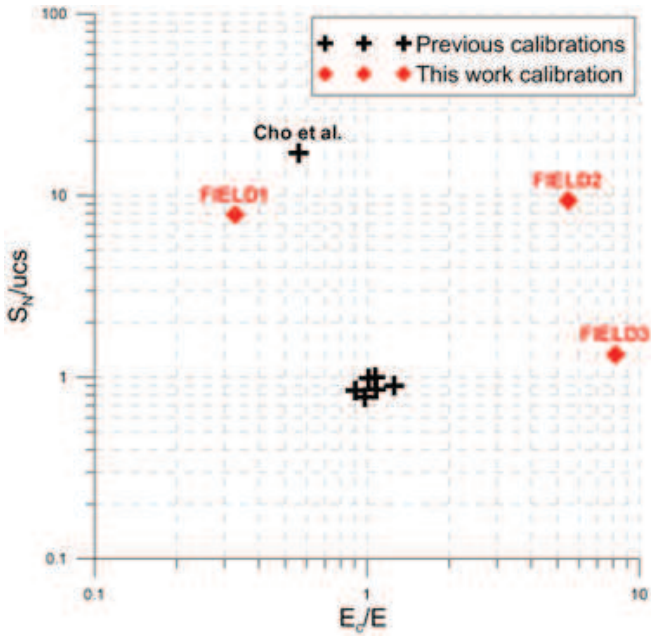

Fig. 5.16. Ratio between the parallel-bon strength (S_N) and the uniaxial compressive strength (ucs) versus the ratio between the effective stiffness (E_c) and the Young modulus (E). The previous calibrations are some of the ones presented in Table 5.2. Logarithmic scale in both axis.

5.5. Summary

It could be said that rock and sandstone behaves like a cemented granular material in which cement may break. Parallel-bond in PFC^{3D} can mimic the mechanical behaviour corresponding with rock and sandstone. In this thesis the parallel-bond is used together with the linear friction model between particles. The calibration of the contact parameters (micro parameters) has to be performed using reference macro parameters obtained in the laboratory.

In this thesis rock is represented to perform sand production problems. First of all, the interaction between particles and fluid must be represented correctly. When the solid-fluid interaction is performed, some properties, as the PSD and porosity selection must have a major consideration. Moreover, the practical computability has to be taken into account. DEM models can be very greedy on computer resources and computational constraints need to be also considered when designing the model. Because of that, the time step have been limited in the simulations in this thesis. Limiting the time step leads to a particle scaling, increasing particle radii, and to the need of using micro-parameters

which are scale-independent. Other considerations, as the number of particles has also to be into account in next chapters. A study of the influences of all the parameters to the computational cost has been presented.

The rock mechanical properties of three different materials have been presented and are being calibrated using the Young's modulus, the Poisson's ratio and the uniaxial compressive strength. To calibrate these parameters, different triaxial and axial compressive tests have been performed. The stiffness is calibrated comparing the Young modulus resulted in the axial compressive test with the one given by the field data; the ratio between the normal and the shear stiffness is calibrated comparing the Poisson's ratio calculated in the triaxial tests with the one given by the field data; and the bond strength and λ comparing the uniaxial compressive strength obtained in the axial compressive tests performed and the one given by the field data.

Chapter 6 - Fluid-particle interaction using CFD-DEM

6.1. Introduction

In Chapter 4 and Chapter 5, DEM tools for simulating the mechanical behaviour of geomaterials were introduced. Most geomaterials are permeated by fluids and the interaction between those fluids and the geomaterial particles should be taken into account, especially when, as it occurs here, particle erosion and transport is important for the process under study.

First of all, some concepts of fluid dynamics and CFD are recalled. After that, the basics of particle-fluid interaction are explained and the different numerical approaches for studying this interaction are presented, with particular emphasis in the one used here, namely CFD-DEM. Finally, previous examples of sand production studies and other applications using CFD-DEM and other similar methods are reviewed.

6.2. Fluid dynamics and CFD

Fluid flow is usually described by differential equations, as it is explained below. CFD are methods to obtain numerical solutions discretizing and approximating those equations by a system of algebraic equations (Ferziger & Peric, 1999).

Fluid dynamics describes the behaviour of the fluid focusing on the macroscopic level, where the fluid is treated as a continuum medium. The fluid particle, the individual "element" considered in fluid dynamics, is actually not a single molecule, but consists of a large number of molecules in a small region with respect to the scale of the considered domain, but still sufficiently large in order to be able to define a meaningful and non-ambiguous average of the velocities and other properties of the individual molecules

and atoms occupying this volume. The approximations and the results are applied and given at discrete locations in space and time (Ferziger & Peric, 1999). The equations describing fluid flows and mass transfer are versions of the conservation laws of classical physics as conservation of momentum (Newton's second law of motion) and conservation of mass. For a Newtonian fluid the conservation of momentum equation becomes the Navier-Stokes equation, which can be expressed as Eq. 6.1, and the conservation of mass can be expressed as Eq. 6.2

$$\rho_f \frac{\partial u}{\partial t} + \rho_f u \nabla u = -\nabla p + \mu_f \nabla^2 (u) + \frac{1}{3} \mu_f \nabla \cdot (\nabla u) \qquad \text{Eq. 6.1}$$

$$\nabla \cdot (\rho_f u = 0) \qquad \text{Eq. 6.2}$$

where ρ_f is the fluid density, *u* is the fluid velocity, *p* is the fluid pressure and μ_f is the fluid viscosity.

There are two dimensionless numbers to categorize the behaviour of the fluid: the Mach number and the Reynolds number. The Mach number is a dimensionless number that quantifies the compressibility of a fluid. The Mach number is defined as

$$M = \frac{u}{a} \qquad \text{Eq. 6.3}$$

where *a* is the speed of sound in the fluid. When $M < 1$ the flow is subsonic and when $M > 1$ the flow is supersonic. A fluid is considered incompressible for flows in which $M < 0.3$. Navier-Stokes and continuity equations for incompressible flows reduce to

$$\rho_f \frac{\partial u}{\partial t} + \rho_f u \nabla(u) = -\nabla p + \mu_f \nabla^2(u) \quad \text{Eq. 6.4}$$

$$\nabla \cdot u = 0 \quad \text{Eq. 6.5}$$

The Reynolds number quantifies the relative importance of the inertial forces of the fluid and the viscous forces for a given flow conditions

$$Re = \frac{\rho_f u L_D}{\mu_f} \quad \text{Eq. 6.6}$$

where L_D is the characteristic linear dimension of the problem. It characterizes different flow regimes, such as laminar or turbulent flow. For Reynolds numbers *Re*<2000 the flow is laminar, when $2000 \leq Re \leq 4000$ the regime is a transition flow, and for *Re*>4000 the flow is turbulent. However, these limits may vary slightly depending on the boundary conditions of the problem (Finnemore & Franzini, 2002). When the fluid flows through a granular material the characteristic linear dimension of the problem is the grain diameter.

In the analysis of groundwater flows Darcy's law (Chapter 2, Eq. 2.4) is commonly used. However, Darcy's law is an experimental formula only valid for laminar flows (low Reynolds numbers) in relatively homogeneous materials (Finnemore & Franzini, 2002; Chareyre et al., 2012). In that case the flow is also called a Darcy's flow.

CFD is a computational model for fluid dynamics. This approach follows a basic procedure: geometry of the problem is defined with its physical bounds and boundary conditions, the initial conditions are created for a transient problem, a mesh containing discrete fluid elements (cells) is created, and a postprocessor is used for the analysis and the visualization of the results.

Coupled CFD (CCFD) add-on is the CFD code used in all the simulations and studies performed in this thesis. The CCFD code is a product of ITOCHU Techno-Solution Corporation (CTC) of Tokio, Japan. CCFD is a finite volume method code that calculates the heat and flow of the fluid. CCFD uses a finite element method nonlinear structural analysis system called FINAS which allows the interaction of fluids and structural shapes (ITOCHU, 2007).

CCFD allows the use of structured and unstructured grids. Structured grids are formed by hexahedral, tetrahedral and prismal cells, and unstructured grids can have irregular patterns designed by the user. CCFD calculates the fluid velocity and the fluid pressure at the centre of each cell a discretization strategy known as a collocated grid. The boundary conditions are set on cells boundaries and initial conditions are set in the centre of each cell. Using these pressure values at the centre of the cells, the pressure values are interpolated and calculated at the centre of the cell faces. Pressure gradients at the centre of the cell are calculated from the fluid pressure values at the centre of the faces using an equation according to the Gauss divergence theorem (Itasca, 2008b).

The numerical method used by CCFD is Finite Volume Method (FVM) that solves the integral form of the differential equations (Itasca, 2008b). When FVM is used, the solution domain is subdivided into a finite number of contiguous control volumes (CV), and the conservation equations are applied to each CV (Ferziger & Peric, 1999). CCFD uses SIMPLE (Semi Implicit Method for Pressure Linked Equations) algorithm to solve non transient problems. This algorithm starts using boundary conditions values and solves momentum equation for fluid velocity. After that, advects fluid and calculates pressure gradient term. Finally, adjust fluid velocity and pressure iteratively until a volume conservative solution is found (Itasca, 2008b). Many other methods exist to solve Navier-Stokes equation; SMAC (Simplified Marker And Cell) algorithm is also used by CCFD for transients calculations.

A numerical method for turbulent flow can be specified by the user if it is necessary; therefore, Reynolds numbers relevant for the problem should be evaluated before the simulation. On the other hand, Mach number should also be studied to check the condition $M < 0.3$ because the code uses an incompressible fluid flow approximation.

6.3. Particle-fluid interaction

In general, particles in granular materials are surrounded by fluid (gas or liquid). In some problems the interaction between particles and fluid is of paramount of importance to understand the mechanical problem, especially when the fluid flow affects not only the stress of the system, but also its mass through granular transport (erosion). To simulate this interaction two models have to be coupled, one for the solid phase and another one for the fluid phase. To describe the phenomena involved, the governing equations for both phases and relationships between them are needed.

When the solid phase is represented by discrete elements several fluid-coupling techniques are available (Zhu et al., 2007). An important classification criterion is the different length and time scales at which they aim to solve the fluid mechanics. Several approaches are presented below.

The particle Reynold's number is defined as

$$Re_p = \rho_f d_p n|u-v|/\mu_f \qquad \text{Eq. 6.7}$$

where ρ_f is the fluid density, d_p is the particle diameter, n is the porosity, μ_f is the fluid viscosity, u is the fluid velocity and v is the particle velocity. Comparing this equation to the general Reynold's number equation for a fluid (Eq. 6.6), it can be observed that the characteristic linear dimension considered is the diameter of the particle.

6.3.1. Numerical approaches to simulate particle-fluid interaction

In a particle-fluid flow system two different models are used and coupled: one for the solid phase (where discrete particles follow the solution of Newton's equations of motion) and another one for the fluid phase.

Different techniques have been developed depending on the different length and time scales of each model. Fluid flow can be modelled using discrete approaches (e.g. Molecular Dynamic Simulation (MDS), Lattice-Boltzmann (LB), Pore-Scale Finite Volume (PFV), Pseudo-Particle Method (PPM) and Smoothed Particle Hydrodynamics (SPH)) or continuum approaches (e.g. Direct Numerical Simulation (DNS), Large Eddy Simulation (LES) and CFD techniques). All of these approaches can be coupled with DEM and many of them have been tried already, for example LB-DEM (Cook et al., 2004), PFV-DEM (Catalano, 2013; Chareyre et al., 2012), PPM-DEM (Ge & Li, 2001, 2003a,b), CFD-DEM (Tsuji et al., 1993), DNS-DEM (Hu, 1996; Pan et al., 2002), LES-DEM (Zhou et al., 2004a,b,c) and Smoothed Particle Hydrodynamics (SPH)-DEM (Potapov et al., 2001).

Although DNS and LB are based on CFD, generally, the term CFD is used for the computational fluid dynamic techniques that solve the fluid dynamic equations in a computational cell longer than DNS and LB computational cells ones, because DNS and LB approaches have a sub-particle length scale, whilst CFD cells contain different particles. Therefore, CFD-DEM model is commonly used because of its generally perceived superior computational convenience as compared to DNS or LB-DEM (Zhu et al., 2007). It is recognised, however, that PFV-DEM methods may also overcome the high computational cost of the microscale models using a sub-particle length scale.

6.3.2. CFD-DEM

The numerical approach usually referred as CFD-DEM coupling (Zhu et al., 2007) is derived from classical treatments of fluidized dense suspensions (Anderson & Jackson,

1967). In them, a pore-scale locally averaged version of the Navier-Stokes equations is used to represent fluid motion, and typically solved numerically using CFD techniques.

CFD-DEM was pioneered by Tsuji et al. (1993) and Kawaguchi et al. (1998) to simulate the formation of bubbles in two and later three-dimensional gas-fluidized beds. It is now an increasingly favoured approach for process and chemical engineering problems (Zhu et al., 2007). Geomechanical applications of CFD-DEM have been documented by El Shamy & Zeghal (2005, 2007) who used the method to study sand boiling in artesian conditions and seismic shear-induced liquefaction in water-saturated sands. A CFD-DEM formulation, different in detail yet similar in concept to the one presented below, was used by Zhou et al. (2011) in a study of sand production.

In CFD-DEM the particle velocity adds a drag force to the fluid momentum balance equations and the porosity affects directly the flow through the fluid governing equations. In this approach description of the fluid flow takes place at the computational cell level, whilst description of the solid phase is made through particles. Each particle in the cell has its own velocity, while the fluid velocity is the same for the entire cell. For each particle within a cell, the drag force is different, because it depends on the individual particle velocity, but also the buoyancy and pressure forces are different, due to their dependence of particle radius.

6.3.2.1. Forces on the particles due to fluid

As presented in the previous chapter, particle motion in DEM is described by Newton's second law. In the presence of a fluid, a force is added due to interaction with fluid. The equilibrium equations for a particle are now:

$$m\frac{dv}{dt} = \sum_j F_j^c + F^f + F^g \qquad \text{Eq. 6.8}$$

$$I\frac{d\omega}{dt}=\sum_j M_j \qquad \text{Eq. 6.9}$$

where v and ω are the translational and angular velocities of the particle, respectively, F_j^c and M_j are the contact force and torque acting on the particle by particle j or walls, F^f is the particle-fluid interaction force on the particle, and F^g is the gravitational force.

Several component forces may contribute to fluid-particle interaction. In this thesis we only use the drag force (the force due to the difference between the fluid velocity and the particle velocity), the buoyancy force and the pressure gradient force. Although other component interaction forces may be considered, as for example the virtual mass force, Basset force and lift forces (e.g. Li et al., 1999; Xiong et al., 2005; Potic et al., 2005), they are neglected. These forces are only important when particles suffer high rotations, or in high pressure gradient conditions or very low fluid density.

When the Reynolds number is very low, in the laminar flow regime, the drag force on a single spherical particle is given by Stoke's law (Finnemore & Franzini, 2002)

$$F_{laminar}=3\pi\mu_f d_p^2(u-v) \qquad \text{Eq. 6.10}$$

This is called the Stokes-Einstein equation (Beetstra et al., 2006). This result is valid in the limit where both porosity approaches 1 and the Reynolds number approaches 0 (Re_p < 1) (Finnemore & Franzini, 2002; Beetstra et al., 2006). In more general fluid flow regimes, the drag resistance force for an isolated sphere particle in a fluid is described by Newton's equation:

$$F_d=C_d\pi\rho_f d_p^2|u-v|(u-v)/8 \qquad \text{Eq. 6.11}$$

where C_d is the drag coefficient, ρ_f is the fluid density, d_p is the particle diameter, u is the fluid velocity and v is the particle velocity. The particle fluid drag coefficient, C_d, expresses the effect of solid shape and surface properties on the interaction between the particle and the fluid. C_d is nearly always experimentally obtained (Ferziger & Peric, 1999) and it has been observed experimentally that it is dependent on the particle Reynold's number, Re_p, and liquid properties (Finnemore & Franzini, 2002). As cited by DallaValle (1948), Wadell (1934a,b) collated existing data for spheres and found that the drag coefficient (also called coefficient of resistance) is a function of Reynolds number (Fig. 6.1).

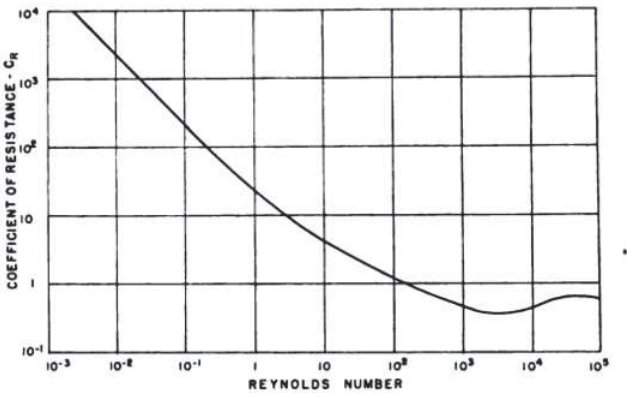

Fig. 6.1. Coefficient of resistance (drag coefficient) as a function of Reynolds number (DallaValle, 1948).

Comparing Eq. 6.10 and Eq. 6.11, it can be derived that the drag coefficient for very low Reynolds number flows is $\frac{24}{Re_p}$ (Finnemore & Franzini, 2002).

There are different expressions for the drag coefficient in the literature used by different researchers. The most used and best known are

$$C_d = 24\left(1+0.15Re_p^{0.687}\right)/Re_p \quad \left(Re_p < 1000\right) \qquad \text{Eq. 6.12}$$

$$C_d = 0.44 \quad \left(Re_p > 1000\right) \qquad \text{Eq. 6.13}$$

Eq. 6.12 was presented in Wen & Yu (1966) and Eq. 6.13 is a result of the observation of the turbulent region in Fig. 6.1 (DallaValle, 1948).

Di Felice (1994) proposed another expression for the drag coefficient of spherical particles which provides an adequate representation of the available empirical data over the full practical range of particle Reynold numbers (Di Felice, 1994).

$$C_d = \left(0.63 + \frac{4.8}{\sqrt{Re_p}} \right)^2 \qquad \text{Eq. 6.14}$$

When there is more than one particle the drag force cannot be derived analytically. Particle configuration and particle and fluid properties affect the general drag force due to the reduction of the space of fluid, the sharp velocity gradient generated and the increase of the shear stress on particles surfaces. A voidage function $f(n)$ is added to the drag force expression

$$F_d = f(n) C_d \pi \rho_f d_p^2 |u - v| (u - v) / 8 \qquad \text{Eq. 6.15}$$

In general, two methods have been widely used to determine voidage functions. The first one is based on empirical correlations for bed expansion and pressure drop in fluidized beds (Ergun, 1952; Wen & Yu, 1966). Wen & Yu (1966) correlated the voidage function with the porosity using experimental data. Ergun (1952) correlated directly the energy loss (which can be related to a drag force) with a function of the porosity also using experimental data.

The experimental data was obtained using different water flow rates and calculating the porosity changes in the beds of granular solids and the pressure drop (Ergun, 1952; Wen

& Yu, 1966). In this case, the effect of the presence of other particles is considered in terms of local porosity and two different expressions are derived depending on the porosity value:

$$F_d = \frac{1}{6}\pi d_p^3 \frac{\beta(v-u)}{1-n} \qquad \text{Eq. 6.16}$$

$$\beta = \frac{1-n}{d_p^2 n^2}\left[150(1-n)\mu_f + 1.75(1-n)\rho_f d_p |u-v|\right] \quad (n \le 0.8) \qquad \text{Eq. 6.17}$$

$$\beta = \frac{3}{4} C_d \frac{|u-v|\rho_f (1-n)}{d_p} n^{-1.7} \quad (n > 0.8) \qquad \text{Eq. 6.18}$$

Eq. 6.17 was proposed by Ergun (1952) for spherical particles. Eq. 6.18 was proposed by Wen & Yu (1966).

However, in some cases the step change in drag forces that Ergun (1952) and Wen & Yu (1966) expressions produce at a porosity of 0.8 (Fig. 6.2) can be problematic; in these cases, the continuous single-function Di Felice (1994) correlation can be used (Kafui et al., 2002). The expression proposed by Di Felice (1994) is related to the flow regimes or particle Reynolds number. The value of the exponent varies in a rather large range (from -3 to 10) (Zhu et al., 2007).

$$f(n) = n^{-\chi} \qquad \text{Eq. 6.19}$$

$$\chi = 3.7 - 0.65\exp\left[-(1.5\log Re_p)^2/2\right] \qquad \text{Eq. 6.20}$$

Even though there are differences between both correlations, the results for a porosity of 0.4 are the same (Di Felice, 1994), as it can be observed also in Fig. 6.2. However, the difference between both correlations increase when the porosity is less than 0.4 (Fig. 6.3).

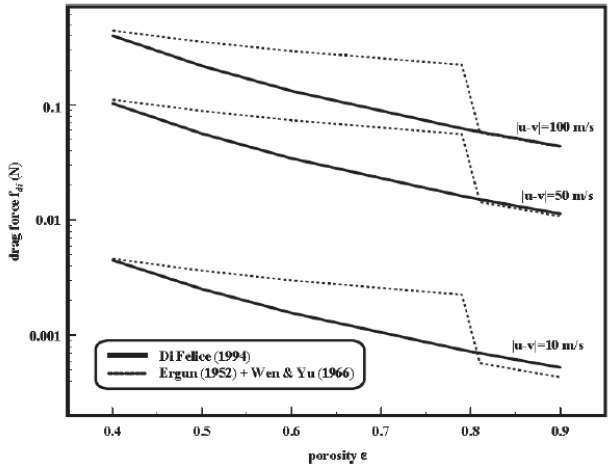

Fig. 6.2. Drag forces acting on 4 mm diameter particle as predicted using a combination of the Ergun (1952) and Wen & Yu (1966) correlations compared with the predictions from Di Felice (1994) correlation for a range of porosities at three relative velocities between the fluid and particles (Kafui et al., 2002).

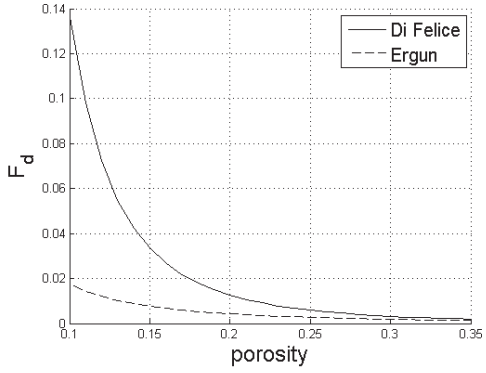

Fig. 6.3. Drag forces on 4 mm diameter particle as predicted by Ergun (1952) and Di Felice (1994) correlations for a range of porosities less than 0.4. u-v = 10 m/s.

Other researchers have derived expressions for particle drag forces by means of LBM simulations (Hilt et al., 2001; Beestrta et al., 2006; Benyahia et al., 2006). The drag forces derived by Hilt et al. (2001) are only valid for low Reynold number fluid flows ($Re_p < 120$). On the other hand, Beetstra et al. (2006) derived another drag relation from LBM results, which is slightly more accurate than the relation of Hill et al. (2001) and valid over a wider range of Reynolds numbers (up to 1000). Finally, Benyahia et al. (2006) blended Hilt et al. (2001) and Beetstra et al. (2007) correlations and constructed an extended drag correlation (called EHKL) which is applicable to the full range of Reynolds numbers. Expressions for dimensionless forces are

$$F_{dimensionless} = 1 + \frac{3}{8Re_p} \quad n \geq 0.99 \quad \text{and} \quad Re_p \leq \frac{2(F_2 - 1)}{3/8 - F_3} \qquad \text{Eq. 6.21}$$

$$F_{dimensionless} = F_0 + \mathrm{F}_1 Re_{\mathrm{p}}^2 \quad n < 0.99 \quad \text{and} \quad Re_p \leq \frac{F_3 + \sqrt{F_3^2 - 4F_1(F_0 - F_2)}}{F_1} \qquad \text{Eq. 6.22}$$

where the dimensionless forces for higher Reynolds numbers, F_0, F_1, F_2 and F_3 are defined in Benyahia et al. (2006) and are dependent on the porosity. Fig. 6.4 compares the EHKL drag force with the Ergun (1952) and Di Felice (1994) forces for Reynolds numbers between 40 and 240 (Reynolds number depends on the porosity). It can be observed that when the porosity increases the EHKL tendency is the opposite as the other two drag forces. The EHKL drag force has a lower value than Ergun (1952) and Di Felice (1994) drag forces when the porosity is less than 0.2; the EHKL drag force increases when the porosity increases, and Ergun (1952) and Di Felice (1994) drag forces decreases when the porosity increases. Even though the mean value for the three drag forces is similar when the porosity has a low value the Di Felice (1994) drag force has a higher value than the other two drag forces. When the porosity is around 0.4 EHKL drag force differs from the empirical drag forces.

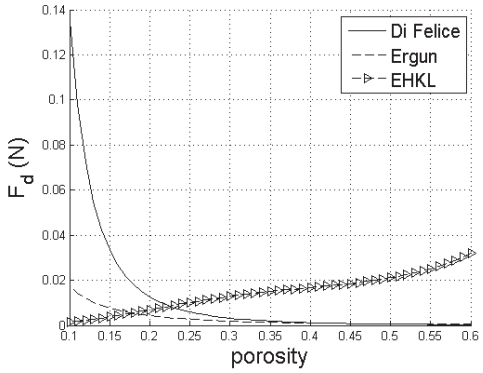

Fig. 6.4. Drag forces on 4 mm diameter particle as predicted by Ergun (1952), Di Felice (1994) and EHKL (Benyahia et al., 2006) correlations for a range of porosities between 0.1 and 0.6. *u*-*v* = 10 m/s.

Indeed, it has been reported (Yin & Sundaresan, 2008, 2009; Holloway & Sundaresan, 2010) that these equations are valid only within the constraints of the numerical simulation from which they were derived (systems composed by two different particle diameter sizes and with a maximum value of the solid diameter ratio is 4 and the two solid phases are static).

Rotondi et al. (2015) validated several relationships governing solid-fluid dynamic interaction forces against experimental data for a single particle settling in a suspension of other smaller particles. It was observed that force relationships based on LBM did not perform as well as other interaction types tested. The first major conclusion in their study was the poor predictability of the LBM approaches in estimating of the settling velocity of a single particle in a solid-fluid suspension. It is to be noted that they were used outside their normal range of validity. In comparison, results from the approaches based on estimations from empirical data were very similar, overall. An example is given in Fig. 6.5.

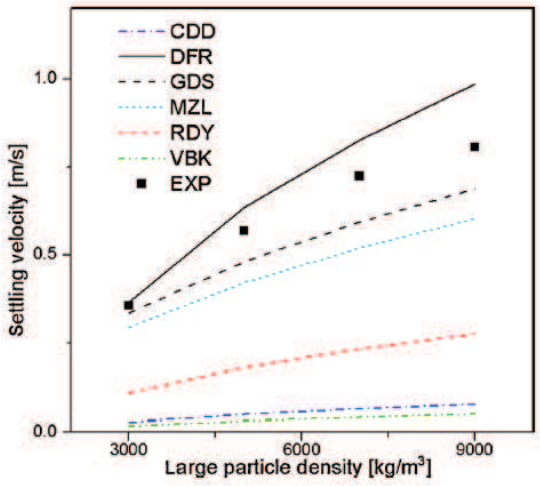

Fig. 6.5. Settling velocity versus the density of the particles simulated with different models (Rotondi et al., 2015) and compared to experimental data. GDS is a combination of Ergun (1952) and Wen & Yu (1966) equations, VBZ is Beestra et al. (2006) correlation, DFR is Di Felice (1994), and MZL (Mazzei & Lettieri, 2007), CDD (Cello et al., 2010) and RDY (Rong et al., 2014) are different LBM models. EXP is experimental from Martin et al. (1981).

Besides the drag force, the pressure gradient force is also usually considered. The pressure gradient force is expressed as

$$F_{gradp} = \frac{4}{3}\pi R^3 \nabla p \qquad \text{Eq. 6.23}$$

where R is the particle radius and p the fluid pressure. The pressure gradient is equivalent to the Darcy's law (Eq. 2.4). When the sample is fully saturated, the porosity is low and the Reynolds number is also low, the pressure gradient is quantitatively more important than the drag force (Furtney et al., 2013). This is the reason why this equation is the only part contemplated in the fluid force in these conditions.

The buoyancy is another kind of pressure gradient force, due to the gravity

$$F_{buoyancy} = \frac{4}{3}\pi R^3 \rho_f g \qquad \text{Eq. 6.24}$$

where *g* is the gravity acceleration. The buoyancy force is the only force acting on the particle when particles are simply submerged in a static fluid (Furtney et al., 2013).

There are other forces that can be also considered, but, as already stated above, they are not considered in this thesis. Some examples are the virtual mass force (that related to the force required to accelerate the surrounding fluid), the Basset force (that describes the force due to the lagging boundary layer development with changing relative velocity) and the lift forces, as Saffman lift force (caused by the pressure differential on the surface of the particle resulting from the velocity differential due to rotation) and the Magnus lift force (Zhu et al., 2007).The virtual mass force relates to the force required to accelerate the surrounding fluid, and is also called the apparent mass force because it is equivalent to adding mass to a particle (Zhu et al., 2007).

6.3.2.2. Effects on fluid flow due to particles

Fluid flow is also affected by the particles in a particle-fluid flow system. A body force due to particles velocity is added in the Navier-Stokes equation and the porosity is also included in different terms of the equation. The body force is a drag force per volume acting on the fluid due to particles velocity. The governing equations comply with the law of conservation of mass and momentum in terms of local-average variables (Anderson & Jackson, 1967). The formulations were proposed by Gidaspow (1994) and assume that the pressure drop shares between the fluid and solid phases. The Navier-Stokes equation and the continuity equation are

$$\rho_f \frac{\partial nu}{\partial t} + \rho_f u \cdot \nabla (nu) = -n\nabla p + \mu_f \nabla^2 (nu) + f_b \qquad \text{Eq. 6.25}$$

$$\frac{\partial n}{\partial t} + \nabla \cdot (nu) = 0 \qquad \text{Eq. 6.26}$$

f_b is the body force expressed as

$$f_b = \frac{\sum_j F_d^j}{V_e} \qquad \text{Eq. 6.27}$$

where F_d^j is the drag force due to the particle *j*. There is only one body force for the entire cell. In each cell the porosity is calculated as follows

$$n = \frac{V_e - V_b}{V_e} \qquad \text{Eq. 6.28}$$

where V_e is the volume of the cell and V_b is the total volume of all the particles.

6.3.2.3. Numerical implementation in CCFD-PFC3D

The CCFD code presented in Section 6.2 is also an add-on that can be coupled with PFC^{3D} to implement a version of the CFD-DEM method. The fluid force added to the particles has three terms: drag, buoyancy and pressure gradient

$$F^f = F_d + \frac{4}{3}\pi R^3 \left(\nabla p - \rho_f g\right) \qquad \text{Eq. 6.29}$$

where F^f is the force applied by the fluid, F_d is the drag force, R is the radius of the particle, p is the fluid pressure, g is the gravity and ρ_f is the fluid density.

CCFD add-on uses the empirical proposal by Wen and Yu for the drag force

$$F_d = \left(\frac{1}{2} C_d \rho_f \pi R^2 |u - v| (u - v) \right) n^{-\chi} \qquad \text{Eq. 6.30}$$

Where C_d is the drag coefficient, u is the fluid velocity, v is the particle velocity, R is the particle radius, n is the porosity and χ is a correction factor (Eq. 6.20). The drag coefficient is given by an empirical expression proposed Di Felice (1994), the DallaValle Eq. 6.14

$$C_d = \left(0.63 + \frac{4.8}{\sqrt{Re_p}} \right)^2 \qquad \text{Eq. 6.31}$$

where Re_p is the particle Reynolds number. The fluid flow, affected by the particles, follows the Eq. 6.25 and Eq. 6.26.

Fig. 6.6 shows a fluid grid containing DEM particles in a cell. CCFD calculates the fluid velocity and the fluid pressure at the centre of each cell from which a force is added to the particle equilibrium equation. On the other hand, the DEM component of the model calculates the particle velocities and the porosity.

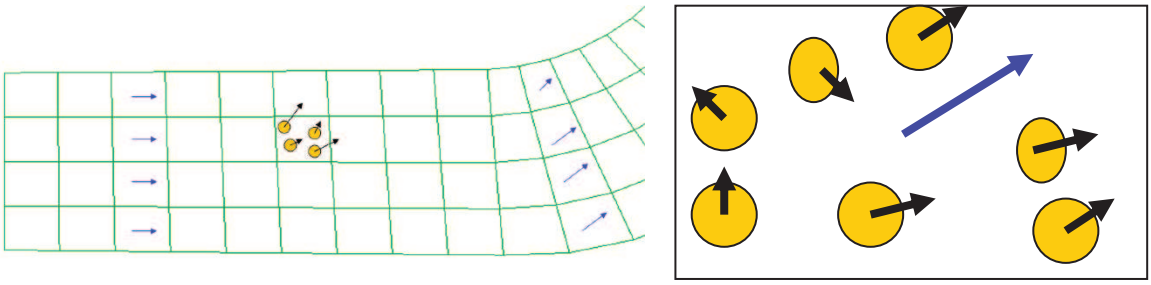

Fig. 6.6. The figure on the left shows a fluid grid containing different DEM particles in a cell. The figure on the right shows a fluid cell containing different DEM particles. The blue arrow represents the fluid velocity and black arrows represent the velocity for each particle.

The coupling methodology of CCFD add-on assumes that the local porosity is evenly distributed within one cell and describes the average coupling forces occurring within one cell. Therefore, a number high enough of PFC^{3D} particles should fit inside a CFD cell (Itasca, 2008b). That condition is indirectly expressed through the following inequality:

$$\frac{\Delta x_{cfd}}{2R} > 5 \qquad \text{Eq. 6.32}$$

Where Δx_{cfd} is the length of the cell and R is the particle radius. When particles in the sample have different radii the value used is the average. This condition is not enforced by the code and is only given as guidance to choose the length of the cells.

In the case where the particles overlap more than one fluid element, CCFD uses three different methods to calculate the volume body force and the porosity: the location of the centroid, a polyhedron representation of the particles, and an approximate method. The one used in this thesis is the polyhedron method that represents a particle as a cube with height, length and width equal to the diameter of the particle. The intersection volume of this cube with the cells is apportioned, conserving the total particle volume. The fluid-particle drag force is equally apportioned. The porosity is recalculated for each

DEM cycle; therefore, changes of porosity are taken into account throughout the simulation.

During simulation the two code exchange data only at given times. The coupling interval is the time interval between exchanges of data. During the coupling interval both codes run sequentially using their own time step, different for each one. After the coupling interval has elapsed data is exchanged again. The coupling interval is set by the user in CCFD add-on and is unique for all the simulation. Fig. 6.7 shows the calculation cycle of the coupling and Table 6.1 summarize the data each code calculates and passes to the other.

Table 6.1. Summary of the data each code calculates, uses, and passes to the other.

Data	**Calculated by**	**Given to/Used by**
Fluid velocity	CCFD	PFC^{3D}
Pressure gradient	CCFD	PFC^{3D}
Porosity	PFC^{3D}	PFC^{3D} and CCFD
Fluid force	PFC^{3D}	PFC^{3D}
Body force	PFC^{3D}	CCFD

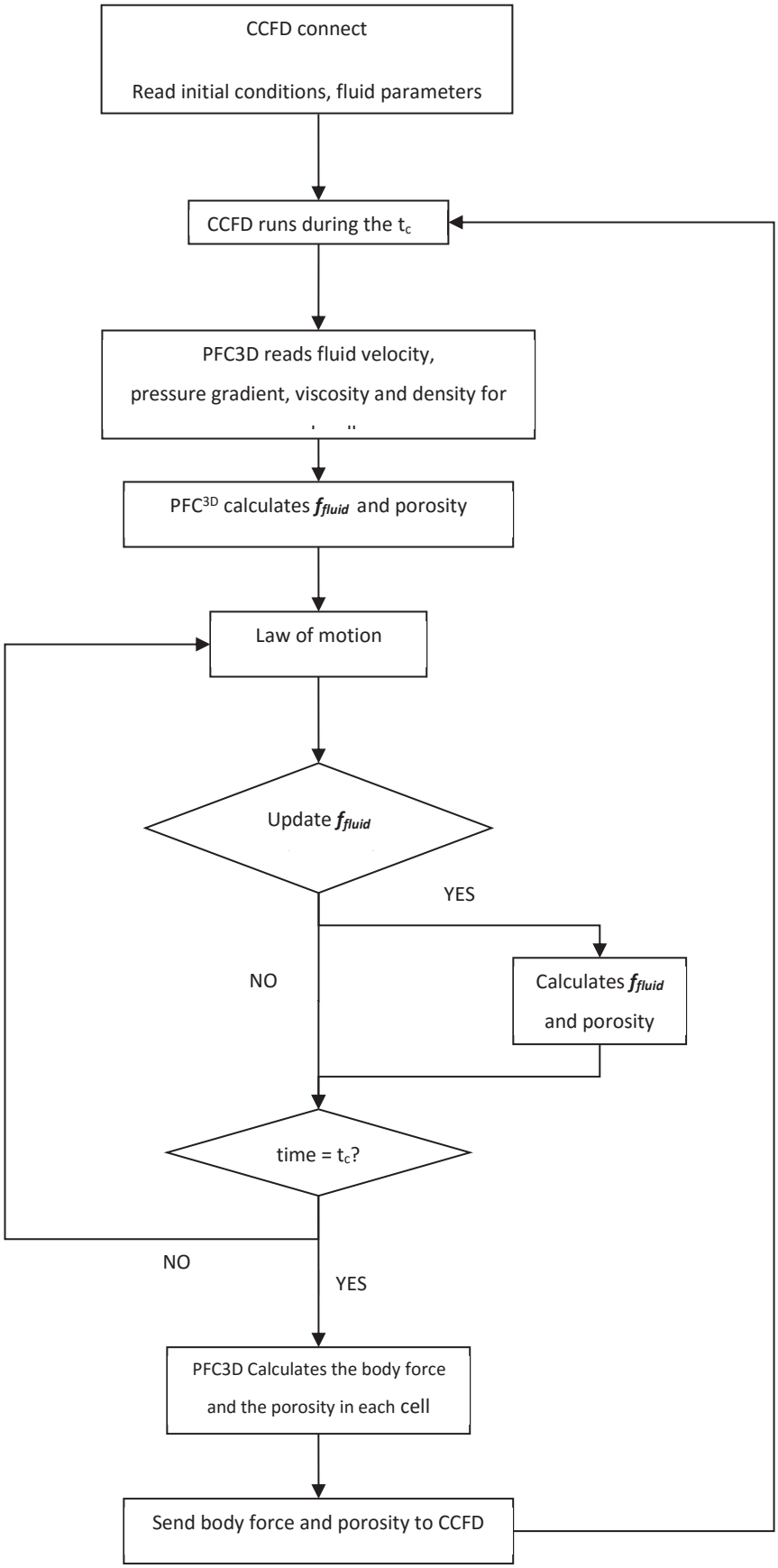

Fig. 6.7. Calculation cycle of PFC^{3D} and CCFD add-on

6.4. Previous works on sand production using fluid-particles coupling methods

Sand production process have been studied by several researchers developing fluid-solid coupling methods in DEM (e.g. Dorfmann et al., 1997; O'Connor et al., 1997; Cook et al., 2004; Grof et al., 2009; Marrion & Woods, 2009; Quadros et al., 2010; Cheung, 2010; Boutt et al., 2011). The majority are 2D-DEM-based models and implemented fluid flow systems based on Darcy's law. The most interesting aspects of this previous work are reviewed below.

Dorfmann et al. (1997) performed 2 dimensional DEM simulations to study the mechanisms of the cavity growth and the influence of the pressure gradient and capillary forces on the formation of a stable arch configuration around the cavity. They considered a 2-phase Darcian flow (the wetting fluid and the non-wetting fluid), where the drag force was calculated with the fluid pressure on each particle (force that equals Eq. 6.23 for a radial fluid flow in 2 dimensions). The capillary is expressed in terms of the liquid bridge radius connecting two grains and the capillary pressure (defined as the difference in fluid pressure between the non-wetting fluid and the wetting fluid). A scheme of the model is shown in Fig. 6.8. The contact model used was a linear frictional model: contact properties include friction and normal and tangential stiffness. The model had semi-circular shape. The results indicated that pressure gradient had a greater influence on cavity growth than capillary force, especially at low gradient and capillary force magnitudes; however, as the capillary magnitude increased, it had a larger influence on sand cavity growth and stability.

O'Connor et al. (1997) observed the perforation channel collapse due to the fluid flow using a 2D DEM model. They only considered 1 phase flow. The particles were bonded. The simulations were carried out in a quarter of a circular shaped domain. A set of numerical experiments using different flow rates indicated that sanding was primarily a phenomenon reminiscent of a cavitation process (when the material at the hole boundary consolidates, material surrounding it moves inwards and circumferential zones of material yield radially when tensile strength of the cement is reached) (Fig. 6.9).

The authors compared the results with unspecified experimental results and qualitative descriptions of sanding mechanisms in the literature and concluded that the predictive capabilities of the model were still poor. They gave reasons for this poor performance: the model was only 2D, the fluid and solid phases were artificially constrained, the fluid flow was approximated to a Darcian flow, and, finally, bonds did not support shear stresses (only tensile bonding was supported).

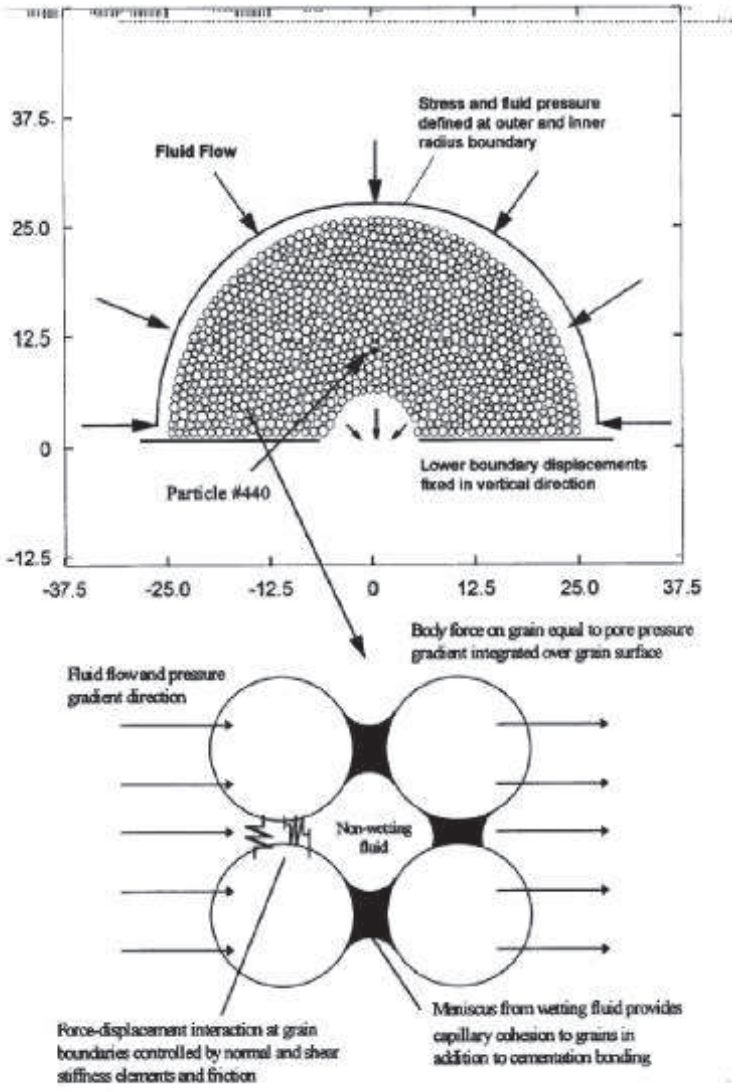

Fig. 6.8. Discrete Element Model schematic (Dorfmann et al., 1997).

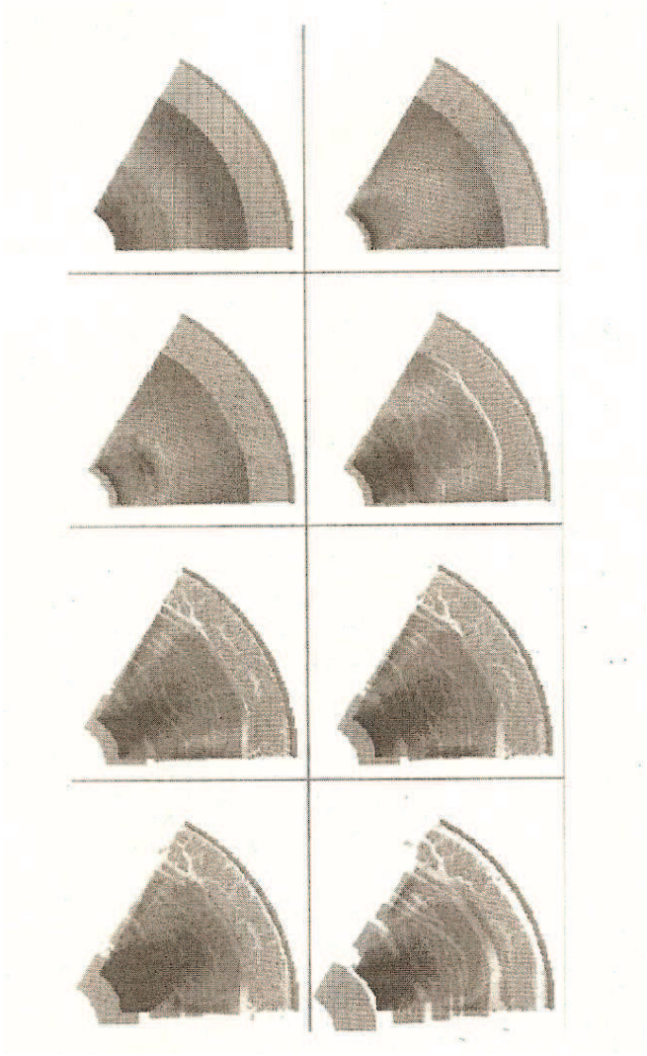

Fig. 6.9. Simulated matrix cavitation under fluid loading (O'Connor et al., 1997).

Failures due to the slurry injection were observed by Cook et al. (2004). They examined the angular distribution of broken bonds for different confining stresses. The model used was a 2D DEM with a coupling method inspired by the molecular model of a fluid (at the molecular level, fluid pressure is generated by the collisions of individual fluid molecules with the walls of the fluid's container). Instead of modelling the fluid, the model imitates this molecular collisions using small particles (source particles) at the other side of the borehole wall (inside the hole, where there are no 'solid' particles). The source particles collide with the larger elements that define the borehole wall. At each time step a constant force is applied to the source particle. The collisions of these particles on the borehole wall simulate the fluid pressure on the borehole, the only interaction

considered between the fluid and the particles. The fluid was a 1 phase flow and the particles were bonded. The contact between particles was simulated with a linear-elastic frictional model and the sample was in a rectangular shaped domain. They concluded that the simulation results reproduced qualitatively the macroscopic failure processes associated with borehole fracturing and breakout.

Grof et al. (2009) performed 3D CFD-DEM simulations to study particle erosion. A linear-elastic model was set for the contact behaviour between particles without bonding. A 2-phase incompressible Navier-Stokes flow was coupled and the forces applied to the particles due to the fluid were the drag force, the lift force, the buoyancy force and the capillary force. They observed the onset of sanding (when particles detach between each other) at the microscopic level and they performed parametric studies in terms of dimensionless groups determining the strength of cohesive/capillary forces and the magnitude of the drag (or gravitational) force. The dimensionless parameters are

$$B_0 = \frac{(\rho_s - \rho_l)R^2 g}{\gamma} \qquad \text{Eq. 6.33}$$

$$V^* = \frac{V}{R^3} \qquad \text{Eq. 6.34}$$

$$\psi = \frac{\eta u}{\gamma} \qquad \text{Eq. 6.35}$$

where ρ_s and ρ_l are the solid and fluid densities, R is the sphere radius, g is the gravitational acceleration, γ is the surface tension, V is the volume of the liquid bridge, η is the fluid viscosity and u is the superficial velocity. Parametric maps were generated as the main output from the study (Fig. 6.10); those maps allowed a priori estimation of the critical conditions for the on-set of particle erosion (sanding) regimes. It can be

observed in Fig. 6.10 that for some values of the dimensionless parameters particles detached, and for other values particles hold.

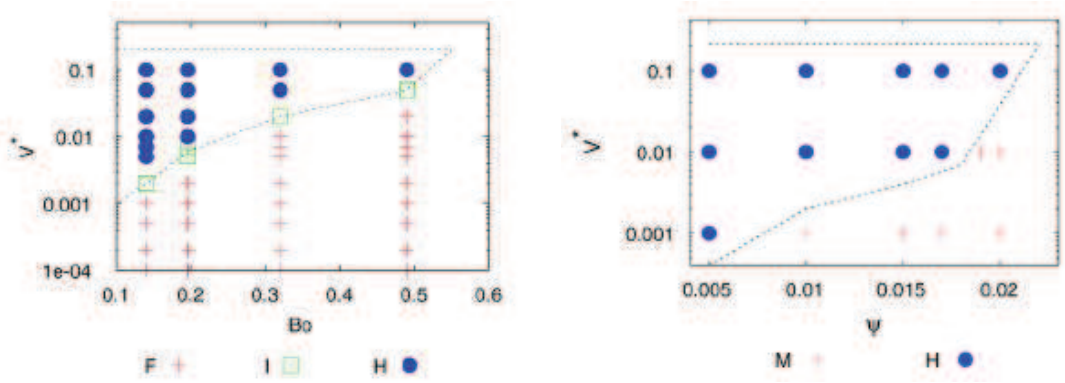

(a) (b)

Fig. 6.10. a) summary of the effect of parameters B_o and V^* on different scenarios (Scenario H: the cluster of particles holds; Scenario I: partial detachment of particles (some particles detach and pull down more particles); Scenario F: the cluster of particles is detached at once.); b) summary of the effect of parameters ψ and V^*on different scenarios (Scenario H: the entire cluster of particles holds; Scenario M: particles detach and move due to flow).

On the other hand, a qualitative study about the wormholes created when the fluid flows through the material was presented by Marrion & Woods (2009) using a 2D DEM model in a circular shaped domain. A 2-phase Darcian flow and no inter-particle contact forces were considered. The forces applied to the particles due to the fluid flow were pressure forces, viscous forces and capillary forces. A stochastic erosion criterion was used to simulate the particle erosion (removal). The model predicted and concluded that the non-uniform distributions of permeability significantly modify the characteristics of the erosion. 2D DEM model coupled with a darcian fluid was also presented by Jensen & Preece (2011). Their simulations showed that as the cohesion decreases, the number of particles breaking from matrix increases.

LBM was also used to study sand production. Quadros et al. (2010) coupled a 2D DEM particle model with the LBM. Linear-elastic frictional contacts and bonding were present. A Newtonian flow was considered and the drag force was applied on the particles. The sample was represented in a rectangular shaped domain. The main objective of their study was observing the qualitative relationship between some

parameters (material strength, boundary stresses, pressure gradients and grain size) and the sand production rate and also between the inter-grain friction and the strength with the creation of a stable arch at the end. In their study they indicated some limitations of this modelling approach: only relatively low pressure differentials can be imposed in the simulations and the LBM has a high computational cost.

Boutt et al. (2011) also coupled DEM with LBM for modelling sand production. The main objectives of their work were the observation of formation and destruction of stable arches and the qualitative study of the influence of shape and inter-particle friction on the sand production. They modelled two dimensional unbounded particles with normal and tangential stiffness and intergranular friction. The fluid flow was an incompressible Newtonian flow which applied a drag force on the particles. They observed that particle shape and friction were shown to both significantly increase production rates.

Zhou et al. (2011) developed a 3D CFD-DEM model to simulate the sand erosion by fluid flow. Spherical particles were bonded and contact forces between particles followed a linear-elastic law. The fluid-particle forces considered were the pressure gradient force, the drag force and the gravitational force. The sample was represented in a portion of a cylindrical domain. They concluded that sand erosion is significantly affected by fluid flow rate and bonding properties; erosion rate increased with the decrease of sand strength and the increase of fluid rate (Fig. 6.11).

In her PhD thesis, Cheung (2010) performed simplified CFD-DEM simulations for sand production. Particle contacts were modelled with a linear-elastic law and they a parallel-bond model was also used. The three-dimensional sample was represented in a cylindrical shaped domain. The 1-phase fluid was modelled calculating solely the continuity equation (Eq. 6.5). The Navier-Stokes equation was not considered. Moreover, the drag force was only applied in one direction, on the particles. The effect of the particles on the fluid was not considered. The drag force was calculated using Ergun (1952) and Wen & Yu (1966) equations (Eq. 6.17 and Eq. 6.18). The fluid flow was constant during time. She performed some simulations on dry material to validate the model comparing the results with an analytical solution presented by Risnes et al. (1982). After the validation, she studied the different stresses for different fluid flow

velocities and bond strengths, the patterns of the particle stresses, contact forces, bonds and particle rotations, the sensitivity of different parameters on the results and tested different materials. However, by assuming radial flow, it is not suitable for investigating the impact of the flow at the tip of the perforation where the fluid flow is in all directions (Rahmati et al., 2013).

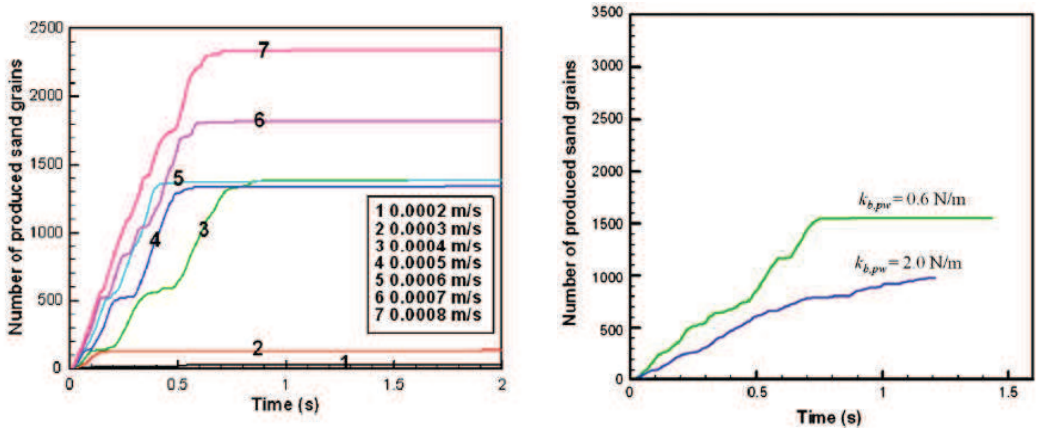

(a) (b)

Fig. 6.11. a) Number of produced sand grains with time for different fluid superficial velocities; b) number of produced grains with time for different particle-wall bonding coefficient (Zhou et al., 2011).

Rahmati et al. (2013) reviewed in their paper some of the models that have been used for sand production. It was reported that DEM is promising to simulate the detachment of individual particles because it captures the motion and interaction of individual sand grains. However, it was also concluded that it is computationally expensive and therefore it is not applicable to large-scale problems.

6.5. Other applications using CFD-DEM

Different researches have been carried out using CFD-DEM in problems other than sand production. Some of these works are presented below. Table 6.2 at the end of the section summarize these works.

Tsuji et al. (1993) and Kawaguchi et al. (1998) pioneered the use of coupled DEM particle idealization and homogenized fluid model to simulate the formation of bubbles in two-dimensional gas-fluidized beds. The drag force used in that model was derived from the Ergun (1952) and Wen & Yu (1966) equations.

Two-dimensional fluidized beds were also simulated by Kafui et al. (2002). In this case, a virtual or added mass force accounting for the resistance of the fluid mass that is moving at the same acceleration as the particle was considered a part of the drag force. The drag force used in this case was the one proposed by Di Felice (1994). Hoomans et al. (1996) also simulated two-dimensional fluidized beds. The drag force considered was the one obtained with the Ergun equation and the correlation presented by Wen & Yu (1966).On the other hand, Xu & Yu (1997) simulated three-dimensional fluidized beds. The drag force was based on Di Felice (1994) proposed equation.

Xiong et al. (2005) used CFD-DEM to simulate a three-dimensional gas-solid injector. The gas is considered turbulent using a two-equation k-epsilon closure. The fluid-particle interaction forces considered are: the drag force, the Magnus lift force, the Saffman lift force, the history force and the other force.

Langston et al. (1995) used CFD-DEM to simulate three-dimensional granular flows in hoppers. The model was three-dimensional and particles passed through a radial flow of air. The air/particle interaction (drag) force is modelled using the Ergun equation. The results obtained for discharge rates were reasonable and the particle velocity and the void structures provided information on the transient and oscillatory nature of the flow fields which are not accessed by the steady-state continuum models.

El Shamy & Zeghal (2005) used a coupled three-dimensional hydromechanical model using CFD-DEM to analyse the mesoscale pore fluid flow and microscale solid phase deformation of saturated granular soils. In this case the fluid medium used for modelling was water. The force exerted on the particles contents the drag force by the fluid and the buoyancy. Averaged fluid-particle interaction was quantified using semiempirical relationships Ergun (1952) and Wen & Yu (1966) proposed.

Zhao & Shan (2013) coupled DEM and CFD to simulate the behaviour of fluid-particle interaction and to investigate the characteristics of sand heap formed in water through hopper flow. It was concluded that the influence of fluid-particle interaction on the behaviour of granular media was well captured in all the simulated problems. The interaction forces being considered included the drag force and buoyancy force, and the drag force used was the one proposed by Di Felice (1994).

Jiang et al. (2015) coupled DEM with CFD in 2 dimensions to simulate methane hydrate bearing sediments that induce submarine landslides. A thermo-hydro-mechanical bond contact law was employed. In the interaction between the particles and the fluid the pressure gradient force and the drag force were considered. The drag force used was the combination of the Ergun (1952) equation and the on proposed by Wen & Yu (1966) (Eq. 6.17 and Eq. 6.18). The performed simulations of submarine landslide induced by methane hydrate dissociation proved that the CFD-DEM worked successfully and could capture various observed behaviours.

Table 6.2. Summary of the CFD-DEM works

Authors	Study	Dim.	Drag force	Other fluid forces
Tsuji et al. (1993)	Formation of bubbles in gas-fluidized beds	2D	Ergun (1952) and Wen & Yu (1966)	
Kawaguchi et al. (1998)	Formation of bubbles in gas-fluidized beds	2D	Ergun (1952) and Wen & Yu (1966)	
Kafui et al. (2002)	Fluidized beds	2D	Di Felice (1994)	Virtual mass force
Hoomans et al. (1996)	Fluidized beds	2D	Ergun (1952) and Wen & Yu (1966)	
Xu and Yu (1997)	Fluidized beds	3D	Di Felice (1994)	
Xiong et al. (2005)	Gas-solid injector	3D		Magnus lift, Saffman lift, and history force
Langston et al. (1995)	Hoopers	3D	Ergun (1952)	
El Shamy & Zeghal (2005)	Pore fluid flow and solid deformations of saturated soils	3D	Ergun (1952) and Wen & Yu (1966)	Buoyancy
Zhao and Shan (2013)	Hoppers		Di Felice (1994)	Buoyancy
Jiang et al. (2015)	Methane hydrate bearing sediments	2D	Ergun (1952) and Wen & Yu (1966)	Pressure gradient force

6.6. Representing CFD results

ParaView (Section 4.8) is also used here to represent CFD results. For continuum fields, as it is the fluid model in CFD, VTK (introduced in Section 4.8) provides data representations for a variety of grid types (structured, unstructured, polygonal and image data) (Ahrens et al., 2005). Fig. 6.12 shows the structured grids that can be represented in ParaView. Moreover, grids with any pattern can also be constructed defining the coordinates of each point of the cell.

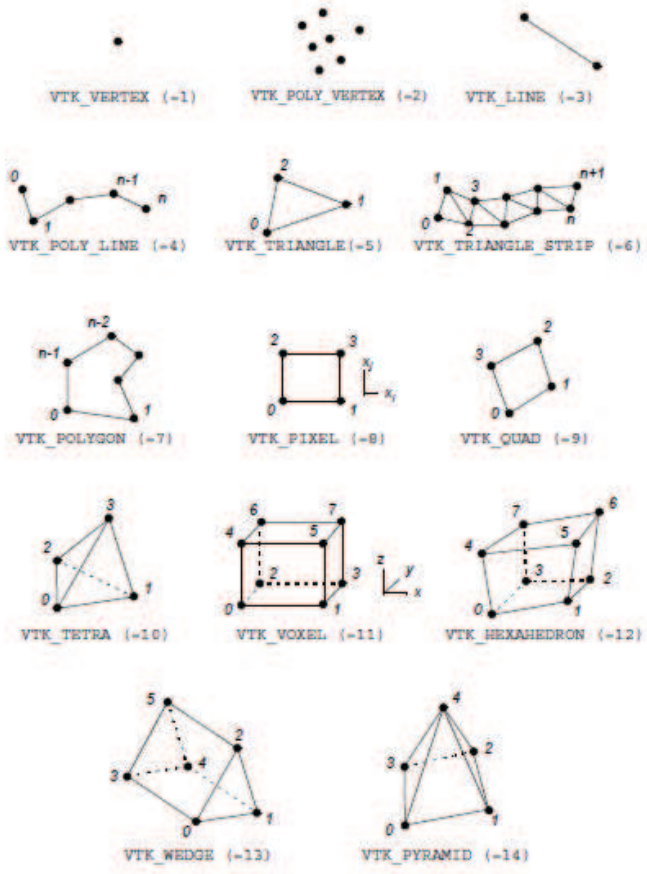

Fig. 6.12. Different structured cells for continuum data represented in ParaView

In each cell, ParaView represents a magnitude using a colour scale (using a given variable, as a scalar, a vector component or a vector magnitude). Arrows can be also

represented in each cell, to give information as vectors, as it was presented also in Section 4.8 for particles).

Examples of a scalar represented in different cells are shown in the next figures. Fig. 6.13 is a x-y plane representation where each colour represents different values of the void ratio. Each value is presented in each cell and cells are hexahedral. Fig. 6.14 represents the porosity also in a cylindrical shape with a hole inside. Finally, Fig. 6.15 represents a cut of the same cylinder.

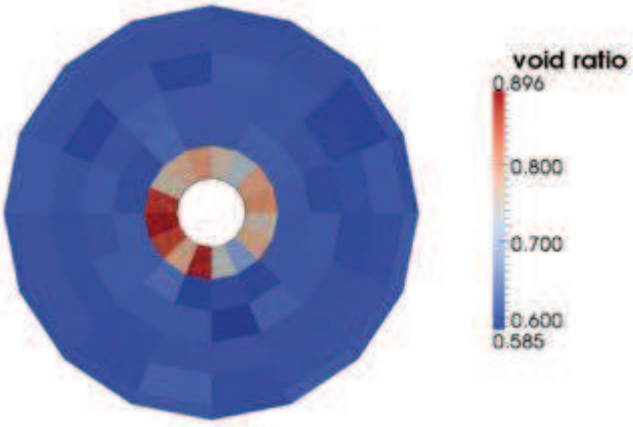

Fig. 6.13. Void ratio represented in ParaView in different cells. The grid is hexahedral (structured). Plane x-y

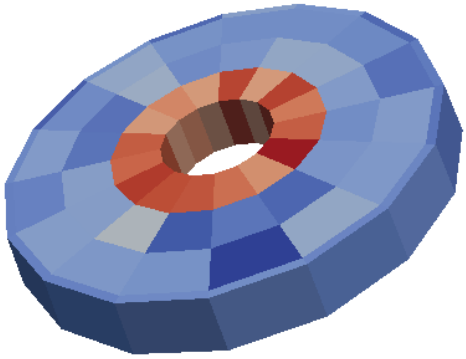

Fig. 6.14. 3D representation of a cylinder with a hole inside. Cells are hexahedral and cell color is used to represent the different porosity values.

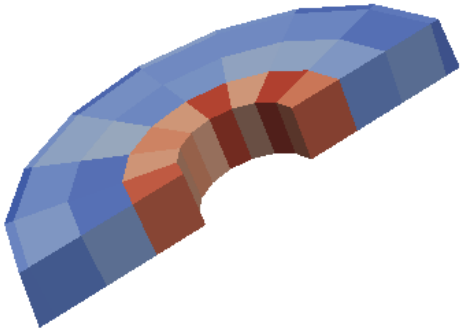

Fig. 6.15. Cut of the 3D representation of a cylinder with a hole inside.

The output CCFD data files have to be adapted to a data file format that ParaView could read. A MATLAB script to do that is included in Appendix D.

6.7. Summary

Granular materials are usually permeated by fluid. The interaction between soil particles and fluid becomes important when the fluid flow affects, not only the total stress of the system, but also mass transport of the solid matrix. To simulate this interaction two models have to be coupled, one for the solid phase and another one for the fluid phase. Several fluid-coupling techniques are available when the solid phase is represented by discrete elements: LB-DEM, PPM-DEM, CFD-DEM, DNS-DEM, LES-DEM and SPH-DEM.

CFD-DEM model is one of the most used because of its relatively small computational burden. One of the reasons is that CFD cells contain different particles. CFD is a computational model for fluid dynamics, where the fluid is treated as a continuum medium. The code used in this thesis is the CCFD add-on that couples with PFC^{3D}. This code calculates the fluid pressure and the fluid velocity in each cell, which contains a different number of DEM particles. PFC^{3D} calculates the particle velocities and the porosity. A force due to the fluid is added on the Newton's second law for each particle, and a body force is added in the Navier-Stokes equation for the fluid flow due to the presence of the fluid; a porosity term is also affecting the fluid flow equations.

Different researches have been carried out using CFD-DEM (e.g., Tsuji et al., 1993; Kawaguchi et al., 1998; Kafui et al., 2002; Hoomans et al., 1996; Xu & Yu, 1997, Xiong et al., 2005, Langston et al., 1995; El Shamy & Zeghal, 2005). Fluidized beds in two dimensions have been studied by most of them (Tsuji et al., 1993; Kawaguchi et al., 1998; Kafui et al., 2002; Hoomans et al., 1996). Xu &Yu (1997) performed simulations of 3D fluidized beds. Other applications as gas-solid injectors (Xiong et al., 2005), hoopers (Langston et al., 1995; Zhao & Shan, 2013) have been also of interest for using CFD-DEM models. Finally, El Shamy & Zeghal (2005) used CFD-DEM to study deformations of saturated granular soils in three dimensions, and Jiang et al. (2015) performed 2 dimensional CFD-DEM simulations to study methane hydrate bearing sediments.

Sand production process has been studied by several researchers using different particle-fluid coupling methods with DEM (e.g., Dorfmann et al., 1997; O'Connor et al., 1997; Cook et al., 2004; Grof et al., 2009; Marrion & Woods, 2009; Quadros et al., 2010; Cheung, 2010; Boutt et al., 2011). Most of them are 2D-DEM-based models and the fluid flow assumed Darcy's law, therefore implicitly disregarding fluid flows with a high Reynolds number.

Chapter 7 - Validation of the CFD-DEM

7.1. Introduction

In Chapter 8 and Chapter 9 sand production simulations coupling DEM and CFD are performed and presented. In this chapter the modelling approach is tested in simpler -but still relevant- cases, to allow clearer understanding of some aspects affecting the fluid-particle interaction

First of all, (Section 7.2) simulations with a single particle are performed to understand the effect of the drag force, and the sensitivity of the damping force and the viscosity, on the interaction between the fluid and the particle. As the CFD-DEM is a powerful tool to simulate the erosion and the particle movement in the fluid, this is a common test some researchers have performed to validate a fluid-particle coupled model (e.g. Jiang et al., 2015; Zhao et al., 2014).

CFD-DEM is also a good tool to simulate flow through dense soils. The classical benchmark test for this kind of analysis has been the oedometer test, which has been already explored by different researchers (e.g. Jiang et al., 2015; Élias, 2013; Catalano, 2013); to evaluate the method the similarly important but less explored case of the permeameter test has been used as a benchmark in this chapter (Section 7.3).

7.2. Simple tests: single particle in a tube

Validation and sensitivity tests are performed to understand the behaviour of the DEM-CFD coupling with a single particle. Three different cases are explored: a particle falling inside a vertical tube where the fluid is not flowing, a particle dragged by the fluid inside a horizontal tube and a particle decelerated by fluid with no flow inside a horizontal tube.

All simulations with a single particle lasted between 1 and 3 minutes. However, the equilibrium in most of them was achieved in less than one minute. The efficiency increases or decreases with the variation of the damping and the viscosity depending on the difference between the particle velocity and the fluid velocity.

7.2.1. Particle falling inside a tube: sedimentation velocity

A simulation of a particle falling inside a vertical tube is performed. An analytical solution for the limit velocity of a sphere falling in a fluid is given by Stoke's Law (Eq. 6.10), which, as explained in Section 6.3.2.1, is only valid for low Reynolds numbers (Re_p < 1). The analytical solution for the terminal velocity is

$$v_{\text{lim}} = \frac{2}{9}\frac{(\rho_p - \rho_f)}{\mu_f} g R^2 \qquad \text{Eq. 7.1}$$

Where v_{lim} is the limit velocity, ρ_p and ρ_f are the particle and fluid densities, μ_f is the fluid viscosity, g is the acceleration gravity and R is the particle radius. The limit velocity is the velocity when the buoyancy force and the drag force equals to the weight; in that moment the total force and the acceleration are 0.

The height of the tube is 0.08 m and the radius 5 mm (Fig. 7.1). The fluid is water, with a density of 1000 kg/m^3 and a viscosity of 1 mPa·s. This values result in a Reynolds number (Eq. 6.7) of 0.6.

To construct the CFD mesh, 40 vertical divisions and 20 circumferential divisions are made (Fig. 7.2). The boundary conditions are no flux at the bottom and at the lateral boundaries and null pressure at the top boundary.

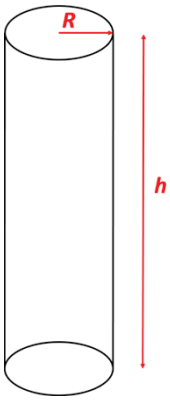

Fig. 7.1. Vertical tube

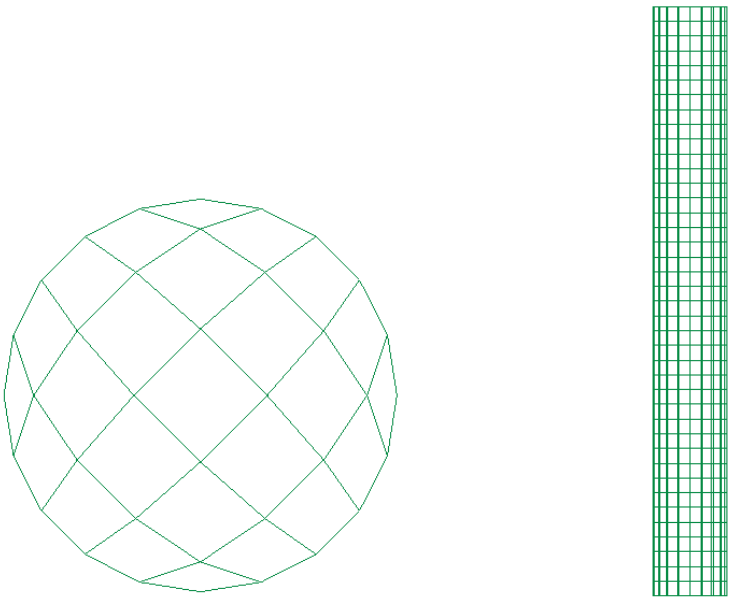

Fig. 7.2. Mesh of the vertical tube: xy plane (left) and xz plane (right).

A particle is created at the top of the tube and at the centre of the top boundary. The particle has a radius of 0. 03 mm and a density of 2500 kg/m^3. The local damping is set to 0 and the simulation is run until 0.1 seconds using a coupling time of 0.5 ms. Stoke's terminal velocity (Eq. 7.1) for this problem is 0.0029 m/s.

Fig. 7.3 shows the results of the simulation. The position of the particle is the distance measured from the top of the tube. The fluid force is the sum of the drag force, the buoyancy and the force due to the pressure gradient. The particle velocity is normalized

by the limit velocity, the fluid force is normalized by the buoyancy force and the position is normalized by the particle diameter.

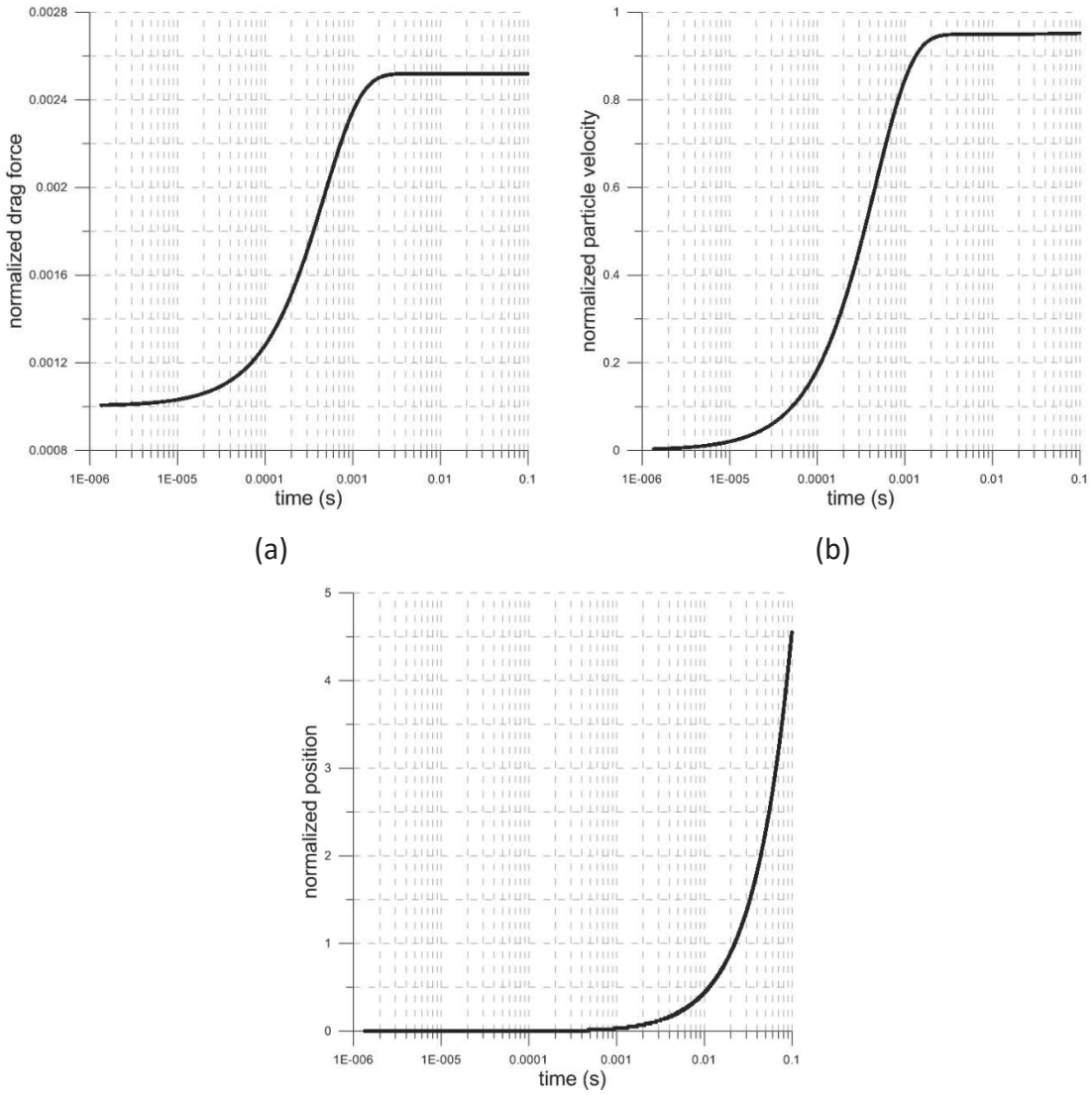

Fig. 7.3. Results of the dropping simulation. (a) Normalized drag force versus time, (b) normalized particle velocity versus time, and (d) normalized position versus time. The position is calculated from the top of the tube, and positive downwards. The particle velocity is normalized by the limit velocity, the fluid force is normalized by the buoyancy force and the position is normalized by the particle diameter. All figures are represented in a logarithmic scale.

The drag force increases until a steady state is reached, after which the drag force remains constant during the simulation. At the beginning the only fluid force acting on the particle is that of buoyancy ($1.1 \cdot 10^{-6}$ mN). The drag force is 0 because motion has

not yet started. The gravity on the particle is $2.8 \cdot 10^{-6}$ mN. Due to the difference between the fluid force and the weight (vertical forces with opposite direction) the particle starts moving downwards increasing its velocity. As the particle velocity increases the drag force increases (due to the difference between the particle and the fluid velocities) increasing the fluid force upwards until it reaches the same value as the gravity force. During this process the particle decelerates until it reaches terminal velocity.

The run time for this simulation is 40 min for a simulation time of 0.1 s.

7.2.2. Pure drag: effect of viscosity and damping

Simulations of a weightless particle dragged by the fluid flow inside a horizontal tube are now performed. Buoyancy is also excluded from these simulations, so that the only force between particle and fluid is the drag force.

For low Reynolds number fluid drag can be again expressed by Stoke's expression (Eq. 6.10). The governing equations for a single particle are

$$F_{laminar} = m\frac{dv}{dt} \qquad \text{Eq. 7.2}$$

$$6\pi\mu_f R(u-v) = \frac{4}{3}\pi R^3 \rho_p \frac{dv}{dt} \qquad \text{Eq. 7.3}$$

where $F_{laminar}$ is the Stoke's expression (Eq. 6.10), m is the particle mass, v is the particle velocity, μ_f is the fluid viscosity, u is the fluid velocity, R is the particle radius, and ρ_p is the particle density. The analytical solution calculated from Eq. 7.3 for the velocity and the position of the particle are

$$v = u\left[1 - \exp\left(-\frac{9\mu_f}{2\rho_p R^2}t\right)\right] \qquad \text{Eq. 7.4}$$

$$x = u\left(t + \frac{2\rho_p R^2}{9\mu_f}\left(\exp\left[-\frac{9\mu_f}{2\rho_p R^2}t\right] - 1\right)\right) + x_0 \qquad \text{Eq. 7.5}$$

where x is the particle position, and x_0 is the initial position.

The length of the tube is L = 0.08 m and the radius R = 5 mm (Fig. 7.4). The fluid is water, with a density of 1000 kg/m^3 and a viscosity of 1 mPa·s.

To construct the mesh, 40 horizontal divisions and 20 circumferential divisions are made (Fig. 7.5). The boundary conditions are U = 1 mm/s velocity at the entrance of the tube (left) and P = 0 pressure at the opposite boundary.

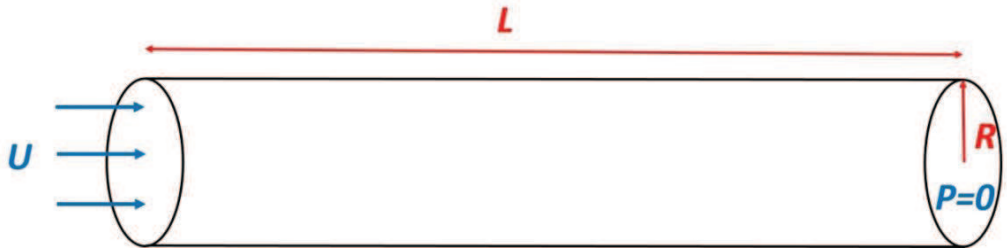

Fig. 7.4. Horizontal tube

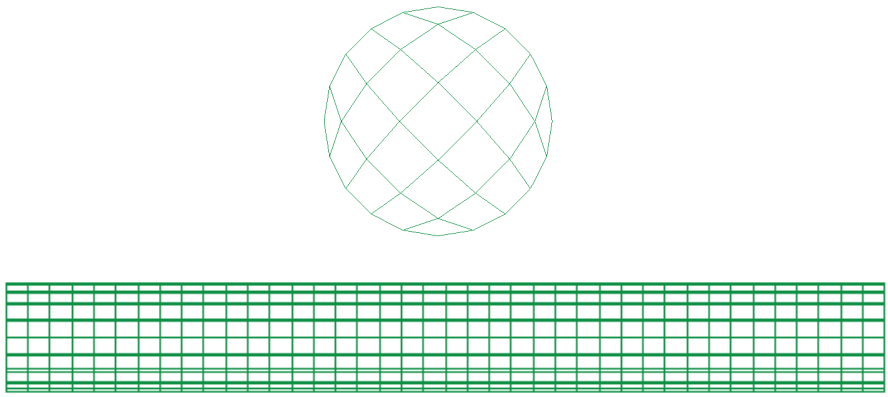

Fig. 7.5. Mesh of the horizontal tube: yz plane (left) and xz plane (right)

A particle is created at the entrance of the tube (at x_0 = 2 mm of the entrance of the tube) and at the centre of the section. The particle has a radius of 0.03 mm and a density of 2500 kg/m^3.Local damping is set to 0 and the simulation is run until a total simulation time of 0.01 seconds using a coupling time of 0. 5 ms. The particle Reynolds number in this scenario is 0.06, it means that the Stoke's law (Eq. 6.10) is also valid. Following the analytical solution (Eq. 7.4) we can define a transient time (t_{trans}), as the 99% of the fluid velocity. In this problem t_{trans} = 0.99 mm/s. The analytical transient time is 0.0023 s.

The results of the simulation are presented in Fig. 7.6. Position is distance from the beginning of the tube. Only the drag component of the fluid force is represented because it is the only fluid force considered. The drag force is normalized by the initial drag force, the particle velocity is normalized by the fluid velocity and the position is normalized by the particle diameter. The fluid force decreases and the particle velocity increases. At the beginning the fluid velocity is 1 mm/s and the particle velocity is 0; due to this difference, the drag force drags the particle increasing its velocity. As the particle velocity increases it gets closer to the fluid velocity, thus decreasing the drag force. When the particle velocity reaches the same value as the fluid velocity the drag force becomes 0 and the particle velocity stabilizes reaching a steady state with a velocity of 1 mm/s. The numerical transient time in this simulation is 0.0023 s, the same as the analytical transient time.

Fig. 7.7 shows the body force on the fluid and the fluid velocity. Both are calculated in the cell where the particle is (following the particle movement). The body force is the same as the drag force on the particle but in the opposite direction. The fluid flow velocity is always the same and 0. Due to the low Reynolds number the fluid is not affected by the movement of the particle.

The results in Fig. 7.7 can be compared with an analytical solution. Fig. 7.8 shows the analytical results and compares them to the numerical ones. The numerical result is the same as the analytical one.

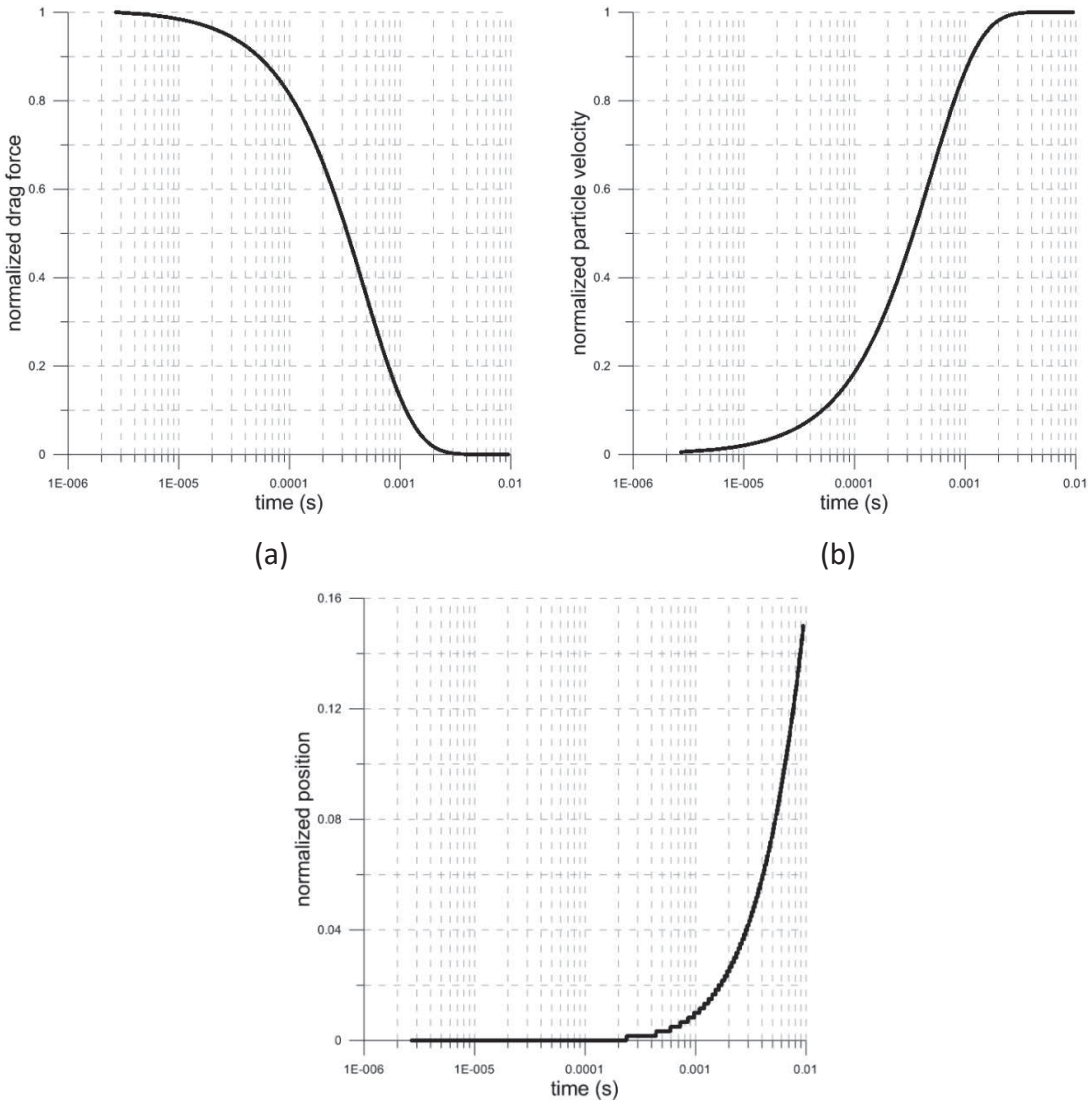

Fig. 7.6. Results of the dragged particle simulation. (a) Normalized drag force versus time, (b) normalized particle velocity versus time, and (c) normalized position versus time. All figures are represented in a logarithmic scale. The position is calculated from the centre of the tube. Drag forces are normalized by the initial drag force in the direction of the fluid flow and particle velocities are normalized by the fluid velocity. All figures are represented in a logarithmic scale.

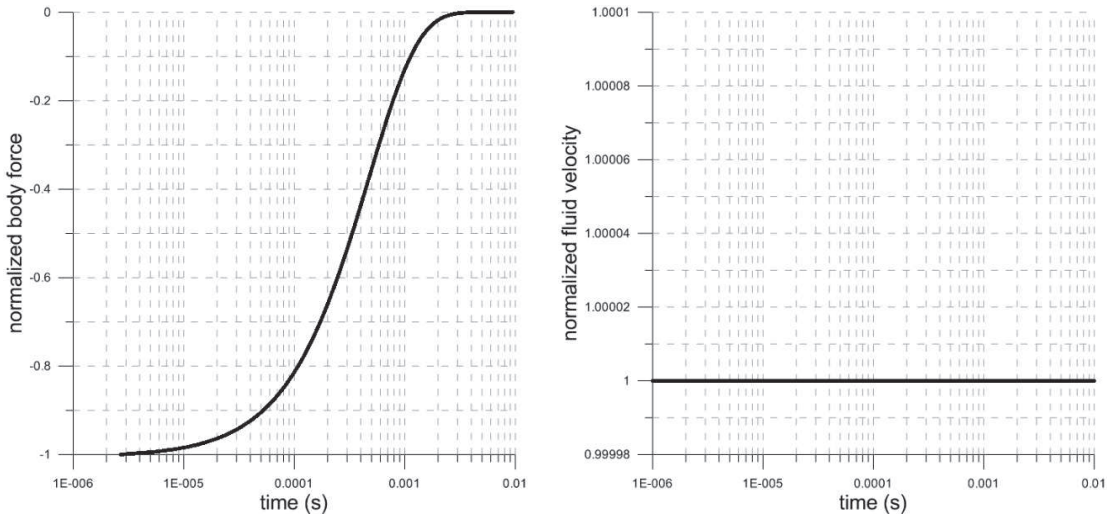

(a) (b)

Fig. 7.7. Results of the fluid flow in the cell where the particle is. (a) normalized body force versus time, and (b) normalized fluid velocity versus time. All figures are represented in a logarithmic scale. Body force is normalized by the initial drag force in the direction of the fluid flow and fluid velocity is normalized by the imposed boundary fluid velocity. All figures are represented in a logarithmic scale.

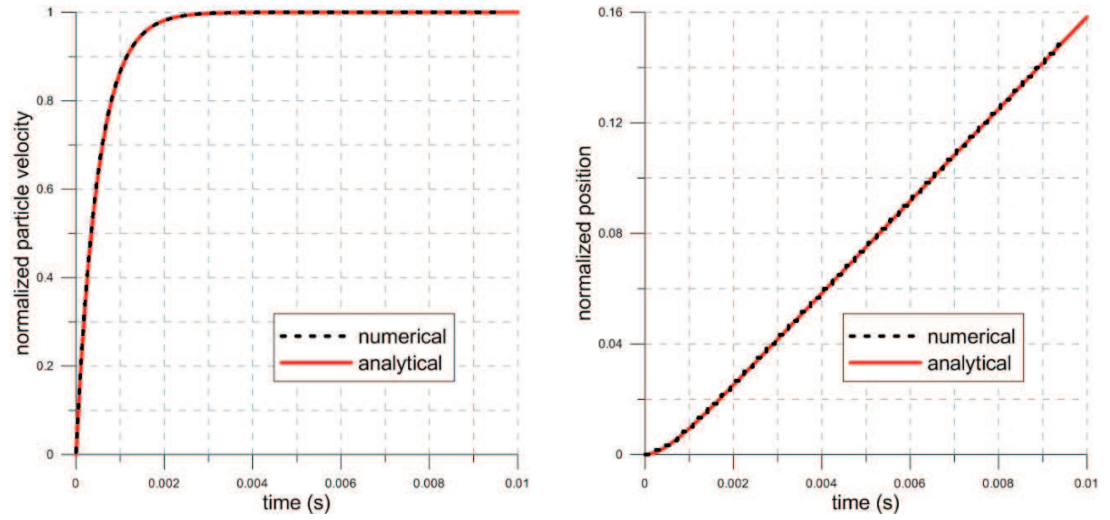

(a) (b)

Fig. 7.8. (a) Numerical and analytical solutions for particle velocity versus time and (b) position versus time.

Even though there are no buoyancy and gravity forces, some displacement on the vertical direction is computed. Moreover, there is also displacement on the horizontal position (perpendicular to the direction of the flow). In Fig. 7.9 it is shown the displacements, the drag forces and the particle velocity in the horizontal (perpendicular

to the direction of the fluid flow) and vertical directions. It can be observed that values are very low compared with the ones presented in the direction of the flow (Fig. 7.6).

The reason why there is horizontal and vertical particle velocity is that there is some drag force in both directions. The horizontal and vertical drag forces are due to the horizontal and vertical fluid velocities (Fig. 7.10). These fluid velocities are supposed to be 0 but they are not because of the round-off error of the numerical fluid simulation. The same simulation without a particle has been also performed (Fig. 7.11) and the results confirmed that the fluid flow has some horizontal and vertical velocities, what means that they are not caused by the presence of the particle. When the coupling is done these velocities transfer moment to the particle. In Fig. 7.9a and Fig. 7.9b there are some 'jumps' in the graphs. These jumps are in each time coupling (0.005 s). Every time the CCFD and PFC3D couple the fluid transfers horizontal and vertical velocities to the particle and the drag forces in these directions increase.

Simulations with different local damping values (δ in Eq. 4.27) were performed to understand the effect of the damping on the drag force and the particle velocity. The damping values tested are 0.4 and 0.8. Fig. 7.12 compares the results of these simulations and the reference case presented above (with a damping value of 0). The limit behaviour in terms of particle velocity and drag force is equal in all simulations, but as damping increases the drag force decrease is slower, and the limit velocity is attained later and further from the entrance. Increasing the damping value the overshoot in velocity over the analytical solution disappears and the position lag with respect that solution increases.

The effect of different fluid viscosities was also explored. Results for viscosity 0.01 and 100 mPa·s, are compared with those from the reference viscosity of 1 mPa·s presented in Fig. 7.13. It can be observed how a more viscous fluid results in a shorter transient and an increased velocity overshoot. For the less viscous fluid the simulation ends before the velocity transient is finished.

From these parametric analyses it can be concluded that in the study of transient situations induced by fluid-particle interaction the effect of increased local damping is similar to that of reducing fluid viscosity.

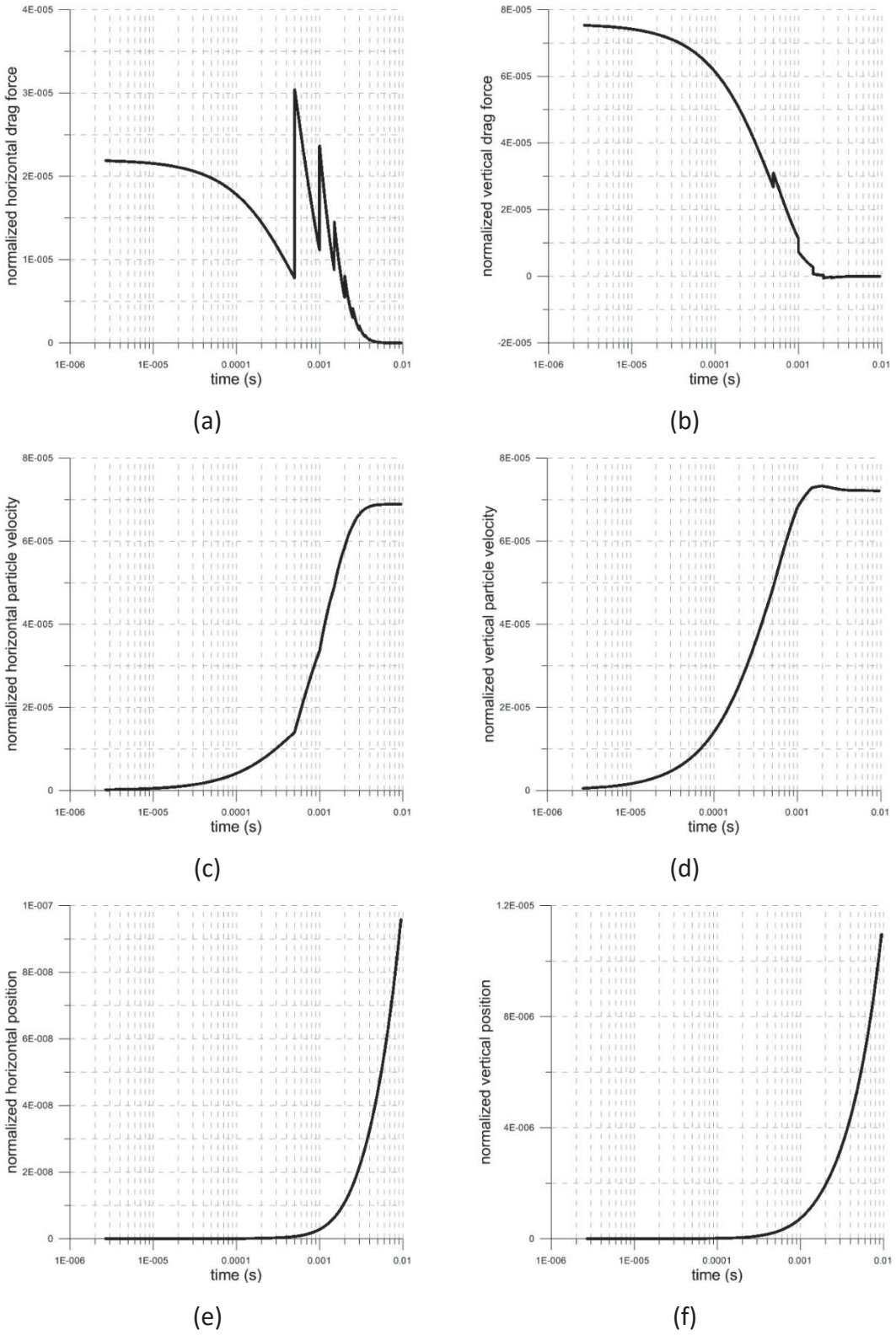

Fig. 7.9. Results of the dragged particle simulation on the horizontal and vertical directions. (a) Normalized horizontal drag force versus time, (b) normalized vertical drag force versus time, (c) normalized horizontal particle velocity versus time, (d) normalized vertical particle velocity versus time, (e) normalized horizontal position versus time, and (f) normalized vertical position versus time. The position is calculated from the centre of the tube. Drag forces are normalized by the initial drag force in the direction of the fluid flow, positions are normalized by the particle diameter and particle velocities are normalized by the fluid velocity. All figures are represented in a logarithmic scale.

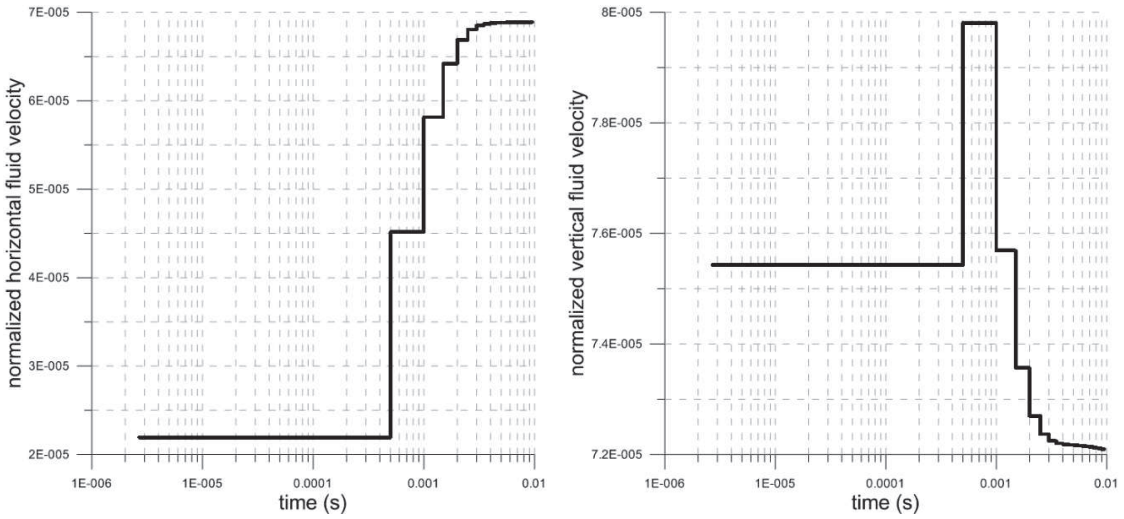

(a) (b)

Fig. 7.10. Results of the fluid flow in the cell where the particle is on the horizontal and vertical directions. (a) Normalized horizontal fluid velocity versus time, and (b) normalized vertical fluid velocity versus time. All figures are represented in a logarithmic scale. Fluid velocities are normalized by the boundary velocity condition on the direction of the flow. All figures are represented in a logarithmic scale.

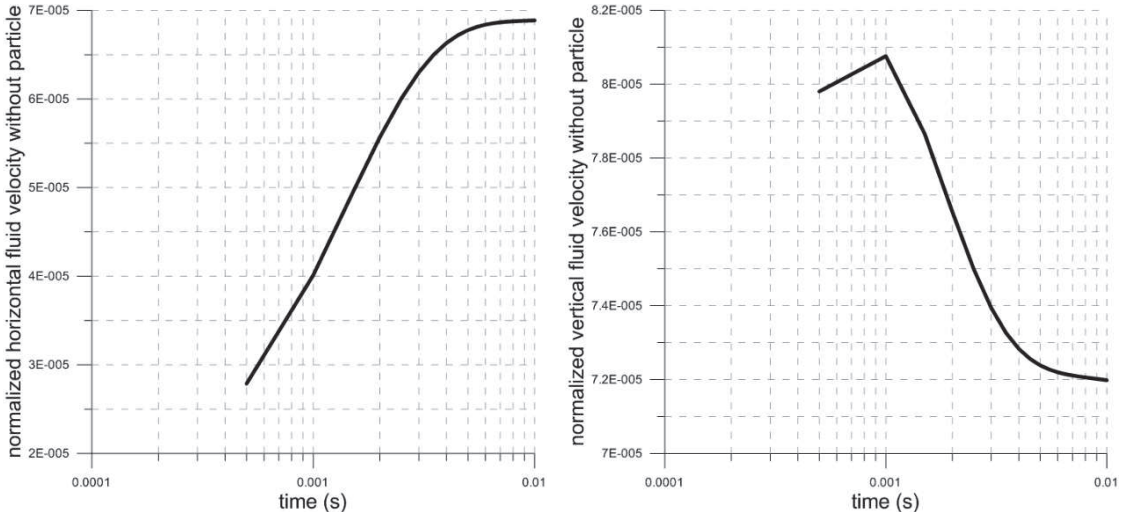

(a) (b)

Fig. 7.11. Results of the fluid flow without the particle on the horizontal and vertical directions. (a) Normalized horizontal fluid velocity versus time, and (b) normalized vertical fluid velocity versus time. All figures are represented in a logarithmic scale. Fluid velocities are normalized by the boundary velocity condition on the direction of the flow. All figures are represented in a logarithmic scale.

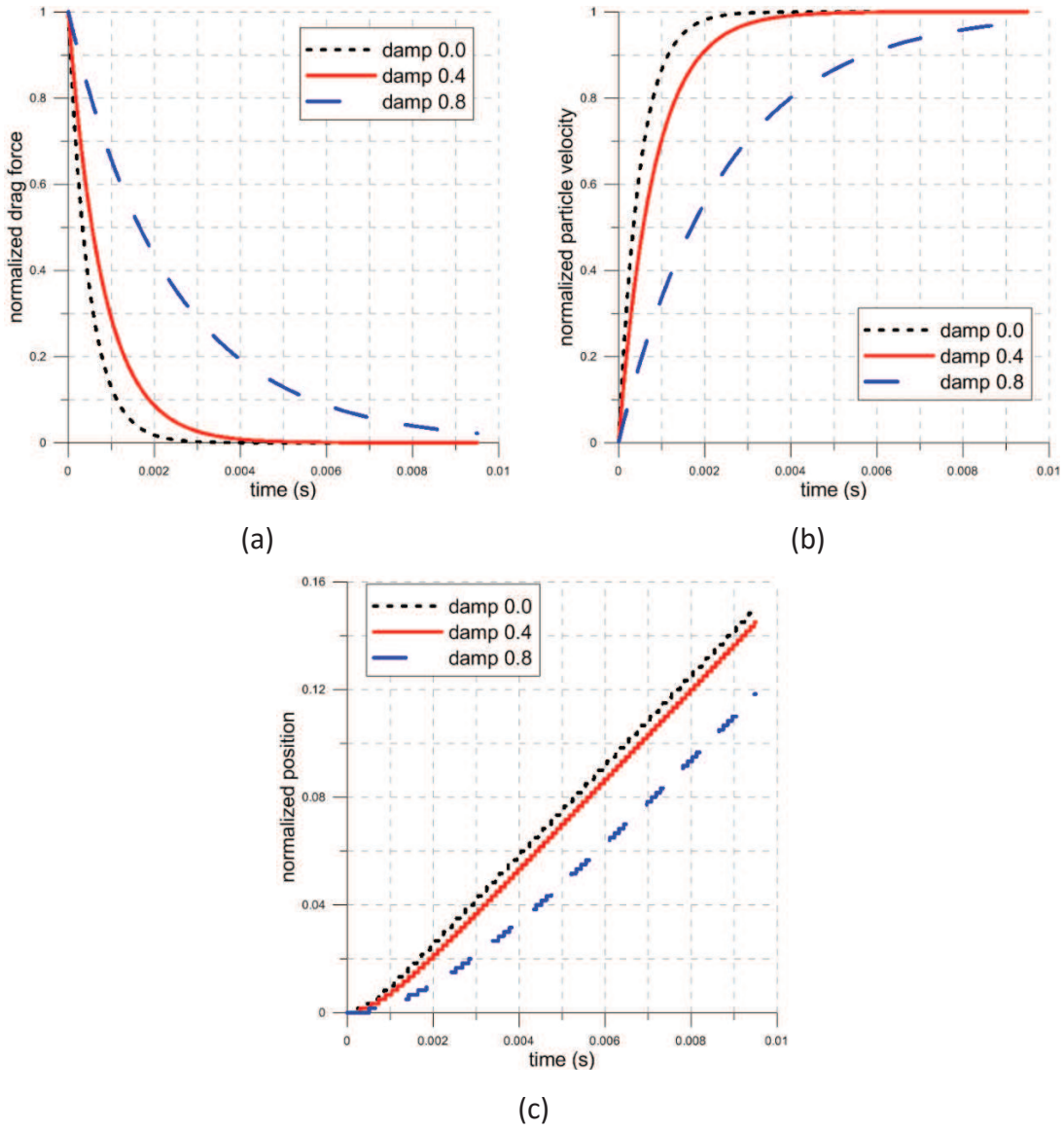

Fig. 7.12. Results of the dragged particle simulation with different damping values. (a) normalized drag force on the direction of the fluid flow versus time, (b) normalized particle velocity on the direction of the fluid force versus time, and (c) normalized position on the direction of the fluid flow versus time The position on the direction of the fluid flow is calculated from the beginning of the tube, and positive going to the opposite side of the tube, and horizontal and vertical positions are calculated from the centre of the tube. Only the drag force of the fluid force is represented. Drag forces are normalized by the initial drag force in the direction of the fluid flow, positions are normalized by the particle diameter and particle velocities are normalized by the fluid velocity.

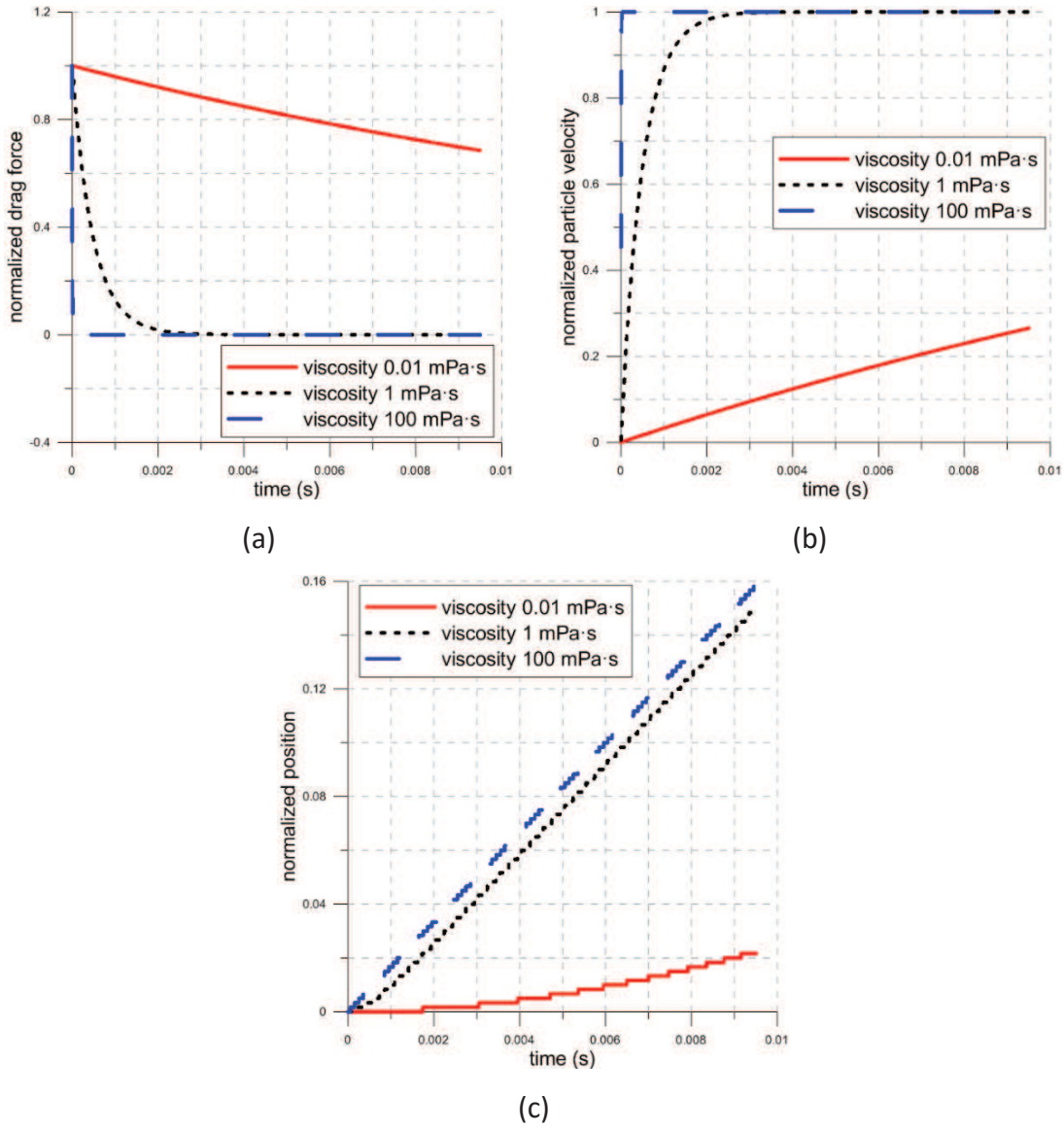

Fig. 7.13. Results of the dragged particle simulation with different damping values. (a) Normalized drag force on the direction of the fluid flow versus time, (b) normalized particle velocity on the direction of the fluid force versus time, and (c) normalized position on the direction of the fluid flow versus time. The position on the direction of the fluid flow is calculated from the beginning of the tube, and positive going to the opposite side of the tube, and horizontal and vertical positions are calculated from the center of the tube. Only the drag force of the fluid force is represented. Drag forces are normalized by the initial drag force in the direction of the fluid flow and the reference viscosity, positions are normalized by the particle diameter and particle velocities are normalized by the fluid velocity.

7.2.3. Particle decelerated by fluid with no flow in a horizontal tube

Simulations of particle deceleration by static fluid inside a horizontal tube are performed. Again, buoyancy and gravity are not taken into account and the only force between the particle and the fluid is the drag force.

In this problem the drag force exerted on the particle is passive: the fluid initial velocity is 0 and its presence decelerates the particle. As in the previous section, drag force can be again expressed by Stoke's expression, and the governing equations for a single particle are the same (Eq. 7.2 and Eq. 7.3). The difference is that the initial fluid velocity is $u = 0$ and the initial particle velocity is v_0. The analytical solutions calculated for the velocity and the position of the particle are

$$v = v_0 \exp\left(-\frac{9\mu_f}{2\rho_p R^2} t \right) \qquad \text{Eq. 7.6}$$

$$x = \frac{2v_0\rho_p R^2}{9\mu_f}\left(1 - \exp\left[-\frac{9\mu_f}{2\rho_p R^2} t \right] \right) + x_0 \qquad \text{Eq. 7.7}$$

The length of the tube is $L = 0.08$ m and the radius R = 5 mm (Fig. 7.4). The fluid is water, with a density of 1000 kg/m^3 and a viscosity of 1 mPa·s.

To construct the mesh, 40 horizontal divisions and 20 circumferential divisions are made (Fig. 7.5). The boundary conditions are $U = 0$ m/s velocity at the entrance of the tube (left) and $P = 0$ pressure at the opposite boundary. A particle is created at the entrance of the tube (at $x_0 = 2$ mm of the entrance of the tube) and at the centre of the boundary. The particle has a radius of 0.03 mm, a density of 2500 kg/m^3 and an initial horizontal velocity of 1 mm/s. The local damping is set to 0 and the simulation is run until 2 seconds using a coupling time of 0.01 s. The Reynolds number in this problem is 0.6, it means

that the Stoke's law (Eq. 6.10) is also valid. Following the analytical solution (Eq. 7.6) we can define a transient time (t_{trans}), as the 0.01 % of the initial particle velocity. In this problem t_{trans} = 0.01 mm/s. The analytical transient time is 0.0023 s.

The results are shown in Fig. 7.14. The drag force on the particle is negative because the particle velocity is higher than the fluid velocity; therefore, the fluid decelerates the particle until the same velocity as the fluid (0) is reached.

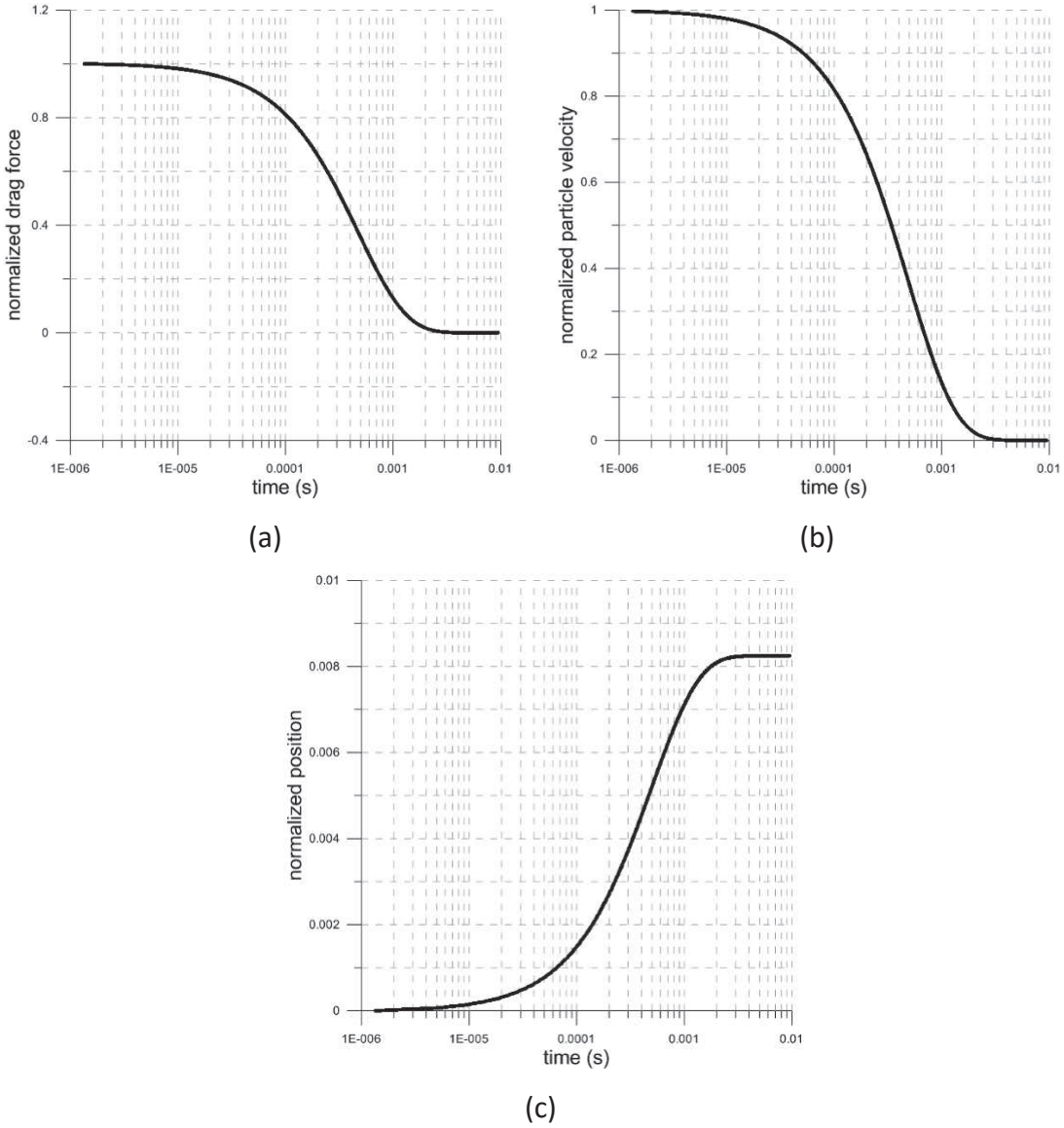

Fig. 7.14. Results of the decelerated particle simulation. (a) Normalized drag force versus time, (b) normalized particle velocity versus time, and (c) normalized position versus time. The position is calculated from the beginning of the tube, and positive going to the opposite side of the tube. Only the drag component of the fluid force is represented. The particle velocity is normalized by the limit velocity, the drag force is normalized by the initial force in the initial particle velocity direction and the position is normalized by the particle diameter. All figures are represented in a logarithmic scale.

Fig. 7.15 shows the body force on the fluid and the fluid velocity. Both are calculated in the cell where the particle is (following the particle movement). The body force is the same as the drag force on the particle but in the opposite direction. The fluid flow velocity is 0 until 0.0005 s, when the first coupling occurs. At that point, the particle transfers moment to the fluid and its velocity increases. The numerical transient time in this simulation is 0.0023 s, the same as the analytical transient time. The numerical results in Fig. 7.14 can be compared with an analytical solution. Fig. 7.16 shows the analytical results and compares them to the numerical ones.

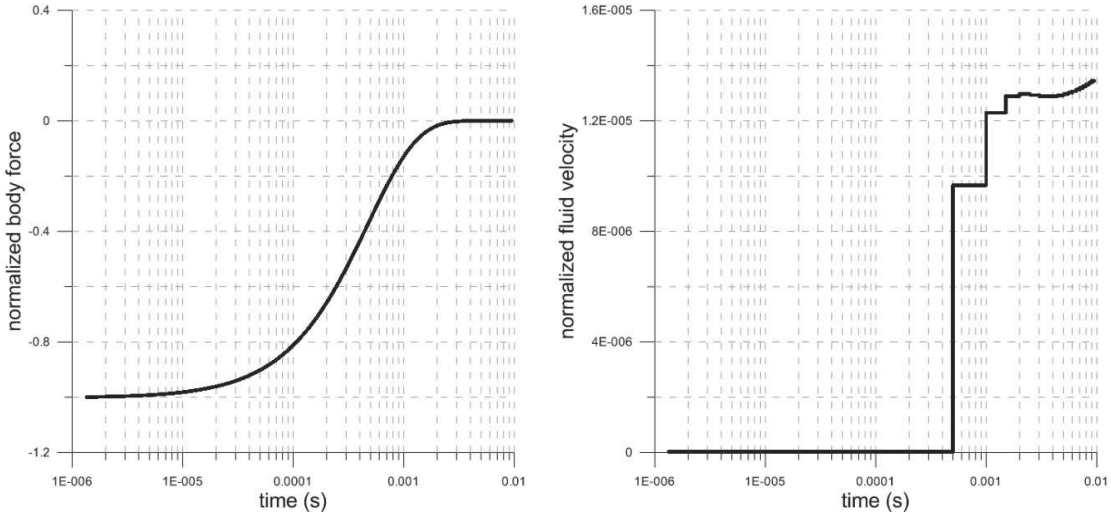

(a) (b)

Fig. 7.15. Results of the fluid flow in the cell where the particle is. (a) normalized body force versus time, and (b) normalized fluid velocity versus time. All figures are represented in a logarithmic scale. Body force is normalized by the initial drag force in the direction of the fluid flow and fluid velocity is normalized by the imposed boundary fluid velocity. All figures are represented in a logarithmic scale.

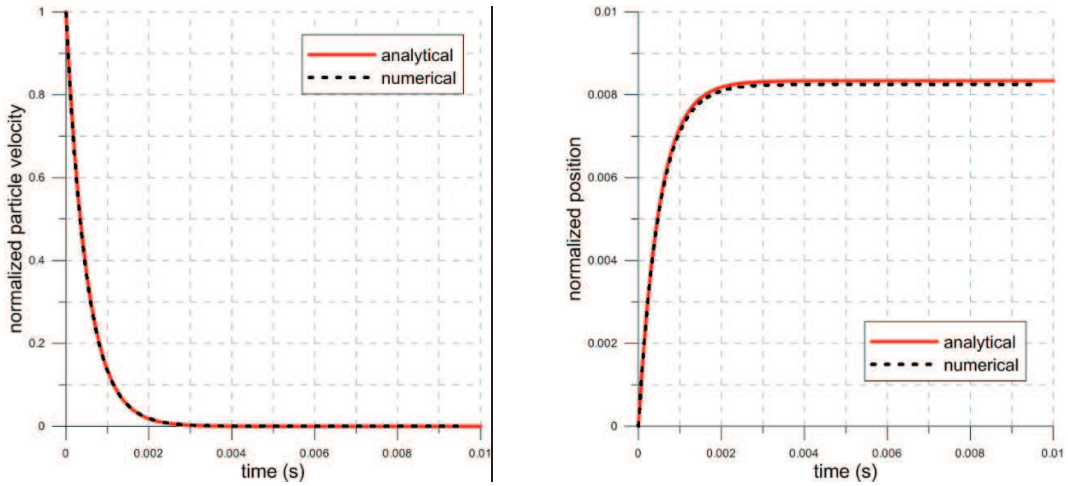

Fig. 7.16. (a) Numerical and analytical solutions for normalized particle velocity versus time and (b) normalized position versus time. Particle velocity is normalized by the initial particle velocity and position is normalized by the particle diameter.

There is also some displacement on the vertical and horizontal (perpendicular to the initial particle velocity direction) directions. In Fig. 7.17 illustrates the displacements, fluid forces and particle velocity in these directions. It can be observed that values are very low comparing them with the ones presented in the direction of the flow (Fig. 7.14).

The reason why there is horizontal and vertical particle velocities and also drag forces in these directions are the same as exposed in Section 7.2.2. The horizontal and vertical fluid velocities during the simulation are those presented in Fig. 7.18. In Fig. 7.19 it can be seen that there is horizontal and vertical fluid velocities also when the simulation is performed without particle due to a round-off error.

Simulations with different local damping values (δ in Eq. 4.27) were performed to understand the effect of the damping on the drag force and the particle velocity. The damping values tested are 0.4 and 0.8. The results are presented in Fig. 7.20. At the end of all the simulations the velocity of the particle is 0. The effect of the damping in the simulation makes the particle decelerate faster. The result is that when the damping value is increased, the particle stops at a point closer to the entrance of the tube.

The effect of the viscosity is also presented (Fig. 7.21). Again, an increase in viscosity results in shorter transients and the particle stops at a point closer to the entrance of the tube.

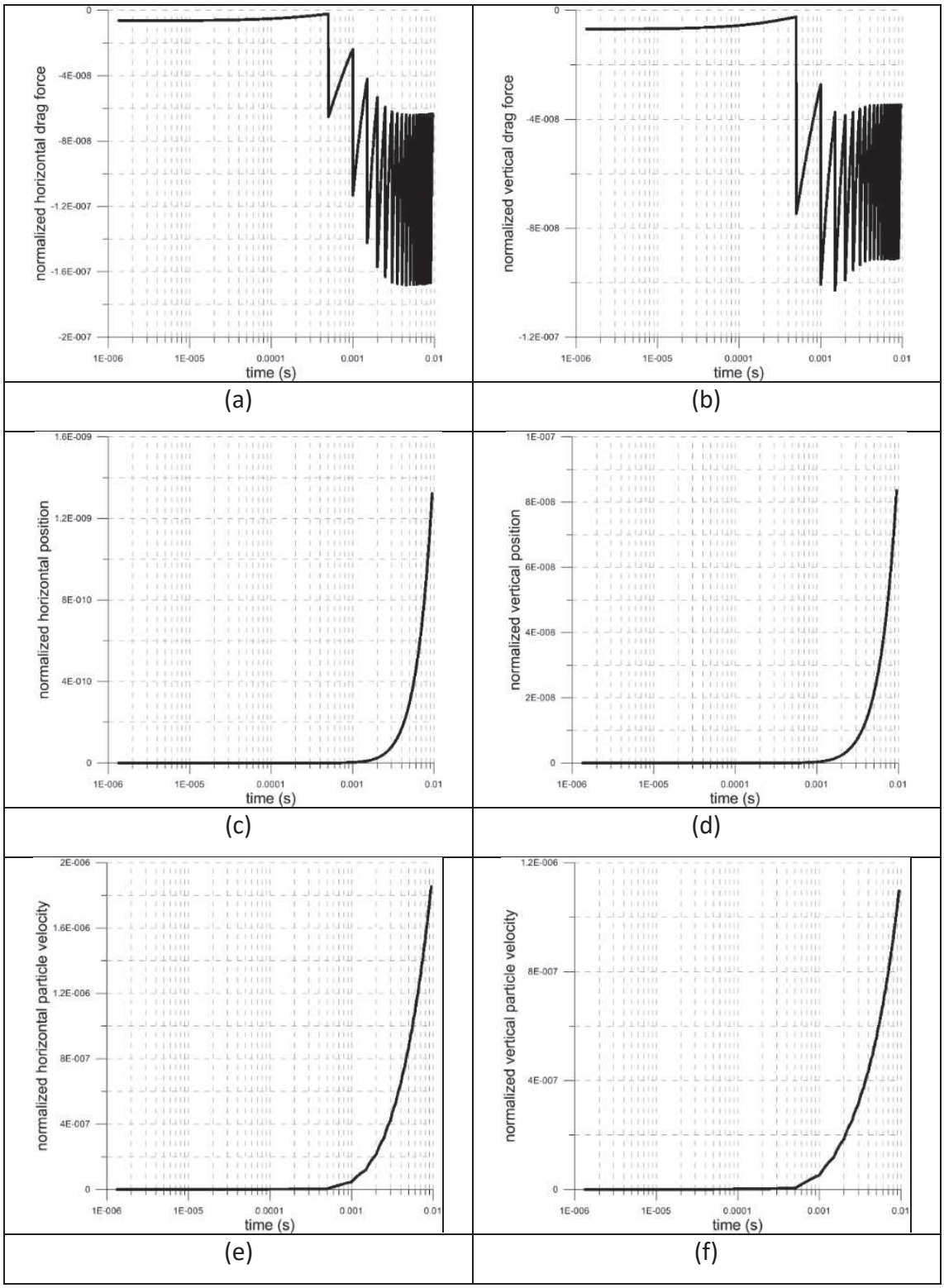

Fig. 7.17. Results of the decelerated particle simulation on the horizontal and vertical directions. (a) Normalized horizontal drag force versus time, (b) normalized vertical drag force versus time, (c) normalized horizontal particle velocity versus time, (d) normalized vertical particle velocity versus time, (e) normalized horizontal position versus time, and (f) normalized vertical position versus time. The position is calculated from the center of the tube. The particle velocity is normalized by the limit velocity, the drag force is normalized by the initial force in the initial particle velocity direction and the position is normalized by the particle diameter. All figures are represented in a logarithmic scale.

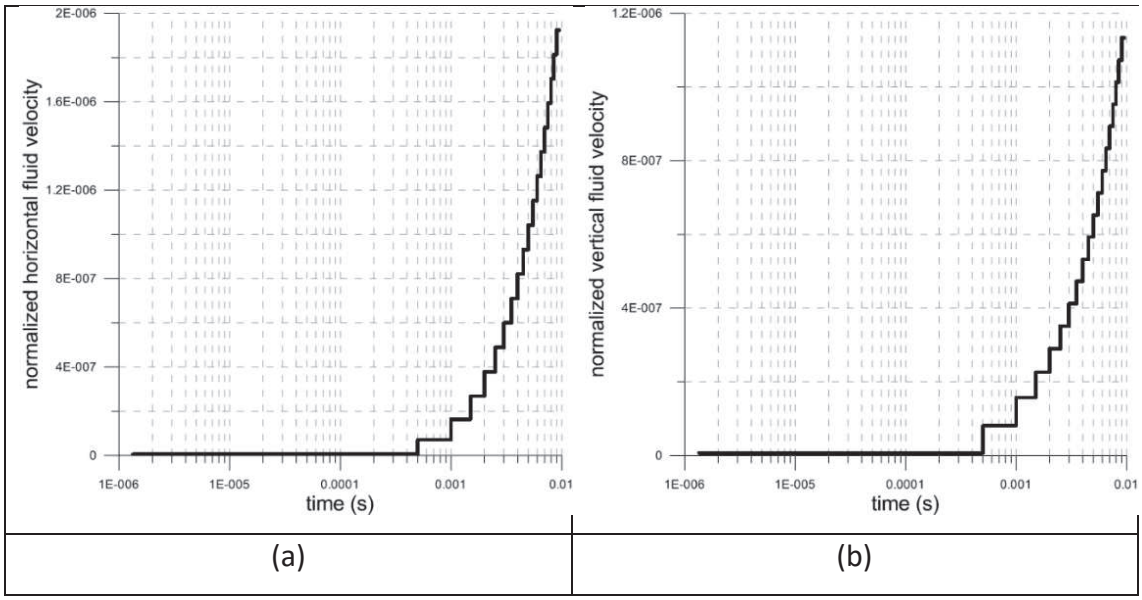

Fig. 7.18. Results of the fluid flow in the cell where the particle is on the horizontal and vertical directions. (a) normalized horizontal fluid velocity versus time, and (b) normalized vertical fluid velocity versus time. All figures are represented in a logarithmic scale. Fluid velocities are normalized by the boundary velocity condition on the direction of the flow. All figures are represented in a logarithmic scale.

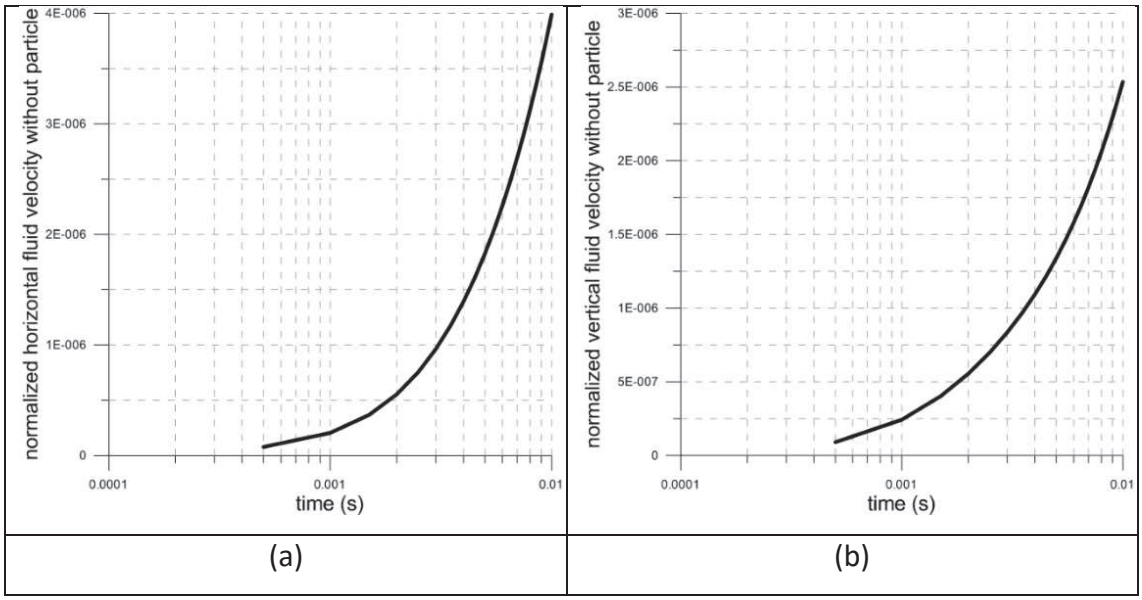

Fig. 7.19. Results of the fluid flow without the particle on the horizontal and vertical directions. (a) normalized horizontal fluid velocity versus time, and (b) normalized vertical fluid velocity versus time. All figures are represented in a logarithmic scale. Fluid velocities are normalized by the boundary velocity condition on the direction of the flow. All figures are represented in a logarithmic scale.

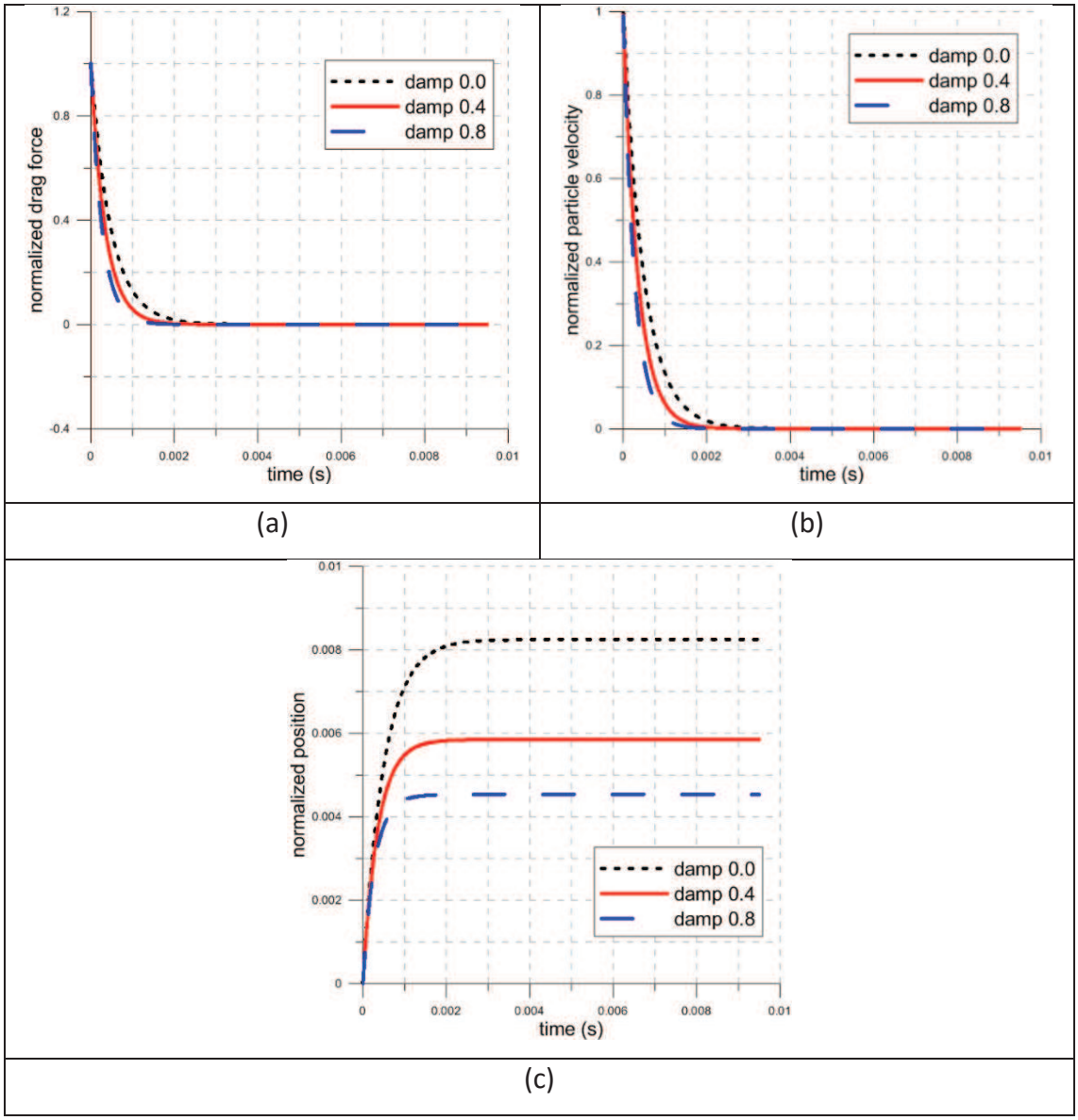

Fig. 7.20. Results of the decelerated particle simulation for different damping values. (a) normalized drag force on the direction of the initial particle velocity versus time, (b) normalized particle velocity on the direction of the initial particle velocity versus time, and and (c) normalized position on the direction of the initial particle velocity versus time. The position on the direction of the initial particle velocity is calculated from the beginning of the tube, and positive going to the opposite side of the tube, and the horizontal and the vertical directions from the center of the tube. The particle velocity is normalized by the limit velocity, the drag force is normalized by the initial force in the initial particle velocity direction and the position is normalized by the particle diameter.

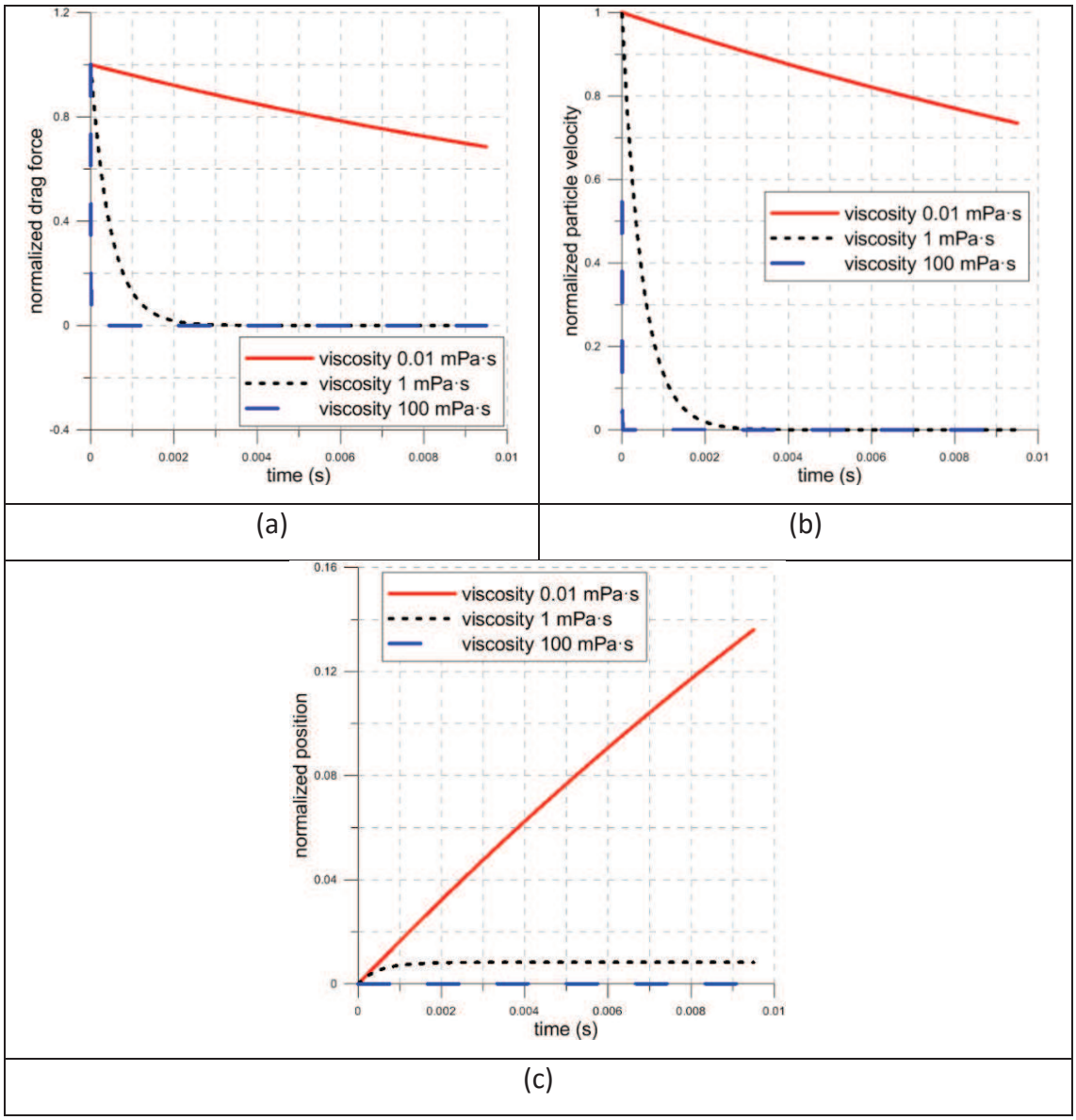

Fig. 7.21. Results of the decelerated particle simulation for different viscosity values. (a) normalized drag force on the direction of the initial particle velocity versus time (b) normalized particle velocity on the direction of the initial particle velocity versus time, and (c) normalized position on the direction of the initial particle velocity versus time The position on the direction of the initial particle velocity is calculated from the beginning of the tube, and positive going to the opposite side of the tube, and the horizontal and the vertical directions from the center of the tube. The particle velocity is normalized by the limit velocity, the drag force is normalized by the initial force in the initial particle velocity direction and the position is normalized by the particle diameter.

7.2.4. Conclusions of single particle tests and sensibility studies

In Sections 7.2.2 and 7.2.3 some simulations with a single particle have been performed with a low Reynolds number and the results compared to the Stokes analytical solution. The numerical results are consistent with the analytical solutions in the direction of the

fluid flow or the particle velocity. In the perpendicular directions, where the particle and the fluid are not supposed to move, some numerical discrepancies are found due to the numerical round-off error.

The running time of all the simulations in Section 7.2.2 and 7.2.3 is 1 min for a simulation time of 0.01 s.

The sensibility analysis has given some interesting results about the influence of the local damping and the viscosity in the solution. In Fig. 7.22 a parametric study of the previous simulations is presented. First of all, it should be noted that the effect of fluid viscosity in the transient time is the same for the simulation with an accelerated particle and the one with and a decelerated particle. When the viscosity is increased the transient time decreases. Moreover, the transient time is the same for both simulations at a given value of the viscosity.

On the other hand, the effect of the local damping is quite different. Increasing the local damping increase the transient time when the particle is accelerated by the fluid, but decreases the transient time when the particle is decelerated by the fluid. The local damping is a force added to decelerate the particle. For that reason, when the particle is being decelerated by the fluid the local damping increases its deceleration. But, on the other hand, when the particle is being accelerated by the fluid, the local damping adds an opposite force to the fluid force and increases the time to reach limit velocity.

The effect of the damping is an important fact that must be considered in coupled simulations. In most DEM simulations local damping is used because it is practical to speed the simulation and the macro results appear to improve (i.e. are smoothed) when damping is added. However, it has been presented in this section that the local damping can affect the result of a single particle position what makes the selection of the local damping value an important fact to be considered. This effect is again presented in Section 8.5 comparing results with different local damping values in sand production simulation, and was also discussed in Climent et al. (2013).

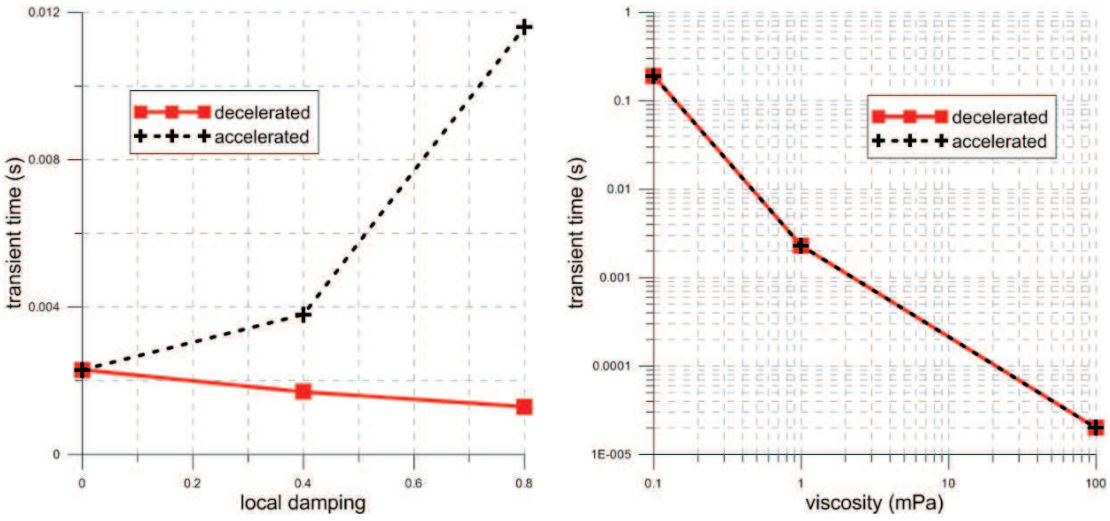

(a) (b)

Fig. 7.22. (a) Transient time versus local damping, and (b) transient time versus viscosity in a logarithmic scale when the particle is accelerated by the fluid and when the particle is decelerated by the fluid.

7.3. Permeability in particle-flow methods: particle Reynolds number

A model permeameter was built to validate the CFD-DEM coupling in a more complex setting.

The Kozeny-Carman equation is a relationship proposed by Kozeny (1927) and later modified by Carman (1937), both cited in Bear (1972), Carrier (2003) and Chapuis & Aubertin (2003). The equation is a relationship between the permeability (introduced in Section 2.2.2) and the porosity of a porous medium and it was developed after considering a porous material as an assembly of capillary tubes for which Navier-Sokes equation in a laminar flow regime can be used. Therefore, the equation is obtained assuming Darcian conditions (Bear, 1972; Carrier, 2003). The Kozeny-Carman equation can be expressed as

$$k = C\frac{n^3}{S_a^2(1-n)^2} \qquad \text{Eq. 7.8}$$

where *k* is the permeability, *C* is a numerical constant called Kozeny's constant, S_a is the specific surface, and *n* is the porosity.

C depends on the geometrical form of the individual channels in the model and the tortuosity (the ratio between the length of the curved fluid velocity and the distance between the extremes of the curve). As cited by Bear (1972) and Chapuis & Aubertin (2003), Carman (1937) obtained the best fit in his experimental results with $C = \frac{1}{5}$.

The specific surface of a porous material (S_a) is defined as the total interstitial surface area of the pores per unit bulk volume of the porous medium (Bear, 1972). The main difficulty of calculating the hydraulic conductivity using the Kozeny-Carman equation lies in the determination of the soil specific surface. It is frequently measured experimentally or estimated (Chapuis & Aubertin, 2003). The specific surface of a spherical solid particle is equal to the ratio between its surface area and its volume. The specific surface can be written in terms of diameter of a spherical solid particle (Trani & Indraratna, 2010)

$$S_a = \frac{6}{d_p} \qquad \text{Eq. 7.9}$$

where d_p is the particle diameter. Then, the Kozeny-Carman equation becomes (Bear, 1972)

$$k = \frac{d_p^2}{180} \frac{n^3}{(1-n)^2} \qquad \text{Eq. 7.10}$$

Calculating d_p becomes a difficulty when the material contains different particle diameters. d_p is commonly calculated and estimated using the grain size curves (Chapuis & Aubertin, 2003; Carrier, 2003; Trani & Indraratna, 2010). A PSD (presented in Section 2.2.1) of a soil material can be discretized in different diameters d_i. Each of this diameters have its corresponding mass per cent finer given by p_i. d_p can be calculated as follows (Trani & Indraratna, 2010; Chapuis & Aubertin, 2003)

$$d_p = \sum_{i=1}^{j} \left(p_i / d_{av,i} \right) \qquad \text{Eq. 7.11}$$

where $d_{av,i}$ is the geometric average of two adjacent diameters. This equation has been tested successfully with materials with an average coefficient of uniformity (Eq. 2.1) of about 3 (Chapuis & Aubertin, 2003). Further increases in the C_u shows limitations of the PSD in modelling void sizes of well-graded soils because large particles with high individual mass but low in number are over-represented in the model and produce a high number of large pores (Trani & Indraratna, 2010). As C_u increases the number of small particles filling the void between the larger particles would increase, leading to smaller void sizes. As cited by Trani & Indraratna (2010), Humes (1996) suggested an improvement by adopting the particle size distribution by surface area (PSDsa) method. If the soil material is composed of discretised diameters d_i and their mass probabilities of accurrence p_{mi}, respectively, then their probabilities by surface area can be obtained following generalised equation

$$p_{sai} = \frac{p_{mi}}{d_{av,i}} \sum_{i=1}^{j} \frac{p_{mi}}{d_{av,i}} \qquad \text{Eq. 7.12}$$

and then the p_{sai} can be used substituying p_i in Eq. 7.11.

However, Kozeny-Carman equation is not appropriate if the particle size distribution has a long, flat tail in the fine fraction (Carrier, 2003). The prediction of the permeability using Kozeny-Carman assumes that the specimen is homogenous, and it cannot predict the permeability of a heterogeneous specimen (Chapuis & Aubertin, 2003). In the model presented in this section, sample is homogeneous, which simplifies the calculation of this diameter.

As it is explained in Sections 2.2.2 and 6.2, Darcy's law is only valid for low particles Reynolds number (Eq. 6.7). There are different studies about the Reynolds number limit of the Darcy's law (e.g. El Shamy & Zeghal, 2005; Wahyudi et al., 2002). Wahyudi et al. (2002) found experimentally that the critical Reynolds number is 4.3 for five sands geographically different. El Shamy & Zeghal (2005) simulations revealed that water seepage through granular soils followed Darcy's law when the particle Reynolds number was less than about 1.

The permeability is determined in the laboratory with an instrument called permeameter. In a permeameter, the fluid flows through a small cylindrical porous sample of a length *L* and a cross-sectional area A (Fig. 7.23). The flow is one dimensional (through the length of the sample) and steady. The sample is placed between two porous plates that provide almost no resistance to the flow through them. A constant pressure difference is applied across the tested sample (between points *a* and *b* in Fig. 7.23), producing a steady flow at a rate *Q*.

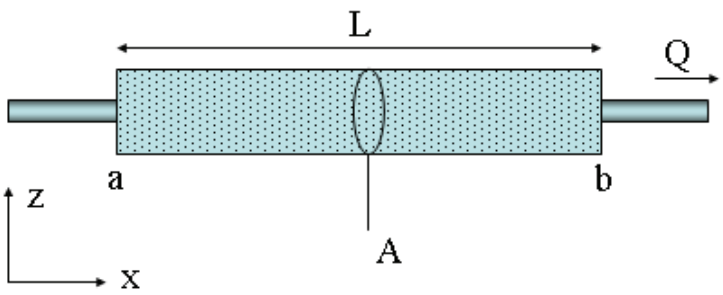

Fig. 7.23. Scheme of a permeameter

Using Darcy's law (Eq. 2.4 and Eq. 2.5), the discharge *Q* can be calculated

$$Q = \frac{-kA}{\mu_f}\frac{P_b - P_a}{L} \qquad \text{Eq. 7.13}$$

where *k* is the permeability, *A* is the section of the cylinder where the sample is contained, μ_f is the viscosity of the fluid, P_a-P_b is the fluid pressure drop when it flows through the sample, where *a* and *b* are the extremes of the cylinder where the sample is created and the fluid flows through it, and *L* is the length of the sample. The permeability can be isolated

$$k = \frac{-Q\mu_f L}{A\left(P_b - P_a\right)} \qquad \text{Eq. 7.14}$$

A numerical model of a permeameter was built as shown in Fig. 7.24. The discrete analogue is contained in a cylinder of 20 mm radius and 60 mm length. This container for the DEM model is overlapped by a larger CFD mesh (Fig. 7.25) which is extended at both ends of the solid container by two coaxial cylinders of smaller radius (5 mm). These fluid-only extensions of the model are practical to enforce appropriate boundary conditions: a longitudinal flow velocity (v_i) is imposed at the entrance (Fig. 7.24), and atmospheric pressure (0) is imposed at the outlet. All the remaining external surfaces of the model are designated as impermeable (no flow).

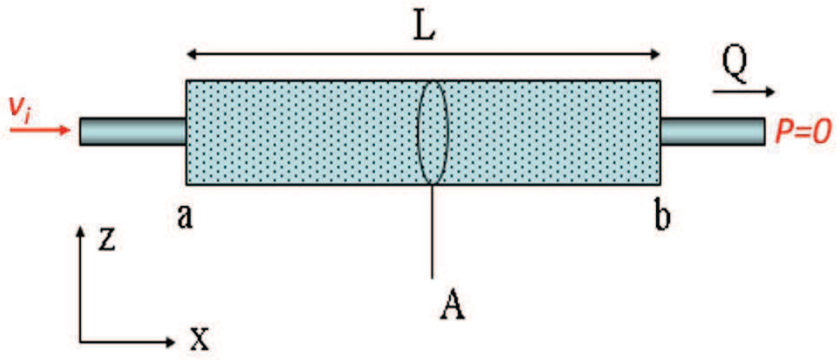

Fig. 7.24. Geometry of the permeameter model. The discrete analogue whose permeability is computed is contained in the internal cylinder (from point *a* to point *b*). The sample has a cylindrical shape and the fluid flows through it.

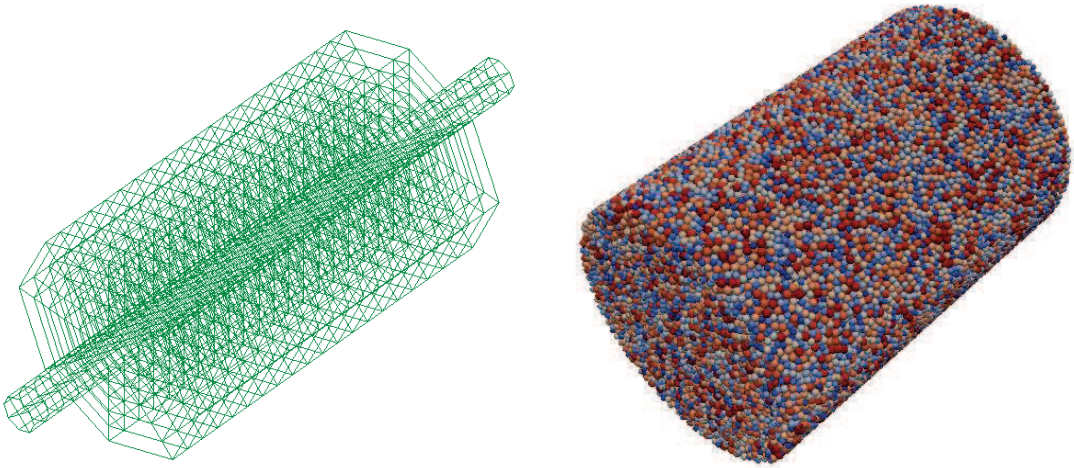

Fig. 7.25. CFD mesh for the permeameter study (left) and DEM model (right)

A discrete analogue of a bonded granular material was generated to fill the permeameter. The porosity of the sample is 0.4 and particles are generated randomly with radii between 0.4 and 0.6 mm. The DEM parameters represent an ideal sandstone, described in Section 8.3.2. All contacts are bonded with bond strength set high enough so that no particle moves during the simulation.

Permeability is computed measuring fluid pressure at the extremes of the DEM container (points *a* and *b* of the scheme in Fig. 7.24).

The parameters needed to calculate the permeability (Eq. 7.10) are the porosity and the particle diameter. The porosity is 0.4, as it is explained above, and the particle diameter is 1 mm, calculated as the medium value between 0.8 and 1.2 mm.The permeability calculated by the Kozeny-Carman equation (Eq. 7.10) is then $2.5 \cdot 10^{-9}$ $m^{2\cdot}$.

Some simulations with different particle Reynolds numbers (from 0.001 to 320) were run and the permeability is calculated in each of the simulations (Table 7.1).

Fig. 7.26 and Fig. 7.27 shows the distribution of the velocity, fluid pressure and drag force in a colour maps of the simulation 1. It can be observed that for Reynolds numbers less than 1, the permeability is $1.3 \cdot 10^{-9}$. Chapuis & Aubertin (2003) pointed out that Kozeny-Carman equation usually predicts permeability values between 1/3 and 3 times the measured value. The measured permeability is 0.52 times the permeability predicted with Kozeny-Carman equation, which is within that margin. When the Reynolds number is increased, the permeability decreases, reaching a value of one order of magnitude inferior for a Reynolds number of 320. El Shamy & Zeghal (2005) pointed out that to assure that the Darcy's law is valid, the particle Reynolds number should be less than 1. The results in this work are consistent with that limit. The permeability decreases a lot for high particle Reynolds numbers. In Table 7.1 the measured permeability when the particle Reynolds number is 320 is two orders of magnitude smaller than the expected permeability. This is consistent also with experimental results. Wahyudi et al. (2002) calculated the friction factor for different sands and different particle Reynolds numbers (Fig. 7.28). As it is shown in Fig. 7.28 the friction factor increase and deviates of what it is expected when the particle Reynolds number is between 100 and 1000. The friction factor is a theoretical friction that gives an idea of the frictional energy loss based on the velocity of the fluid and the resistance due to friction. The friction factor increases the difficulty of the fluid to flow between the grains and decreases the permeability.

Table 7.1. Results for the permeability of the sample for different fluid velocities. Measured permeability is normalized by the permeability calculated with Kozeny-Carman equation

v_i (m/s)	Measured Permeability (m^2)	Normalized measured permeability	Particle Reynolds number
1.6	$1.5 \cdot 10^{-11}$	0.006	320
$1.6 \cdot 10^{-1}$	$8 \cdot 10^{-10}$	0.32	32
$1.6 \cdot 10^{-2}$	$8 \cdot 10^{-10}$	0.32	3.2
$1.6 \cdot 10^{-3}$	$1.3 \cdot 10^{-9}$	0.52	0.32
$5 \cdot 10^{-4}$	$1.3 \cdot 10^{-9}$	0.52	0.1
$1 \cdot 10^{-4}$	$1.3 \cdot 10^{-9}$	0.52	0.02
$5 \cdot 10^{-5}$	$1.3 \cdot 10^{-9}$	0.52	0.01
$1 \cdot 10^{-5}$	$1.3 \cdot 10^{-9}$	0.52	0.002
$5 \cdot 10^{-6}$	$1.3 \cdot 10^{-9}$	0.52	0.001

Fig. 7.26. Fluid velocity at the end of the simulation using the permeameter. On the left the coloured map of the 3D sample, in the middle a yz plane of the permeameter and on the right the scale of the colours representing the fluid velocity in m/s.

(a) (b)

Fig. 7.27. (a) Fluid pressure at the end of the simulation and (b) drag force at the end of the simulation.

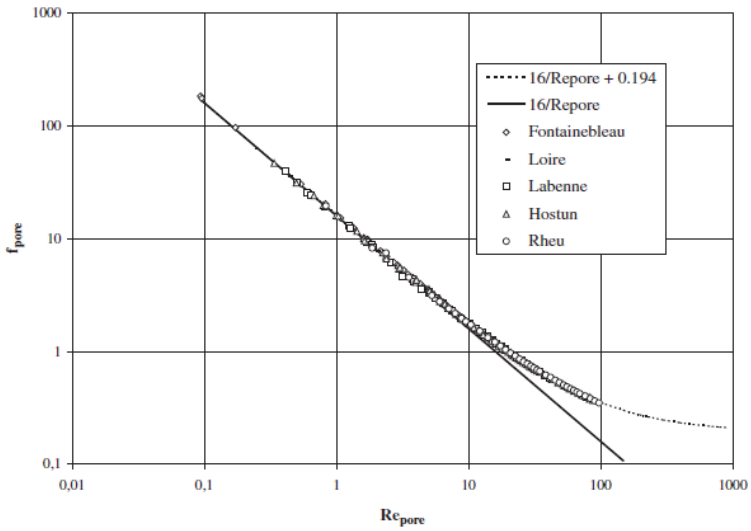

Fig. 7.28. Friction factor versus particle Reynolds number. Two analytical correlations and experimental results for different sand beds (Wahyudi et al., 2002).

7.4. Summary

In this chapter the CFD-DEM coupled model is tested. Simulations using a single particle and a permeameter using a sample are performed.

When a single particle is dropped inside a vertical tube filled with static fluid, the particle moves with an acceleration until the fluid force upwards equals the gravity downwards. At the end a limit velocity is reached. The CFD-DEM model reproduced correctly the Stokes solution.

When a weightless particle is dragged by fluid in a horizontal tube, the limit velocity is the imposed fluid velocity. When the damping is increased the process to the equilibrium is decelerated and the particle reaches the limit velocity later and further. On the other hand, even though the particle increases its velocity when the fluid viscosity is increased, its trajectory does not change a lot.

When a weightless particle is shot inside a quiescent fluid, the particle is decelerated by the fluid until it stops. The effect of increasing the damping value is that the particle

decelerates faster and reaching the equilibrium before. The position of the particle at the end of the simulation is different for different damping values. On the other hand, the effect of the viscosity is the same as in the simulation where the particle is dragged by the fluid, an increase in viscosity results in shorter transients.

In simulations with a single particle a parametric study has been presented to understand the influence of the local damping and the viscosity. The fluid viscosity affects in the same way the transient time in simulation where the particle is dragged by the fluid and the simulation where the particle is decelerated. When the viscosity is increased the transient time decreases and the transient time is the same for both simulations at a given value of the viscosity.

However, the local damping increase the transient time when the particle is dragged by the fluid, but decreases the transient time when the particle is decelerated b the fluid. The local damping is a force added to decelerate the particle, which means that it accelerates the process when the particle is decelerated by the fluid, but decelerates the process to the equilibrium when the particle is accelerated by the fluid. In has been concluded that the choice of the local damping in DEM can have an important effect in DEM simulations and this effect must be considered in coupled simulations.

Finally, a study of the permeability of a sample is performed. Different simulations with different fluid velocities are carried out and the permeability calculated. As long as the particle Reynolds number remains below 1. The result is within the margin predicted by the Kozeny-Carman equation.

Chapter 8 - Simulations of sand production on idealized sandstone

8.1. Introduction

In this chapter coupled CFD-DEM simulations of sand production are presented for a discrete analogue of ideal sandstone which was proposed by Cheung (2010). The focus here is on the basic performance of the CFD-DEM fluid-solid coupling approach when applied to the sand production problem. By using Cheung's sandstone analogue the complications associated with mechanical calibration (as explained in Chapter 5) are left aside for the moment. It also has the added advantage of allowing some comparisons with the results obtained using her simplified fluid-solid coupling scheme.

First of all, a simulation of dry perforation is presented and discussed by reference to Risnes analytical solution in Section 8.2. In Section 8.3 fluid is introduced in the model in a simplified setting, using hydrostatic initial conditions. Simulations with an imposed fluid velocity are later presented in Section 8.4. The effect of numerical damping is explored in Section 8.5. The chapter ends with some comparisons with Cheung results.

8.2. Dry perforation

An initial simulation was performed without coupling fluid using only the DEM module. Effective and total stresses coincide in this case.

8.2.1. Description of the model

The model geometry considered in the coupled CFD-DEM simulations is shown in Fig. 8.1a. The geometry of this model is one particular case of the Risnes et al. (1982) idealization. Therefore the model can be considered to represent a horizontal slice of a confined vertical cylinder of sandstone with a cylindrical hole in the middle.

For given grain size the computational cost of DEM increases with the cube of model volume. Acceptable computing times were obtained with the dimensions shown in the Fig. 8.1a; outer radius *Ro* of 50 mm, height h of 5 mm and a central cavity with radius *Ri* of 5 mm. The central cavity radius of the model is far smaller than those typical of producing wells, bit is within of the typical range of entrance holes of field perforations in sandstone (Bellarby, 2009). Similar sized holes are also common in laboratory tests designed to study the mechanics of sand production (e.g. Tronvoll et al., 1998; Ispas et al., 2006; Younessi et al., 2013). The ratio between inner and outer radius in the model was selected by considering typical dimensions of experimental set-ups.

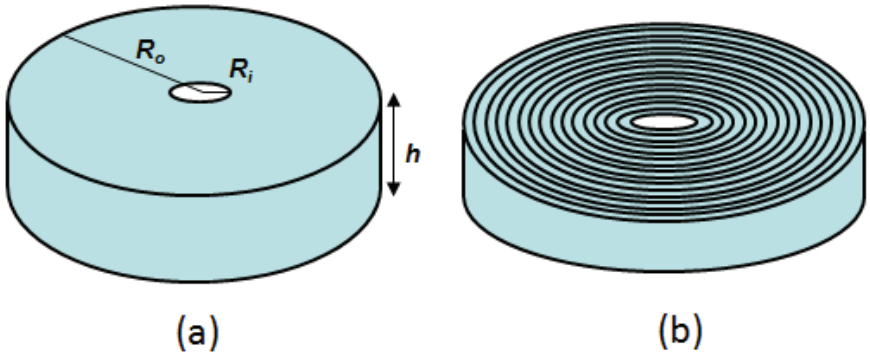

Fig. 8.1. (a) Model geometry, and (b) annulus rings created to calculate the continuum stress.

The DEM analogue was proposed by Cheung (2010) to represent ideal sandstone. For computational ease the discrete material has radii evenly distributed between 0.4 mm

and 0.6 mm, which is near the upper end of sandstone grain sizes, and porosity of 0.4, which is larger than that of most reservoir sandstones. The Biot parameter was fixed to a common value in sandstones (1).

The DEM input parameters are given in Table 8.1 and Table 8.2. The contact model used is the linear frictional contact model (Section 4.3.2.1), and the parallel-bond model is also used to simulate the cement between particles (Section 4.4). Damping, introduced in Section 4.5, is set to 0.7.

Table 8.1. Contact model parameters

Contact (parallel-bond model) parameters			
K^N, kN·m^{-1}	1×10^5	K^N_{pb}, kPa·s^{-1}	1×10^{12}
K^S, kN·m^{-1}	1×10^5	K^S_{pb}, kPa·s^{-1}	1×10^{12}
μ	0.25	S^N_{pb}, kPa	4.4×10^6
α_{bond}	0.25	S^S_{pb}, kPa	4.4×10^6

Table 8.2. Other DEM parameters

Number of particles	46035	Damping constant	0.7
$R_{DEM,particle}$, mm	0.4 to 0.6	$\rho_p\times10^3$, kg·m^{-3}	2.65

However, the analytical parameters that fitted the numerical results are similar than parameters obtained experimentally for sandstones (Section 8.2.2). Specimen formation follows a radius expansion procedure within frictionless walls to attain the target initial isotropic stress after which bond installation proceeds. All the contacts are

bonded, and all bonds are identical. After specimen formation the wall friction coefficients of the two horizontal platens are changed to 0.1. More details are given by Cheung (2010).

In contrast with the calibration in Chapter 5, where parameters were chosen to match laboratory tests results (uniaxial compressive tests and triaxial tests), Cheung (2010) adjusted some micromechanical model parameters to match some aspects of the Risnes et al. (1982) analytical solution (see Section 3.6). Thus, the parallel-bond strength was chosen to match the peak stress value in the circumferential stress distribution, which is controlled by the cohesive strength in the analytical solution. Also, the friction coefficient is chosen to match the size of the plastic zone, which is controlled by the failure angle in the analytical solution. Stiffness values were chosen to match the effect of the Poisson's ratio, which controls the circumferential and the radial stresses values in the elastic region. This matched calibration is also explained in Section 8.2.2.

The external radial DEM wall was servocontrolled to maintain the radial effective stress at 300 MPa, which is the confining stress of the sample. This value is higher than the usual stresses in laboratory sand production tests or in the field; it was chosen to ensure that large breakouts appeared under most scenarios and thus be able to fully explore the behaviour of the model. The internal radial wall was erased at the beginning of the simulation. The simulation was run until a steady state was reached, as observed when the average stress for each ring became constant in time. Particles that moved inside the hole (the entire particle was within the inner radius) during the simulation were automatically removed and considered produced.

Calculation of the stresses from the DEM data was based on a well-established procedure (Potyondy & Cundall, 2004; O'Sullivan, 2011) in which representative or notional average grain stresses are first computed and then these are averaged in the reference volume to obtain the representative volume stress. Stresses in PFC^{3D} are thus calculated using only particle contact forces and are therefore effective stresses.

Due to the axial symmetry of the model geometry, stresses are assumed to be only dependent on the radial distance. The stress averaging volumes chosen were 15 annulus rings, shown in Fig. 8.1b. The number of annulus rings was chosen to fit a minimum

number of particles per ring to average the continuum stress (if there are too few particles the average has no sense as a continuum stress). It was observed that the results, and especially the peak stress value, depend on the number of rings; when the number of annulus rings decreased the stress value of the peak decreased too and it was not very clear where this peak was located in the sample (Fig. 8.2). Due to this sensitivity, the maximum number of ring compatible with the grain discretization was chosen.

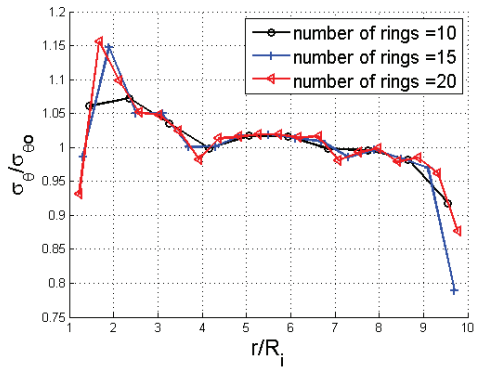

Fig. 8.2. Numerical normalized radial stress distribution using different number of rings

8.2.2. Validation with the analytical solution

The stress distributions resulting from the simulation can be directly compared with the stress distribution predicted by the Risnes et al. (1982) solution (see Section 3.6) for the same stress conditions, adjusting the material parameters entering the analytical solution to obtain a good fit.

First of all, the sensitivity of the stress distribution to each analytical parameter was established, so they could be adjusted to fit the numerical result easier. The parameters that were found best to fit the numerical result were then compared with parameters known from sandstones. Alvarado (2007) studied two sandstones in the laboratory (Castlegate and Saltwash). The friction angle of both sandstones was around 10-30 MPa,

and the friction angle was around 30°. The parameter alpha was taken as the usual for a sandstone (1).

The normalized averaged radial and circumferential effective stresses for different radial distances from the borehole are presented in Fig. 8.3. The effective stresses are normalized by the effective stress at the outer boundary, and the radial distance is normalized by the inner radius. The peak of the circumferential effective stress defines the limit between the created plastic zone and the elastic zone. The limit in this case lies between 8 and 11 mm.

Also shown in Fig. 8.3, radial and circumferential effective stresses are obtained with the analytical solution (Risnes et al., 1982). These are obtained with the following set of parameters: S_o = 20 MPa, $\varphi = 30^{\circ}$ ($\phi = 60^{\circ}$), $\nu = 0.44$. A value of permeability is not necessary here because there is no fluid flow in the analytical solution.

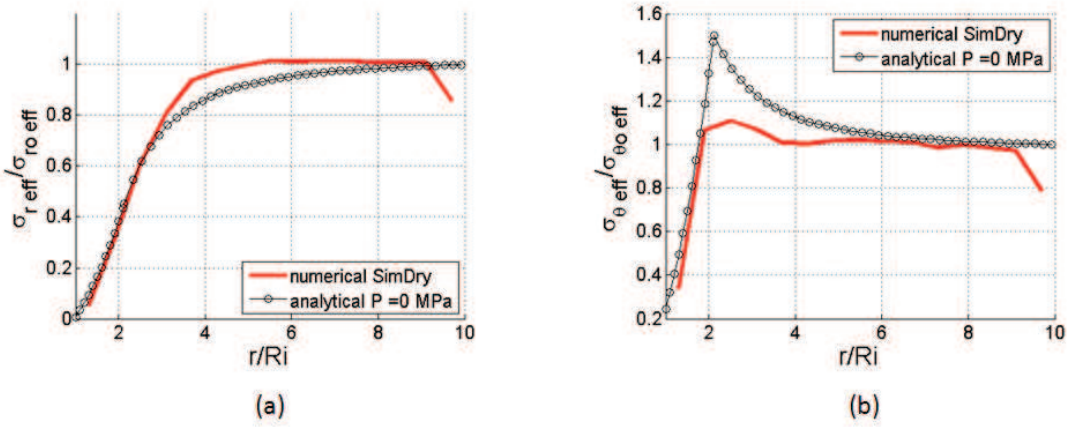

Fig. 8.3. (a) Normalized radial effective stress, and (b) normalized circumferential effective stress at the end of SimDry simulation. The results are compared with the analytical solution (Risnes et al., 1982). $\sigma_{zo} = 300000$kPa.

In Fig. 8.3 there is a decrease in the effective stress near the outer boundary. This is due to the effect of the rigid cylindrical boundary on the discrete packing that decreases the porosity and the contacts between particles (Marketos & Bolton, 2010). This effect also appears in later figures.

There is an overall good match between the numerical and the analytical solutions for the radial and circumferential effective stresses distributions. However, peak values of the circumferential effective stress differ, with the numerical one being far smaller. Several reasons might explain this difference. First, even though the analytical solution is a quasi-static process, the numerical solution is a dynamic process where stress equilibrium is only reached at the end. This could lead to some differences in the results between the analytical and the numerical solutions. Moreover, particles in the numerical model can be produced: this is not a feature of the analytical model and is accompanied by stress relaxation. Another reason for this difference lies in the smoothing effect that the averaging procedure imposes on the numerical stress. The averaging smoothing effect is compounded with the asymmetric response of the DEM specimen. To illustrate that effect the specimen geometry is divided in 4 regions (Fig. 8.4) in order to understand how the asymmetry is affecting the equivalent continuum effective stresses result.

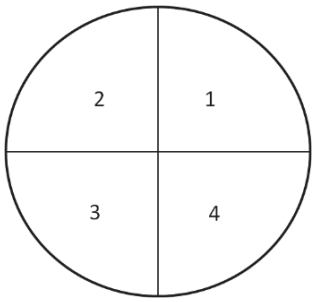

Fig. 8.4. xy plane. The geometry is divided in 4 regions: region 1 (x>0 and y>0), region 2 (x<0 and y>0), region 3 (x<0 and y<0) and region 4 (x>0 and y>0).

In Fig. 8.5 it is shown that the average stress distribution is very different depending on the region of the sample that is considered. In particular there is one region (Fig. 8.5a) where the stress peak at the plastic limit is almost erased. This, as will be shown below, corresponds to the region in which more sand is produced.

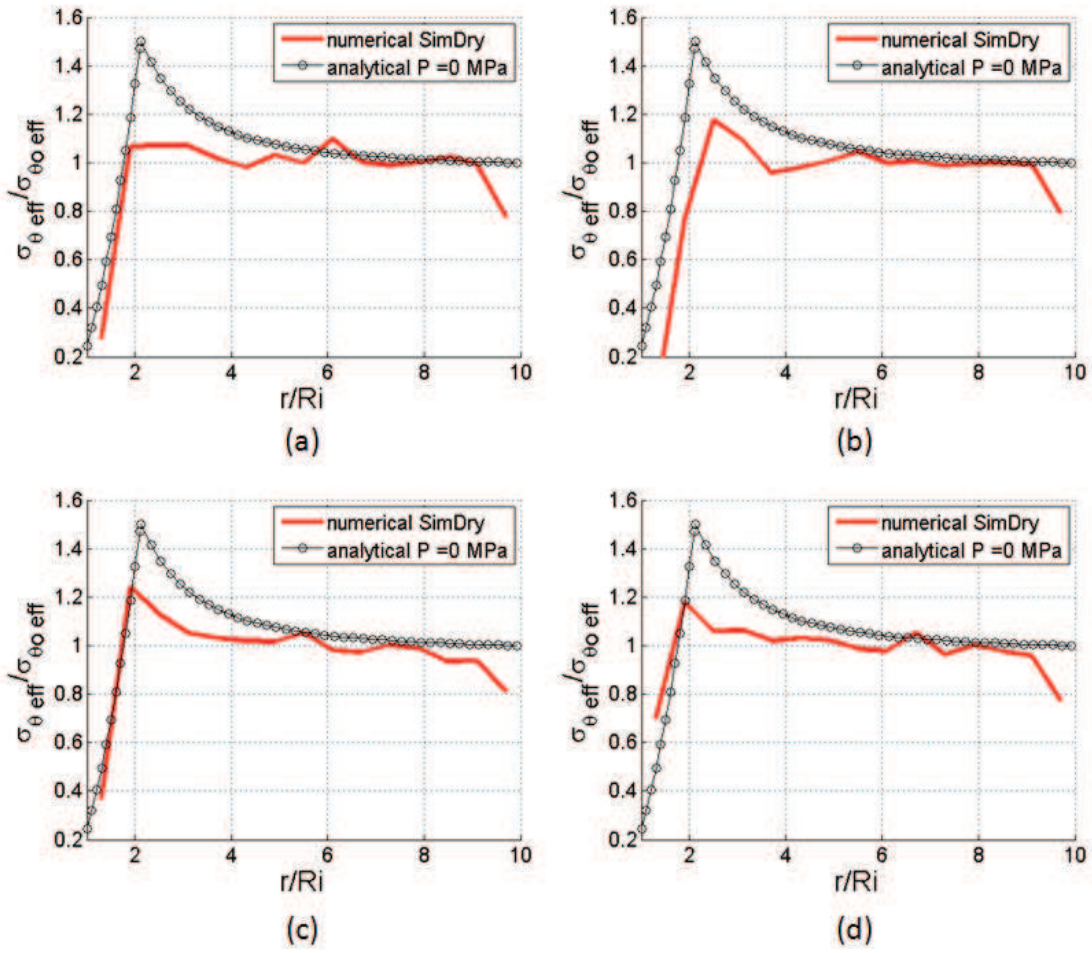

Fig. 8.5. Analytical solution and normalized circumferential effective stresses at the end of SimDry in (a) region 1, (b) region 2, (c) region 3, and (d) region 4.

8.2.3. Sand production

The sand production evolution during the simulation without fluid flow is presented in Fig. 8.6. The sand production starts at the beginning of the simulation and it has a very high sand production rate. After 0.01 s it stabilizes. Production is continuous and not in sudden steps or burst. In typical cases where production is driven by a radial flow, sand is produced in cluster or blocks of grains (Zhou et al., 2011); on the other hand, when no flow is applied, the sand is produced grain by grain and produced continuously. The observation of smooth sand production curve in this case is in agreement with Zhou et al. (2011) for their simulations of “pressure sanding” i.e. cases were sanding was induced with no-flow initial conditions.

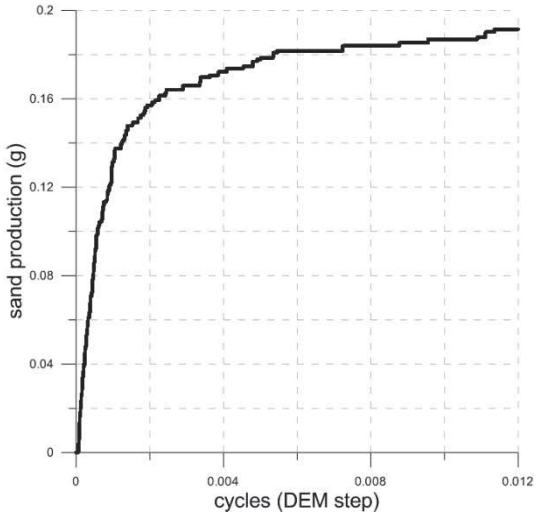

Fig. 8.6. Sand production evolution for SimDry.

8.2.4. Micro-scale results

As shown in Section 8.2.2, there is an asymmetry in the pattern of effective stress relaxation. To understand the reason for this asymmetry, the normal parallel-bond forces present at the initial state are illustrated in Fig. 8.7. Fig. 8.7 shows an important asymmetry for the normal parallel-bonds forces at initial state; there is a region where forces are mostly compressive (positive) and another region where forces are tensile (negative). Where bond forces are initially tensile bonds are easier to break than bonds which are in regions where forces are compressive.

The reason behind this microscopic asymmetry at the beginning of the simulation is not clear. One of the reasons may be that the height of the sample is not big enough (5 particles) to create a real homogeneous sample. Moreover, even though the mean stress on the walls is equal to each other, the stress between particles inside the sample in different regions is not considered and calculated before the simulations to compensate differences between regions.

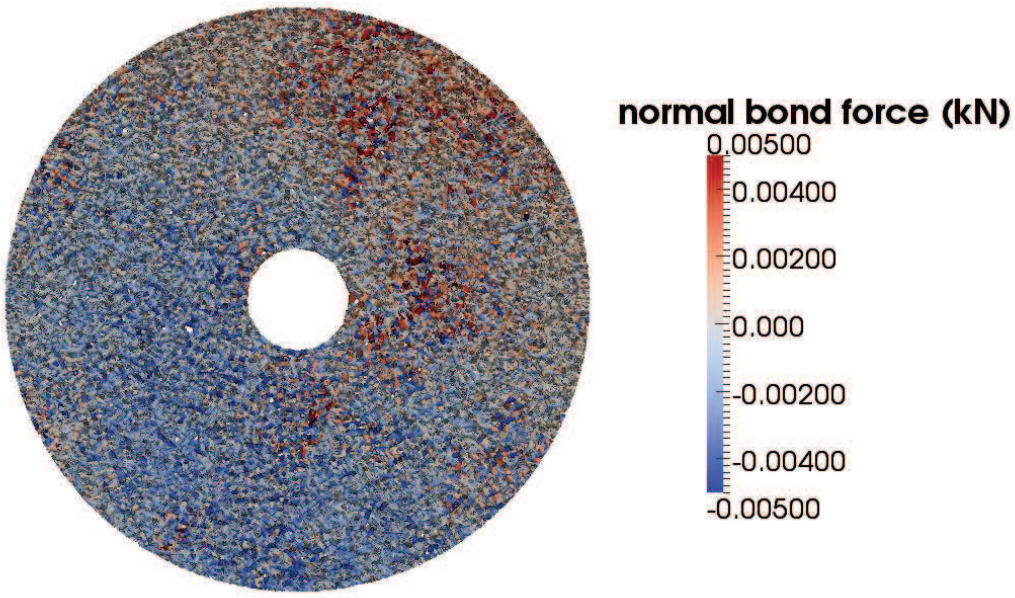

Fig. 8.7. xy plane. Normal bond forces at the initial state. The outer radius represented is 30 mm.

A micro-level illustration of the heterogeneity is shown in a plot of contact density. The density of contacts at the initial and the final states are presented in Fig. 8.8. Here and in several subsequent plots the evaluation zones are made to coincide (in plain view) with the CFD zones (used for the fluid in Section 8.3). Sand production near the hole results in a reduction of contact density. This reduction is more marked in the upper left quarter.

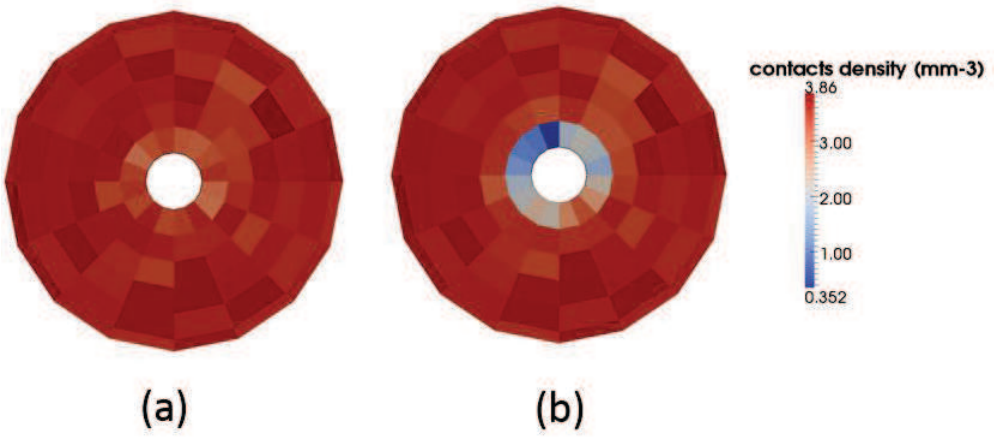

Fig. 8.8. xy plane. Contact density (number of contact forces per cell volume) (a) at the initial state and (b) at the end of SimDry. The outer radius represented is 30 mm.

A complementary view of the same aspect is given by the density of broken bonds at the end of simulation, presented in Fig. 8.9. The bond failure modes (normal or shear bond failure) are also presented. The region where most bonds are broken, next to the hole, is the same as the region where most contacts are lost. Moreover, the majority of the broken bonds failed in the normal direction (tension).

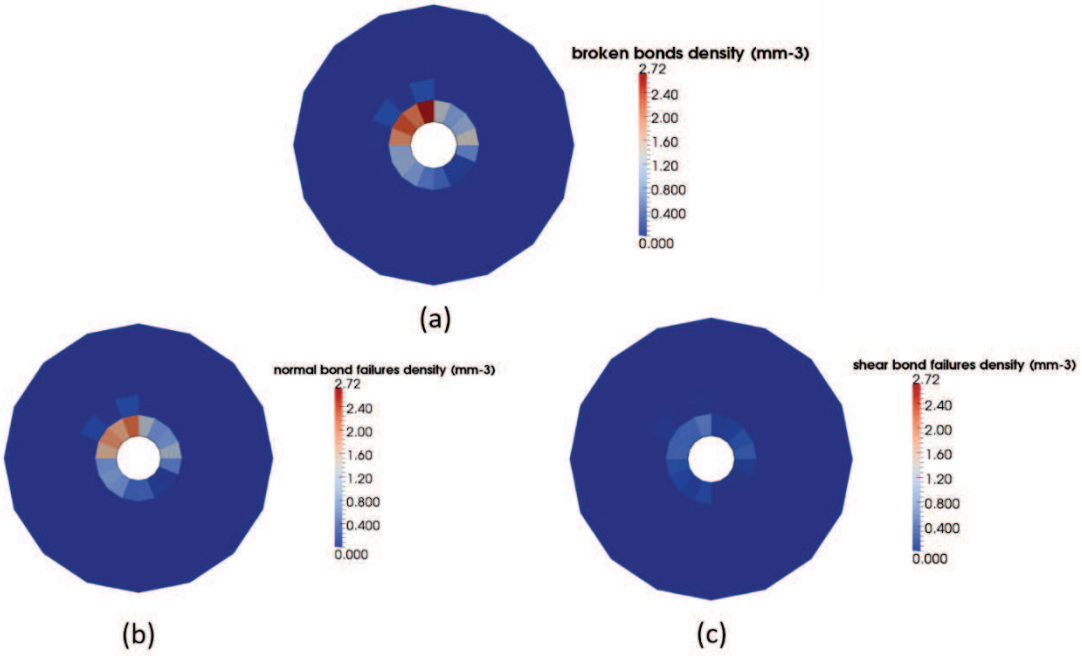

Fig. 8.9. xy plane. (a) Broken bonds density (number of broken bonds per cell volume) (b) normal bond failures density (number of normal bond failures per cell volume) and (c) shear bond failures density (number of shear bond failures per cell volume) at the end of SimDry. The outer radius represented is 30 mm.

Radial and circumferential particle effective stresses at the initial and end states are shown in Fig. 8.10. The circumferential effective stresses decrease in the region where contacts break. The same asymmetric distribution of the breakage is apparent from the variation of stresses.

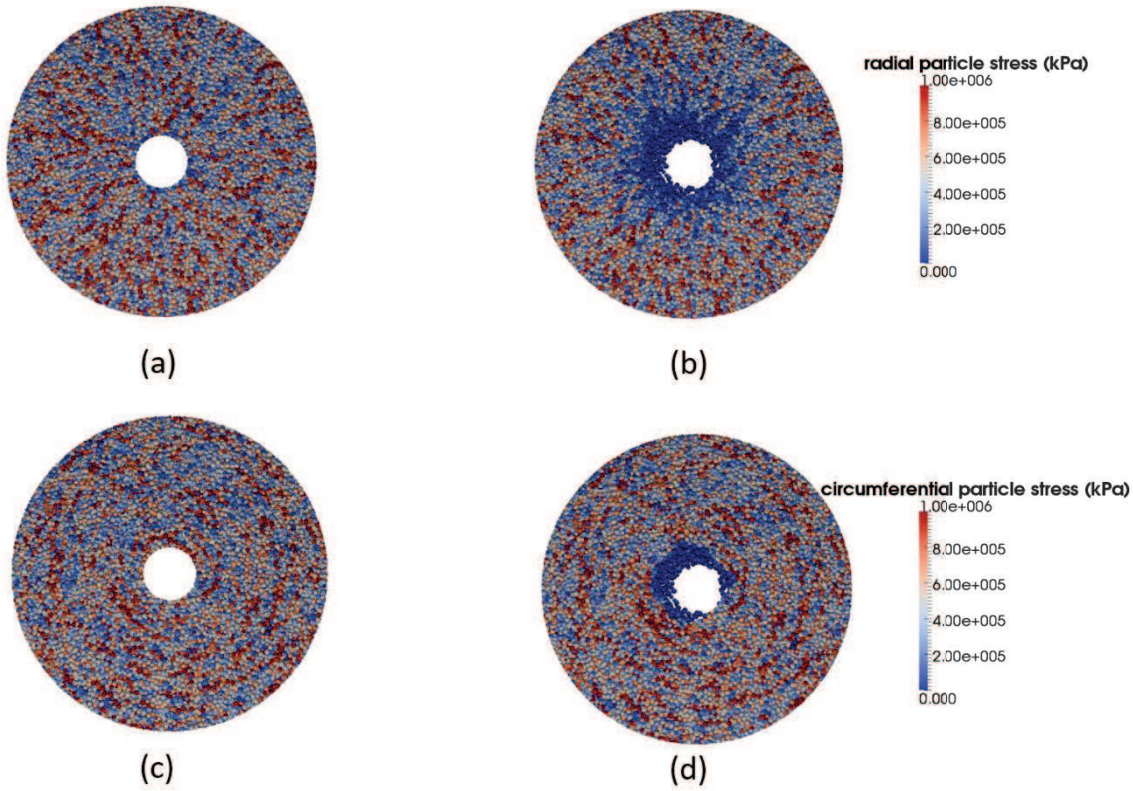

Fig. 8.10. xy plane. Particle radial effective stresses (a) at the initial state and (b) at the end of SimDry; particle circumferential effective stresses (c) at the initial state, and (d) at the end of SimDry. The outer radius represented is 30 mm.

8.3. Perforation under hydrostatic conditions

8.3.1. Fluid model

The CFD mesh is hexahedral (Fig. 8.11). The CCFD add-on assumes that the local porosity is evenly distributed within one cell. The chosen number of divisions was: 10 radial divisions, 16 circumferential divisions and 1 vertical division. The mesh was chosen also so that the computed flow was not strongly affected by mesh properties. It was observed that the number of vertical divisions did not affect fluid flow. On the other hand, a minimum number of 16 circumferential divisions was necessary to reproduce accurately analytical solutions of radial flow towards a cylindrical cavity.

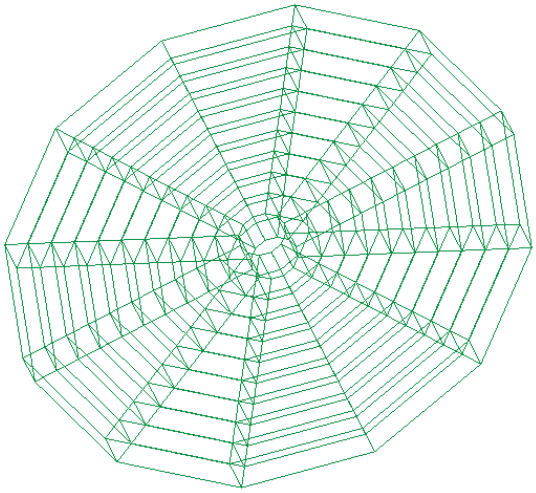

Fig. 8.11. CFD mesh of the model

The boundary conditions for the fluid on the bottom and top boundaries of the cylinder are the natural boundary conditions (slip condition), with no vertical fluid velocity. If flow was imposed in the model the velocity would be set at the outer cylindrical surface (from outside to inside the cylinder) and the pressure on the inner surface is set to 0 (natural outflow condition). For the hydrostatic simulations here presented the same pressure value is imposed at every boundary.

The coupling interval should be small enough to resolve the desired coupling behavior. Coupling information should be exchanged several times as a particle moves across a fluid element. This condition is satisfied when the following inequality is met:

$$\frac{\Delta x_{cfd}}{|v|t_c} > 3 \qquad \text{Eq. 8.1}$$

where t_c is the coupling interval and v the particles velocity. (Itasca, 2008b). In practice, the DEM time step is often smaller than the CFD time step. Therefore, several cycles of DEM are needed to meet one CFD step. The coupling interval t_c chosen in this model is 10^{-5} s.

8.3.2. DEM and fluid parameters: simulation program

The DEM sample is the same as the one generated in Section 8.2.1 (Table 8.1 and Table 8.2). The fluid parameters used are shown in Table 8.3.

Table 8.3. Fluid parameters

Fluid system parameters	
$\rho_f \times 10^3$, kg·m^{-3}	1.00
μ_f, kPa·s	1×10^{-6}
Fluid cells	10 radial, 16 circumferential and 1 vertical

The simulation program is presented in Table 8.4. All the simulations had no fluid flow initial conditions. SimDry is the simulation performed in Section 8.2 with no fluid. Two simulations (Sim50 and Sim150) are performed at varying levels of pore pressure (50 and 150 MPa) and, since initial total stress is maintained at the same level, varying effective initial stress. An additional simulation (Sim300-50) was performed with an effective radial stress of 300 MPa and a pore pressure of 50 MPa. This simulation was carried out to understand if the results are due to the change of the effective stress or to the presence of the fluid.

It should be noticed that the DEM walls apply effective (intergranular) stresses and not total stresses. Fluid pressures, on the other hand, are applied as separate boundary conditions on the CFD grid, but they are not directly entered into the DEM computation. Therefore, the comparison with the predictions of the analytical solution requires an indirect procedure. Using the mechanical parameters adjusted in the dry case, and changing the fluid parameters (i.e. fluid flow and pore pressures), the Risnes et al. (1982) solution is evaluated at the higher pore pressures (50 and 150 MPa). The higher pore pressures were applied as boundary conditions of the internal and external radial

boundaries of the CFD grid. Relevant radial effective stress values, σ'_{ro} at the external radial wall for the DEM simulation are elastic values, obtained from the adjusted Poisson ratio, the vertical total stress and the relevant value of pore pressure through

$$\sigma'_{ro} = \frac{\nu}{1-\nu}\sigma_{zo} + \frac{1-2\nu}{1-\nu}\alpha P_o - \alpha P_o \qquad \text{Eq. 8.2}$$

These values were applied in the DEM simulation as targets for the servo control of the external radial wall. At the internal radial wall the effective stress was zero in all cases and, therefore the internal radial wall was erased at the beginning of the simulation.

Table 8.4. Simulation program for hydrostatic initial conditions

	Fluid	σ'_{ro} **(MPa)**	P_o **(MPa)**
SimDry	No	300	0
Sim50	Yes	200	50
Sim150	Yes	120	150
Sim300-50	Yes	300	50

All the simulations were run until a steady state was reached, as observed when the average stress for each ring became constant in time. Particles that moved inside the hole (the entire particle was within the inner radius) during the simulation were automatically removed and considered produced. Note that even though the fluid has no flow as initial condition, it may flow later depending on the dynamic interaction between the fluid and the particles.

8.3.3. Simulation results

Fig. 8.12 compares the circumferential effective stresses obtained in the different numerical simulations with those predicted by the Risnes et al. (1982) solution. Introducing fluid in the numerical solution has an effect similar to that which was observed in the analytical solution: the plastic zone radius is reduced in size and larger effective stresses are sustained. However, in the numerical results the stress peaks are always less sharp. A likely reason for that difference is the averaging of inhomogeneity on the numerical solution that was discussed before.

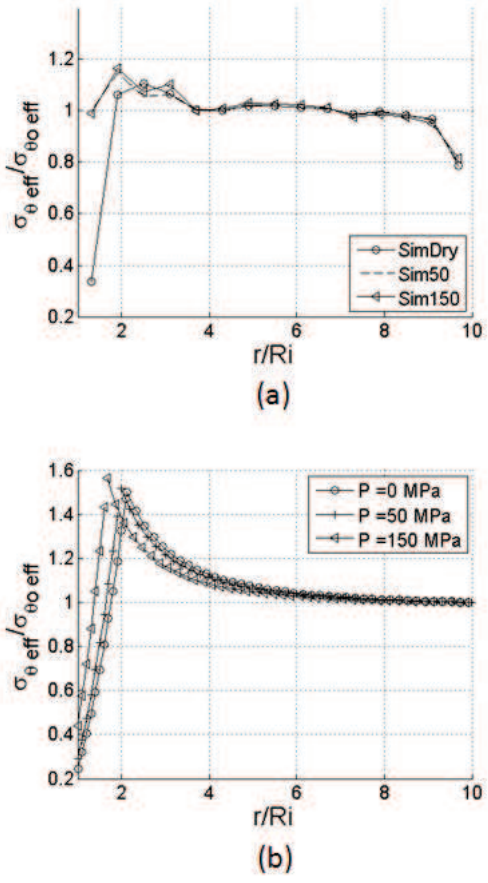

Fig. 8.12. Normalized circumferential effective stresses (a) at the end of SimDry, Sim50 and Sim150 and (b) the analytical solutions for pore pressures of 0 MPa (P = 0), 50 MPa (P = 50) and 150 MPa (P = 150).

It is also clear that the slight difference between the two levels of fluid pressure that appears in the analytical solution is not visible in the numerical results. This is unsurprising, since the fluid force acting on the DEM particles is not sensitive to the absolute level of fluid pressure, but only to pressure gradients and velocity differences (Eq. 6.29 and Eq. 6.30). In the analytical solution, when the Biot parameter α is 1, the effective stresses result is also not affected by the fluid pressure value. The differences that can be observed in the analytical solution are due to the different effective stresses at the initial state. These differences are not reflected in the numerical solution because in the numerical simulations the fluid acts as a damping force that slows the particles and make them reach the equilibrium before the effective stress values that they are supposed to achieve without the fluid drag force. This effect is further clarified later.

The stabilizing presence of fluid is explored in detail by comparing results for Sim50 (results for Sim150 are the same) with results from the dry simulation. The contact densities are shown in Fig. 8.13, showing a larger reduction next to the cavity for the dry case. There are also less broken contacts in the simulation with fluid. Particle radial and circumferential effective stresses are presented in Fig. 8.14 for the simulations with fluid showing a much reduced relaxation zone. Finally, the void ratio next to the hole at the end of SimDry is larger than the one of Sim50 (Fig. 8.15).

The reason why the plastic region in the dry case is bigger than the plastic region in the simulation with water follows from the drag force (Eq. 6.30). For simulations with fluid, when the fluid flow velocity is higher than the particle velocity, the drag force is positive and increases the particle velocity. However, when the fluid velocity is lower than the particle velocity (as is the case here, where it is initially 0), the drag force becomes negative, and the fluid flow decreases the initial particle velocity. The drag force acts thus as a stabilizing force, slowing (decelerating) the particles and accelerating the equilibrium process. This effect does not appear in the analytical solution because in the analytical solution this local transients in the fluid flow are not contemplated.

The damping effect of fluid presence in particle motion has a counterpart in the fluid motion itself. Hydrostatic initial conditions imply no fluid flow. However, at the end of the simulation the fluid flow velocity is not 0. As explained previously, the drag force

acts in both directions (the fluid acts on the particles and the particles act on the fluid). When contacts are broken particles move to the hole and they apply a body force to the fluid. This body force is a volumetric average of all the drag forces (Eq. 6.30) of each particle.

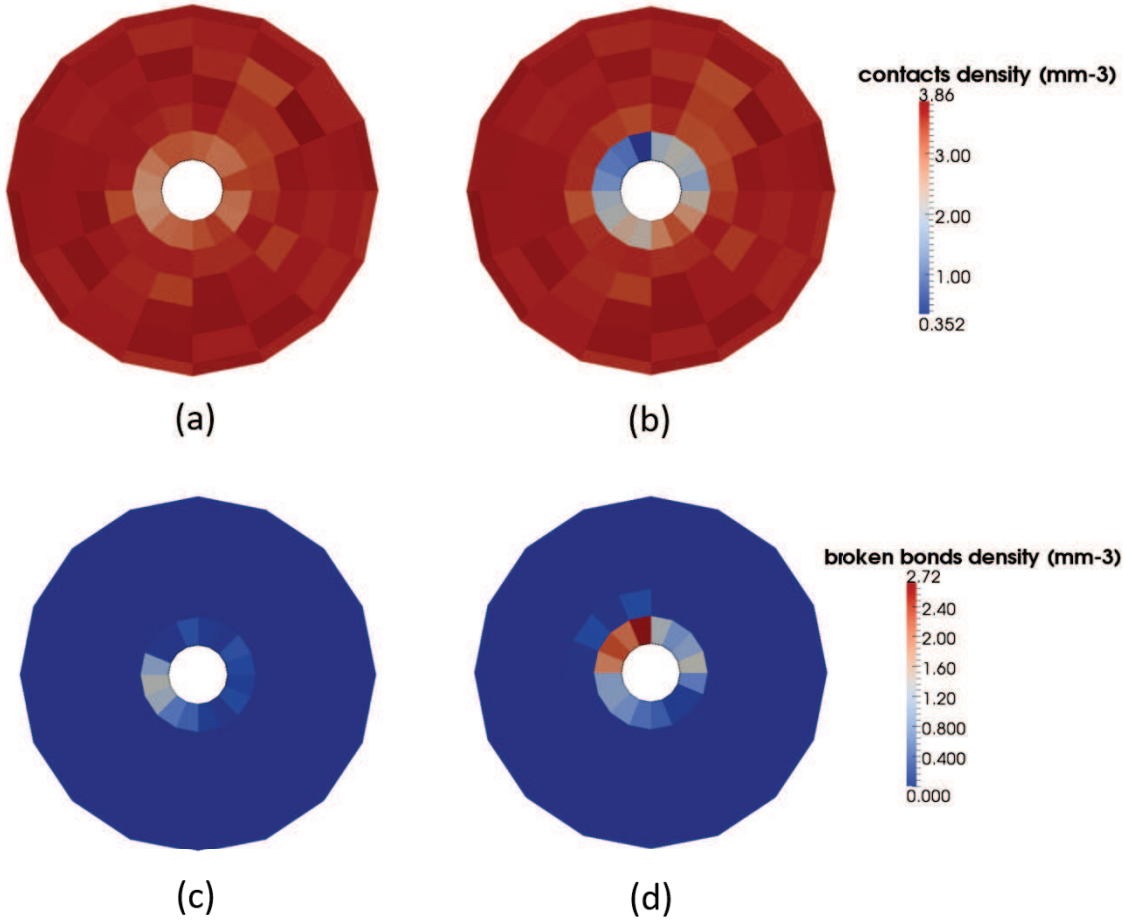

Fig. 8.13. xy plane. Contact density (number of contacts per cell volume) for (a) Sim50 and (b) SimDry. Broken bonds density (number of contacts per cell volume) for (c) Sim50 and (d) SimDry. The outer radius represented is 30 mm.

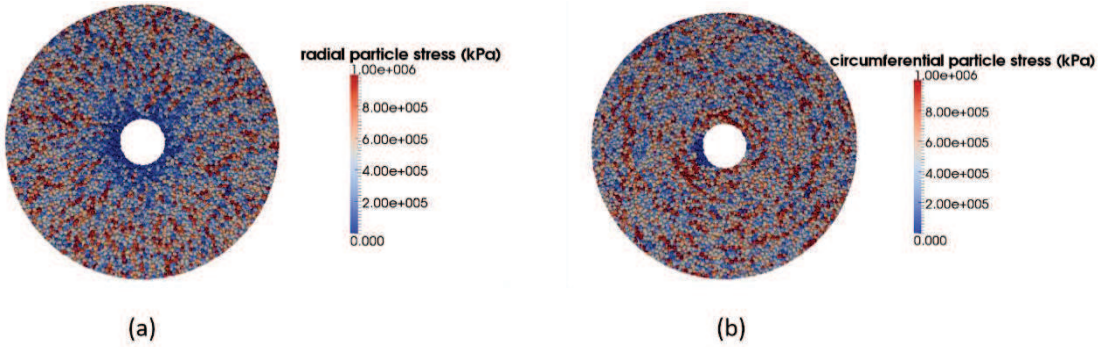

Fig. 8.14. xy plane. (a) Particle radial effective stresses, (b) circumferential effective stresses for Sim50. The outer radius represented is 30 mm.

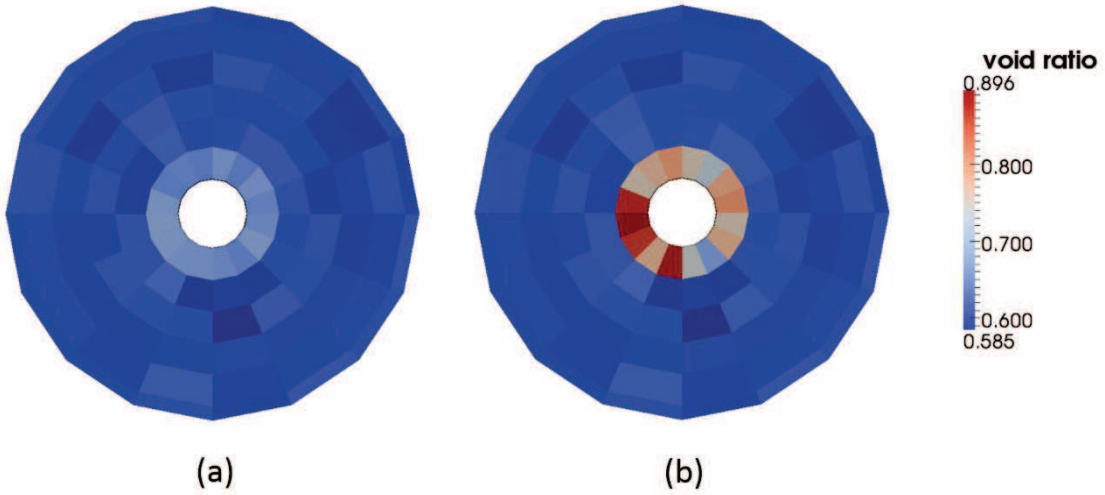

Fig. 8.15. xy plane. (a) Void ratio for Sim50, and (b) void ratio for SimDry. The outer radius represented is 30 mm.

Fig. 8.16 presents the body force due to particle motion in each cell, the fluid flow velocity in each fluid cell and the particle velocity magnitude in each cell at two different times: at the beginning of the simulation –when the inner wall has just being retired- and almost at the end of the simulation. As shown, fluid flow velocity, body force and particles speed have their largest values in the same region where stresses are lower and contacts are broken. At the beginning, particles start moving and transfer body force to the fluid. At the end, particles move slower and the body force reduces, reaching an equilibrium.

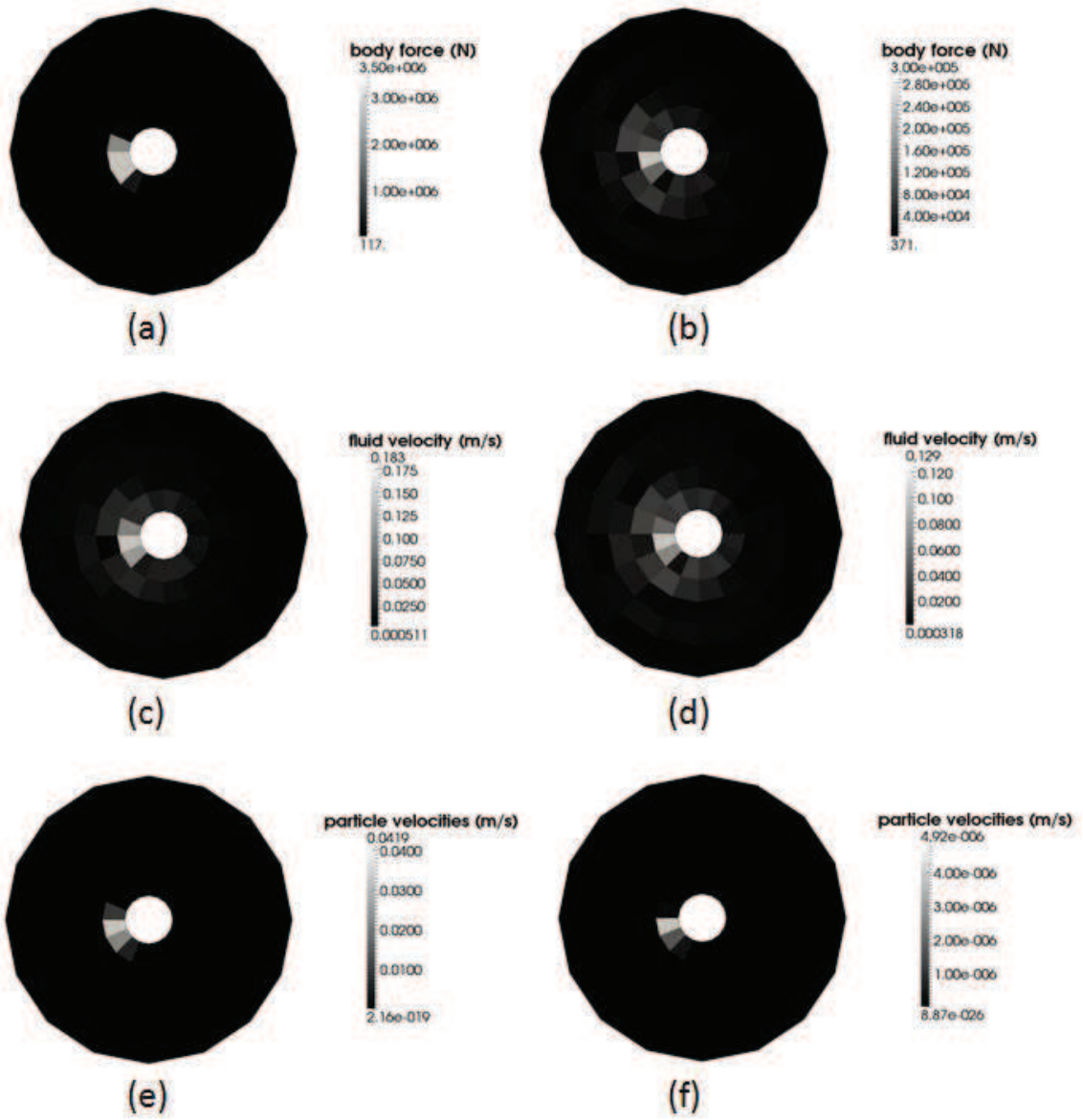

Fig. 8.16. xy plane. Body force (a) at the beginning of Sim50, and (b) at the end of Sim50; fluid velocity (c) at the beginning of Sim50 and (d) at the end of Sim50; and particle velocities (e) at the beginning of Sim50, and (f) at the end of Sim50. The outer radius represented is 30 mm.

In principle, the results presented above (namely the smaller size of the plastic region) may not be due to the presence of the fluid, but rather to an effect of the decrease of the boundary radial effective stress when compared with the dry simulation. In order to understand whether the results are due to the presence of the fluid or to the change in the effective stress, a simulation with an effective radial stress of 300 MPa and a pore pressure of 50 MPa was performed and compared with the ones with an effective stress of 300 MPa and no fluid applied. If the reason why of the decrease of the plastic region in the simulations with an effective stress of 200 MPa and 120 MPa and fluid applied

was only the decrease of the effective stress and not the presence of the fluid, the results of the new simulation would not be the same The results are compared with the analytical solution (Fig. 8.17). It can be observed that the same decrease of the plastic region when the fluid flow is applied is also presented in this simulation, therefore the decrease of the plastic region is not because of the lower effective stress, but because of the presence of the fluid. In this simulation no sand was produced, as it was not produced in the previous ones.

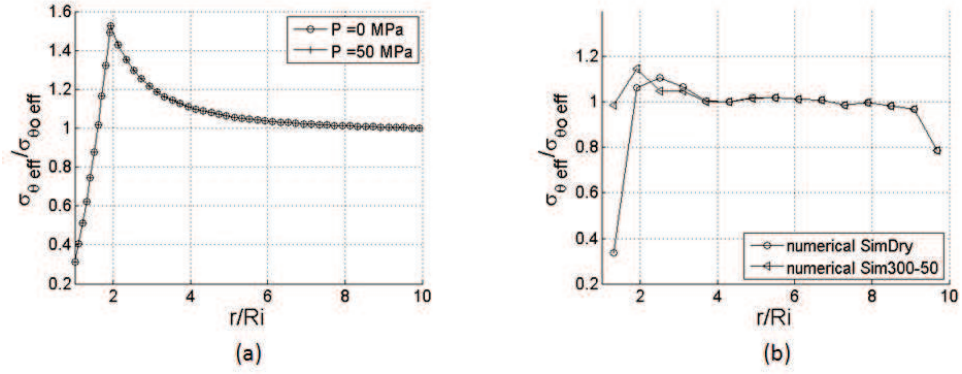

Fig. 8.17. Normalized circumferential effective stress for SimDry and Sim300-50 simulations. (a) Analytical and (b) numerical solutions.

8.4. Perforation under radial flow

Two simulations with fluid flow imposed at the outer boundary (Fig. 8.18) are now presented (Table 8.5). At the inner boundary the fluid pressure is set to 0. The fluid boundary conditions are imposed simultaneously to the inner removal after the DEM specimen is formed. The DEM parameters are those presented in Table 8.1 and Table 8.2 and the fluid parameters those in Table 8.3. The fluid velocity at the inner boundary is calculated during the simulation and is presented in Table 8.5. Note that this velocity at the inner boundary is not constant during the simulation because porosity around the hole changes when particles move into the hole. Only when erosion stops fluid velocity at the inner boundary becomes constant.

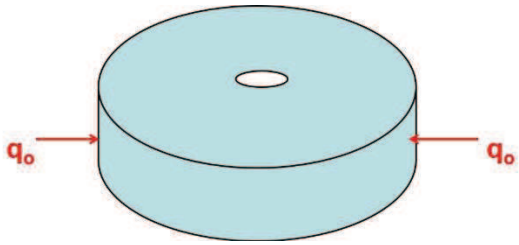

Fig. 8.18. Fluid boundary condition at the outer boundary

Table 8.5. Simulation program for fluid flow initial conditions

Simulation name	**Velocity at the inner boundary (m/s)**	σ'_{ro} **(MPa)**	**Po (MPa)**
SimV1	1.7	200	50
SimV2	7.1	200	50

Broken contacts around the hole are represented in Fig. 8.19. It can be observed that when the fluid velocity increases the plastic region (the region where the contacts are broken) increases. Moreover, when the fluid velocity is high all the sample plastifies (the plastic region reaches the outer boundary). The asymmetry is also observed for the simulation SimV1, but not for SimV2. The reason why the asymmetry does not appear in the simulation with higher fluid velocity could be that the fluid drag force is high enough to break easily all bonds.

Fig. 8.21 shows the circumferential stress during time for simulation SimV1. It is shown that the steady state is reached and the stresses around the hole do not change during time.

Three types of behaviors can be interpreted from the results. First of all, the type A response is the one presented for hydrostatic initial conditions (Sim50 and Sim150); in this case sand is not produced and the plastic region is smaller than the one in the simulation with no fluid (SimDry). Type B response is the result of a simulation with fluid flow conditions but that reaches a steady state at the end (SimV1), as it is observed in Fig. 8.21; in this simulations, the plastic region is bigger than the one in the simulation with no fluid and, even though a steady state is reached (Fig. 8.21), the sand production

did not decrease and it stabilizes giving a sand production rate constant during time (Fig. 8.21). Finally, a type C (SimV2) response is the result of a high velocity, where the steady state is never reached and all the sample plastifies at the end of the simulation. Sand production for all simulations is presented in Fig. 8.22. In type B and type C simulations the production starts later than in the no flow simulation but the rate is higher than the no flow simulation.

(a) (b)

Fig. 8.19. xy plane. Contact forces between particles for (a) SimV1 final state and (b) SimV2 intermediate state. Both are represented at the same time since the removal of the inner wall. The outer radius represented is 20 mm.Circumferential stress distribution for these simulations is presented in Fig. 8.20. The peak in SimV1 is not observed; the reason could be the great asymmetry presented in that case. A steady state is not represented for SimV2 because such state is never reached.

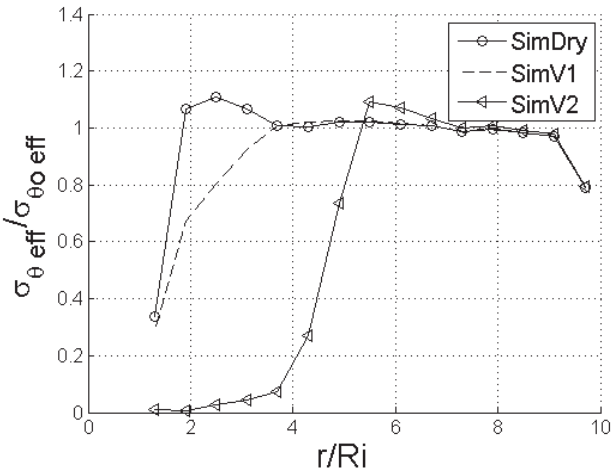

Fig. 8.20. Normalized circumferential effective stress at the end of SimDry and SimV1 simulations and at an intermediate state of SimV2.

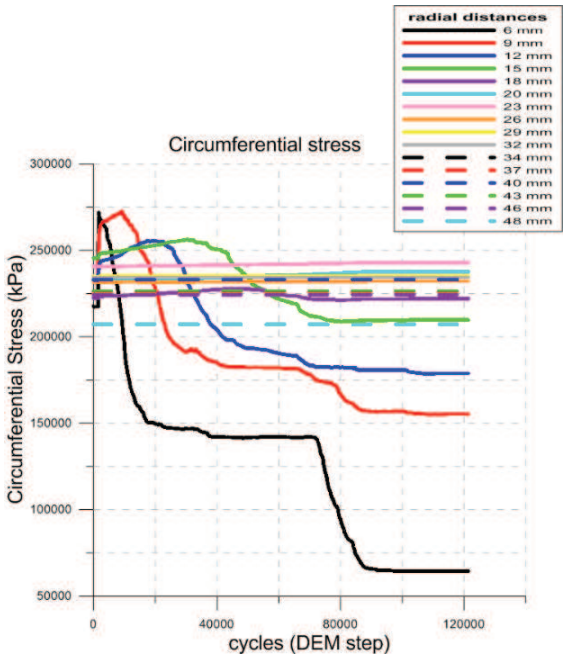

Fig. 8.21. Circumferential stress evolution for different radial distances from the removed inner boundary of SimV1

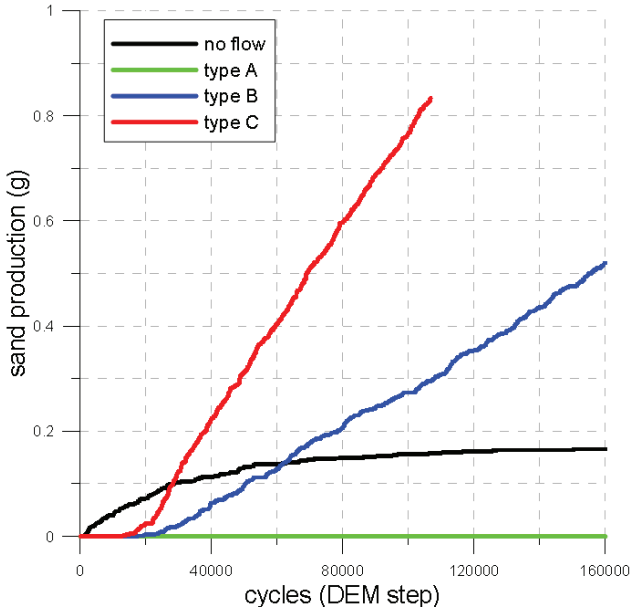

Fig. 8.22. Sand production rates for simulations SimDry (no flow), Sim50 and Sim150 (type A), SimV1 (type B) and SimV2 (type C).

8.5. Effect of local damping

To understand the effect of the local damping a series of simulations with different damping values are performed (Table 8.6). Simulations are carried out without fluid and with an imposed fluid flow velocity.

Table 8.6. Simulation program to study the sensibility to damping

Simulation name	Fluid flow	Inner velocity (m/s)	Local damping (δ)
Noflow0	No	-	0.0
Noflow3	No	-	0.3
Noflow5	No	-	0.5
Noflow9	No	-	0.9
Fluid0	Yes	0.35	0.0
Fluid3	Yes	0.35	0.3
Fluid9	Yes	0.35	0.9

The normalised averaged circumferential stresses for the simulations with no flow are presented in Fig. 8.23. The stresses are normalized by the stress on the outer boundary. The plastic region increases and the circumferential stress value in the peak decreases when the local damping decreases. When the local damping is set to 0, the steady state is never reached and the stresses decrease to zero.

Contact forces between particles for simulations with no flow conditions are also represented in Fig. 8.24. It can be observed that around the wellbore contacts break and that the effect of local damping is to reduce the number of broken contacts.

Fig. 8.25 and Fig. 8.26 show the stresses and the contact forces with different local damping values when the fluid velocity at the inner boundary is set to 0.35 m/s. Damping has much less effect than in the dry case. A likely cause is that motion of broken particles towards the hole is already dampened by the fluid presence.

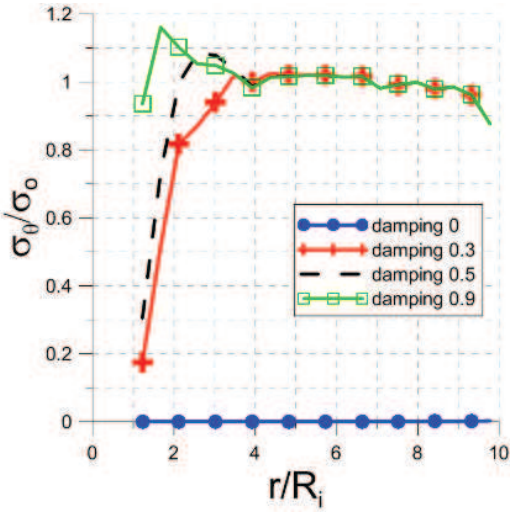

Fig. 8.23. Normalized circumferential stresses at the end of the simulations with no fluid flow for different damping values.

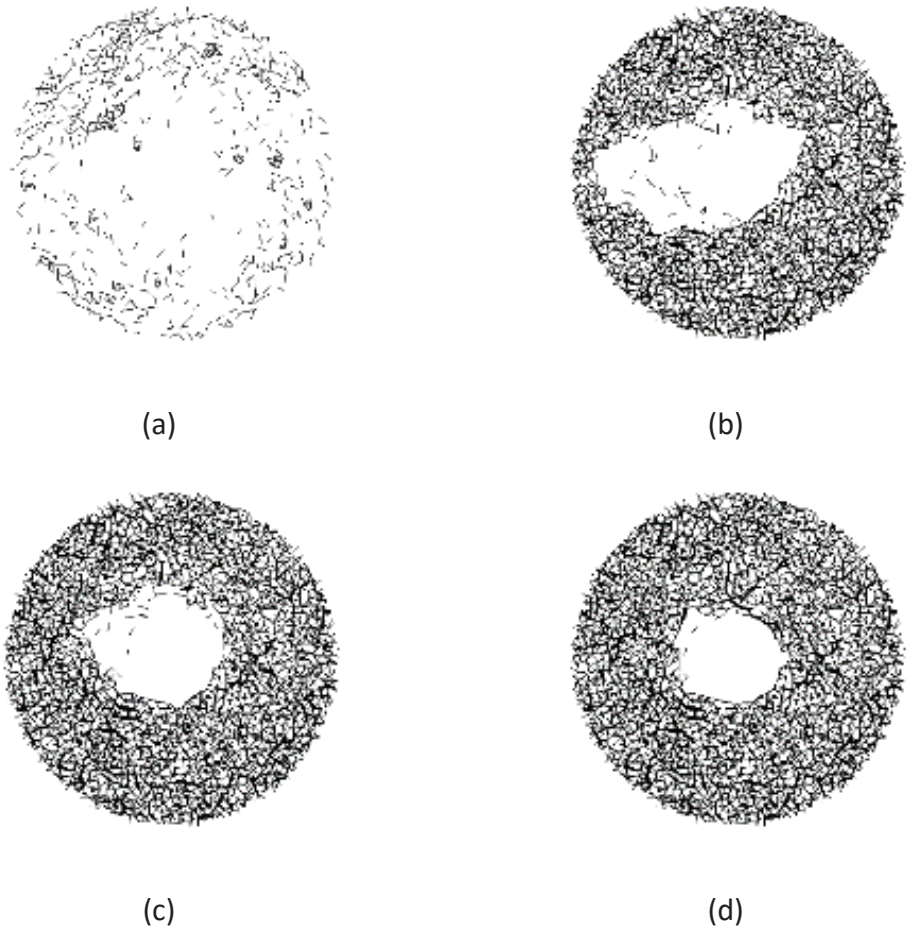

Fig. 8.24. xy plane at the medium height (2.5 mm). Contact forces for no fluid flow simulations with different damping values: (a) 0, (b) 0.3, (c) 0.5, and (d) 0.9. The outer radius represented is 20 mm.

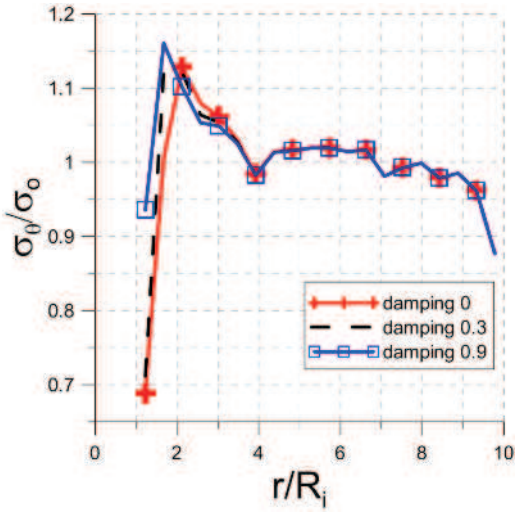

Fig. 8.25. Normalized circumferential stresses at the end with u_i = 0.35 m/s for different local damping values.

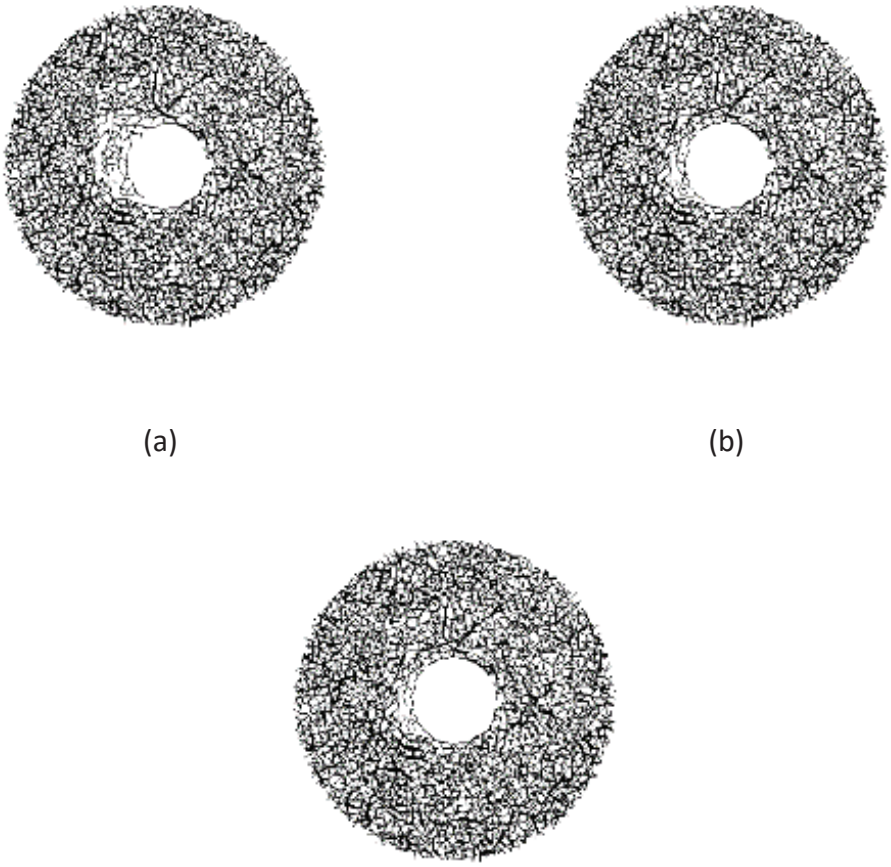

Fig. 8.26. xy plane. Medium height (2.5 mm). Contact forces for ui = 0.35 m/s with different local damping values: (a) 0, (b) 0.3, (c) 0.9. The outer radius represented is 20 mm.

The results indicate that local damping has an important effect in the results, especially when no fluid flow is applied. When a fluid flow is applied, local damping has much less effect; a likely cause is that particle motion is already damped by the fluid (see Section 8.3.3). Local damping decreases the number of broken contacts around the wellbore and decreases the plastic region.

The observations made in this analysis have two significant corollaries

1. Since local damping effects are redundant when fluid coupling is already present, all sand production simulations performed from now onwards (Chapter 9) are carried out without damping.

2. The observed mechanical equivalence between the effect of local damping and particle – fluid interaction may be exploited in other DEM-based simulations. Local damping may be used as a computationally advantageous substitute for the direct inclusion of a hydrostatic fluid effect via CFD coupling. This may offer a novel approach to calibrate local damping for a given problem, as the value that produces the same effect as direct inclusion of a CFD coupling.

8.6. Comparison with Cheung results

Cheung (2010) performed simulations using a simplification of the fluid-particle interaction. Only the effect of the fluid flow in particles was considered but not the opposite, (i.e. the effect of the particles on the fluid flow).

In her work the drag force used and the drag coefficient followed Eq. 6.16, Eq. 6.17, Eq. 6.18, Eq. 6.12, and Eq. 6.13. The fluid flow was steady, not variable, and only radial (from the outer boundary to the inner boundary) and the circumferential direction was not permitted (it means that the possible effect of the circumferential flow near the cavity was not taken into account). The fluid scheme of Cheung's model is represented in Fig. 8.27.

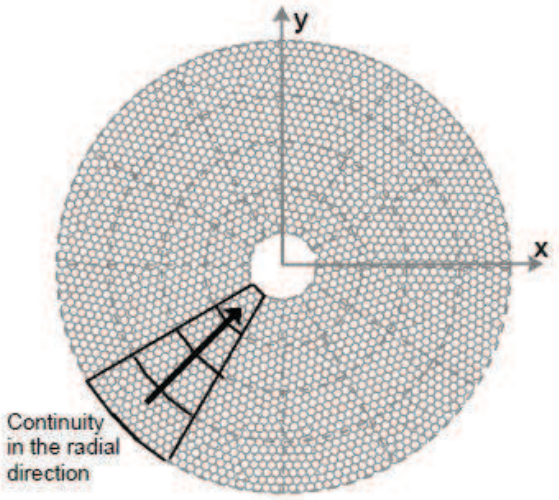

Fig. 8.27. Simplified fluid modelling method assuming radial flow only (Cheung, 2010)

The effect of the fluid in Cheung's results (Fig. 8.28) is similar than the Risnes solution (Fig. 3.19), when the fluid flow is applied, the plastic region increases and the stress at the boundary between the plastic and the elastic region decreases.

Cheung (2010) also studied the effect of the local damping value in the DEM simulations (Fig. 8.29) and the result was similar as the one obtained in Section 8.5. As the damping increased, the plastic region decreased. However, Cheung did not compare the effect of the damping with and without fluid.

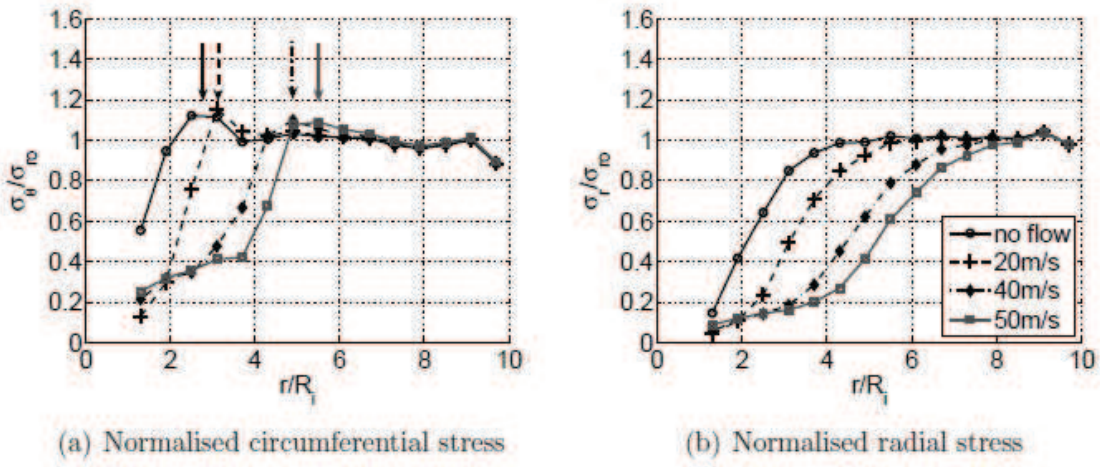

Fig. 8.28. DEM results with different velocities at the inner boundary (Cheung, 2010)

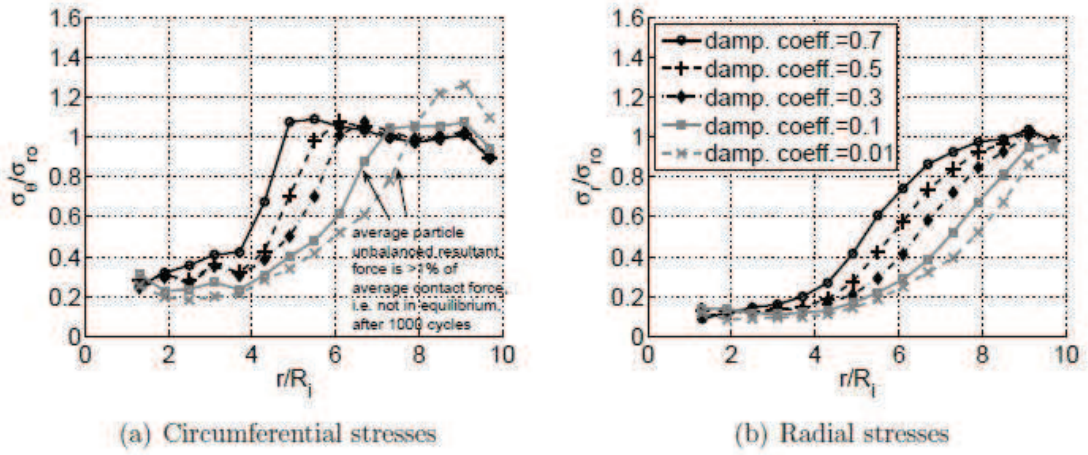

Fig. 8.29. DEM results with fluid flow and different damping values (Cheung, 2010).

In both works the vertical initial stress is of the same order of magnitude. However in Cheung's work the minimum fluid flow velocity is 20 m/s while in this thesis the fluid velocities are less than 2 m/s. High fluid velocities are likely to result in very diminished fluid damping effects on produced particle motion, such as those presented here in Section 8.3.3 (observed in Fig. 8.12). As explained there, when the fluid velocity is lower than the particle ejection velocity the drag force becomes negative. As a consequence the plastic region becomes smaller in simulations with relatively slow flow than in those without fluid. In Chapter 8 we present real oil field data (Table 9.1). Fluid velocities calculated from that data are not much higher than 0.01 m/s. Fluid velocities of 20 m/s seem to be unrealistic.

Another significant difference between the work performed here and that of Cheung relates to the attainment of steady state. In Cheung's work only 10^3 DEM steps were performed in the simulations. In this thesis more than 10^5 DEM steps were needed to achieve the steady state. This suggests that in Cheung's work the steady state may not have been reached. Our experience is that sometimes the simulation needs more time to run to be sure that this state has been reached because discontinuous 'jumps' after apparent equilibration frequently appear (as explained in Section 9.6 in the next chapter). Due to that reason, we performed exactly the same simulation without fluid as the one presented by Cheung. After 1000 DEM steps the plastified zone was still increasing and the steady state had not been reached (Fig. 8.30). That lead us to think that Cheung's simulations were not stabilized and the fluid rate was increased before a

steady state was reached at the previous rate. That explains the apparent difference of results, by which Cheung was able to apply greater fluid velocities without breaking all the sample, as it happened with SimV2 in Section 8.4.

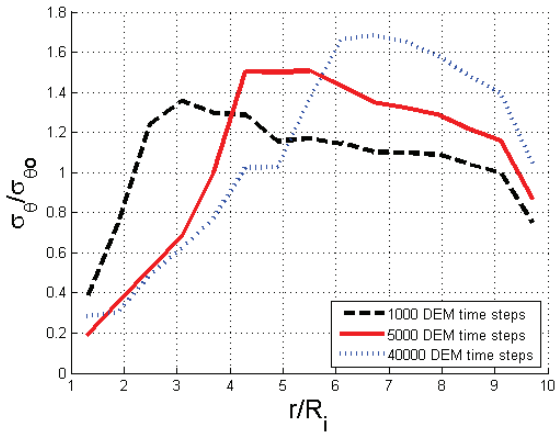

Fig. 8.30. Repeating of the DEM simulation without fluid using exactly the same parameters as Cheung (2010) after 1000, 5000 and 10000 DEM time steps.

8.7. Summary

A discrete analogue of an ideal sandstone idealization near a wellbore has been presented and simulations without fluid and with fluid have been performed. The model has a cylindrical shape with an inner hole that represents the wellbore. The DEM parameters were previously calibrated to match macroscopic sandstone behaviour.

A first simulation without fluid was performed and the results were used to calibrate the analytical parameters of the Risnes et al. (1982) solution. There was an overall good match between the numerical and the analytical solutions. However, peak values of the circumferential effective stress differ. Some of the reasons of that difference could be: (1) the numerical solution is a dynamic process where stress equilibrium is only reached at the end but the analytical solution is a quasi-static process; (2) particles in the numerical model can be produced leading a stress relaxation; (3) there is an asymmetry in the pattern of effective stress relaxation that produces a smoothed effect when the average is calculated. The plastic region around the hole was also asymmetric. The

micro-scale results were presented, showing where the contacts and bonds boke during the simulation. The majority of the broken bonds failed in tension. The same region where contacts and bonds broke reduced the circumferential particle stress.

Simulations with fluid in hydrostatic initial conditions were also carried out. The fluid used in those simulations was water. In the numerical solution the fluid presence introduces a damping force that slows particle motion. In these simulations there are less contacts and bonds that broke, and the void ratio around the hole is smaller than the one presented in the simulation without fluid.

Sand is not produced when the hydrostatic initial conditions were used with the fluid. However, for the simulation without fluid sand production starts at the beginning of the simulation, it has very high production rate and it stabilizes after 0.01s.

Two simulations with fluid flow boundary conditions were also tested. When a fluid flow is imposed the plastic region increases. When the fluid velocity increases the plastic region becomes bigger. The fluid flow increases also the sand production rate. After some threshold fluid velocity the simulation never reaches equilibrium and all the sample plastified.

Local damping decreases the number of broken contacts around the wellbore and decreases the plastic region. Local damping has an important effect in the results, especially when no fluid flow is applied. When a fluid flow is applied, local damping has much less effect because particles are already damped by the fluid.

Results were also compared to previous work by Cheung (2010). In her work the flow was steady, not variable, and assumed radial. Moreover, the effect of the particles on the fluid was not considered. In Cheung's work fluid hydrostatic conditions were not applied, and the minimum fluid flow velocity was very high. For that reason, the damping effect of the fluid was not observed in Cheung's thesis. Cheung simulations were performed using high fluid velocities that seemed above the total production threshold in our model. Repeating her simulation in dry conditions we concluded that it was likely that the steady state apparently observed in her simulations was not actually achieved, because of the discontinuous nature of the sand production phenomenon.

Chapter 9 - Numerical analysis of sand production near producing wells with fluid flow condition. Real cases

9.1. Introduction

In Chapter 8 simulations of sand production in an ideal sandstone analogue were performed. In this chapter the discrete analogues calibrated on real field sandstone data in Chapter 5 are tested for sand production. The computational cost increases very significantly and as explained, a specific procedure had to be developed to scale, adjust and represent the material, the fluid and the coupling.

Section 9.2 presents the data of the three different target oil fields. A preliminary assessment of the conditions of those fields with respect to sand production is described in Section 9.3. Sections 9.4 to 9.6 describe in detail the construction of the models employed in the simulations; finally in Section 9.7 the results are presented.

9.2. Field data

Field data of three different oil fields was provided by IESL (Table 9.1). The rock mechanical properties of the sandstones present in those fields were presented in Chapter 5. Other quantities related to the geometry of the well, the fluid or the production are shown in Table 9.1. The overburden is the vertical stress supported by the reservoir. The pore pressure is the pressure of the fluid in the reservoir. The thickness is the height of the producing reservoir. The oil gravity is the oil density calculated at a temperature of 60^{o} and a pressure of 1 atm, (see Section 3.2.3). The hole size is the diameter of the well. The minimum, average and maximum flow rates are the minimum, average and maximum flow rates measured at the top of the well. The sand

rate is the observed field sand production rate, as defined in Section 3.3. There is no sand rate data for FIELD2 and FIELD3 because significant sand production had not been recorded for them.

Table 9.1. Field data

		FIELD1	FIELD2	FIELD3
Geomechanical models	Overburden (MPa)	45,1	57	50,3
	Minimum Horizontal Stress (MPa)	38,4	51,1	44,4
	Maximum Horizontal Stress (MPa)	40,6	54,4	48,4
	Pore pressure (MPa)	21,2	27,2	24,7
	Thickness (m)	18,6	746,8	100,5
	Viscosity (mPa·s)	0,91	2,93	1,4
	Oil gravity (gcm^{-3})	0,8976	0,9092	0,8721
	Water density (gcm^{-3})	1,02	1,02	1,02
	Hole size (cm)	21,59	21,59	21,59
Production data	Minimum Flow rate (m^3/s)	0,0009	0,025	
	Average Flow rate (m^3/s)	0,011	0,0257	0,0418
	Maximum Flow rate (m^3/s)	0,0294	0,0263	0,1044
	Sand rate (pptb)	10		

9.3. Preliminary sand production estimates

9.3.1. Empirical prediction

In Section 3.5.1 an empirical model developed by Palmer et al. (2003) was presented. This is a model representative of current industrial approaches to predict sand production (IESL, 2016). That model predicts the onset of sand production correlating the critical bottom hole flowing pressure, the reservoir pressure and the total principal major and minor stresses. The criterion for sanding is

$$CBHFP < \frac{3\sigma_1 - \sigma_3 - \sigma_Y}{2 - A_p} - P_r \frac{A_p}{2 - A_p} \qquad \text{Eq. 9.1}$$

where *CBHFP* is the critical bottomhole flowing pressure (the fluid pressure at the bottom of the hole), P_r is the current average reservoir pressure, σ_1 and σ_3 are the total principal major and minor stresses, A_p is a poroelastic constant $A_p = \frac{1-2\nu}{1-\nu}\alpha$ (where ν is the Poisson ratio, defined in Eq. 2.20, and α is the Biot coefficient, defined in Eq. 2.48) and σ_y is the formation strength near the opening

$$\sigma_y = 3.1 \cdot S_{TWC} \qquad \text{Eq. 9.2}$$

where S_{TWC} is the strength as determined in the thick-walled cylinder test. When the fluid pressure at the hole is smaller than *CBHFP* the sand is produced.

CBHFP can be calculated for each one of the materials presented in Chapter 5 and this chapter (Table 5.3 and Table 9.1). The parameters used and calculated are summarized in Table 9.2. σ_1 is the 'overbuden' (Table 9.1) and σ_2 is the 'minimum horizontal stress' (Table 9.1).

Table 9.2. Input parameters for the empirical relation

	FIELD1	**FIELD2**	**FIELD3**
Poisson ratio (ν)	0.1126	0.1067	0.1717
Biot coefficient (α)	0.9267	0.8689	0.7648
A_p	0.8091	0.7651	0.6063
S_{TWC} **(MPa)**	12.2	30.13	103.4
σ_y **(MPa)**	37.82	93.4	320.54
σ_1 **(MPa)**	45.1	57	50.3
σ_2 **(MPa)**	38.4	51.1	44.4
CBHFP **(MPa)**	35.21	4.6	-164.3

The oil field is expected to produce sand when the fluid pressure at the hole (at the cavity of the well) is smaller than the *CBHFP* calculated. The meaning of a negative *CBHFP* is that the field is safe and no sand is expected to be produced. FIELD1 will produce when the fluid pressure at the cavity is smaller than 35.21 MPa, FIELD2 will produce when the fluid pressure at the cavity is smaller than 4.6 MPa and, because of the negative value obtained for *CBHFP* FIELD3 is expected to not produce sand at all.

The drawdown necessary to produce sand in FIELD2 is around 23 MPa. On the other hand, FIELD1 has already a reservoir pore pressure smaller than the *CBHFP*. Therefore, the Palmer et al. (2003) criterion indicates that FIELD1 will produce sand under any exploitation condition.

9.3.2. Analytical solution

To obtain a first approximation to the three cases, the analytical solution described in Section 3.6 (Risnes et al., 1982) was evaluated using their data. The solution requires as input a number of material parameters: Poisson's ratio (ν), internal friction angle of the material (φ), Biot parameter α, cohesive strength (S_0), permeability (k_c) and fluid viscosity (μ_f). The analytical solution also depends on boundary conditions: radial total stress at the inner boundary (σ_{ri}), vertical total stress at the outer boundary (σ_{zo}), (from which the radial total stress at the outer boundary (σ_{ro}) is deduced assuming elastic behaviour), and, either the fluid pressure at the outer and inner boundaries (P_o, P_i) or the fluid flow rate (q).

Table 9.3 presents the parameters used to calculate the analytical solution. The friction angle, Biot parameter and Poisson's ratio are taken from Table 5.6. Cohesive strength is calculated as (Jaeger et al., 2007)

$$S_0 = \frac{UCS}{2\tan\phi} \qquad \text{Eq. 9.3}$$

$$\phi = 45^{\circ} + \frac{\varphi}{2} \qquad \text{Eq. 9.4}$$

where *UCS* is the uniaxial compressive strength, φ is the internal friction angle (both given in Table 5.6).

The permeability and pore pressure are taken from Table 9.1; except for FIELD1 where permeability data was lacking and a value of 200 mD was assumed. The inner radius is the half of the hole size (Table 9.1). The total vertical stress at the outer boundary is the overburden (Table 9.1). The flow rate is the maximum flow rate (Table 9.1).

Table 9.3. Input parameters for the Risnes analytical solution

Parameter	**FIELD1**	**FIELD2**	**FIELD3**
Cohesive strength (MPa)	0.97	3.07	13.7
Friction angle (°)	27.4	34.6	47.45
Biot coefficient	0.9267	0.8689	0.7648
Poisson's ratio	0.1126	0.1067	0.1717
Permeability (mD)	*200*	200	181
Inner radius (cm)	10.795	10.795	10.795
Total vertical stress at the outer boundary (MPa)	45.1	57	50.3
Flow rate (m^3/s)	0.0294	0.0263	0.1044
Pore pressure (MPa)	21.2	27.2	24.7

Fig. 9.1 show the predictions of the analytical solution field data for maximum flow rate conditions. The analytical solution predicts that all materials plastify around the hole. However, the plastic radius is very small (this is the reason why it is not appreciated in Fig. 9.1). The ratio between the plastic radius and the inner radius is 1.04 for FIELD1, 1.09 for FIELD2, and 1.01 for FIELD3. Therefore, the Risnes analytical solution, suggests that the situation is more unfavourable for FIELD 2 than for FIELD 1, opposite of what was suggested by the empirical criterion presented in the previous section. Both the

empirical criterion and the analytical solution suggest that FIELD 3 conditions are the most favourable.

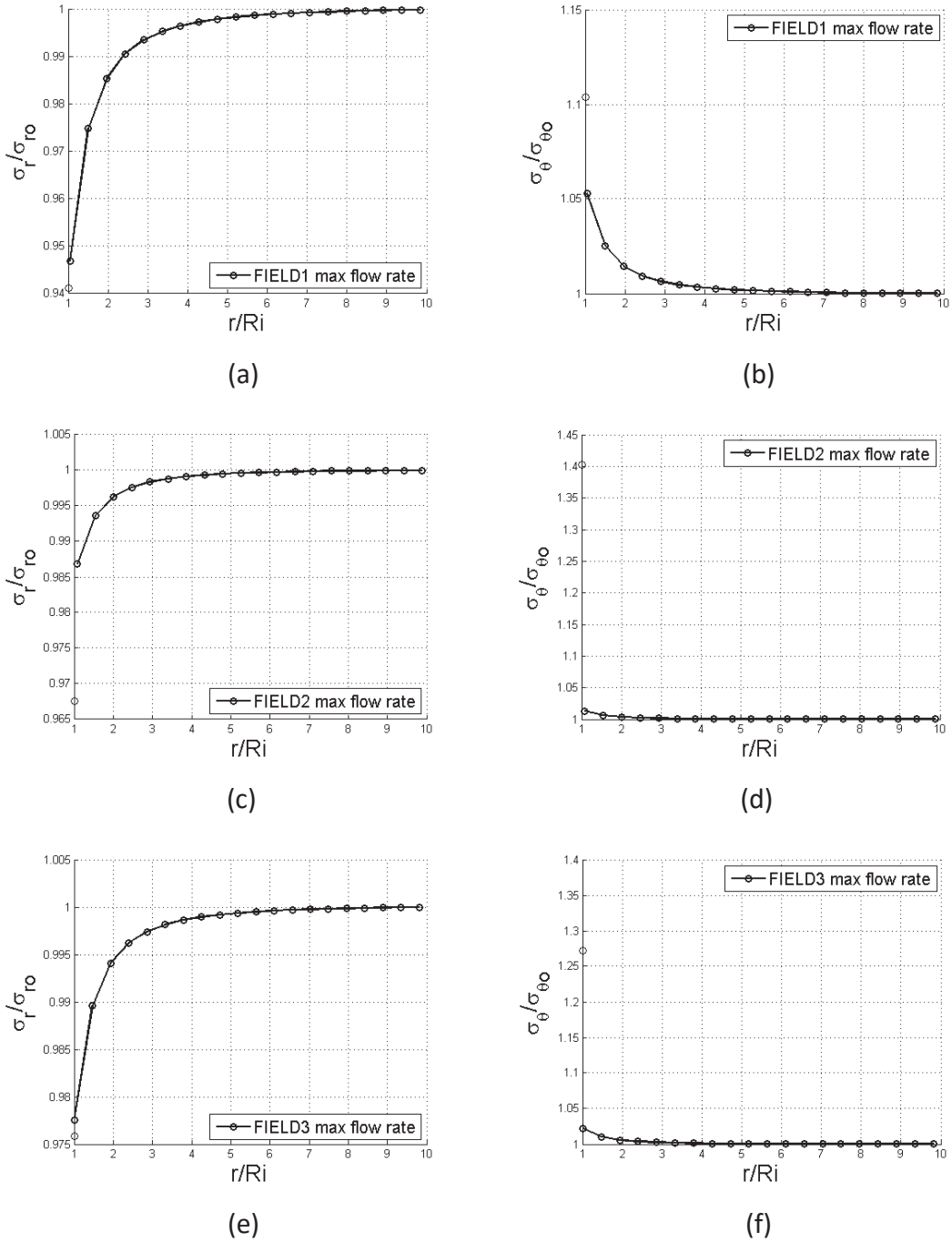

Fig. 9.1. Analytical solutions. a) Radial and b) circumferential stresses of FIELD1, c) radial and d) circumferential stresses of FIELD2, and e) radial and f) circumferential stresses of FIELD 3.

9.4. Discrete model

9.4.1. Geometrical constraints

The geometry of these models, like those in Chapter 8, represents a horizontal slice of a confined vertical cylinder of sandstone with a cylindrical hole in the middle (Fig. 9.2).

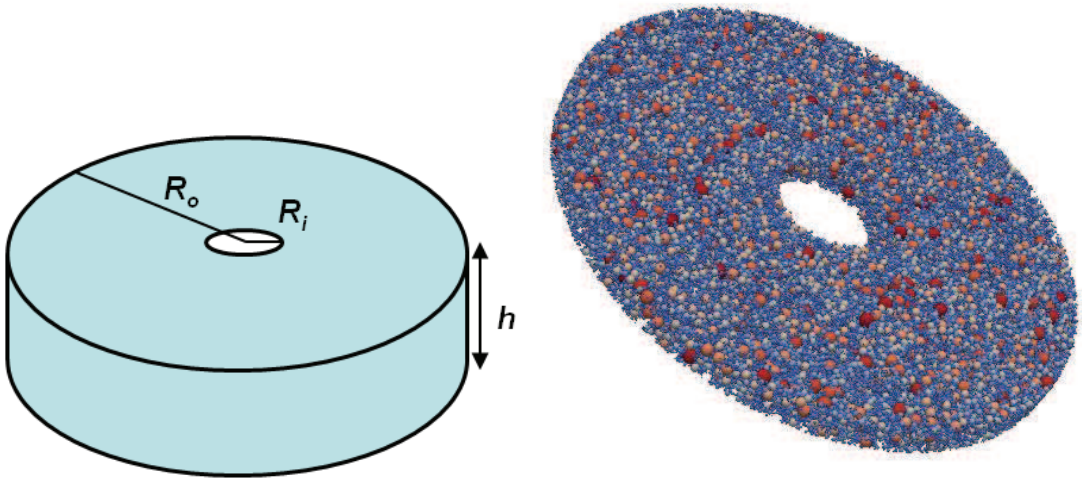

Fig. 9.2. Geometry model (left) and the sample generated (right) colored by the particle diameter size

It is useful to have some means to estimate the number of elements required to fill the model. The specimen for computation is a hollow cylinder of height h, external radius R_0 and internal radius R_i. Given porosity n, the specimen solid volume, V_s, is then

$$V_s = \pi h\left(R_o^2 - R_i^2\right)(1-n) \qquad \text{Eq. 9.5}$$

The volume of a particle having the mean diameter d_{50} is

$$V_{50} = \frac{\pi}{6} d_{50}^3 \qquad \text{Eq. 9.6}$$

The ratio of the precedent gives the number of mean particles that can be fitted within the specimen, N_{50}

$$\frac{V_s}{V_0} = N_{50} = \frac{6h\left(R_o^2 - R_i^2\right)}{d_{50}^3}(1-n) \qquad \text{Eq. 9.7}$$

This is best expressed using non-dimensional ratios

$$N_{50} = 6\left(\frac{h}{d_{50}}\right)\left(\frac{R_i}{d_{50}}\right)^2\left(\left(\frac{R_o}{R_i}\right)^2 - 1\right)(1-n) = 6n_h n_i^2\left(n_R^2 - 1\right)(1-n) \qquad \text{Eq. 9.8}$$

Clearly, the PSD is far from uniform and therefore the number of particles N_{DEM} will be different. This is expressed multiplying the above expression by a correction factor, f_G

$$N_{DEM} = f_G N_{50} = 6 f_G n_h n_i^2\left(n_R^2 - 1\right)(1-n) \qquad \text{Eq. 9.9}$$

The outer radius should be large enough to allow for the development of a produced plasticized region without interference from the outer boundary. From experience with simulations in Chapter 8 this requires an outer radius about 8-10 times the inner radius, or, according to the formula above, n_R = 8-10.

Moreover, to maintain a good representative sample of grain-scale interactions the perimeter of the internal hole should contain at least 20 particles, this implies $n_i \approx 10/\pi$.

The factor f_G is very dependent on the shape of the PSD curve. It may also depend significantly on the geometry of the model, but a first estimate may be obtained from the cylindrical specimens that were used in Chapter 5 to perform triaxial and axial compressive tests. Table 9.4 presents the values that result.

Table 9.4. Values of the number of particles in the triaxial and axial compressive tests (Section 5.4.5), N_{50} and f_G.

	FIELD1	**FIELD2**	**FIELD3**
N_{DEM}	38960	47890	46810
N_{50}	14160	15650	25260
f_G	2.8	3.1	1.9

At this stage we may obtain a relation for each case to be studies between the ratio n_h and the total number of particles in the discrete model, NDEM. These relations are plotted in Fig. 9.3.

There are no definite criteria on which to establish a minimum number of mean particles per slice height. It is clear that low numbers (say 3) would increase the risk of artificial arching; it is also clear that the number of particles in the model increases quickly with n_h. Trying to balance these criteria, we chose the height of the model to be big enough to contain at least 4-5 d_{50} particles (which gives $n_v \approx 5$).

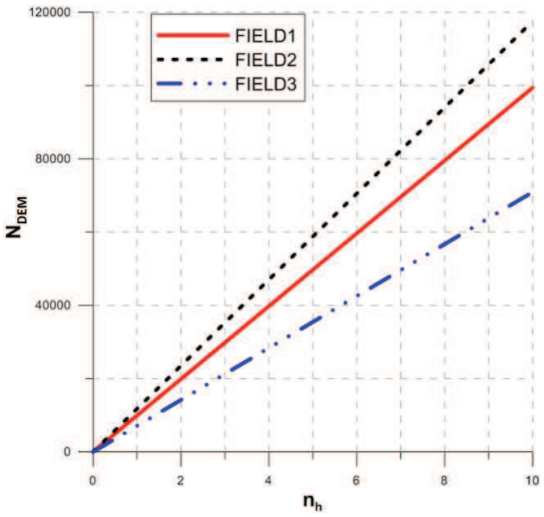

Fig. 9.3. Number of particles versus n_h (n_R = 8 and n_i = $10/\pi$)

9.4.2. Computational constraints

As explained in Chapter 5, total computation time, T_{comp} may be roughly estimated as

$$T_{comp} = \kappa_{sim} \frac{t_{sim}}{t_{step}} N_{el} \qquad \text{Eq. 9.10}$$

The experience with the sand production simulations runs in Chapter 8 indicated that the complexity constant κ_{sim} was about $2\mu s/\text{particle}$. It did also indicate that, when sand production is significant, the simulation time t_{sim} should not be much below 0.2 s to identify a stress steady state at given flow conditions. Of course, if sand is not produced, equilibrium time is much shorter. As explained below up to three successive flow conditions were to be applied at each model, suggesting that counting on a total of 0.5 s may be enough. These values lead to the relations between tstep and element number illustrated in Fig. 9.4.

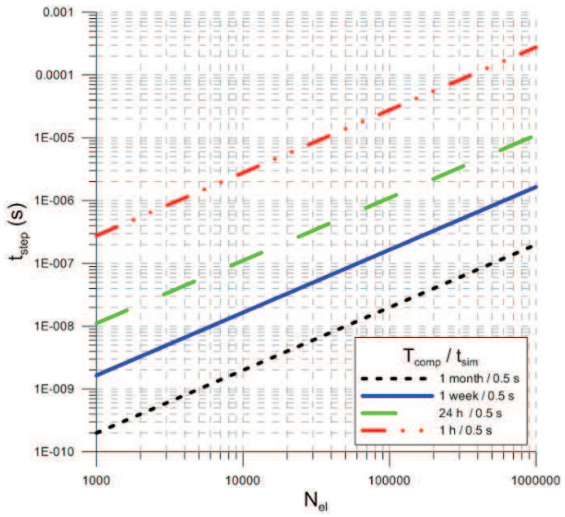

Fig. 9.4. Time step versus number of particles for different computational times and a simulation time of 0.5 s.

Examining the previous figure it would appear that to obtain results in a reasonable amount of time (less than a month, say) for models of around 50000 particles the simulation time step, t_{step}, cannot be much smaller of 10^{-8} s.

9.4.3. Scaling

To attain a desired time step of around 10^{-8} s we need to examine what is the critical step of the discrete analogues used for each material and, if this turns out to be smaller than 10^{-8} s, establish what is the factor *N* by which particle radius should be scaled up. Radius scaling, as explained in Section 5.3.2, has as a direct consequence the scaling up of critical time step

$$t_{crit,sc} = N t_{crit} \qquad \text{Eq. 9.11}$$

where t_{crit} is the time step using the original particle size and $t_{crit,\ sc}$ is the time step when the particles are scaled up.

As explained in Section 5.3.2, the simulation time step is the minimum of all the critical times calculated for all the particles

$$t_{crit} = 0.8\sqrt{m / \sum K_c} \qquad \text{Eq. 9.12}$$

where m is the mass of the particle and $\sum K_c$ is the stiffness (summing all the contributions of each contact of the particle). As it is also explained in Section 5.3.2, such minimum value is controlled mostly by the size of the smallest particles in the simulation. Other influential factors are the size ratio between largest and smallest particles, coordination number and contact stiffness. Therefore, t_{crit} depends on the particle size, the effective stiffness calibrated (Table 5.7) and the coordination number. To estimate the minimum critical step we should consider the smallest particle in contact with *CN* number of the biggest particles

$$t_{crit} \approx 0.8\sqrt{\frac{\rho_p 4\pi R_{PA}^3}{CN \cdot 3 \cdot 2E_c \dfrac{R_{PA}R_{PB}}{(R_{PA}+R_{PB})}}} \qquad \text{Eq. 9.13}$$

where ρ_p is the density of the particles, R_{PA} is the radius of the smallest particle, R_{PB} is the radius of the biggest particle, E_c is the calibrated effective stiffness and *CN* is the coordination number.

Fig. 9.5 represents the time step thus calculated for the three fields versus the coordination number. The smallest of the time steps represented for each one of the

fields is used to estimate the critical time step. The time step extract of this figure is represented in Table 9.5, and the scale factor *N* necessary to attain a time step around 10^{-8} s using the Eq. 9.11 is also given.

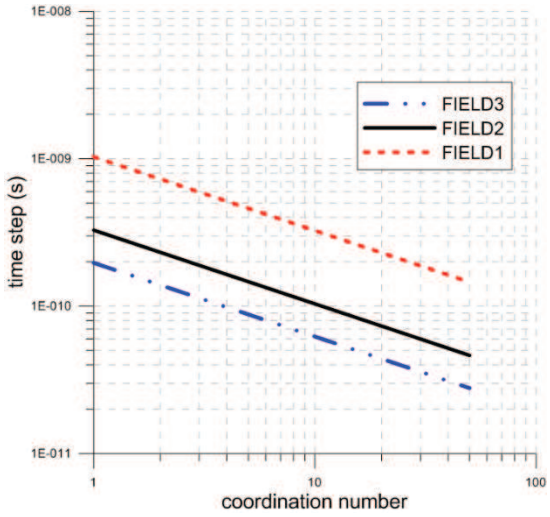

Fig. 9.5. Time step versus coordination number for each field

Table 9.5. Scaling factor for each reservoir

	FIELD1	**FIELD2**	**FIELD3**
t_{crit} **(s)**	$2 \cdot 10^{-10}$	$5 \cdot 10^{-11}$	$3 \cdot 10^{-11}$
Scaling factor N	50	170	300

Geometrical scaling of particle sizes needs to be taken into account when interpreting simulation results, by applying appropriate down-scaling factors at post-processing. Thus, particles produced during the simulation are scaled down to compute the mass of sand produced (m_{sand})

$$m_{sand} = \rho_p V_{sand} = \rho_p \frac{V_{DEM}}{N^3} = \frac{m_{DEM}}{N^3} \qquad \text{Eq. 9.14}$$

where ρ_p is the density of the particles, V_{sand} is the volume of the particles, N is the scale factor, V_{DEM} is the volume of the DEM scaled up particles and m_{DEM} is the mass of the DEM scaled up particles.

9.4.4. Final model dimensions

Balancing all the constraints presented above required a significant number of trials, due to the approximations involved in the simplified expressions presented above. The final model geometry parameters for each field are presented in Table 9.6, were R_o is the outer radius, R_i is the inner and h is the height.

Table 9.6. Geometry parameters

	FIELD1	**FIELD2**	**FIELD3**
R_o**(m)**	0.27	1.44	2.4
R_i **(m)**	0.03	0.18	0.3
h **(m)**	0.024	0.2	0.3
n_R	9	8	8
n_i	$15.7/\pi$	$14.7/\pi$	$13.6/\pi$
n_h	4	5.2	4.3
N_{DEM}	42408	48174	48667

9.5. Fluid flow and fluid-solid interaction model

9.5.1. Fluid mesh

The fluid model has the same overall geometry as the mechanical model. The CFD cells are hexahedral (Fig. 9.7). Cells are created dividing the geometry in three directions: radial, vertical and circumferential. To size the CFD mesh the general criterion is to be

able to accommodate a statistically significant number of particles within a single fluid cell, so that the effect of particles on fluid flow changes smoothly. To achieve that, as explained in Chapter 6 (Section 6.3.2.3) the following criterion may be used as a guideline

$$\frac{\Delta x_{cfd}}{2R} > 5 \qquad \text{Eq. 9.15}$$

where Δx_{cfd} the length of the cell and R is the particle radius. Given the DEM model geometry on the vertical direction a single cell was enough. On the radial direction this condition imposes an upper bound on the number of radial subdivisions on the fluid mesh, Z, since

$$\Delta x_{cfd} = \frac{R_o - R_i}{Z} > 5d_{50} \qquad \text{Eq. 9.16}$$

or, using the non-dimensional geometrical ratios introduced above,

$$\frac{n_R - 1}{Z} > \frac{5}{n_i} \qquad \text{Eq. 9.17}$$

which lead to the upper bound condition

$$Z < \frac{(n_R - 1)n_i}{5} \qquad \text{Eq. 9.18}$$

For the values of n_i and n_R relevant here (Table 9.6 are $13/\pi$ - $16/\pi$ and 8-9) that would lead to a desirable upper limit to m of 6-8.

On the other hand, circumferential direction divisions have another restriction. Due to the difference between the shape of the inner hole and the surface of the cells, if the number of circumferential divisions is too small, a void space between the surface of the cell and the cylindrical wall appears (Fig. 9.6a). This could lead to an error in the calculation of the porosity in the cells next to the cavity, with significant implications for the evaluation of fluid-solid interaction forces. To minimize that error the number of circumferential divisions must be increased (Fig. 9.6b).

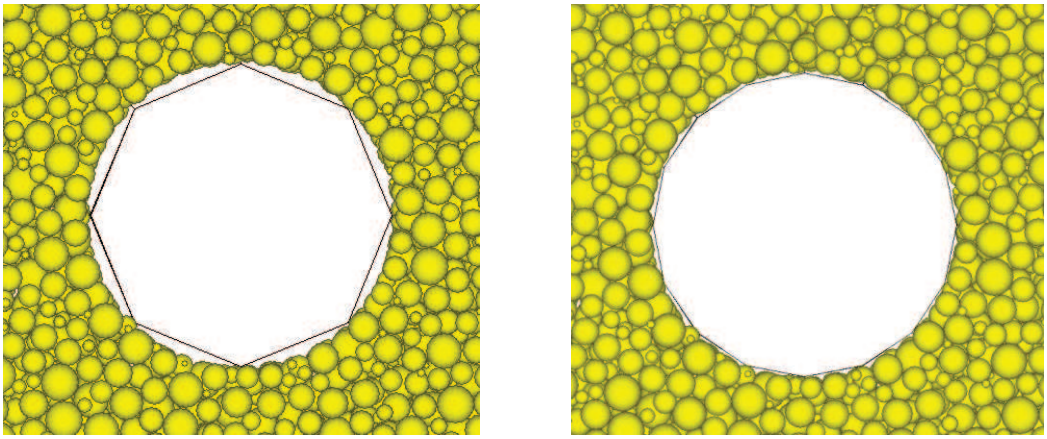

(a) (b)

Fig. 9.6. Particles (yellow) next to the cavity at the beginning of the simulation and fluid CCFD cell surfaces (black lines) with (a) 8 circumferential divisions, and (b) 16 circumferential divisions.

The porosity in each one of the cells next to the cavity can be expressed as

$$n' = \frac{V_{por}}{V_{cell}} = n + \frac{V_{void}}{V_{total}} \qquad \text{Eq. 9.19}$$

where n' is the calculated porosity in those cells, n is the target porosity (the overall model porosity), V_{por} is the total void volume in the whole cell, V_{cell} is the total volume of the cell and V_{void} is the volume of the void between the particles (the wall of the cavity) and the cell surface. To minimize the difference between n' and n, the ratio $\frac{V_{void}}{V_{total}}$ should not be much greater than 0.1. Both volumes can be calculated as

$$V_{total} = \frac{\pi l_R h}{n_c n_v}\left(l_R + 2R_i\right) \qquad \text{Eq. 9.20}$$

$$V_{void} = \left(\pi R_i^2 - \frac{1}{2} n_c R_i^2 \sin\frac{2\pi}{n_c}\right)\frac{h}{n_v} \qquad \text{Eq. 9.21}$$

where $l_R = \frac{R_o - R_i}{n_R}$, R_o is the outer radius of the whole cylinder, R_i is the inner radius of the cylinder, n_R is the number of radial divisions, h is the height of the sample, n_c is the number of circumferential divisions and n_v is the number of vertical divisions. Moreover, limitations in the volume-building capabilities of CCFD require that the number of circumferential divisions must be a multiple of 4 to obtain a hollow cylinder. Using n_v = 1, n_R = 6-8, and the geometry parameters in Table 9.6, the ratio $\frac{V_{void}}{V_{total}}$ is calculated for each one of the models (Table 9.7). A minimum number of 16 circumferential divisions were necessary to avoid porosity calculation errors around the cavity.

Table 9.7. Ratios $\frac{V_{void}}{V_{total}}$

	FIELD1	**FIELD2**	**FIELD3**
$\frac{V_{void}}{V_{total}}$ for $n_c = 12$	0.18	0.14	0.15
$\frac{V_{void}}{V_{total}}$ for $n_c = 16$	0.13	0.07	0.11

As is clear the number of circumferential divisions required to limit the conformity error in the inner cells results in smaller dimensions that those in principle desirable to contain a statistically large number of particles. In fact, the number of particles for the smallest cells may be approximated as

$$N_{sp} = \frac{6 f_G V_{total}}{\pi N d_{50}^3}(1-n) \qquad \text{Eq. 9.22}$$

where f_G is the correction factor introduced in Section 9.4.1 (Eq. 9.8), V_{total} is the volume of the cell (Eq. 9.19), N is the scaling factor introduced in Section 9.4.3 (Table 9.5) and n is the porosity.

The characteristics of the fluid mesh finally adopted are presented in Table 9.8. The error in porosity due to conformity at the well face is small and, although some cell dimensions are somewhat small, the number of particles evaluated for the smaller cells of the models appears large enough to obtain meaningful averages.

Table 9.8. CFD mesh divisions and the number of particles for the smaller cells

Direction	**FIELD1**	**FIELD2**	**FIELD3**
Radial	8	6	6
Circumferential	16	16	16
Vertical	1	1	1
Number of particles for the smaller cells	*180*	*300*	*130*

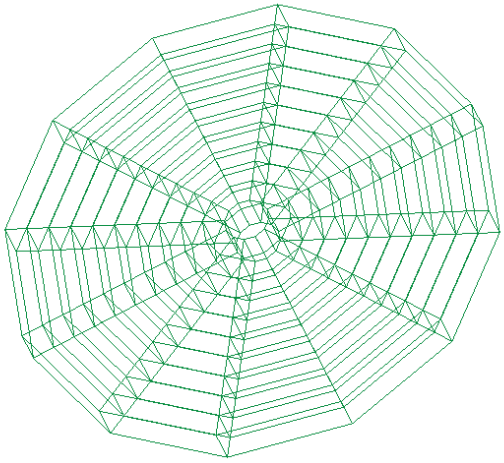

Fig. 9.7. CFD mesh

9.5.2. Boundary conditions

The boundary fluid conditions are shown in Fig. 9.8 and they are given fluid flow extraction rate at the inner boundary (an imposed fluid velocity which goes inside the hole) and imposed fluid pressure at the outer boundary. Fluid pressures are the field fluid pore pressures given in Table 9.1. On the other hand, the flow rates given in Table 9.1 correspond to total well outflow and need to be transformed into unit flow rates. To do that it is assumed that the flow is uniform all along the well surface and therefore

$$v_i = v_{real} = \frac{q_{real}}{2\pi H R_{real}} \qquad \text{Eq. 9.23}$$

where q_{real} is the total well outflow, H is the thickness of the reservoir and R_{real} is the well radius. q_{real}, H and R_{real} are all reported in Table 9.1.

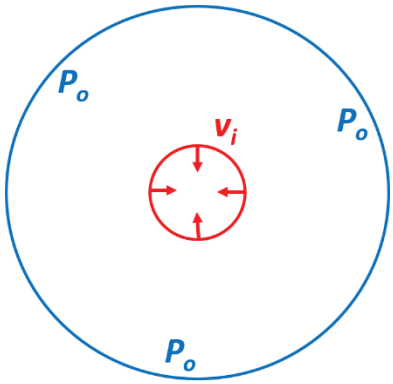

Fig. 9.8. Boundary conditions of the fluid model

9.5.3. Scaling particle-fluid interaction

As explained in the previous section the discrete model needs geometric grain scaling to attain feasible computational times. The mechanical response of the mechanical discrete model is scale invariant, and the same is required from the fluid-solid interaction

The fluid force has three components: drag (Eq. 6.30), the force due to the pressure gradient (Eq. 6.23) and buoyancy (Eq. 6.24). Because of particle scaling (Section 9.4.3), the particle radii are multiplied by a factor N. The scaled radius for each particle is expressed as

$$R_{sc} = NR \qquad \text{(Eq. 9.24)}$$

where R is the original radius and R_{sc} is the radius of the scaled particles.

Fluid forces exerted on the particles are dependent on the particle radii. Due to the scaling, interaction forces between particles and fluid will be different from those acting in the field. This may be avoided by scaling-back the fluid forces at the DEM/CCFD interface. To do this, it should be noted that changing the value of the radii during the calculation of the fluid force is not possible in CCFD, but it is possible to change the forces value, the density and the viscosity.

The best way to scale the drag force is changing the density and the viscosity

$$\rho_{fsc} = \frac{\rho_f}{N^2} \qquad \text{Eq. 9.25}$$

$$\mu_{fsc} = \frac{\mu_f}{N} \qquad \text{Eq. 9.26}$$

where ρ_{fsc} and ρ_f are the scaled density and the real density, and μ_{fsc} and μ_f are the scaled and the real viscosities. Using these scaled fluid parameters, the drag force and the particle Reynolds number are the same as the one without scaling the particles

$$F_d = \frac{1}{2} C_D \rho_{fsc} \pi R_{sc}^2 |u-v|(u-v) = \frac{1}{2} C_D \rho_f \pi R^2 |u-v|(u-v) \qquad \text{Eq. 9.27}$$

$$Re_p = \frac{2\rho_{fsc} R_{sc} |u-v|}{\mu_{fsc}} = \frac{2\rho_f R |u-v|}{\mu_f} \qquad \text{Eq. 9.28}$$

where all the parameters are defined in Section 6.3.2. Then, the pressure gradient force should be changed directly

$$F_{gradp,sc} = \frac{4}{3}\pi R^3 \nabla p = \frac{4}{3}\pi \frac{R_{sc}^3}{N^3}\nabla p = \frac{F_{gradp}}{N^3} \quad \text{Eq. 9.29}$$

and the buoyancy should be also changed directly

$$F_{buoyancy,sc} = \frac{4}{3}\pi R^3 \rho_f = \frac{4}{3}\pi \frac{R_{sc}^3}{N^3} N^2 \rho_{fsc} = \frac{F_{buoyancy}}{N} \quad \text{Eq. 9.30}$$

In summary, the fluid-particle interaction takes place as if the particles had not been scaled up in the DEM model.

9.5.4. Adjusting porosity

Practical DEM models idealize materials as collections of spheres (using other shapes increases the computational expense by orders of magnitude). Current algorithms for model generation (as REM, described in Section 5.4.2) make it difficult to attain using spherical particles porosities that are much below 0.3. As explained in Section 5.4.2, the porosities of the DEM models used in this chapter are higher than the porosities of reference sandstones. As illustrated in Chapter 6 using permeameter computations, the effect of model porosity on model permeability is well described by the Kozeny-Carman relation at low particle Reynolds number. Hence, a mismatch in model and field porosity would imply a consequent mismatch in model and field permeability. This mismatch needs then to be corrected. The porosity of the three materials is transformed and adjusted before transferring information between DEM and CFD.

The porosity computed in DEM can be accessed and manipulated before being passed to the CFD model to compute pore flow. A quadratic transformation that scales the

computed DEM porosity n_{DEM} into a different value n_{CFD} is introduced into the interaction between the particles and the fluid (Fig. 9.9). The transformation is fitted so that the initial state of each material (points 1, 2 and 3 in the Fig. 9.9) is exactly represented and that the two limit states of perfect compaction (point 4) and total erosion (point 5) are also included.

The adjusted porosity n_{CFD} is the one used during the simulation to calculate the drag force and the body force.

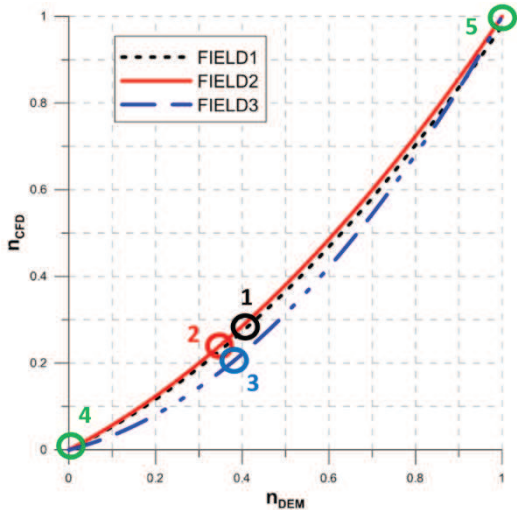

Fig. 9.9. Example porosity transformation between the discrete solid model and the fluid model.

9.5.5. Recovering perforation dimensions

The area where fluid and sand are produced is not the same as the original field because the radius of the hole and also the thickness are different. The total volume of fluid produced and sand production are divided per area of the model cavity (producing area)

$$SF = \frac{m_{sand}}{2\pi h R_i} \qquad \text{Eq. 9.31}$$

$$FP = \frac{q\Delta t_{sim}}{2\pi h R_i} \qquad \text{Eq. 9.32}$$

where *SF* is the sand flow, *FP* is the fluid produced, *h* is the height of the sample, R_i is the radius of the inner cavity, *q* is the fluid discharge and Δt_{sim} is the increment of time during the discharge.

9.6. Simulation set-up

Specimen formation followed the same procedure as Section 5.4.2: a radius expansion method in which small particles with linear contacts, seeded within frictionless walls (two horizontal walls and two radial walls, as in Section 8.2.1), were expanded to attain the target initial values of porosity and stress. Then the parallel bonds were installed. After specimen formation the wall friction coefficients for the two horizontal platens were changed to 0.1. No assumption of axial symmetry was enforced during specimen formation.

The simulation starts when the inner radial wall is removed and the inner boundary is transformed into a mass sink, to represent the effect of longitudinal mass transport within the cavity. Particles that completely cross this boundary are deleted and considered produced.

During the simulations the horizontal upper and lower walls of the DEM model are fixed, the external radial wall is used to apply the desired effective stress level and the internal radial wall is removed. Removing the internal radial wall is equivalent to applying zero effective stress at the cavity boundary. Following the analysis presented in Chapter 8, no numerical damping was used in the simulations.

The initial stress conditions are taken from Table 9.1. The total vertical stress is the overburden given in Table 9.1 and the total radial stress at the outer boundary is taken

as the average between the maximum and the minimum tabulated total horizontal stresses. The walls apply the effective vertical and the radial stresses (Table 9.9) that are obtained considering those total stress values and the reservoir pore pressure.

Table 9.9. Initial stress state

	Pore pressure (MPa)	Total vertical stress (MPa)	Effective vertical stress (MPa)	Total radial stress (MPa)	Effective radial stress (MPa)
FIELD1	21.2	45.1	25.5	39.5	19.9
FIELD2	27.2	57	33.4	52.8	29.1
FIELD3	24.7	50.3	31.4	46.4	27.5

Using the field data on flow rates and following Eq. 9.22, 3 different fluid velocities at the inner boundary are calculated for each material: a minimum velocity (v_{min}), an average fluid velocity (v_{av}) and a maximum fluid velocity (v_{max}).

The simulations start applying the minimum fluid velocity and then increase the extraction rate. Table 9.10 shows the different velocities applied for each material and the fluid pressure at the outer boundary.

Table 9.10. Boundary conditions for each oil reservoir

	FIELD1	FIELD2	FIELD3
v_{min}**(mm/s)**	0.7	0.49	-
v_{av} **(mm/s)**	8.7	0.51	6.0
v_{max}**(mm/s)**	23.3	0.52	15.0
P_o **(MPa)**	21.2	27.2	24.7

Before increasing the flow rate it was considered necessary to achieve steady state at the lower flow rate. However, the definition of steady state is not unproblematic. In principle, “steady state” refers here to a situation in which the effective stress variation with radial distance is stationary in time. This should be complemented with an

examination of the contact forces distribution and the sand production rate. A problem arises because the observed sand production sometimes happens in steps, after a period of apparent stability. An example, of this phenomenon from SimV1 (Section 8.4) simulation study is shown in Fig. 9.10. Therefore even an apparently stationary stress state might not be enough.

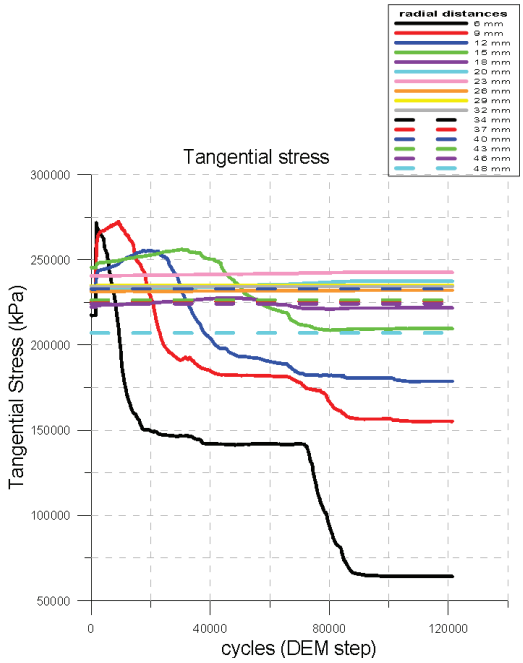

Stress evolution at different radial distances

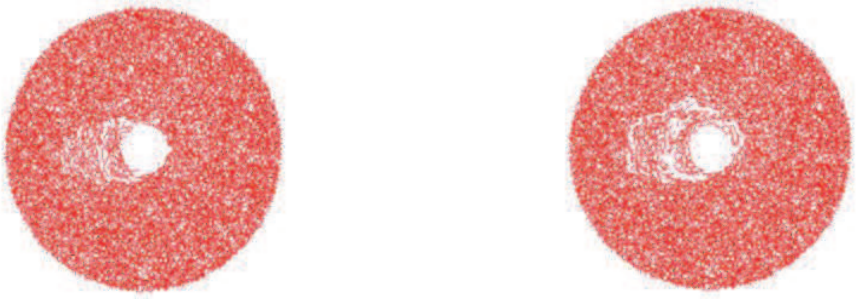

Situation before “jump” Situation after “jump”

Fig. 9.10. Example of “jump” in sand production

Therefore some complementary practical rules were devised to stop the simulations. After a certain run period (t_{sim} = 0.1 s of simulation time)

a) If the stress evolution has been stable for more than a quarter of the precedent simulation time, and sand is not being produced, the problem is deemed stable and the conditions under study should not be conducive to runaway sand production.
b) If after that period the stress evolution has not stabilized and/or the model is still producing sand at a significant rate, the conditions under study indicate a significant risk of permanent sand production. In that case the simulations were continued until other limitations of the system took over (e.g. plastization of the whole sample)

9.7. Results

Following Butlanska et al. (2013), three different kind of results are given for each simulation. Mesoscale results are those expressed using continuum variables like flow rate or stress. Stress is here obtained from particle interaction forces using averaging procedures described in Section 8.2.2. Microscale results are those at the particle scale and expressed and represented for each particle. Finally, the macroscale or main engineering result of interest of each simulation are sand production rates. This is sometimes expressed as sand flow rates (i.e. mass flow rate per unit exposed surface) and sometimes as sand production (mass flow per fluid flow) to compare with field values.

9.7.1. FIELD1

The fluid velocity at the inner boundary was set to 0.7 mm/s, and the simulation was carried out during intervals of t_{sim} = 0.1 s to check the radial and the circumferential stresses and the sand production rate. In this case, the stress was stable during those periods, but the sand rate was still increasing. For that reason, it was needed 11 run periods of t_{sim} = 0.1 s and it was run for a total of 1.1 s with the minimum velocity. After

that, when the steady state was reached, the sand rate was stable and the velocity was increased to the average value at the inner boundary, 8.7 mm/s. The simulation was again run during t_{sim} = 0.1 s, and again the stress was stable but the sand rate was still increasing. The total run periods of t_{sim} = 0.1 s was 5 and the simulation was carried out for a total of 0.5 s. Finally, the fluid velocity was increased at the inner boundary to 23.3 mm/s and the simulation, and a total of 4 run periods of t_{sim} = 0.1 were needed until the sand rate stabilized. The computational time required was between 3 and 4 months.

9.7.1.1. Mesoscale results

Fig. 9.11 shows the stress evolution for 3 different radial distances. From these results it is concluded that a steady state was reached because stresses appeared quite stable. It is also visible how the stress transient dynamics that follow the increases in fluid flow rate are far smaller than the initial one in which well perforation is also simulated by means of inner wall disparition.

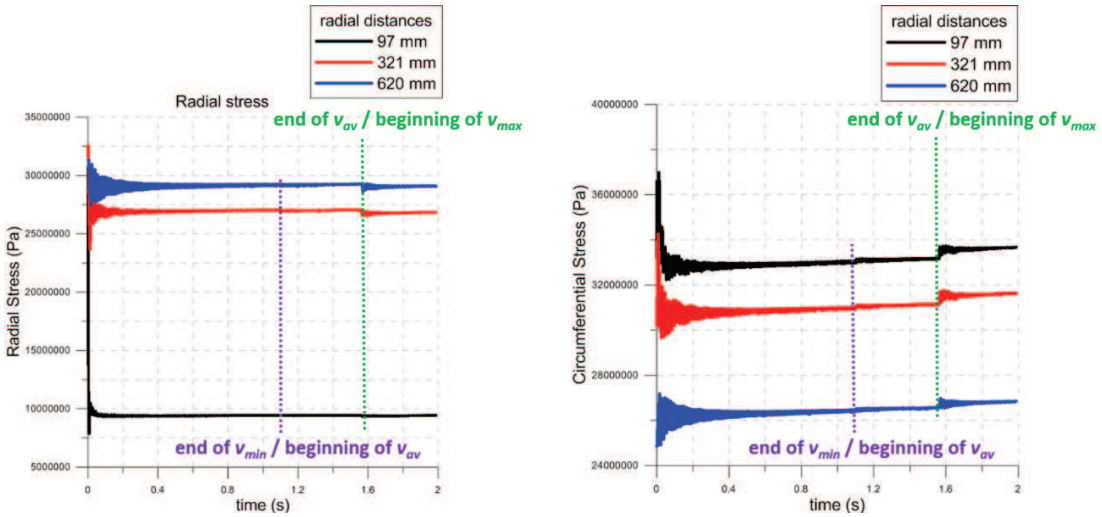

Fig. 9.11. FIELD1. Radial and circumferential stresses evolution at different radial distances from the inner boundary at the end of the simulation with the maximum fluid velocity.

The stress distribution around the sample at the end of each step was exactly the same and it is presented in Fig. 9.12. The circumferential stress shows a large peak at some distance from the inner radius and it does not diminish towards the borehole wall. These are signs indicative of a larger plastified zone than what was predicted by the analytical Risnes solution represented in Section 9.3.2 (Fig. 9.1a and Fig. 9.1b).

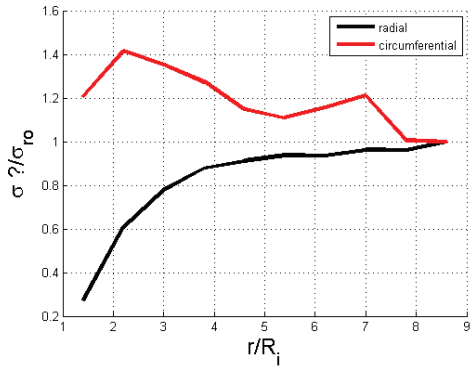

Fig. 9.12. FIELD1. Average total stresses as a function of normalized radial distance at the end of the simulation

The fluid velocity fields at the end of the three extraction steps are presented in Fig. 9.13. The porosity field is shown in Fig. 9.14. The observed flow velocity is coherent with the porosity field at the end of the simulation. The regions of increased flow have a higher porosity value than the rest of the sample. The likely reason of that is the sand produced in this region. It is noticeable how the porosity in that producing region increases slightly as the flow rate is stepped up.

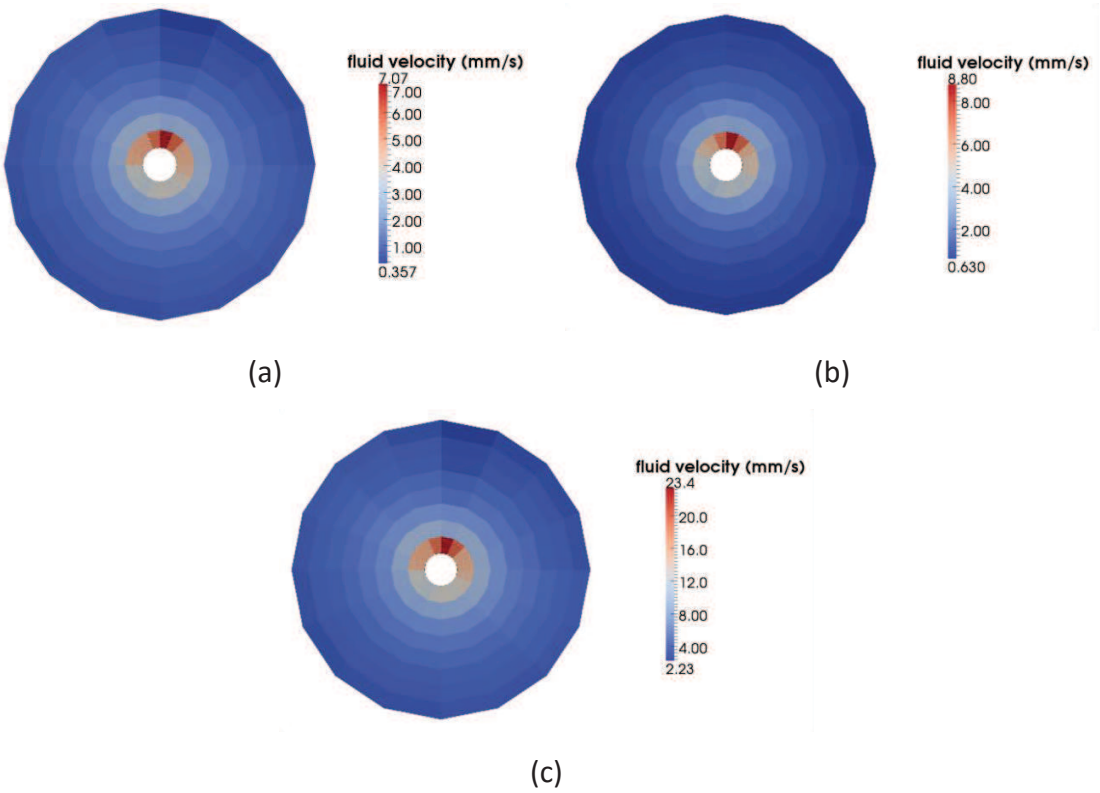

Fig. 9.13. FIELD1. Fluid velocity (xy plane) (a) at the end of the minimum flow-rate step, (b) at the end of the average flow-rate step, and (c) at the end of the maximum flow-rate step.

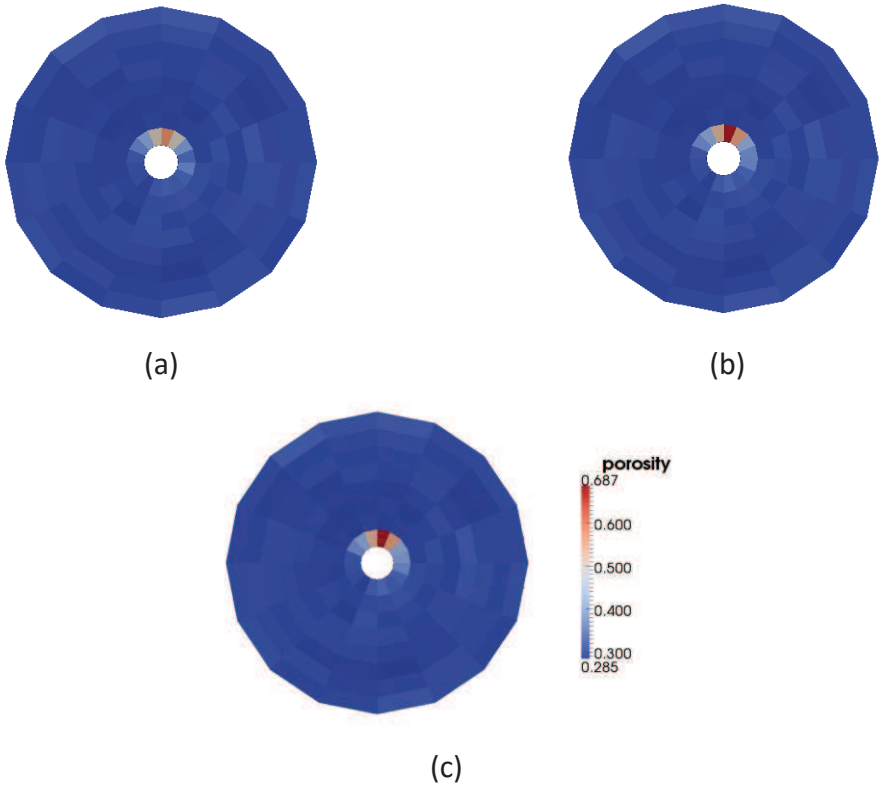

Fig. 9.14. FIELD1. Porosity in each fluid cell (xy plane) (a) at the end of the minimum flow-rate step, (b) at the end of the average flow-rate step, and (c) at the end of the maximum flow-rate step.

9.7.1.2. Microscale results

The contact forces between the particles are represented in Fig. 9.15. Fig. 9.16 shows the single particle nominal stress around the hole (the radial and the circumferential stresses) at the end of each simulation. Most of the particles that moved into the hole were at the same region as the contact break observed in Fig. 9.15. It is also the same region where fluid velocity was increased and the porosity decreased (Fig. 9.13 and Fig. 9.14).

The density of broken bonds at the end of the simulation is presented in Fig. 9.17. Although not presented here, it has been noticed that this maps are almost exactly the same at the end of the initial flow-rate step. That means that the majority of the bonds failed during that initial flow-rate step and that what caused breakage was the perforation. The bond shear failure mode is also presented. The majority of the broken bonds failed in shearing mode. In this case, bonds have broken in an extend region that is not exactly the same as the region where particles are produced.

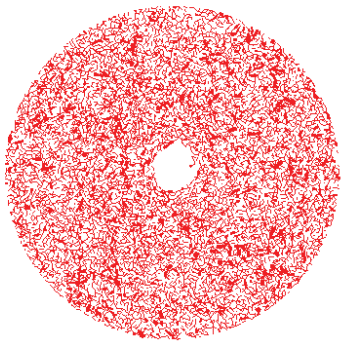

Fig. 9.15. FIELD1. Contact forces around the hole (mid-section horizontal projection; line thickness is proportional to force modulus) at the end of the simulation.

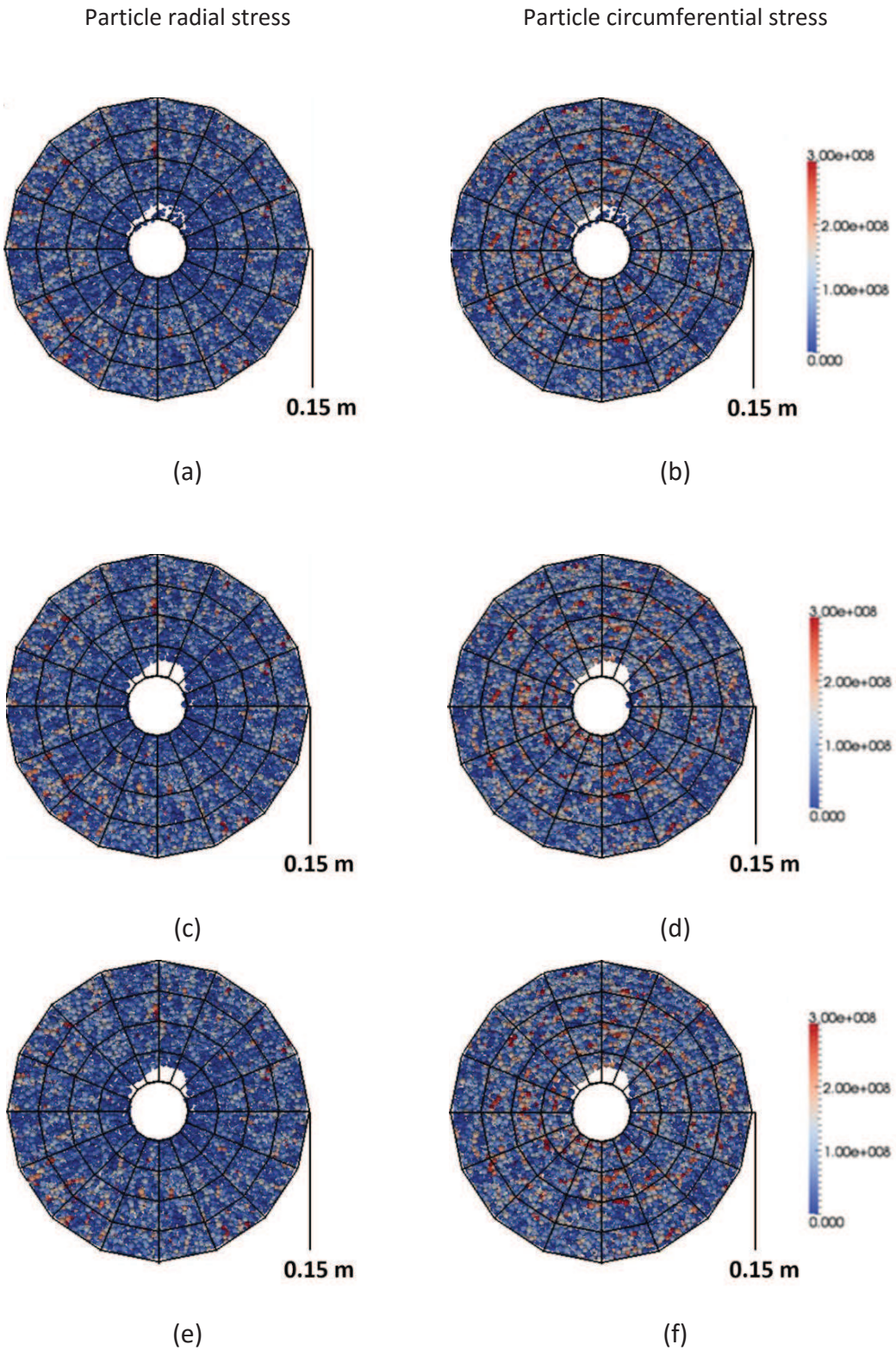

Fig. 9.16. FIELD1. Detail of particle stress in the inner zone (the outer radius represented is 150 mm, $R_o / 1.8$) a) Particle radial effective stress at the end of the minimum flow-rate step, and (b) particle circumferential effective stress at the end of the minimum flow-rate step, c) Particle radial effective stress at the end of the average flow-rate step, and (d) particle circumferential effective stress at the end of the average flow-rate step, e) Particle radial effective stress at the end of the maximum flow-rate step, and f) particle circumferential effective stress at the end of the maximum flow-rate step, (xy plane at specimen mid-height).

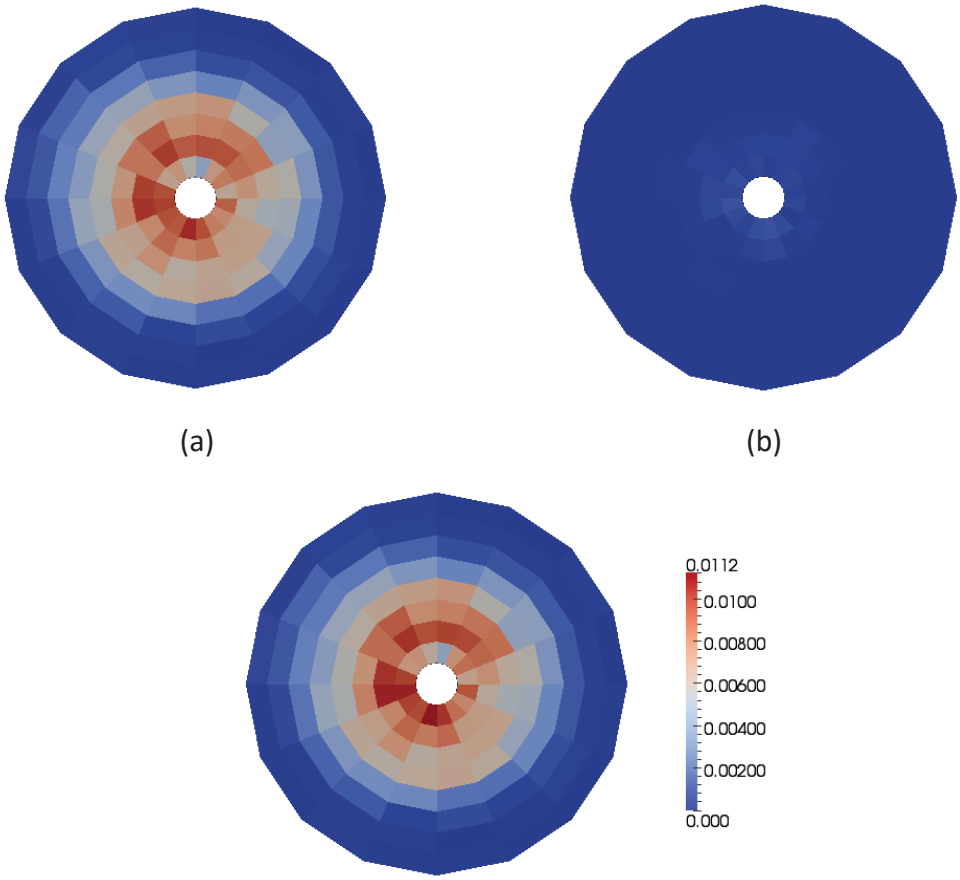

Fig. 9.17. FIELD1. (a) Number of shear failure per volume unit (m^{-3}) at the end of the simulation, (b) number of tensile failures per volume unit (m^{-3}) and (c) number of broken bonds per volume unit (m^{-3}) at the end of all the flow-rate steps (xy plane).

9.7.1.3. Sand production rates

The cumulative sand production rate (the mass of sand produced accumulated during time) and instantaneous sand production rate (the mass of sand produced evolution) are shown in Fig. 9.17. The results indicate a stable situation at the end of each fluid flow velocity step. Sand is mostly produced at the perforation stage under conditions of minimum flow rate. When the system reaches the steady state and it stops producing sand, the velocity is increased to the average velocity, creating another jump on absolute production until it reaches the steady state again. The later flow rate increase has less repercussion on the production of sand.

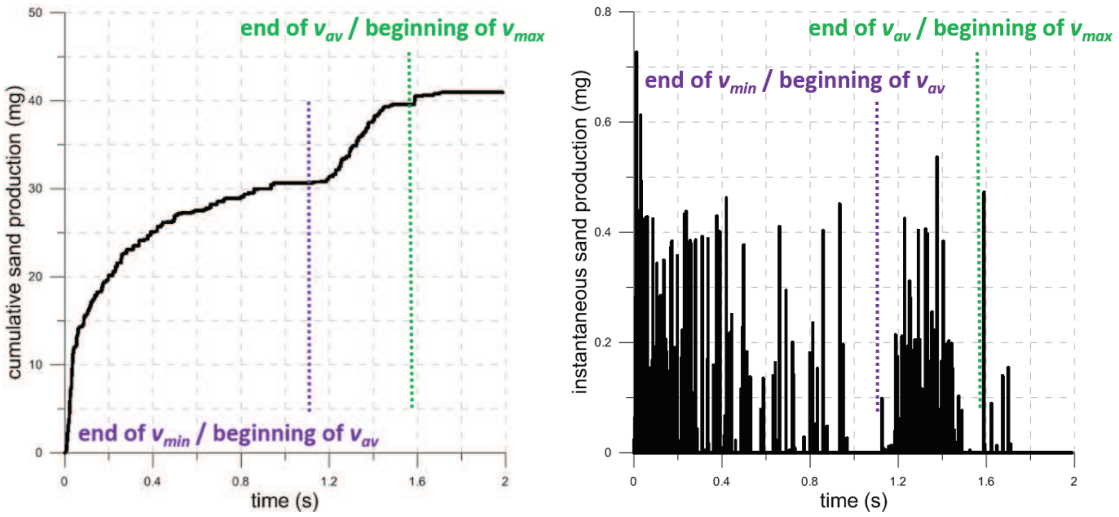

(a) cumulative sand production (b) instantaneous sand production

Fig. 9.18. FIELD1. Sand production during the simulation.

The sand production rate is 31 mg during the 1.1 s at the minimum velocity, this is equivalent to an average sand rate of approximately 3200 pptb. During the second phase of the simulation, with flow at the average velocity, the sand production rate is 9 mg during 0.5 s, an average of 180 pptb. Finally, in the third stage at the maximum flow rate, the sand production rate is 1 mg during 0.4 s, an average of 9 pptb. The sand rate given by IESL is 10 pptb (Table 9.1), which is the usual sand rate in oil reservoirs (Bellarby, 2009; Palmer et al., 2003).

9.7.2. FIELD2

The fluid velocity at the inner boundary was set to 0.49 mm/s, and the simulation was carried out during intervals of t_{sim} = 0.1 s to check the radial and the circumferential stresses and the sand production rate. In this case, the stresses were still decreasing and the sand rate was increasing. For that reason, it was needed 3 run periods of t_{sim} = 0.1 s and it was run for a total of 0.3 s. It was observed that the stress evolution had not stabilized but maintained a decreasing trend to although the sand rate was stabilized.

After that, the fluid velocity at the inner boundary was set to 0.51 mm/s, and the simulation was carried out again during t_{sim} = 0.1 s, observing that the stresses were still decreasing and the sand rate was increasing. One more period of t_{sim} = 0.1 s was needed to reach a stable sand rate. The average flow-rate step was carried out for a total of 0.2 s. Finally, the fluid velocity was increased at the inner boundary to 0.52 mm/s, and again two periods of t_{sim} = 0.1 s were needed to reach a stable sand production rate. The computational time required was between 1 and 2 months.

9.7.2.1. Mesoscale results

Fig. 9.19 shows the stress evolution for 3 different radial distances. It can be observed that the steady state is never reached. In this case, the sample is not stable and stresses tend to decrease. For this reason, it was decided to not wait until a steady state was reached and to increase the fluid velocity before all the sample plastified.

The stress distribution around the sample at the end of each flow-rate step is presented in Fig. 9.20. Observing these figures it seems that the limit between the plastic region and the elastic region is close to the outer radius. In this case, all the sample is plastifying. This result is different from the one predicted by the analytical solution (Fig. 9.1) where the sample remained elastic.

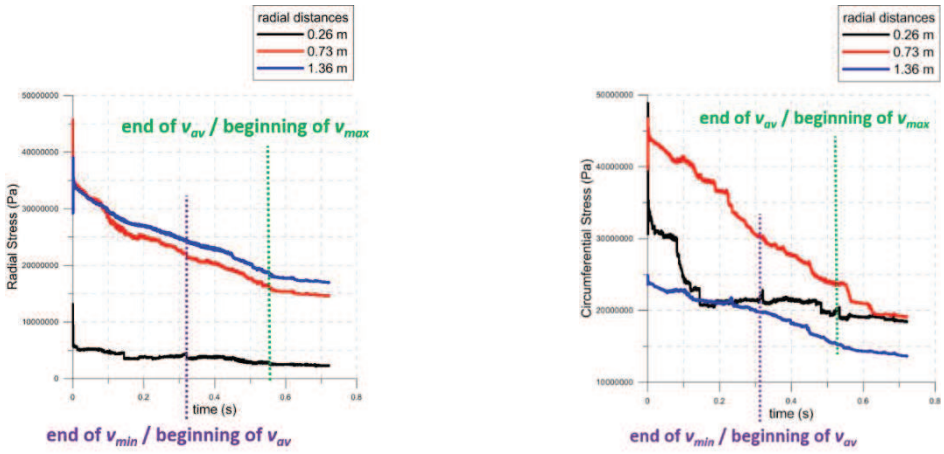

Fig. 9.19. FIELD2. Radial and circumferential stresses evolution at different radial distances from the inner boundary at the end of the simulation with the maximum fluid velocity

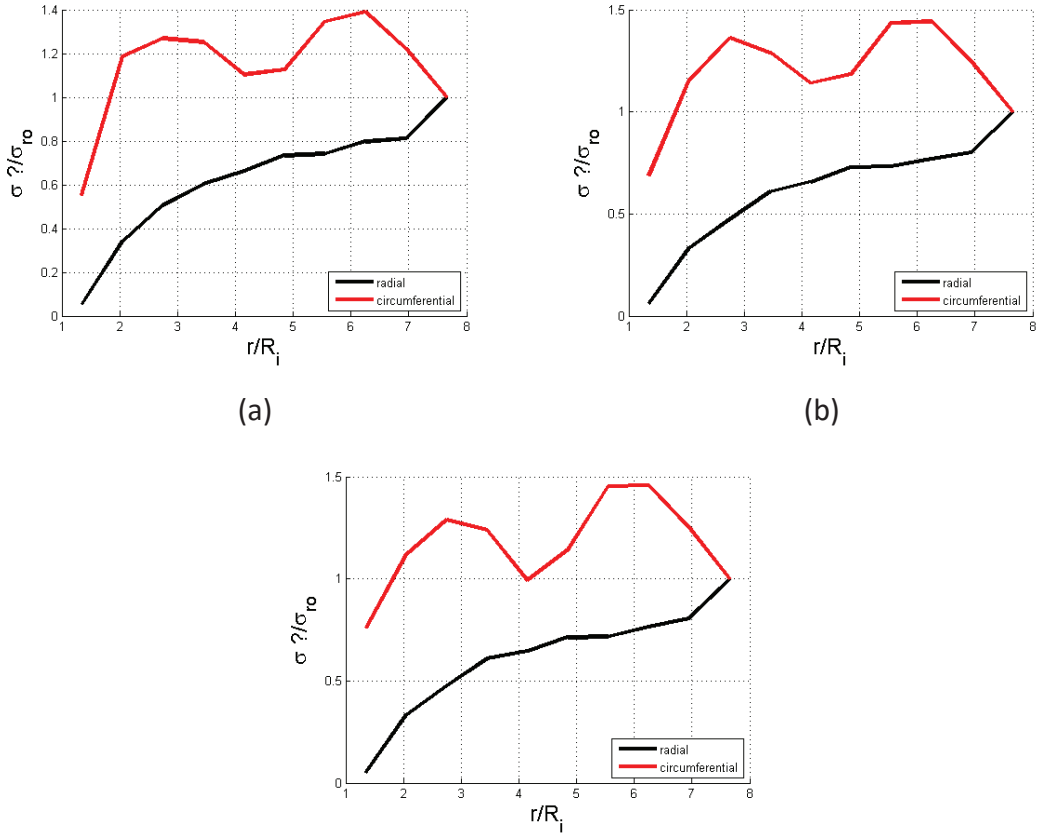

Fig. 9.20. FIELD2. Average total stresses as a function of normalized radial distance at the end of (a) the minimum flow-rate step, (b) the average flow-rate step, and (c) the maximum flow-rate step.

The fluid velocity filed at the end of the three different flow-rate steps is presented in Fig. 9.21. The porosity field is shown in Fig. 9.22. The regions of increased flow have a higher porosity value than the rest of the sample.

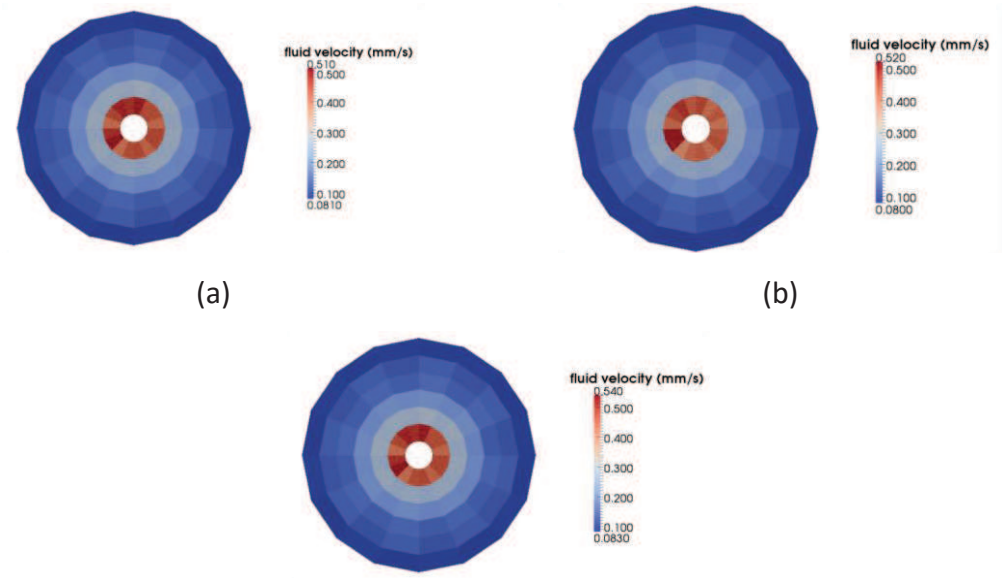

Fig. 9.21. FIELD2. Fluid velocity (xy plane) (a) at the end of the minimum flow-rate step, (b) at the end of the average flow-rate step, and (c) at the end of the maximum flow-rate step.

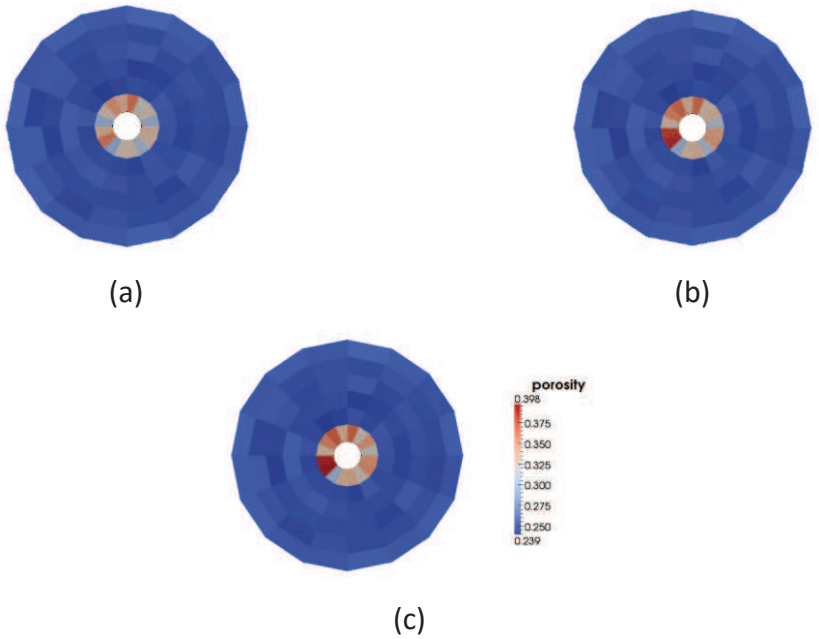

Fig. 9.22. FIELD2. Porosity in each fluid cell (xy plane) (a) at the end of the minimum flow-rate step, (b) at the end of the average flow-rate step, and (c) at the end of the maximum flow-rate step.

9.7.2.2. Microscale results

The contact forces between the particles are represented in Fig. 9.23. Fig. 9.24 shows the single particle nominal stress around the hole. In these figures a plastified zone with clear contacts broken and low circumferential stresses is not observed. The reason is that the all the sample is decreasing the stress and plastifying.

The density of broken bonds at the end of the simulation is presented in Fig. 9.25. The bond shear and tensile failures mode are also presented. The majority of the broken bonds failed in shearing mode. It can be observed that the broken bonds are distributed around all the sample, and not only close to the hole.

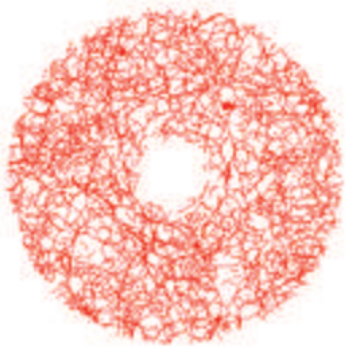

Fig. 9.23. FIELD2. Contact forces around the hole (mid-section horizontal projection; line thickness is proportional to force modulus) at the end of the simulation.

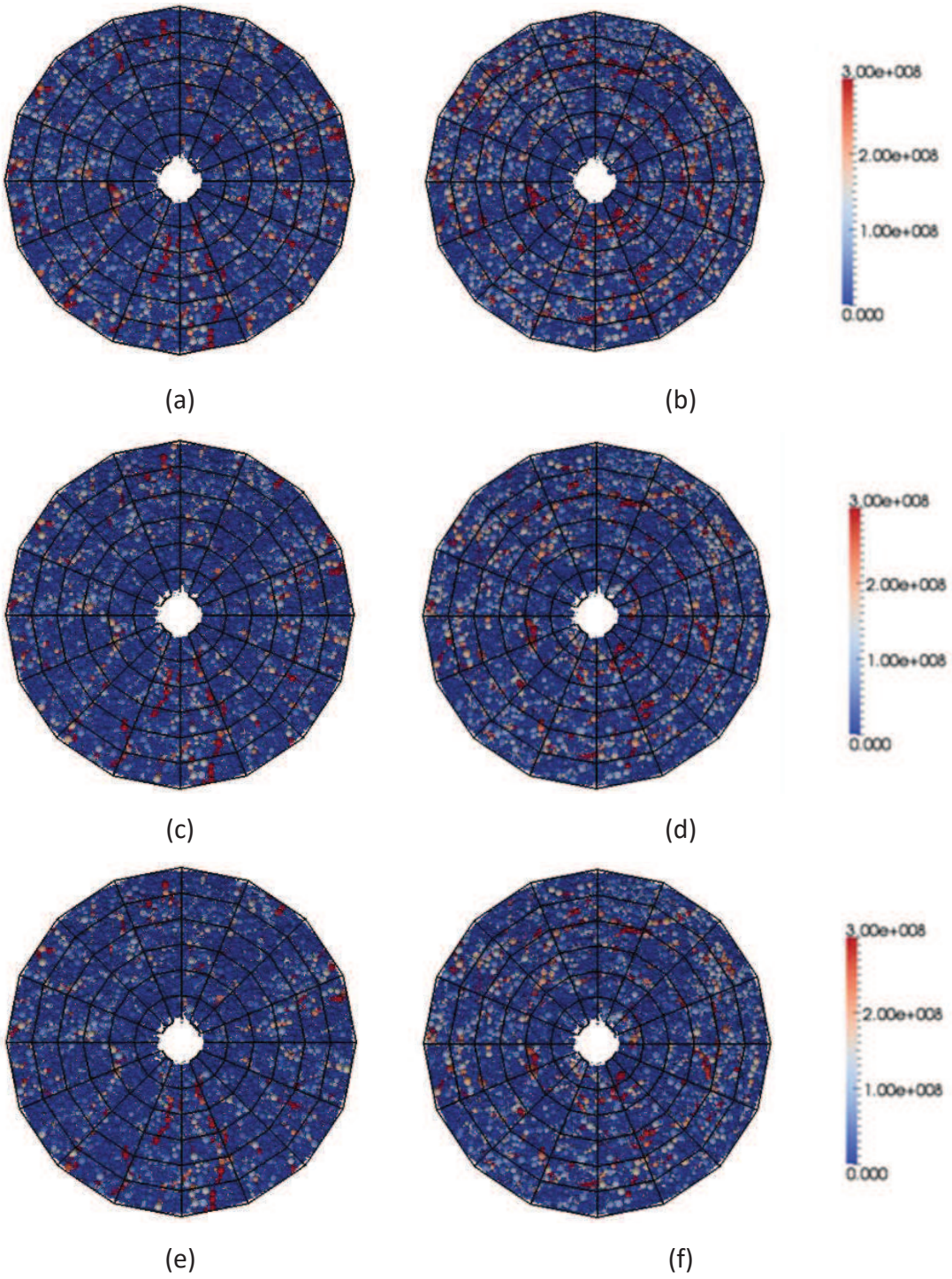

Fig. 9.24. FIELD2. Detail of particle stress in the inner zone (all the sample is represented) a) Particle radial effective stress at the end of the minimum flow-rate step, and (b) particle circumferential effective stress at the end of the minimum flow-rate step, c) Particle radial effective stress at the end of the average flow-rate step, and (d) particle circumferential effective stress at the end of the average flow-rate step, e) Particle radial effective stress at the end of the maximum flow-rate step, and f) particle circumferential effective stress at the end of the maximum flow-rate step, (xy plane at specimen mid-height).

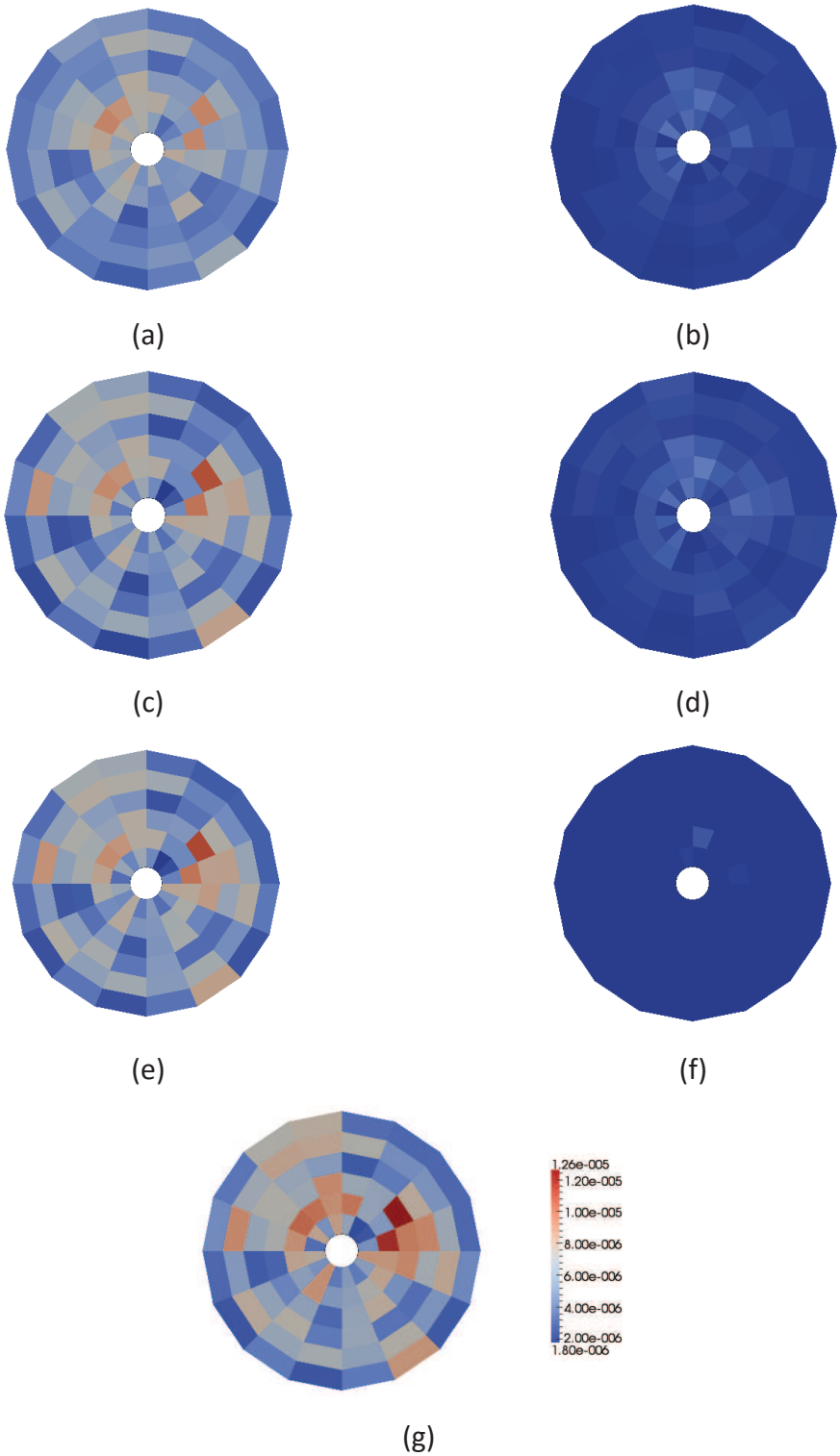

Fig. 9.25. FIELD2. (a) Number of shear failure per volume unit (m^{-3}) at the end of the minimum flow-rate step, (b) number of normal failure per volume unit (m^{-3}) at the end of the minimum flow-rate step, , (c) number of shear failure per volume unit (m^{-3}) at the end of the average flow-rate step, (d) number of normal failure per volume unit (m^{-3}) at the end of the average flow-rate step, (e) number of shear failure per volume unit (m^{-3}) at the end of the maximum flow-rate step, (f) number of normal failure per volume unit (m^{-3}) at the end of the maximum flow-rate step, and (g) number of normal failure per volume unit (m^{-3}) at the end of the maximum flow-rate step (xy plane).

9.7.2.3. Sand production rates

The cumulative sand production rate (the mass of sand produced accumulated during time) and instantaneous sand production rate (the mass of sand produced evolution) are shown in Fig. 9.26. Even though the stresses do not reach a steady state (Fig. 9.19), the sand production seems to indicate a more stable situation at the end of each flow velocity simulation.

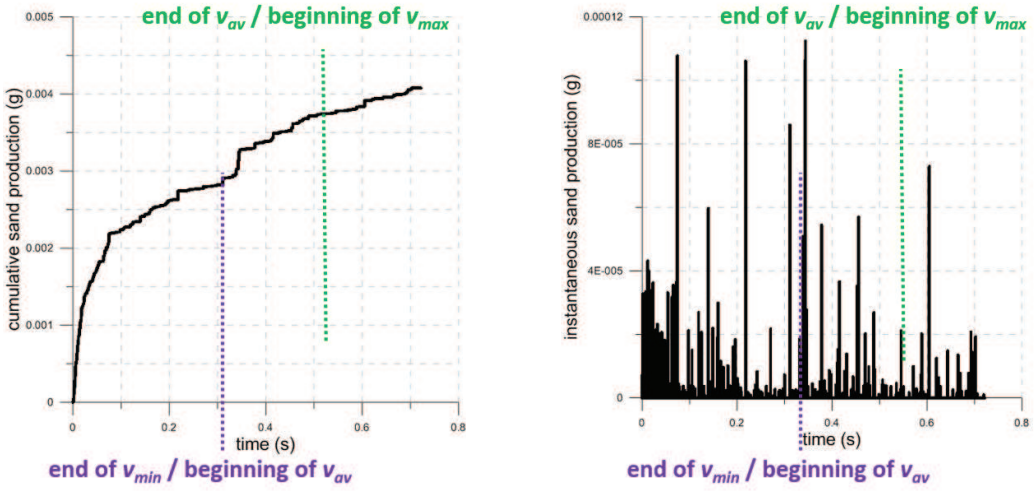

(a) cumulative sand production (b) instantaneous sand production

Fig. 9.26. FIELD2. Sand production during the simulation

The sand produced amounts to 0.0029 g during 0.3 s at the minimum velocity stage. This is equivalent to a sand production rate of some 30 pptb. During the second phase of the simulation, with the average velocity, the sand produced was 0.0009 g during 0.2 s, averaging to a production rate of 13 pptb. During the third phase of the simulation, at maximum velocity, the sand produced was 0.0003 g during 0.2 s, equivalent to a production rate of 5 pptb. This values are similar than usual sand rates in producing oil fields (10 pptb).

9.7.3. FIELD3

First of all, the fluid velocity at the inner boundary was set to 6.0 mm/s, and the simulation was carried out during intervals of t_{sim} = 0.1 s to check the radial and circumferential stresses and the sand production rate. After 0.1 s it was observed that the stresses have not changed and only one particle was produced. To assure that it was a stable state another interval of 0.1 s was carried out and it was observed the same steady state. The first flow-rate step was run for a total of 0.2 s. After that, the fluid velocity at the inner boundary was set to 15.0 mm/s, and the simulation was carried out again periods of t_{sim} = 0.1 s. Stresses were again observed to be stable, but some amount of sand was produced. In case this meant the beginning of a greater amount of sand production rate, 8 periods of t_{sim} = 0.1 s were carried out, and the maximum flow-rate step was simulated a total of 0.8 s. The computational time required was around 2 months.

9.7.3.1. Mesoscale results

Fig. 9.27 shows the stress evolution for 3 different radial distances. From these results it is concluded that the steady state was reached because stresses were stable. Moreover, it can be observed that stresses do not change during the simulation.

The stress distribution around the sample at the end of each fluid-flow step was exactly the same and it is presented in Fig. 9.28. In this case it seems that the sample does not plastify, and all the sample remains elastic. The stress at the inner boundary is much higher than the predicted by the analytical solution (Fig. 9.1).

The fluid velocity field at the end of each flow-rate step is presented in Fig. 9.29. The porosity field is shown in Fig. 9.30. The observed flow velocity is coherent with the porosity field at the end of the simulation. The regions of increased flow have a higher value than the rest of the sample.

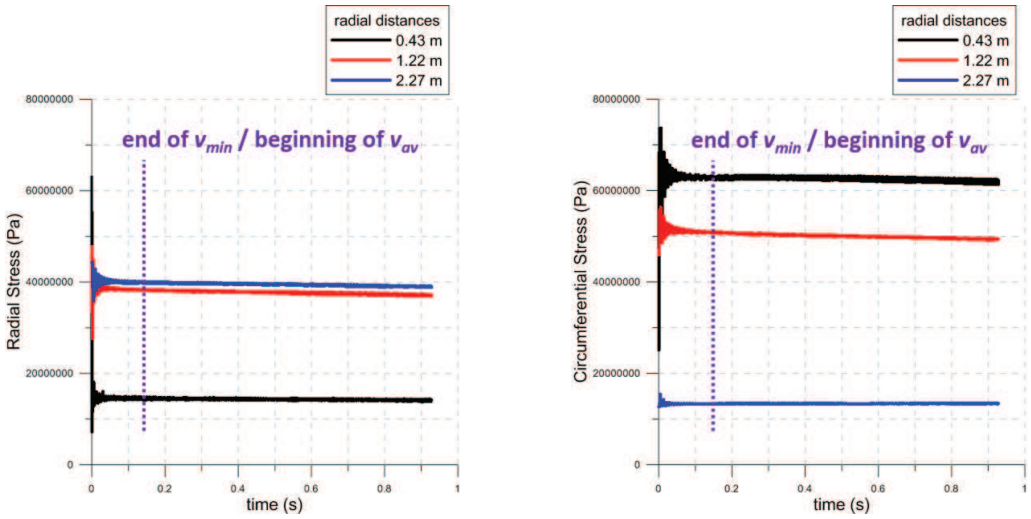

Fig. 9.27. FIELD3. Radial and circumferential stresses evolution at different radial distances from the inner boundary at the end of the simulation with the maximum fluid velocity.

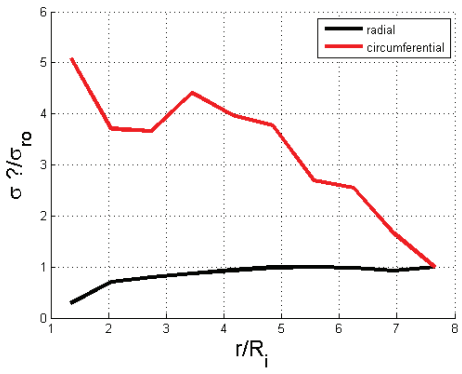

Fig. 9.28. FIELD3. Average total stresses as a function of normalized radial distance at the end of the simulation

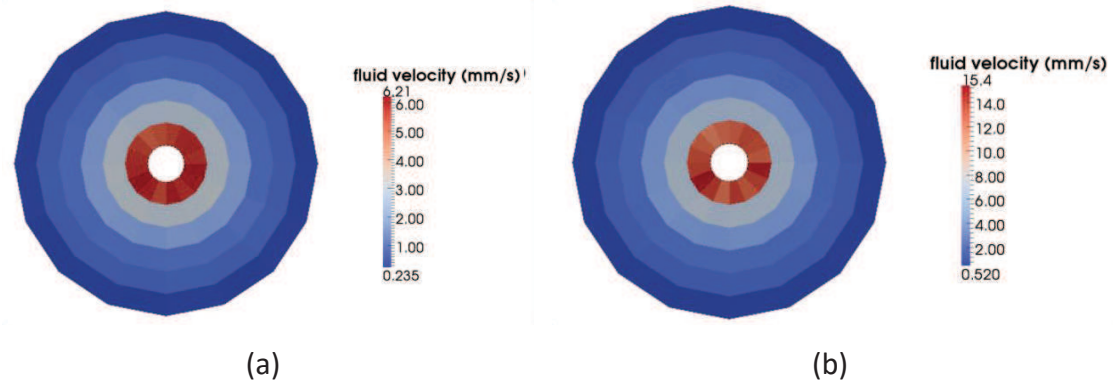

Fig. 9.29. FIELD3. Fluid velocity (xy plane) (a) at the end of the average flow-rate step, and (b) at the end of the maximum flow-rate step.

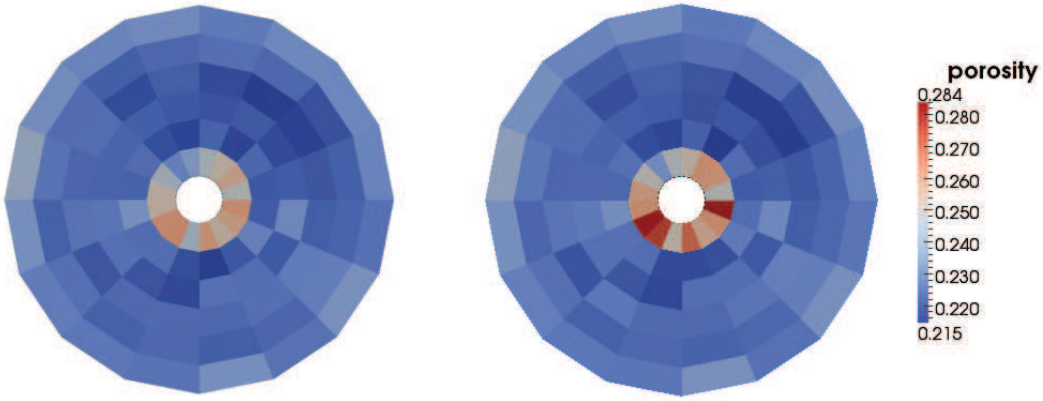

(a) (b)

Fig. 9.30. FIELD3. Porosity in each fluid cell (xy plane) (a) at the end of the average flow-rate step, and (b) at the end of the maximum flow-rate step.

9.7.3.2. Microscale results

Fig. 9.31 shows the single particle nominal stress around the hole. The contact forces between the particles are represented in Fig. 9.32. The region around the hole has not broken contacts and the stress values seem that do not decrease.

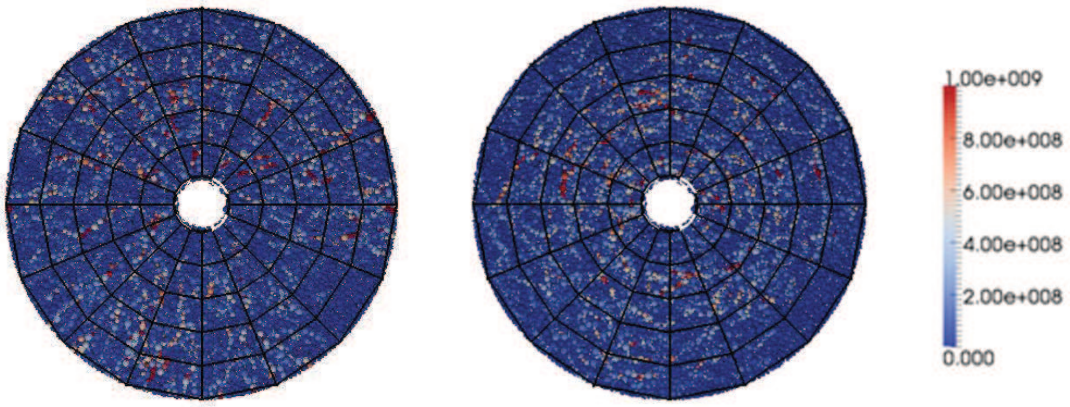

(a) (b)

Fig. 9.31. FIELD3. Detail of particle stress in the inner zone (all the sample is represented) a) Particle radial effective stress at the end of the simulation, and (b) particle circumferential effective stress at the end of the simulation (xy plane at specimen mid-height).

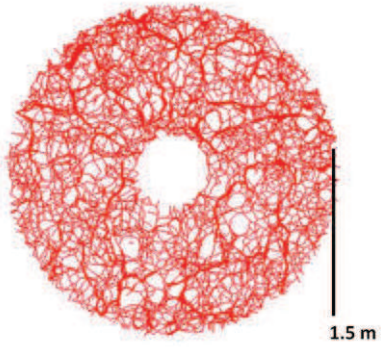

Fig. 9.32. FIELD3. Contact forces around the hole (mid-section horizontal projection; line thickness is proportional to force modulus) at the end of the simulation (the outer radius represented is 1.5 m, $R_o \big/ 1.6$).

9.7.3.3. Sand production rates

The cumulative sand production rate (the mass of sand produced accumulated during time) and instantaneous sand production rate (the mass of sand produced evolution) are shown in Fig. 9.33. In this case the sand production was virtually non-existent.

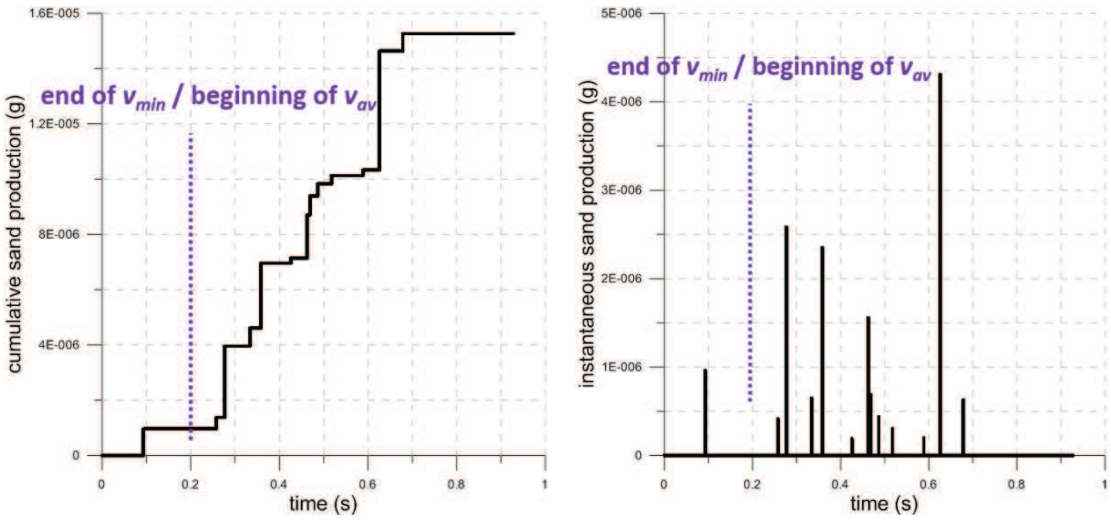

(a) cumulative (b) instantaneous

Fig. 9.33. FIELD3. Sand production during the simulation.

9.7.4. Discussion

Comparing the results of the three different materials, it can be concluded that three different responses are presented: a) the stresses do not change during the simulation (all the sample remains elastic and does not plastify around the hole) and no sand is produced (FIELD3), b) a steady state is reached at the end of the simulations (reaching a state with two regions, a plastic region and an elastic region) and sand is produced (also reaching a steady state) (FIELD1), and c) low sand is produced and the steady state is never reached (the whole sample plastifies) (FIELD2).

In the simulations where the sand is produced, the sand production rate increases at the beginning until it decreases. When the fluid velocity is increased, the sand production rate increases again. Sand rates have higher values when the minimum flow rate is applied. When the sand production stops, it starts again when the flow rate is increased. After that, the sand production has a lower value than the previous one because it has been reached an equilibrium before. If we compare the sand produced in FIELD1 and FIELD2 simulations with the field data (Table 9.1) we can conclude that this model overpredicts the amount of sand produced.

9.7.4.1. Comparison with preliminary sand production estimates: empirical prediction and analytical solution

As the empirical criterion introduced in Section 9.3.1 indicated, FIELD1 has produced sand. For FIELD2 the prediction for sand onset was that this field needed a very high drawdown to produce sand. The drawdown in our simulations was very low (around 400-500 Pa) and sand was produced. However, the sand produced in FIELD2 simulations was much lower than in FIELD1. The prediction for FIELD3 is consistent with the empirical criterion because it did not produce sand.

Comparing the stress distribution around the cavities with the ones predicted by the analytical solution in Section 9.3.2 it is observed that in all the fields the stress peak

prediction is lower than the one simulated. This result is the opposite as the one presented in Chapter 8 (Section 8.2.2, Fig. 8.3), where the peak stress is much higher in the analytical solution. This could be the reason why in the simulations in this chapter the majority of the broken bonds failed in the shear direction (because there is a higher circumferential stress). Simulations in Chapter 8 have the same bond strength and the same bond stiffness in the normal and the shear directions. On the other hand, in this chapter, the shear bond stiffness is higher than the normal bond stiffness for FIELD1 and FIELD2 ($\alpha_{ratio} < 1$ Table 5.7). Following Eq. 4.12 and Eq. 4.13, the shear force carried out by the bond is higher than the normal force and accordingly, the shear stress at the parallel-bond is also higher than the normal stress. The only sample that has a normal bond stiffness higher than the shear bond stiffness is FIELD3. However, FIELD3 has a very low number of bonds broken (80 of 151295 parallel-bond) and they are not statistically sufficient for a reliable conclusion.

FIELD1 simulation plastic radius (Fig. 9.12) is bigger than the analytical solution (Fig. 9.1b). FIELD3 plastic radius does not exist because it has not plastified and all the sample behaves elastically. FIELD2 simulation is the one that presents the most important difference between the analytical solution (Fig. 9.1d) and the simulation result (Fig. 9.20). In FIELD2 simulation all the sample plastified, while in the analytical solution the region that plastifies is a very small one around the cavity.

9.7.4.2. Drag force

Sometimes in petroleum engineering (e.g. Asgian et al., 1995) the fluid force considered is only the pressure gradient force (Eq. 6.23). To understand the difference between the drag force (Eq. 6.30) and the pressure gradient force in this kind of simulation, both are represented for FIELD2 after 0.2 s of the simulation in Fig. 9.34. Body force is the average of the drag forces on the particles in each cell. It can be observed that the minimum value of the drag force is 0.403 N and the maximum value of the pressure gradient force is 0.00008 N. It can be concluded that considering only the pressure gradient force in

the calculation of the fluid force, and not considering the drag force, significantly underestimates the fluid force.

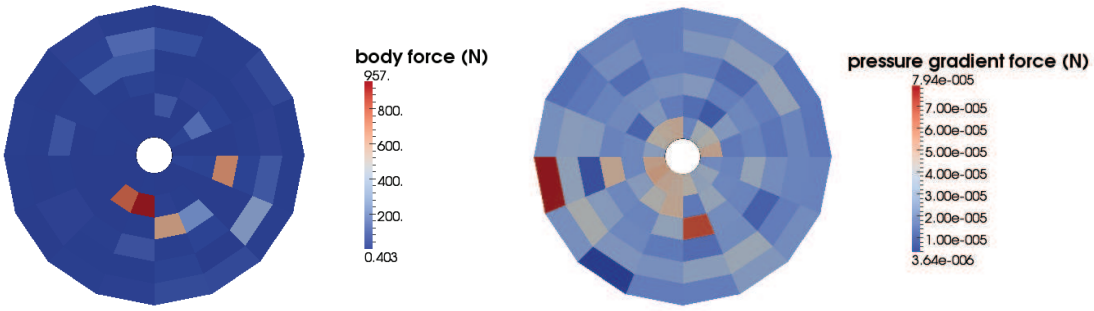

(a) (b)

Fig. 9.34. Average of the drag force (a) and the pressure gradient force (b) of FIELD2 simulation after 0.2s.

9.7.4.3. Drag force and bond breakage

As explained in Chapter 3 (Section 3.4), sand production is a process that involves two mechanisms: failure of the rock around the cavity and transportation of sand particles due to fluid drag. The failure of the rock is usually due to the distribution of the stresses when the perforation is initiated. In Section 3.4 it has also been commented that erosion can occur when the drag force of the fluid is large enough to overcome the cohesive strength of the material and carry the particles away.

We can calculate the minimum drag force needed to break a bond as a simple first approximation. To break a bond a force has to be applied in the normal direction of the bond (tensile failure) (Fig. 9.35). To break a bond the tensile stress due to that force has to be higher than the strength of the bond. The tensile stress is expressed as following Eq. 5.14 (because the rotation in this thesis is prevented, Section 5.3.3)

$$\left|\sigma_{\max,pb}\right| = \frac{F_{pb}^{N}}{A_{pb}} \qquad \text{Eq. 9.33}$$

where F_{pb}^{N} is the computed normal force at the parallel-bond and A_{pb} is the bond area, given by $A_{pb} = \pi R_{pb}^{2}$ (Section 4.4). Supposing that the normal force is the fluid frag force, the tensile stress in the bond is expressed as

$$\sigma_{drag} = \frac{F_d}{A_{pb}} \qquad \text{Eq 8.33}$$

when this tensile stress becomes greater than the bond strength, the bond breaks. Fig. 9.36 shows the tensile stress for pure drag force normalized by the strength of each bond versus the diameter of the particles for each one of the materials presented in this chapter and each one of the velocities. It can be concluded that the bonds that are easier to break due to the drag force are those of the smallest particles.

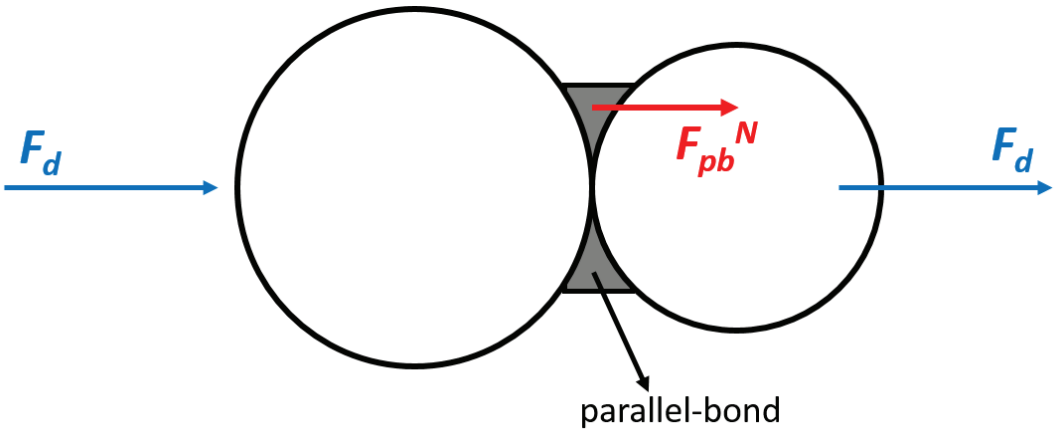

Fig. 9.35. Drag force applied on a parallel-bond.

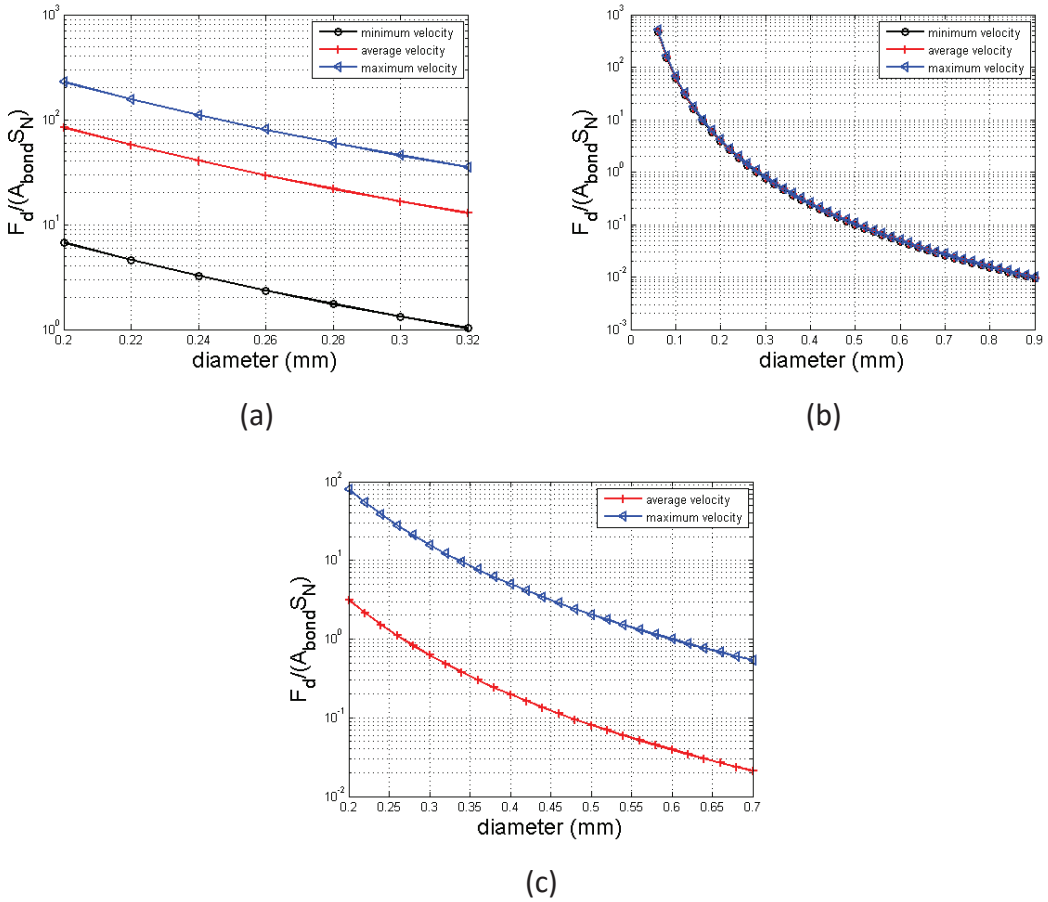

Fig. 9.36. Drag force divided by the bond area normalized by the bond strength for (a) FIELD1, (b) FIELD2, and (c) FIELD3.

PSD of the produced particles and the particles which bonds were broken during the simulations (FIELD1 and FIELD2) are presented in Fig. 9.37 and Fig. 9.38. It can be observed that for FIELD2 the particles that are produced and also the ones which bonds broke are the biggest particles. It seems that that the drag force is not the principal force that breaks the parallel-bonds. Moreover, as it is also appreciated in Fig. 9.17 and Fig. 9.25, the majority of the bonds break at the beginning of the simulation. This is consistent with the idea that the bonds break at the beginning of the simulations (when the inner wall is removed) due to the stress distribution around the cavity.

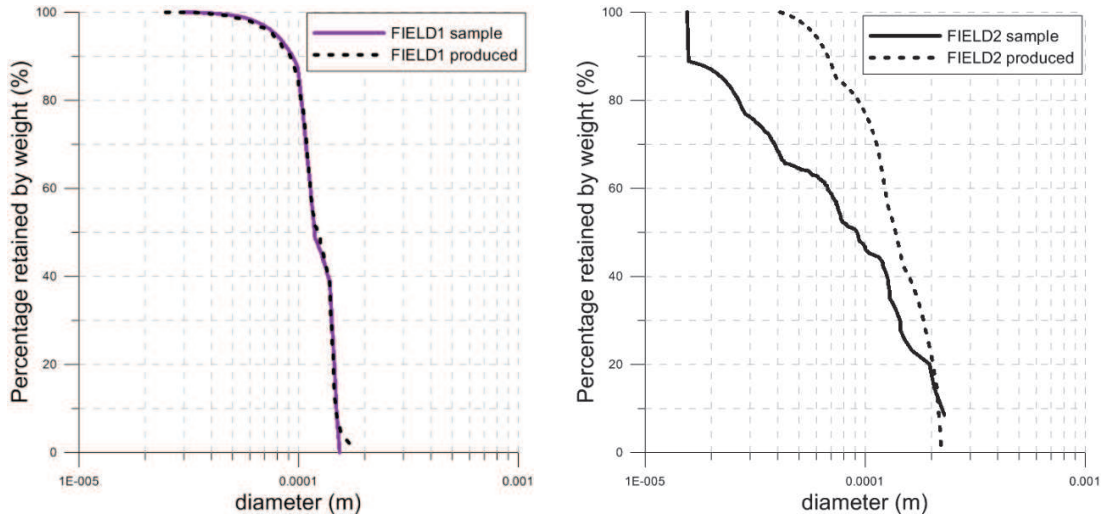

(a) (b)

Fig. 9.37. PSD of the produced particles at the end of the simulation for (a) FIELD1, and (b) FIELD2.

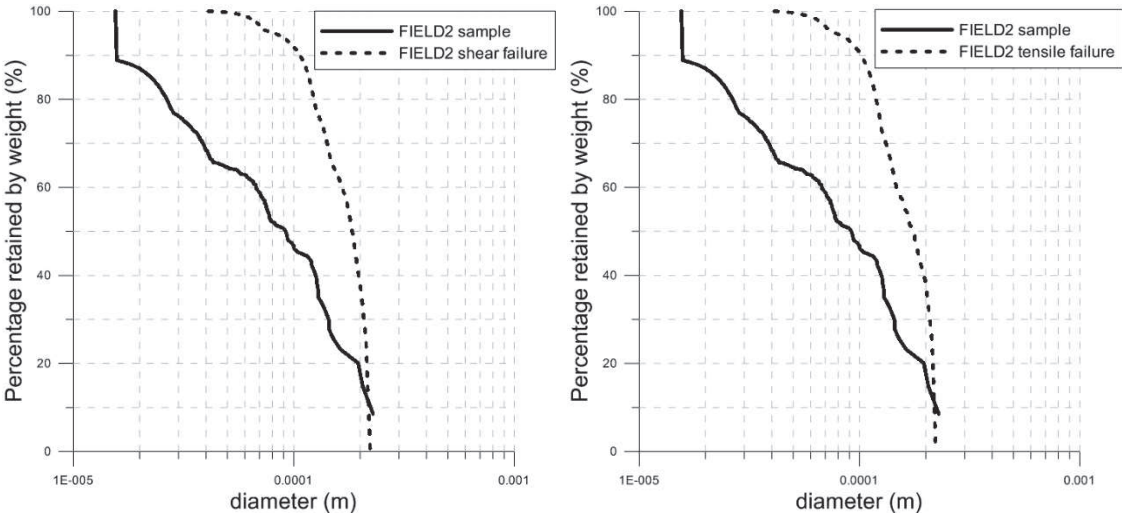

(a) (b)

Fig. 9.38. PSD of the particles of FIELD2 which bonds broke in (a) shear failure, and (b) tensile failure

9.8. Summary

Field data from three different oil fields (FIELD1, FIELD2 and FIELD3) was provided by IESL: stresses, pore pressure, geometry, oil properties, flow rates and sand production. The mechanical properties of the sandstones of these fields were previously calibrated in Chapter 5. As first approximations, an empirical model representative of current industrial approaches to predict the onset of sand production predicts that FIELD1 will

produce, FIELD2 will produce when the fluid pressure at the cavity is smaller than 4.6 MPa and, FIELD3 will not produce sand at all. On the other hand, the Risnes analytical solution suggests that the situation is more unfavourable for FIELD2 than for FIELD1, opposite of what was suggested by the empirical criterion. Both the empirical criterion and the analytical solution suggest that FIELD 3 conditions are the most favourable.

The geometry of the models represent a horizontal slice of a confined vertical cylinder of sandstone with a cylindrical hole in the middle. The outer radius has to be about 8-10 times the inner radius and the perimeter of the internal hole should contain at least 20 particles, and the height of the model should be big enough to contain at least 4 or 5 particles to decrease the risk of artificial arching. To obtain results in a reasonable amount of time models must have around 50000 particles and the simulation time step cannot be much smaller of 10^{-8} s. To attain a desired time step of around 10^{-8} s particles in each one of the materials has been scaled up a factor *N*. This factor depends on the effective stiffness calibrated in Chapter 5 and the coordination number. Finally, due to all these constrains, the final model geometry parameters, as the inner radius and the height, cannot be the same as the original field. This difference should be taken into account when the boundary conditions are calculated and applied in order to be able to compare results.

The CFD cells are hexahedral and are created dividing the geometry in three directions: radial, vertical and circumferential. To size the CFD mesh the general criterion is to be able to accommodate a statistically significant number of particles within a single fluid cell, so that the effect of particles on fluid flow changes smoothly. The boundary conditions are given fluid flow extraction rate at the inner boundary (an imposed fluid velocity which goes inside the hole) and imposed fluid pressure at the outer boundary. Due to the scaling of the particles, the particle-fluid interaction must be also scaled. Fluid forces exerted on the particles are dependent on the particle radii. The drag force is scaled changing the density and the viscosity, and the pressure gradient force and the buoyancy force are changed directly during the interaction. The porosities of the DEM models used in this chapter are higher than the porosities of the reference sandstones. This mismatch is corrected transforming and adjusting before transferring information between DEM and CFD.

Three different responses are presented in the results: a) the stresses do not change during the simulation (all the sample remains elastic and does not plastify around the hole) and no sand is produced (FIELD3), b) a steady state is reached at the end of the simulations (reaching a state with two regions, a plastic region and an elastic region) and sand is produced (also reaching a steady state) (FIELD1), and c) low sand is produced and the steady state is never reached (the whole sample plastifies) (FIELD2). Comparing the sand produced in FIELD1 and FIELD2 simulations with the field data we can conclude that this model overpredicts the amount of sand produced.

The results for FIELD1 and FIELD3 are consistent with the empirical model used in the petroleum industry. On the other hand, the empirical model predicted that FIELD2 would have not produced sand in the field conditions given by data. In our model FIELD2 has produced sand. However, the amount of sand produced is very low compared to FIELD1 sand production.

The peak stresses of the numerical stress distribution around the cavity are higher than the predicted by the analytical solution. The reason of that difference could be that the shear bond stiffness is higher than the normal bond stiffness, leading to a shear force higher than the normal force carried out by the bond. Due to that difference the circumferential stresses of the particles become higher, and also bonds become easier to break in the shear direction.

The drag force has been compared to the pressure gradient force (usually considered as the only fluid force in petroleum engineering). The drag force in one of the models (FIELD2) is 4 orders of magnitude higher than the pressure gradient force. Considering only the pressure gradient force the fluid force is significantly underestimate.

The PSDs of the particles that have been produced and the particles which bonds have broken have been represented. In FIELD2 the particles which bonds have broken are the biggest particles of the model. An estimation study of the drag force as a possible cause of the breakage of a bond has led us to conclude that it would be the bonds of the smallest particles the ones that would break if the drag force was the main cause (or an important cause) of the bonds breakage. It seems that the main reason of the breakage of the parallel-bonds is the stress distribution around the cavity due to the perforation.

Chapter 10 – Conclusion

This thesis has presented a study of the sand production process using a coupled CFD-DEM model. The study has involved the calibration of the DEM rock model against real data, a validation of the CFD-DEM model by performing single particle simulations and analyses of permeability tests, simulations of sand production using a homogeneous sandstone analogue and, finally, the simulation of sand production under realistic conditions. Limitations of the DEM model have been explored and sensitivity analyses examining the effects of the local damping have been performed. In addition, micro-mechanical analyses have been carried out to get a better understanding of the CFD-DEM model and the mechanisms involved in sand production. This chapter summarises the key points that can be concluded from this research.

10.1. DEM rock model and calibration

In this thesis, the parallel-bond in PFC^{3D} with the linear friction model has been used to mimic the mechanical behaviour of rock and sandstone. The calibration of the contact parameters had to be performed using reference macro parameters obtained in the laboratory. Since the objective is to use this rock model in simulations of sand production problems, a number of points required especial consideration:

- Due to practical computational constraints, the time step and the number of particles had to be limited in order to attain reasonable computation times.
- Scale-independent micro-parameters have been used so that mechanical response remains invariant to scaling.
- The proper representation of the interaction between particles influence the selection of some properties such as the PSD and the porosity.

The rock mechanical properties of three different materials used for calibration have been presented. The following properties have been used to calibrate the contact model parameters: the Young modulus, the Poisson ratio and the uniaxial compressive strength given. The calibration has involved simulating a significant number of triaxial and axial compression tests. The stiffness is calibrated based on the computed and observed Young's modulus, the ratio between the normal and the shear stiffness is calibrated from the Poisson's ratio computed in simulated the triaxial tests and the bond strength and parameter λ are obtained from the comparison between the computed and observed uniaxial compression strength.

The fact that the calibration was performed with a higher value of porosity compared to that of the field data explains the differences observed when comparing the calibrated parameters with those obtained by other researchers.

10.2. Validation of the CFD-DEM model

Simulations using a single particle have been performed to test the CFD-DEM coupled model. Single particle simulations give the opportunity to compare the results with an analytical solution such as the Stokes equation for small particle Reynolds numbers. Some conclusions from those simulations are

- CFD-DEM model reproduced correctly the Stokes solution in all the cases.
- Increasing the fluid viscosity always increase the time to achieve the equilibrium.
- Local damping increases the time to equilibrium when the particle is dragged by the fluid, but decreases it when the particle is decelerated by the fluid.
- The choice of the local damping in DEM can have an important effect in DEM simulations. This effect must be considered and explored in coupled simulations.

A study of the permeability of a specimen has been also performed. The result is within the margin predicted by the Kozeny-Carman equation as long as the particle Reynolds number remains below 1 (a limit consistent with that obtained in experimental studies).

10.3. Sand production simulations on idealized sandstone

A first simulation without fluid of an ideal sandstone idealization has been carried out and the results compared with an analytical solution (Risnes et al., 1982). Subsequently, sand production has been simulated using different fluid flow conditions. Conclusions from those simulations can be summarized as:

- There was an overall good match between the numerical and the analytical solutions but differences are observed concerning the peak values of the circumferential effective stress.
- DEM can reproduce the dynamic process where stress equilibrium is only reached at the end of the process and the fact that particles are produced. This is more realistic than analytical solutions where the process is considered quasi-static.
- Asymmetries in the rock can lead to an asymmetry in the pattern of stress and plastic region around the hole. DEM is capable to reproduce those asymmetries.
- When hydrostatic conditions are applied, the fluid acts as a damping force decelerating the particles because the fluid velocity is lower than the particles' velocity. Consequently, the sand production starts later than in the simulation without fluid and the plastic region is smaller at the end of the simulation.
- When the fluid flow velocity is increased the plastic region increases, as predicted in the analytical solutions. The fluid flow velocity also increases the sand production rate.

- Local damping decreases the number of broken contacts around the wellbore and reduces the plastic region. Local damping has a more important effect on the results when no fluid flow is applied.

10.4. Sand production analysis with fluid flow near producing wells using field data

Sand production analysis of three different field data have been performed. Significant features of the analyses were:

- Particles were scaled up to reduce the DEM time step. Due to the scaling of the particles, the fluid had also to be scaled in order to have the required interaction between particles and fluid.
- The dimensional proportions have to be modified to reduce the number of particles and to attain acceptable computing times.
- The porosity had to be adjusted for the coupling between DEM and CFD because the DEM porosity was not the same as the one corresponding to the real field data.

The simulations for each oil well were performed using different fluid velocities. Different patterns of results have been obtained:

- No plastification occurs in the domain and no sand is produced.
- Plastification around the hole occurs but elastic behavior remains in some regions of the domain. Sand is produced.
- All the domain becomes elastic and sand is produced.

Finally, comparing the drag force with the gradient pressure force and the strength of the parallel-bonds, we have observed that

- Not considering the drag force in the calculation leads to a severe underestimation of the fluid force.
- The drag force increases the probability of a bond breakage for smaller particles.
- It appears that the drag force is not the principal force that breaks the parallel-bonds. Instead the main cause of breakage is the stress distribution around the cavity when the perforation is performed.

10.5. Future work

Based on the development and the results of the research reported in the Thesis, further study of the PBM calibration, of the coupled fluid-particle model and of the sand production simulations is proposed.

10.5.1. Improvement of the PBM calibration

The PBM calibration is still somewhat simplistic. The difference between the number of macro properties and micro properties to be calibrated is high and some simplifying hypotheses have been assumed. A better calibration of PBM parameters should be developed; using more macro parameters in the procedure is suggested. In sand production problems, creating a sample that can represent the porosity and PSD of the original data would improve the calibration parameters and also the coupling between the fluid and the particles (removing the need to change the porosity in the coupling definition).

The PBM calibration has been performed using a scale-independent formulation. However, the effect of the scaling up should be studied further, especially the scaling of the interaction between particles and fluid.

10.5.2. Improving the coupling fluid-particle model

The fluid-particle model used in this work has the advantage of considering also the effect of the particles on the fluid. Moreover, the fluid velocity is affected by the porosity change and the movement of the particles, which gives a better understanding of the effect of the fluid around the wellbore, where porosity and fluid velocity direction changes are larger. However, the fluid-particle model cannot simulate the actual pressure of the fluid on each particle, as only the effect of pressure gradients on the particles is considered. A coupling model which could incorporate the effect of the pressure on the particles could improve the simulations of san production under hydrostatic conditions.

10.5.3. Effect of the perforation relative dimensions in sand production simulations

In this work, the perforation dimensions had to be changed because of the restriction in the number of particles necessary to achieve a reasonable computation time. Even though a scaling on the results have been done, the ratio between the wellbore radii and the particle radii is different than the real data field. The effect of changing this ratio should be examined.

Chapter 10 – Conclusion

This thesis has presented a study of the sand production process using a coupled CFD-DEM model. The study has involved the calibration of the DEM rock model against real data, a validation of the CFD-DEM model by performing single particle simulations and analyses of permeability tests, simulations of sand production using a homogeneous sandstone analogue and, finally, the simulation of sand production under realistic conditions. Limitations of the DEM model have been explored and sensitivity analyses examining the effects of the local damping have been performed. In addition, micro-mechanical analyses have been carried out to get a better understanding of the CFD-DEM model and the mechanisms involved in sand production. This chapter summarises the key points that can be concluded from this research.

10.1. DEM rock model and calibration

In this thesis, the parallel-bond in PFC^{3D} with the linear friction model has been used to mimic the mechanical behaviour of rock and sandstone. The calibration of the contact parameters had to be performed using reference macro parameters obtained in the laboratory. Since the objective is to use this rock model in simulations of sand production problems, a number of points required especial consideration:

- Due to practical computational constraints, the time step and the number of particles had to be limited in order to attain reasonable computation times.
- Scale-independent micro-parameters have been used so that mechanical response remains invariant to scaling.
- The proper representation of the interaction between particles influence the selection of some properties such as the PSD and the porosity.

The rock mechanical properties of three different materials used for calibration have been presented. The following properties have been used to calibrate the contact model parameters: the Young modulus, the Poisson ratio and the uniaxial compressive strength given. The calibration has involved simulating a significant number of triaxial and axial compression tests. The stiffness is calibrated based on the computed and observed Young's modulus, the ratio between the normal and the shear stiffness is calibrated from the Poisson's ratio computed in simulated the triaxial tests and the bond strength and parameter λ are obtained from the comparison between the computed and observed uniaxial compression strength.

The fact that the calibration was performed with a higher value of porosity compared to that of the field data explains the differences observed when comparing the calibrated parameters with those obtained by other researchers.

10.2. Validation of the CFD-DEM model

Simulations using a single particle have been performed to test the CFD-DEM coupled model. Single particle simulations give the opportunity to compare the results with an analytical solution such as the Stokes equation for small particle Reynolds numbers. Some conclusions from those simulations are

- CFD-DEM model reproduced correctly the Stokes solution in all the cases.
- Increasing the fluid viscosity always increase the time to achieve the equilibrium.
- Local damping increases the time to equilibrium when the particle is dragged by the fluid, but decreases it when the particle is decelerated by the fluid.
- The choice of the local damping in DEM can have an important effect in DEM simulations. This effect must be considered and explored in coupled simulations.

A study of the permeability of a specimen has been also performed. The result is within the margin predicted by the Kozeny-Carman equation as long as the particle Reynolds number remains below 1 (a limit consistent with that obtained in experimental studies).

10.3. Sand production simulations on idealized sandstone

A first simulation without fluid of an ideal sandstone idealization has been carried out and the results compared with an analytical solution (Risnes et al., 1982). Subsequently, sand production has been simulated using different fluid flow conditions. Conclusions from those simulations can be summarized as:

- There was an overall good match between the numerical and the analytical solutions but differences are observed concerning the peak values of the circumferential effective stress.
- DEM can reproduce the dynamic process where stress equilibrium is only reached at the end of the process and the fact that particles are produced. This is more realistic than analytical solutions where the process is considered quasi-static.
- Asymmetries in the rock can lead to an asymmetry in the pattern of stress and plastic region around the hole. DEM is capable to reproduce those asymmetries.
- When hydrostatic conditions are applied, the fluid acts as a damping force decelerating the particles because the fluid velocity is lower than the particles' velocity. Consequently, the sand production starts later than in the simulation without fluid and the plastic region is smaller at the end of the simulation.
- When the fluid flow velocity is increased the plastic region increases, as predicted in the analytical solutions. The fluid flow velocity also increases the sand production rate.

- Local damping decreases the number of broken contacts around the wellbore and reduces the plastic region. Local damping has a more important effect on the results when no fluid flow is applied.

10.4. Sand production analysis with fluid flow near producing wells using field data

Sand production analysis of three different field data have been performed. Significant features of the analyses were:

- Particles were scaled up to reduce the DEM time step. Due to the scaling of the particles, the fluid had also to be scaled in order to have the required interaction between particles and fluid.
- The dimensional proportions have to be modified to reduce the number of particles and to attain acceptable computing times.
- The porosity had to be adjusted for the coupling between DEM and CFD because the DEM porosity was not the same as the one corresponding to the real field data.

The simulations for each oil well were performed using different fluid velocities. Different patterns of results have been obtained:

- No plastification occurs in the domain and no sand is produced.
- Plastification around the hole occurs but elastic behavior remains in some regions of the domain. Sand is produced.
- All the domain becomes elastic and sand is produced.

Finally, comparing the drag force with the gradient pressure force and the strength of the parallel-bonds, we have observed that

- Not considering the drag force in the calculation leads to a severe underestimation of the fluid force.
- The drag force increases the probability of a bond breakage for smaller particles.
- It appears that the drag force is not the principal force that breaks the parallel-bonds. Instead the main cause of breakage is the stress distribution around the cavity when the perforation is performed.

10.5. Future work

Based on the development and the results of the research reported in the Thesis, further study of the PBM calibration, of the coupled fluid-particle model and of the sand production simulations is proposed.

10.5.1. Improvement of the PBM calibration

The PBM calibration is still somewhat simplistic. The difference between the number of macro properties and micro properties to be calibrated is high and some simplifying hypotheses have been assumed. A better calibration of PBM parameters should be developed; using more macro parameters in the procedure is suggested. In sand production problems, creating a sample that can represent the porosity and PSD of the original data would improve the calibration parameters and also the coupling between the fluid and the particles (removing the need to change the porosity in the coupling definition).

The PBM calibration has been performed using a scale-independent formulation. However, the effect of the scaling up should be studied further, especially the scaling of the interaction between particles and fluid.

10.5.2. Improving the coupling fluid-particle model

The fluid-particle model used in this work has the advantage of considering also the effect of the particles on the fluid. Moreover, the fluid velocity is affected by the porosity change and the movement of the particles, which gives a better understanding of the effect of the fluid around the wellbore, where porosity and fluid velocity direction changes are larger. However, the fluid-particle model cannot simulate the actual pressure of the fluid on each particle, as only the effect of pressure gradients on the particles is considered. A coupling model which could incorporate the effect of the pressure on the particles could improve the simulations of san production under hydrostatic conditions.

10.5.3. Effect of the perforation relative dimensions in sand production simulations

In this work, the perforation dimensions had to be changed because of the restriction in the number of particles necessary to achieve a reasonable computation time. Even though a scaling on the results have been done, the ratio between the wellbore radii and the particle radii is different than the real data field. The effect of changing this ratio should be examined.

Bibliography

Ahrens, J., Geveci, B., & Charles, L. (2005). *ParaView: An End-User Tool for Large Data Visualization, Visualization Handbook*, Elsevier, ISBN-13: 978-0123875822.

Al-Awad, M. N. J. & Al-Ahaidib, T. Y. (2005). Estimating the amount of free sand in the yielded zone around vertical and horizontal oil wells. *SPE Technical Symposium of Saudi Arabia Section.* Dharan, SA.

Alvarado, G. (2007). *Influence of late cementation on the behaviour of reservoir sands* (PhD thesis). University of London, UK.

Anderson, T. B., & Jackson, R. (1967). A fluid mechanical description of fluidized beds. *Industrial and Engineering Chemistry Fundamentals, 6(4)*, 527–539.

Arroyo, M., Butlanska, J., Gens, A., Calvetti, F., & Jamiolkowski, M. (2011). Cone penetration tests in virtual calibration chamber. *Géotechnique, 61*, 525-531.

Asgian, M. I., Cundall, P. A. & Brady, B. H. G. (1995). The mechanical stability of propped hydraulic fractures: a numerical study. *Proceedings of the SPE 69th Annual Technical Conference and Exhibition* (Vol. 1, pp. 475-489), New Orleans, US.

Batchelor, G.K. (2000). *An introduction to fluid dynamics*. Cambridge University Press.

Bear, J. (1972). *Dynamics of fluids in porous media*. Elsevier.

Beetstra, R., van der Hoef, M. A., & Kuipers, J. A. M. (2006). Drag force from lattice Boltzmann simulations of intermediate Reynolds number flow past mono- and bidisperse arrays of spheres. *AIChE Journal*, *53*.

Beetstra, R., van der Hoef, M. A., & Kuipers, J. A. M. (2007). Numerical study of segregation using a new drag force correlation for polydisperse systems derived from lattice-Boltzmann simulations. *Chemical Engineering Science, 62*, 246-255.

Bellarby, J. (2009). *Well completion design*. Developments in Petroleum Science, Vol. 56. Oxford: Elsevier.

Benyahia, S., Syamial, M., & O'Brien, T. J. (2006). Extension of Hill-Koch-Ladd drag correlation over all ranges of Reynolds number and solids volume fraction. *Powder Technology*, *162*, 166-174.

Berg, R. R. (1986). *Reservoir Sandstones*. Englewood Cliffs, NJ: Prentice Hall.

Bibobra, I., Sylvester, O., & John-Lander, I. (2015). Minimizing the risk of erosion damage of some wells in Niger Delta Field with clampon DSP monitor. *International Journal of Petroleum Engineering, 2(4)*, 121-127.

Bokkers, G. A., van Sint Annaland, M., & Kuipers, J. A. M. (2004). Mixing and segregation in a bidisperse gas-solid fluidised bed: a numerical and experimental study. *Powder Technology, 140*, 176-186.

Boutt, D. F., Cook, B. K., & Williams, J. R. (2011). A coupled fluid-solid model for problems in geomechanics: application to sand production. *International Journal for Numerical and Analytical Methods in Geomechanics*, *35*, 997-1018.

Butlanska, J. (2014). Cone penetration test in a virtual calibration chamber (PhD thesis). Universitat Politècnica de Catalunya, ES.

Butlanska, J., Arroyo, M., & Gens, A., (2009). Homogeneity and symmetry in DEM models of cone penetration. *Proceedings of the 6th International Conference on the Micromechanics of Granular Media* (pp. 425-428).

Butlanska, J., Arroyo, M., Gens, A., & O'Sullivan, C. (2013). Multi-scale analysis of cone penetration test (CPT) in a virtual calibration chamber. *Canadian Geotechnical Journal*, *51(1)*, 51-66.

Calvetti, F., di Prisco, C. & Nova, R., (2004). Experimental and numerical analysis of soil-pipe interaction. *Journal of Geotechnical and Geoenvironmental Engineering*, *130*, 1292-1299.

Carrier, W. D. (2003). Goodbye, Hazen; Hello, Kozeny-Carman. *Journal of Geotechnical and Geoenvironmental Engineering*, *129(11)*, 1054-1056.

Catalano, E. (2013). *A pore-scale coupled hdromechanical model for biphasic granular media* (PhD thesis). Université de Grenoble, FR.

Cello, F., Di Renzo, A., & Di Maio, F. P. (2010). A semi-empirical model for the dragforce and fluid–particle interaction in polydisperse suspensions. *Chemical Engineering Science, 65*, 3128–3139.

Chapuis, R.P., & Aubertin, M. (2003). On the use of the Kozeny-Carman equation to predict the hydraulic conductivity of soils. *Canadian Geotechnical Journal*, *40*, 616-628.

Chareyre, B., Cortis, A., Catalano, E., & Barthelemy, E. (2012). Pore-scale modeling of viscous flow and induced forces in dense sphere packings. *Transport in Porous Media, 92(2)*, 473-493.

Chen, X., Tan, C., & Haberfield, C. (1999). Solutions for the deformations and stability of elastoplastic hollow cylinders subjected to boundary pressures. *International Journal for Numerical and Analytical Methods in Geomechanics*, 23, 779-800.

Cheung, L. Y. G., (2010). *Micromechanics of sand production in oil wells* (PhD thesis). University of London, UK.

Cheung, L. Y. G., O'Sullivan, C., & Coop, M. R. (2013). Discrete element method simulations of analogue reservoir sandstones. *International Journal of Rock Mechanics & Mining* Sciences, 63, 93–103.

Cho, N., Martin, C. D., & Sego, D. C. (2007). A clumped particle model for rock. *International Journal of Rock Mechanics & Mining Sciences, 44*, 997-1010.

Choi, H. & Joseph, D. D. (2001). Fluidization by lift of 300 circular particles in plane Poiseuille flow by direct numerical simulation. *Journal of Fluid Mechanics, 438*, 101-128.

Ciantia, M. O., Arroyo, M., Calvetti, F., & Gens, A. (2015). An approach to enhance efficiency of DEM modelling of soils with crushable grains. *Géotechnique*, *65(2)*, 91-110.

Cleary, P. W., & Sawley, M.L. (2002). DEM modelling of industrial granular flows: 3D case studies and the effect of particle shape on hopper discharge. *Applied Mathematical Modelling, 26*, 89-111.

Climent, N., Arroyo, M., O'Sullivan, C., & Gens, A. (2013). Sensitivity to damping in sand production DEM-CFD coupled simulations. *In POWDERS AND GRAINS 2013: Proceedings of the 7th International Conference on Micromechanics of Granular Media* (No. 1, pp. 1170-1173). AIP Publishing.

Climent, N., Butlanska, J., Arroyo, M. & Gens, A., (2011). Triaxial and cone penetration tests in a discrete analogue of Toyoura sand. *Proceedings of Second International FLAC/DEM Symposium.* Melbourne, AU.

Cook, B. K., Lee, M. Y., DiGiovanni, A. A., Bronowski, D. R., Perkins, E. D., & Williams, J. R. (2004). Discrete element modelling applied to laboratory simulation of near-wellbore mechanics. *International Journal of Geomechanics*, *4:1(19)*.

Coop, M. & S. Willson (2003). Behavior of hydrocarbon reservoir sands and sandstones. *Journal of Geotechnical and Geoenvironmental Engineering, 129 (11)*, 1010-1019.

Craig, R. F. (1992). *Soil mechanics* (5th ed.). Chapman & Hall.

Cui, L. & O'Sullivan, C., (2006). Exploring the macro- and micro-scale response of an idealised granular material in the direct shear apparatus. *Géotechnique*, *56 (7)*, 455-468.

Cui, L., O'Sullivan, C. & O'Neill, S. (2007). An analysis of the triaxial apparatus using a mixed boundary three-dimensional discrete element model. *Géotechnique*, *57 (10)*, 831-844.

Cundall, P.A. (1987). Distinct element models of rock and soil structure. In *Analytical and Computational Methods in Engineering Rock Mechanics* (Brown, E.T. Ed.). London: George Allen and Unwin (pp. 129-163).

Cundall, P. A. & Strack, O. D. L. (1979). A discrete numerical model for granular assemblies. *Géotechnique, 29 (1)*, 47-65.

DallaValle, J. M. (1948). *Micromeritics, the technology of fine particles*. New York: Pitman Pub. Corp.

Di Felice, R. (1994). The voidage function for fluid-particle interaction systems. *International Journal of Multiphase Flow, 20*, 153-159.

Di Felice, R. & Rotondi, M. (2012). Fluid-particle drag force in binary-solid suspensions. *International Journal of Chemical Reactor Engineering*, *10(1)*, A29.

Di Renzo, A. & Di Maio, F. P. (2004). Comparison of contact-force models for the simulation of collisions in DEM-based granular flow codes. *Chemical Engineering Science, 59*, 525-541.

Dickson, U. O. (2014). *Mechanistic models for predicting sand production: a case study of Niger delta wells* (Master of Science thesis). The African University of Science and Technology.

Ding, X., Zhang, L., & Zhu, H. (2013). Effect of model scale and particle size distribution on PFC3D simulation results. *Rock Mechanics and Rock Engineering*, DOI 10.1007/s00603-013-0533-1.

Dorfmann, A., Rothenburg, L., & Bruno, M. S. (1997). Micromechanical modeling of sand production and arching effects around a cavity. *International Journal of Rock Mechanics and Mining Sciences, 34*, No. 3-4.

Dresen, G., Stanchits, S., & Rybacki, E. (2010). Borehole breakout evolution through acoustic emission location analysis. *International Journal of Rock Mechanics & Mining Sciences, 47*, 426-435.

Durrett, J. L., Golbin, W. T., Murray, J. W., & Tighe, R. E. (1977). Seeking a solution to sand control. *Journal of Petroleum Technology*, 1664-1672.

El Shamy, U., & Zeghal, M. (2005). Coupled continuum-discrete model for saturated granular soils. *Journal of Engineering* Mechanics, 131(4).

El Shamy, U., & Zeghal, M. (2007). A micro-mechanical investigation of the dynamic response and liquefaction of saturated granular soils. *Soil Dynamics and Earthquake Engineering, 27*, 712-729.

Élias, J. (2013). DEM simulation of railway ballast using polyhedral elemental shapes. *Proceedings on the III International Conference on Particle-based Methods. Fundamentals and Applications. PARTICLES 2013.* Stuttgart, DE.

Ergun, S. (1952). Fluid flow through packed columns. *Chemical Engineering Progress, 48*, 89-94.

Fattahpour, V., Moosavi, M., & Mehranpour, M. (2012). An experimental investigation on the effect of rock strength and perforation size on sand production. *Journal of Petroleum Science and Engineering, 86-87*, 172-189.

Ferziger, J. H. & Peric, M. (1999). *Computational methods for fluid dynamics* (2nd ed.). Berlin, DE: Springer.

Finnemore, E. J., & Franzini, J. B. (2002). *Fluid Mechanics*. New York, US: McGraw-Hill.

Fjar, E., Holt, R. M., Horsrud, P., Raaen, A.M., & isnes, R. (2008). Petroleum Related Rock Mechanics (2nd ed.)

Furtney, J., Zhang, F., & Han, Y. (2013). Review of methods and applications for incorporating fluid flow in the Discrete Element Method. In: Zhu, P., Detournay, C., Hart, R., Nelson, M. (Eds) *Continuum and distinct element numerical modelling in geomechanics*. Itasca International In: Minneapolis, US.

Gabrieli, F., Cola, S., & Calvetti, F. (2009). Use of an up-scaled DEM model for analysing the behaviour of a shallow foundation on a model slope. *Geomechanics and Geoengineering: An International Journal*, *4(2)*, 109-122.

Ge, W., & Li, J. H. (2001). Macro-scale pseudo-particle modelling for particle-fluid systems. *Chinese Science Bulletin, 46*, 1503-1507.

Ge, W., & Li, J. H. (2003a). Macro-scale phenomena reproduced in microscopic systems-pseudo-particle modeling of fluidization. *Chemical Engineering Science, 58*, 1565-1585.

Ge, W., & Li, J. H. (2003b). Simulation of particle-fluid systems with macro-scale pseudo-particle modelling. *Powder Technology, 137*, 99-108.

Geilikman, M. B., & Dusseault, M. B. (1997). Fluid rate enhancement from massive sand production in heavy-oil reservoirs. *Journal of Petroleum Science and Engineering*, *17*, 5-18.

Gidaspow, D. (1994). *Multiphase flow and fluidization: continuum and kinetic theory descriptions*. Boston: Academic Press.

Golchert, D., Moreno, R., Ghadiri, M., & Litser, J., (2004). Effect of granule morphology on breakage behaviour during compression. *Powder Technology*, *143-144 (7)*, 84-96.

Grof, Z., Cook, J., Lawrence, C. J., & Stepanek, F. (2009). The interaction between small clusters of cohesive particles and laminar flow: Coupled DEM/CFD approach. *Journal of petroleum science and engineering, 66*, 24-32.

Hill, R. J., Koch, D. L., & Ladd, J. C. (2001). Moderate-Reynolds-numbers flows in ordered and reandom arrays of spheres. *Journal of Fluid Mechanics, 448*, 243-278.

Holloway, W., Yin, X., & Sundaresan, S. (2010). Fluid-particle drag in inertial polydisperse gas-solid suspensions. *AIChE Journal*, *56*, 1995-2004.

Hoomans, B. P. B., Kuipers, J. A. M., Briels, W. J., & van Swaaij, W. P. M., (1996). Discrete particle simulation of bubble and slug formation in a two-dimensional gas-fluidesed bed. A hard-sphere approach. *Chemical Engineering Science*, *51*, 99-118.

Hu, H. H. (1996). Direct simulation of flows of solid-liquid mixtures. *International Journal of Multiphase Flow*, *22*, 335-352.

Humes, C. (1996). A new approach to compute the void size distribution curves of protective filters. *In Proceedings of Geofilters '96.*

IESL (2014). Personal communication.

Ispas, I., McLennan, J., & Martin, W. (2006). Interim report on perforation testing for improved sand management. Technical report, BP and ASRC Energy Services and TerraTek.

Itasca Consulting Group, Inc. (2008a). *PFC3D – Particle Flow Code in 3 Dimensions, Ver. 4.0 User's Manual*. Minneapolis, US: Itasca.

Itasca Consulting Group, Inc. (2008b), *PFC3D – Particle Flow Code in 3 Dimensions, CCFD add-on manual*. Minneapolis, US: Itasca.

ITOCHU Techno-Solutions Corporation (2007), *CCFD – Theoretical Manual*. Jackson R. (2000) *The dynamics of fluidized particles*. Cambridge, UK: Cambridge University Press.

Jaeger, J. C., Cook, N. G. W., & Zimmerman, R. W. (2007). *Fundamentals of rock mechanics*. Melbourne, AU: Blackwell Publishing.

Jenck, O., Dias, D. & Kastner, R., (2009). Discrete element modelling of a granular platform supported by piles in soft soil – Validation on a small scale model test and comparison to a numerical analysis in a continuum. *Computers and Geotechnics*, *36*, 917-927.

Jensen, R. P., & Preece, D. S. (2000). Modeling of sand production with Darcy's flow coupled with discrete elements. In: Desai (Ed.), *10th International Conference on Computer methods and Advances in Geomechanics* (pp. 819-822). Tucson, US.

Jian, M. J., Yu, H. S. & Harris, D. (2006). Discrete element modelling of deep penetration in granular soils. *International Journal for Numerical and Analytical Methods in Geomechanics, 30*, 335-361.

Jiang, M., Sun, C., Crosta, G. B., & Zang, W. (2015). Comprehensive study of submarine steep slope failures triggered by thermal dissociation of methane hydrates by a coupled CFD-DEM approach. *Engineering Geology*, 10.1016/j.enggeo.2015.02.007.

Kafui, K., Thornton, C., & Adams, M. (2002). Discrete particle-continuum fluid modelling of gas-solid fluidised beds. *Chemical Engineering Science, 57*, 2395-2410.

Kawaguchi, T., Tanaka, T., & Tsuji, Y. (1998). Numerical simulation of two-dimensional fluidized beds using the discrete element method (comparison between the two- and three-dimensional models). *Powder and* Technology, 96, 129-138.

Ku, X., Li, T., & Løvås, T. (2013). Influence of drag force correlations on periodic fluidization behaviour in Eulerian-Lagrangian simulation of a bubbling fluidized bed. *Chemical Engineering Science*, *95.*

Kuncoro, B., Ulumuddin, B, & Palar, S. (2001). Sand control for unconsolidated reservoirs. *Proceeding symposium nasional IATMI 2001.* Yogyakarta, ID.

Langston, P. A., Tüzün, U. & Heyes, D. M. (1994). Discrete element simulation of granular flow in 2D and 3D hoppers: dependence of discharge rate and wall stress on particle interactions. *Chemical Engineering* Science, 50, 967-987.

Langston, P. A., Tüzün, U., & Heyes, D.M. (1995). Discrete element simulation of internal stress and flow fields in funnel flow hoppers. *Powder Technology, 85*, 153-169.

Langston, P. A., Tüzün, U., & Heyes, D.M. (1996). Distinct element simulation of interstitial air effects in axially symmetric granular flows in hoppers. *Chemical Engineering Science, 51*, 873-891.

Li, J. H. (2003). Simulation of particle-fluid systems with macro-scale pseudo-particle modelling. *Powder Technology, 137*, 99-108.

Li, J., langston, P. A., Webb, C., & Dyakowski, T. (2004). Flow of sphero-disc particles in rectangular hoppers – a DEM and experimental comparison in 3D. *Chemical Engineering Science, 59*, 5917-5929.

Li, Y., Zhang, J., & Fan, L. S. (1999). Numerical simulation of gas-liquid-solid fluidization systems using a combined CFD-VOF-DPM method: bubble wake behaviour. *Chemical Engineering Science, 54*, 5101-5107.

Lobo-Guerrero, S., & Vallejo, L. E. (2005). DEM analysis of crushing around driven piles in granular materials. *Géotechnique, 55(8)*, 617-623.

Marketos, G., & Bolton, M. (2010). Flat boundaries and their effect on sand testing. *International Journal for Numerical and Analytical Methods in Geomechanics*, *34*, 821–837.

Marrion, M., & Woods, A. (2009). A Particle-Scale Model of Hydrodynamic Erosion. *FMA'09: Proceedings of the 7th IASME/WSEAS International conference on fluid mechanics and aerodynamics* (pp. 141-149).

Mavko, G., Mukerji, T., & Dvorkin, J. (2003). *The rock physics handbook* (2nd Ed.). Cambridge University Press.

Mazzei, L., & Lettieri, P. (2007). A drag force closure for uniformly dispersed fluidized suspensions. *Chemical Engineering Science, 62*, 6129–6142.

Mogi, K. (2007). *Experimental rock mechanics*. London, UK: Taylor & Francis Group.

Moreland, K. (2014). *The ParaView tutorial.* Sandia National Laboratories.

Morita, N., Whitfill, D. L., Fedde, O. P., & Lovik, T. H. (1989a). Parametric study of sand-production prediction: analyticl approach. *SPE Production Engineering, 4(1)*, 25-33.

Morita, N., Whitfill, D. L., Masssie, I., & Knudsen, T. W. (1989b). Realistic sand production prediction numerical approach. *SPE Production Engineering, 4(1)*, 15-24.

Nouri, A., Vaziri, H., Belhaj, H. & Islam, R. (2004). Sand production prediction: a new set of criteria for modeling based on large-scale transient experiments and numerical investigation. *2004 SPE Annual Technical Conference and Exhibition*. Houston, US. SPE 90273.

Nouri, A., Vaziri, H., Kuru, E., & Islam, R. (2006). A comparison of two sanding criteria in physical and numerical modeling of sand production. *Journal of petroleum science and engineering, 50*, 55-70.

O'Connor, R. M., Torczynski, J. R., Preece, D. S., Klosek, J. T., & Williams, J. R. (1997). Discrete element modeling of sand production. *International Journal of Rock Mechanics and Mining Sciences, 34*(3-4).

O'Sullivan, C. (2011). *Particulate Discrete Element Modelling: a Geomechanics Perspective*. Spon Press, Taylor & Francis.

Palmer, I., Vaziri, H., Willson, S., Moschovidis, Z., Cameron, J, & Ispas, I. (2003). Predicting and managing sand production: a new strategy. *Proceedings of SPE Annual Conference and Exhibition.* Denver, US.

Pan, T. W., Joseph, D. D., Bai, R., Glowinski, R., & Sarin, V., (2002). Fluidization of 1204 spheres: simulation and experiment. *Journal of Fluid Mechanics, 451*, 169-191.

Papamichos, E. (2006). Sand production: Physical and experimental evidence. *Special issue of Revue européenne de génie civil, 10(6-7)*, 803-816.

Papamichos, E., & Vardoulakis, I. (2005). Sand erosion with a porosity diffusion law. *Computers and Geotechnics*, *32*, 47-58.

Papamichos, E., Tronvoll, J., Skjaerstein, A., & Unander, T. E. (2010). Hole stability of Red Wildmoor sandstone under anisotropic stresses and sand production criterion. *Journal of Petroleum Science and Engineering*, *72*, 78-92.

Papamichos, E., Vardoulakis, I., Tronvoll, J., & Skjirstein, A. (2001). Volumetric sand production model and experiment. *International Journal for Numerical and Analytical Methods in Geomechanics, 25*, 789-808.

Park, B., & Min, K. B. (2015). Bonded-particle discrete element modelling of mechanical behaviour of transversely isotropic rock. *International Journal of Rock Mechanics & Mining Sciences*, 76, 243-255.

Penberthy, W., & Shaughnessy, C. (1992). *Sand Control*. Society of Petroleum Engineers.

Pierce, M., Gaida, M., & DeGagne, D. (2009). Estimation of rock block strength. *ROCKENG09: Proceedings of the 3rd CANUS Rock Mechanics Symposium.* Toronto, US.

Potapov, A. V. & Campbell, C. S. (1996). Computer simulation of hopper flow. *Physics of Fluids, 8(11)*, 2884-2894.

Potapov, A. V., Hunt, M. L., & Campbell, C. S. (2001). Liquid-solid flows using smoothed particle hydrodynamics and the discrete element method. *Powder Technology, 116*, 204-213.

Potic, B., Kersten, S. R. A., Ye, M., van der Hoef, M. A., Kuipers, J. A. M., & van Swaaij (2005). Fluidization with hot compressed water in micro-reactors. *Chemical Engineering Science, 60*, 5982-5990.

Potyondy, D. O., & Cundall, P. A. (2004). A bonded-particle model for rock. *International journal of Rock Mechanics & Mining Sciences, 41*, 1329-1364.

Quadros, R., Vargas, E. A., Gonçalves, C. J., & Prestes, A. (2010). Analysis of sand production processes at the pore scale using the discrete element method and lattice Boltzman procedures. *Proceedings of the 44th US Rock Mechanics Symposium and 5th U.S.-Canada Rock Mechanics Symposium*. Salt Lake City, US.

Rahmati, H., Jafarpour, M., Azadbakht, S., Nouri, A., Vaziri, H., Chan, D., & Xiao, Y. (2013). Review of Sand Production Precdiction Models. *Journal of Petroleum Engineering, 2013*, Article ID 864981.

Rhodes, M. J., Wang, X. S., Nguyen M., Stewart, P., & Liffman, K. (2001). Study of mixing in gas-fluidized beds using a DEM model. *Chemical Engineering Science, 56*, 2859-2866.

Risnes, R., Bratli, R. K., & Horsrud, P. (1982). Sand stresses around a wellbore. *Society of petroleum engineers journals*. SPE 9650.

Rong, L. W., Dong, K. J., & Yu, A. B. (2014). Lattice-Boltzmann simulation of fluid flowthrough packed beds of spheres: Effect of particle size distribution. *Chemical Engineering Science, 116*, 508–523.

Rotondi, M., Di Felice, R., & Pagliai, P. (2015). Validation of fluid-particle interaction force relationships in binary-solid suspensions. *Particuology*, *23*, 40-48.

Scholtès, L. & Donzé, F. V. (2013). A DEM model for soft and hard rocks: Role of grain interlocking on strength. *Journal of the Mechanics and Physics of Solids*, *61*, 352-369.

Schöpfer, M. P. J., Abe, S., Childs, C. & Walsh, J. J. (2009). The impact of porosity and crack density on the elasticity, strength and friction of cohesive granular materials: Insights from DEM modelling. *International Journal of Rock Mechanics & Mining Sciences, 46*, 250-261.

Thornton, C. (1997). Force transmission in granular media. *Powder and Particle, 15*, 81-89.

Thornton, C., & Antony, S. J., (2000). Quasi-static shear deformation of a soft particle system. *Powder Technology, 109*, 179-191.

Thornton, C., & Liu, L., (2004). How do agglomerates break? *Powder Technology*, *143-144*, 110-116.

Thornton, C., & Zhang, L. (2010). On the evolution of stress and microstructure during general 3D deviatoric straining of granular media. *Géotechnique*, *60 (5)*, 333-341.

Trani, L. D. O., & Indraratna, B. (2010). The use of particle size distribution by surface area method in predicting the saturated hydraulic conductivity of graded granular soils. *Géotechnique*, *60*(12), 957-962.

Tronvoll, J., Skjirstein, A., & Papamichos, E. (1997). Sand production: Mechanical failure or hydrodynamic erosion? *International Journal of Rock Mechanics and Mining Sciences, 34(3-4).*

Tsuji, Y., Kawaguchi, T., & Tanaka, T., (1993). Discrete particle simulation of 2-dimensional fluidized-bed. *Powder Technology, 77*, 79-87.

van Wyk, G., Els, D. N. J., Bradshaw, S. M., & Sacks, N. (2013). Discrete element simulation of tribological interactions in rock cutting. *International Journal of Rock Mechanics & Mining Sciences, 65*, 8–19.

Vardoulakis, I., Stavropoulou, M., & Papanastasiou, P. (1996). Hydro-mechanical aspects of the sand production problem. *Transport in Porous Media, 22*, 225-244.

Vaziri, H., Lemoine, E. M., and Xiao, Y. (2002). Quantification of sand production induced improvement in productivity index. *Canadian Geotechnical Journal, 39*, 1088-1102.

Vaziri, H., & Xiao, Y., (2002). Assessment of several sand prediction models with particular reference to HPHT wells. *SPE/ISRM Rock Mechanics Conference*. Irving, US.

Veeken, C., Davies, D., Kenter, C., & Kooijman, A. (1991). Sand production prediction review: Developing an integrated approach. *66th Annual Technical Conference and Exhibition of the Society of Petroleum Engineers*. Dallis, US. SPE 22792.

Wahyudi, I., Montillet, A., & Khalifa, A. O. A. (2002). Darcy and post-Darcy flows within different sands. *Journal of Hydraulic Research, 20*.

Wang, H.F. (2000). *Theory of linear poroelasticity*. UK: Princeton University Press.

Wang, Y., & Tonon, F. (2009a). Calibration of a discrete element model for intact rock up to its peak strength. *International Journal for Numerical and Analytical Methods in Geomechanics, 34(5)*, 447-469.

Wang, Y., & Tonon, F. (2009b). Modeling Lac du Bonnet granite using a discrete element model. *International journal of Rock Mechanics & Mining Sciences*, *46*, 1124-1135.

Wen, C. Y. & Yu, Y. H. (1966). Mechanics of fluidization. *Fluid Particle Technology, 62 (62)*.

Xiong, Y. Q., Zhang, M. Y., & Yuan, Z. L. (2005). Three dimensional numerical simulation method for gas-solid injector. *Powder Technology, 160*, 180-189.

Xu, B. H., & Yu, A. B. (1997). Numerical simulation of the gas-solid flow in a fluidized bed by combining discrete particle method with computational fluid dynamics. *Chemical Engineering Science, 52*, 2785-2809.

Yin, X., & Sundaresan, S. (2008). Drag law bidisperse gas-solid suspensions containing equally sized spheres. *Industrial & Engineering Chemistry Research, 48*, 227-241.

Yin, X., & Sundaresan, S. (2009). Fluid-particle drag in low-Reynolds-number polydisperse gas-solid suspensions. *AIChE Journal*, *55*, 1352-1368.

Younessi, A., Rasouli, V., & Wu, B. (2013). Sand production simulation under true-triaxial stress conditions. *International Journal of Rock Mechanics and Mining Sciences, 61*, 130-140.

Yu, H. S. (1992). Expansion of a thick cylinder of soils. *Computers and Geomechanics, 14*, 21-41.

Yu, H. S., & Houlsby, G. T. (1991). Finite cavity expansion in dilatant soils: loading analyisis. *Géotechnique*, *41*, 173-183.

Yu, H. S., & Rowe, R. K. (1999). Plasticity solutions for soil behaviour around contracting cavities and tunnels. *International Journal for Numerical and Analytical Methods in Geomechanics*, *23*, 1245-1279.

Zhang, J., Fan, L. S., Zhu, C., Pfeffer, R., & Qi, D. (1999). Dynamic behaviour of collision of elastic spheres in viscous fluids. *Powder Technology, 106*, 98-109.

Zhao, T., Houlsby, G. T., & Utili, S. (2014). Investigation of a granular batch via DEM-CFD coupling. *Granular Matter*, *16*, 921-932.

Zhao, J., & Shan, T. (2013). Coupled CFD–DEM simulation of fluid–particle interaction in geomechanics. *Powder Technology, 239*, 248-258.

Zhou, H., Flamant, G., Gauthier, D., & Lu, J. (2004a). Numerical simulation of the turbulent gas-particle flow in a fluidized bed by an LES-DPM model. *Chemical Engineering Research and Design*, *82*, 918-926.

Zhou, H., Flamant, G., Gauthier, D., & Lu, J. (2004b). DEM-LES of coal combustion in a bubbling fluidized bed. Part I, gas-particle turbulent flow structure. *Chemical Engineering Science*, *59*, 4193-4203.

Zhou, H., Flamant, G., Gauthier, D., & Lu, J. (2004c). DEM-LES of coal combustion in a bubbling fluidized bed. Part II, coal combustion at the particle level. *Chemical Engineering Science*, *59*, 4205-4215.

Zhou, Z. Y., Yu, A. B. & Choi, S. K. (2011). Numerical simulation of the liquid-induced erosion in a weakly bonded sand assembly. *Powder Technology*, *211(2-3)*, 237–249.

Zhu, H. P., Zhou, Z. Y., Yang, R. Y., & Yu, A. B. (2007). Discrete particle simulation of particulate systems: theoretical developments. *Chemical Engineering Science*, *62(13)*, 3378-3396.

Appendix A – MATLAB code for Risnes et al. (1982) analytical solution

A code for representing Risnes et al. (1982) analytical solution has been developed. The code is composed by different scripts; each script calculates one of the parameters needed for the calculation of the stress. At the end the stress at the elastic region and the stress at the plastic region are calculated separately and plotted together.

Risnes_Driver_test.m

```
% Script to calculate and plot the analytical solution of Risnes et al.
% (1982) for different values of a parameter

clear all;

% Define how many different parameters and which parameter to plot

totaltest = 2;
variable = [0.0 10.0];
variablename = 'analytical P = ';
units = ' MPa';

% Call different scripts to calculate and plot the analytical solution for
% each parameter
% The parameter that is being test with different values should be changed
% at the beginning of the loop


% For the Elastic Region

for ntest = 1:totaltest
   ntest

   P_o  = variable(ntest)*1000000;
   P_i  = variable(ntest)*1000000;
   P_c  = variable(ntest)*1000000;

   Risnes_Inputs;
```

```
   Risnes_Rc;
   Risnes_A1;
   Risnes_Elastic_Stress;

   if ntest==1
        auxi = cellstr(strcat(variablename,num2str(variable(ntest)),units));
        leshenda = [auxi];
    else
        auxi = cellstr(strcat(variablename,num2str(variable(ntest)),units));
        leshenda = [leshenda,auxi];
   end

   Risnes_Plot_Elastic;

end

% For the Plastic Region

for ntest = 1:totaltest
   ntest

   P_o  = variable (ntest)*1000000;
   P_i  = variable (ntest)*1000000;
   P_c  = variable (ntest)*1000000;


   Risnes_Inputs;
   Risnes_Rc;
   Risnes_A1;
   Risnes_Plastic_Stress;

   if ntest==1
        auxi = cellstr(strcat(variablename,num2str(variable(ntest)),units));
        leshenda = [auxi];
   else
        auxi = cellstr(strcat(variablename,num2str(variable(ntest)),units));
        leshenda = [leshenda,auxi];
   end

   Risnes_Plot_Plastic;

end
```

Risnes_Inputs.m

```
% Input parameters for Risnes et al. (1982) analytical solution
% Make sure the parameter you want to test (and that you are giving
% different values in the Risnes_Driver_Tests.m script) is not "on" in this
% script
```

```
% Material parameters

So = 101400;  % Cohesive strength (Pa)
alfa = 60.0;     % Failure angle of material (º) (45º+(frictionangle/2))
beta = 1.0;    % Parameter which defines the rock compressibility (adimensional)
Pois = 0.45;   % Poisson's ratio (adimensional)
k = 2.0e-13;   % Permeability (m^2)

% Geometry parameters

Ri = 0.1;    % Inner boundary radius (m)
Ro = 10.0;     % Outer boundary radius (m)
h = 1.0;     % Height (m)

% Fluid parameters

visc = 0.00293;   % Viscosity (Pa·s)

% Boundary conditions

sigmazo = 65500000;   % Vertical total stress at the outer boundary (Pa)

q = 0.0;              % Flow rate (m^3/s)
P_o = 32000000;       % Pore pressure at the outer boundary (Pa)
P_i = 32000000;       % Pore pressure at the inner boundary (Pa)
P_c = 32000000;       % Pore pressure at the elastic-plastic boundary(Pa)
```

Risnes_Rc.m

```
% Calculation of Rc (radius of the elastic-plastic boundary)

% Parameter t

t = tan(alfa*pi()/180.0)^2-1;

% Calculation of the coefficients of the equation to solve Rc

c1 = (2*So*tan(alfa*pi/180)-visc*q/(2*pi*h*k))*Ri^(-t);
c2 = -((t+2)/t)*c1*Ro^2;
c3 = -((1-2*Pois)/(2*(1-Pois)))*beta*(P_o-P_i);
c4 = ((1-2*Pois)/(2*(1-Pois)))*beta*visc*q/(2*pi*h*k);
c5 = visc*q/(2*pi*h*k);
c6 = -(2-(1-2*Pois)*beta/(1-Pois))*c5*Ro^2;
c7 = -c4*Ro^2;
c8     =     (2*Pois*sigmazo/(1-Pois)+(1-2*Pois)*beta*(P_o+P_i)/(1-Pois)-2*P_i+2*So*tan(alfa*pi/180)/t-
((t+2)/t)*visc*q/(2*pi*h*k))*Ro^2;
c9 = -c3*Ro^2;

% Equation to solve Rc (func=0)
```

```
syms x
func = c1*(x^(t+2))*log(Ro/x)+c2*(x^t)*log(Ro/x)+c3*(x^2)+c4*(x^2)*log(x/Ri)+c5*(x^2)*log(Ro/x)+c6*log(Ro/x)*log(x/Ri)+c7*log(x/Ri)+c8*log(Ro/x)+c9;

% Solve equation, find Rc. (make sure the limits for x are 0 and Ro, or Ri
% and Ro)

Rc = feval(symengine, 'numeric::solve',func,'x=0..1.08');
```

Risnes_A1.m

```
% Calculation of A1

sigmaro = Pois*sigmazo/(1-Pois)+(1-2*Pois)*beta*P_o/(1-Pois);

V = tan(alfa*pi/180)^4+1-Pois*(tan(alfa*pi/180)^2+1)^2;

aa = (2*Ro.^2/(Ro.^2-Rc.^2))*((1/t)*2*So*tan(alfa*pi/180)+sigmaro-P_i-(visc*q/(2*pi*h*k))*log(Rc./Ri))-(1/t)*tan(alfa*pi/180)^2*visc*q/(2*pi*h*k)-(1/t)*(visc*q/(2*pi*h*k))*(Ro.^2+Rc.^2)/(Ro.^2-Rc.^2)-(P_o-P_c)*((1-2*Pois)*beta/(2*(1-Pois)))*((Ro.^2+Rc.^2)/(Ro.^2-Rc.^2)+(log(Ro./Rc)-1)/log(Ro./Rc));

bb = 2*tan(alfa*pi/180)^2*Rc.^t*(tan(alfa*pi/180)^2+(Ro.^2+Rc.^2)/(Ro.^2-Rc.^2))/V;

A1 = aa/bb;

sigmarc = P_i+(visc*q/(2*pi*h*k))*log(Rc/Ri)-(1/t)*(2*So*tan(alfa*pi/180)-visc*q/(2*pi*h*k))+2*tan(alfa*pi/180)^2*A1*Rc.^t/V;
```

Risnes_Elastic_Stress.m

```
% Calculation of the radial and tangential stresses in the Elastic Region

% Radial distances where stresses are calculated (elastic region)

rel=Rc:0.1:Ro;

% Radial and tangential stresses in the elastic region

sigmar_el = (sigmaro+(sigmaro-sigmarc)*(Rc^2/(Ro^2-Rc^2))*(1-(Ro./rel).^2)-(P_o-P_c)*((1-2*Pois)*beta/(2*(1-Pois)))*((Rc^2/(Ro^2-Rc^2))*(1-(Ro./rel).^2)+log(Ro./rel)./log(Ro/Rc)));

sigmatheta_el = (sigmaro+(sigmaro-sigmarc)*(Rc^2/(Ro^2-Ri^2)).*(1+(Ro./rel).^2)-(P_o-P_c)*(1-2*Pois)*beta/(2*(1-Pois))*((Rc^2/(Ro^2-Rc^2))*(1+(Ro./rel).^2)+(log(Ro./rel)-1)./log(Ro/Rc)));
```

```
% Radial and tangential effective stresses in the elastic region

sigmar_el_eff = sigmar_el - beta*P_o;

sigmatheta_el_eff = sigmatheta_el - beta*P_o;

% Radial and tangential stresses normalized by the stress at the outer
% boundary

sigmar_Ro = sigmaro+((sigmaro-sigmarc)*(Rc.^2/(Ro.^2-Rc.^2)).*(1-(Ro./Ro).^2)-(P_o-P_c)*((1-
2*Pois)*beta/(2*(1-Pois)))*((Rc.^2/(Ro.^2-Rc.^2))*(1-(Ro./Ro).^2)+log(Ro./Ro)./log(Ro/Rc)));

sigmatheta_Ro = sigmaro+((sigmaro-sigmarc)*(Rc.^2/(Ro.^2-Ri.^2)).*(1+(Ro./Ro).^2)-(P_o-P_c)*(1-
2*Pois)*beta/(2*(1-Pois))*((Rc.^2/(Ro.^2-Rc.^2)).*(1+(Ro./Ro).^2)+(log(Ro./Ro)-1)./log(Ro/Rc)));

sigmar_el_norm = sigmar_el/sigmar_Ro;
sigmatheta_el_norm = sigmatheta_el/sigmatheta_Ro;
sigmar_el_eff_norm = sigmar_el_eff/(sigmar_Ro-beta*P_o);
 sigmatheta_el_eff_norm = sigmatheta_el_eff/(sigmatheta_Ro-beta*P_o);
```

Risnes_Plastic_Stress.m

```
% Calculation of the radial and tangential stresses in the Plastic Region

% Radial distances where stresses are calculated (plastic region)

rpl=Ri:0.01:Rc;

% Radial and tangential stresses in the plastic region

sigmar_pl = (P_i+(visc*q/(2*pi*h*k))*log(rpl./Ri)-(1/t)*(2*So*tan(alfa*pi/180)-
visc*q/(2*pi*h*k))+2*tan(alfa*pi/180)^2*A1*rpl.^t/V);

sigmatheta_pl = (P_i+(visc*q/(2*pi*h*k))*log(rpl./Ri)-(1/t)*(2*So*tan(alfa*pi/180)-
tan(alfa*pi/180)^2*visc*q/(2*pi*h*k))+2*tan(alfa*pi/180)^4*A1*rpl.^t/V);

% Radial and tangential effective stresses in the plastic region

sigmar_pl_eff = sigmar_pl - beta*P_i;
sigmatheta_pl_eff = sigmatheta_pl - beta*P_i;

% Radial and tangential stresses normalized by the stress at the outer
% boundary

sigmar_Ro = sigmaro+((sigmaro-sigmarc)*(Rc^2/(Ro^2-Rc^2)).*(1-(Ro./Ro).^2)-(P_o-P_c)*((1-
2*Pois)*beta/(2*(1-Pois)))*((Rc^2/(Ro^2-Rc^2))*(1-(Ro./Ro).^2)+log(Ro./Ro)./log(Ro/Rc)));

sigmatheta_Ro = sigmaro+((sigmaro-sigmarc)*(Rc^2/(Ro^2-Ri^2)).*(1+(Ro./Ro).^2)-(P_o-P_c)*(1-
2*Pois)*beta/(2*(1-Pois))*((Rc^2/(Ro^2-Rc^2)).*(1+(Ro./Ro).^2)+(log(Ro./Ro)-1)./log(Ro/Rc)));
```

```
sigmar_pl_norm = sigmar_pl/sigmar_Ro;
sigmatheta_pl_norm = sigmatheta_pl/sigmatheta_Ro;
sigmar_pl_eff_norm = sigmar_pl_eff/(sigmar_Ro-beta*P_i);
sigmatheta_pl_eff_norm = sigmatheta_pl_eff/(sigmatheta_Ro-beta*P_i);
```

Risnes_Plot_Elastic.m

```
% Plot all Risnes solutions for different parameters in the Elastic Region

% Array with all the successive line specifications

lc=cellstr(['k-o';'k-+';'k-<';'k-x';'k->']);

% Firgure 1: Plot Radial Stress in the Elastic Region

figure(1)
hold on;
plot(rel/Ri,sigmar_el_norm,char(lc(ntest)),'linewidth',1);

if ntest==totaltest
   grid on;
   xlabel('r/Ri','fontsize',20);
   ylabel('\sigma_{r}/\sigma_{ro}','fontsize',20);
   AX=legend(leshenda,1);
   LEG = findobj(AX,'type','text');
   set(LEG,'FontSize',15)

end

% Figure 2: Plot Tangential Stress in the Elastic Region

figure(2)
hold on;

plot(rel/Ri,sigmatheta_el_norm,char(lc(ntest)),'linewidth',1);

if ntest==totaltest
   grid on;
   xlabel('r/Ri','fontsize',20);
   ylabel('\sigma_{\theta}/\sigma_{\thetao}','fontsize',20);
   AX=legend(leshenda,1);
   LEG = findobj(AX,'type','text');
   set(LEG,'FontSize',15)

end
```

Risnes_Plot_Plastic.m

```
% Plot all Risnes solutions for different parameters in the Plastic Region

% Array with all the sucessive line specifications

lc=cellstr(['k-o';'k-+';'k-<';'k-x';'k->']);

% Firgure 1: Plot Radial Stress in the Plastic Region

figure(1)
hold on;

plot(rpl/Ri,sigmar_pl_norm,char(lc(ntest)),'linewidth',1);



% Figure 2: Plot Tangential Stress in the Plastic Region

figure(2)
hold on;

plot(rpl/Ri,sigmatheta_pl_norm,char(lc(ntest)),'linewidth',1);
```

Appendix B - MATLAB script to map contact forces

MATLAB scripts to map contact forces.

---

cforces_matlab.m

```
% Matlab file to plot contact forces

clear;

% load data

cforces=dlmread('cforces.dat',',',0,0);
balls=dlmread('ballvelsandstress.dat',',',0,0);

ballcoords=sortrows(balls,1);

%==========================================

% determine the average normal force

numcontacts=size(cforces,1);
numballs=size(ballcoords,1);

% Make a new figure

figure;

axis('equal'); % Make the axes equal
axis('off'); %Turn the axes off
hold on;

zbottom=0.00175;
ztop=0.00325;
rmin=0.0;
rmax=0.03;
linescale=1;  % multiplier for line thickness
ttt=0;

for i =1:numcontacts

distance(i)=sqrt(cforces(i,3)*cforces(i,3)+cforces(i,4)*cforces(i,4));

    if  cforces(i,5)>=zbottom && cforces(i,5)<=ztop && distance(i)>=rmin
    && distance(i)<=rmax
```

```
        ttt=ttt+1;
        m=cforces(i,1); % disk 1 id
        n=cforces(i,2); % disk 2 id

        for kk=1:numballs

              if ballcoords(kk,1)==m
                    x1(1)=ballcoords(kk,2);
                    y1(1)=ballcoords(kk,3);
                    z1(1)=ballcoords(kk,4);

              elseif n<500000 && ballcoords(kk,1)==n % disk-disk contact
        (500000 is a wall)

                    x1(2)=ballcoords(kk,2);
                    y1(2)=ballcoords(kk,3);
                    z1(2)=ballcoords(kk,4);

              elseif n>=500000 % wall-disk contact (500000 is a wall)

                    x1(2)=cforces(i,3);
                    y1(2)=cforces(i,4);
                    z1(2)=cforces(i,5);

              end

          end

% plot according to  magnitude of contact normal force
% determine line width - proportional to force

      mywidth=cforces(i,12)*linescale;

      if mywidth ~=0

          plot(x1,y1,'LineWidth',mywidth,'Color','r');

      end

      end

end
```

Appendix C – MATLAB scripts to make DEM data files for Paraview visualization

MATLAB scripts to generate ParaView data files for DEM.

---

ballsdiamstress_matlab.m

```
clear;

%% Vtp File creation

%%Create vtp file for particle positions
fname=['balldiamandstress.vtp'];

%%Read original data files
dname=['ballvelsandstress2.dat'];
diskdata=dlmread(dname);


fid=fopen(fname,'w');

%%Paraview data file content

fprintf(fid,'<?xml version="1.0"?>\n');
fprintf(fid,'<VTKFile           type="PolyData"           version="0.1"
format="ascii">\n');
fprintf(fid,'\t <PolyData>\n');
npoints1=length(diskdata);
fprintf(fid,'\t \t<Piece NumberOfPoints="%i">\n',npoints1);
fprintf(fid,'\t \t \t<Points>\n');
fprintf(fid,'\t \t \t \t<DataArray type="Float32" NumberOfComponents="3"
format="ascii">\n');

%%Particles positions (3 components)

for i=1:length(diskdata)

   fprintf(fid,'\t         \t         \t         \t         %e         %e
%e\n',diskdata(i,2),diskdata(i,3),diskdata(i,4));

end
fprintf(fid,'\t \t \t \t</DataArray>\n');
fprintf(fid,'\t \t \t</Points>\n');
```

```
fprintf(fid,'\t        \t        \t<PointData        Scalars="Diameter"
Vectors="Velocity">\n');
fprintf(fid,'\t  \t  \t  \t<DataArray  type="Float32"  Name="Diameter"
format="ascii">\n');

%%Particles diameter

for i=1:length(diskdata)
   diam=diskdata(i,5)*2;
   fprintf(fid,'\t \t \t \t %e\n',diam);
end

fprintf(fid,'\t \t \t \t</DataArray>\n');
fprintf(fid,'\t   \t   \t   \t<DataArray   type="Float32"   Name="Stress"
format="ascii">\n');

%%Particles stress


for i=1:length(diskdata)

       stress=diskdata(i,18);

   fprintf(fid,'\t \t \t \t %e \n',stress);

end


fprintf(fid,'\t \t \t \t </DataArray>\n');


for i=1:length(diskdata)
    x=diskdata(i,2); %x coordinate
    y=diskdata(i,3); %y coordinate
    z=diskdata(i,4); %z coordinate
    sigxx=diskdata(i,9); % read sigma xx
    sigxy=diskdata(i,10); % read sigma xy
    sigyy=diskdata(i,13); % read sigma yy

    theta=atan((y-0)/(x-0));
    sintheta=sin(theta);
    costheta=cos(theta);

        pos(i)=sqrt(x^2+y^2);
    sigrr(i)=-1*(sigxx*costheta*costheta    +    sigyy*sintheta*sintheta
+2*sigxy*sintheta*costheta);
    sighoop(i)=-1*(sigxx*sintheta*sintheta + sigyy*costheta*costheta -
2*sigxy*sintheta*costheta);
    sigshear(i)=abs(((sigyy-sigxx)*sintheta*costheta                    +
sigxy*(costheta*costheta - sintheta*sintheta)));


end

fprintf(fid,'\t \t \t \t<DataArray type="Float32" Name="RadialStress"
format="ascii">\n');

%%Particles radial stress
```

```
for i=1:length(diskdata)

   fprintf(fid,'\t \t \t \t %e \n',sigrr(i));

end


fprintf(fid,'\t \t \t \t </DataArray>\n');

fprintf(fid,'\t       \t       \t       \t<DataArray       type="Float32"
Name="TangentialStress" format="ascii">\n');

%%Particles circumferential stress


for i=1:length(diskdata)



   fprintf(fid,'\t \t \t \t %e \n',sighoop(i));

end


fprintf(fid,'\t \t \t \t </DataArray>\n');


fprintf(fid,'\t  \t  \t  \t  <DataArray  type="Float32"  Name="Velocity"
NumberOfComponents="3" format="ascii">\n');


%%Particles velocities (3 components)

for i=1:length(diskdata)

    fprintf(fid,'\t         \t         \t         \t         %e         %e
%e\n',diskdata(i,6),diskdata(i,7),diskdata(i,8));

end

fprintf(fid,'\t \t \t \t </DataArray>\n');



fprintf(fid,'\t \t \t</PointData>\n');
fprintf(fid,'\t \t</Piece>\n');
fprintf(fid,'\t</PolyData>\n');
fprintf(fid,'</VTKFile>\n');

fclose('all');
```

cforces0_matlab.m

```
clear;


%% Vtp File creation

cname=['cforces0.vtp'];

%%Read original data files

dname=['ballvelsandstress2.dat'];
diskdata=dlmread(dname);

dname=['cforces_clean.dat'];
mydata=dlmread(dname);

kname=['cbforces_clean.dat'];
kdata=dlmread(kname);



fid=fopen(cname,'w');

fprintf(fid,'<?xml version="1.0"?>\n');
fprintf(fid,'<VTKFile           type="PolyData"           version="0.1"
byte_order="LittleEndian">\n');
fprintf(fid,'\t <PolyData>\n');
npoints2=length(mydata);
fprintf(fid,'\t               \t<Piece              NumberOfPoints="%i"
NumberOfLines="%i">\n',npoints2*2, npoints2);
fprintf(fid,'\t \t \t<Points>\n');
fprintf(fid,'\t \t \t \t<DataArray type="Float32" NumberOfComponents="3"
format="ascii">\n');


%%Read original data files: position of the two particles of each contact


for i = 1:length(mydata);


    id1 = mydata(i,1);
    id2 = mydata(i,2);

    for j=1:length(diskdata);

        if diskdata(j,1)==id1

            num1=j;
```

```
        end

        if diskdata(j,1)==id2

            num2=j;

        end

    end

    fprintf(fid,'\t  \t  \t  \t  %e  %e  %e\n\t  \t  \t  \t  %e  %e
%e\n',diskdata(num1,2),diskdata(num1,3),diskdata(num1,4),diskdata(num2
,2),diskdata(num2,3),diskdata(num2,4));

end

fprintf(fid,'\t \t \t \t</DataArray>\n');
fprintf(fid,'\t \t \t</Points>\n');

fprintf(fid,'\t \t \t<PointData Scalars="NormalisedContactForce">\n');
fprintf(fid,'\t      \t      \t      \t<DataArray      type="Float32"
Name="NormalisedContactForce" format="ascii">\n');

% normalised contact forces

meanCF = mean(mydata(:,12));

for i = 1:length(mydata);

    fprintf(fid,'\t    \t    \t    \t    %e    \n\t    \t    \t    \t    %e
\n',mydata(i,12)/meanCF,mydata(i,12)/meanCF);
end

fprintf(fid,'\t \t \t \t</DataArray>\n');
fprintf(fid,'\t \t \t</PointData>\n');

fprintf(fid,'\t \t \t<Lines>\n');
fprintf(fid,'\t  \t  \t  \t<DataArray  type="Int32"  Name="connectivity"
format="ascii">\n');
% connectivity here is not the number of contacts for a particle. It is
a number that paraview call connectivity

k = 0 ;

for i = 1:length(mydata);

   fprintf(fid,'\t \t \t \t %i  %i \n',k,k+1);
 k = k+2  ;
end

fprintf(fid,'\t \t \t \t</DataArray>\n');
fprintf(fid,'\t   \t   \t   \t<DataArray   type="Int32"   Name="offsets"
format="ascii">\n');

l=2;

for i = 1:length(mydata);
```

```
    fprintf(fid,'\t \t \t \t %i \n',l);

    l=l+2;
end

fprintf(fid,'\t \t \t \t </DataArray>\n');
fprintf(fid,'\t \t \t</Lines>\n');
fprintf(fid,'\t \t</Piece>\n');
fprintf(fid,'\t</PolyData>\n');
fprintf(fid,'</VTKFile>\n');


fclose('all');
```

Appendix D – MATLAB script to make CFD data files for Paraview visualization

MATLAB script to generate ParaView data files for CFD.

Fluidproperties_matlab.m

```
clear;

%%Read original data files


nname=['Node.dat'];
node=dlmread(nname);

nnode=node(1,1);

ename=['Elem.dat'];
element=dlmread(ename);

nelem=element(1,1);

rname=['Result1.out'];
data=dlmread(rname);

bname=['pfcres1.out'];
pfc=dlmread(bname);

%% Vtu File creation

%%Create vtu file for particle positions


fname=['fluid.vtu'];

fid=fopen(fname,'w');

%%Paraview data file content

fprintf(fid,'<?xml version="1.0"?>\n');
fprintf(fid,'<VTKFile       type="UnstructuredGrid"       version="0.1"
byte_order="LittleEndian">\n');
fprintf(fid,'\t <UnstructuredGrid>\n');
fprintf(fid,'\t                          \t                          <Piece
NumberOfPoints="%i"NumberOfCells="%i">\n',nnode,nelem);
```

```
fprintf(fid,'\t \t \t <Points>\n');
fprintf(fid,'\t  \t  \t  \t  <DataArray  type="Float32"  Name="Position"
NumberOfComponents="3" format="ascii">\n');

%%Nodes positions (3 components)

for i=1:nnode

j=i+1;
fprintf(fid,'\t \t \t \t %E %E E\n',node(j,2),node(j,3),node(j,4));

end

fprintf(fid,'\t \t \t \t </DataArray>\n');
fprintf(fid,'\t \t \t </Points>\n');

fprintf(fid,'\t \t \t <Cells>\n');
fprintf(fid,'\t  \t  \t  \t  <DataArray  type="Int32"  Name="connectivity"
NumberOfComponents="1" format="ascii">\n');

%%Element nodes (8 components)

for i=1:nelem

k=3*i;
fprintf(fid,'\t \t \t \t %i %i %i %i %i %i %i %i  \n',element(k,2)-
1,element(k,3)-1,element(k,4)-1,element(k,5)-1,element(k,6)-
1,element(k,7)-1,element(k,8)-1,element(k,9)-1);

end

fprintf(fid,'\t \t \t \t </DataArray>\n');

fprintf(fid,'\t  \t  \t  \t  <DataArray  type="Int32"  Name="offsets"
NumberOfComponents="1" format="ascii">\n');

%%Number of nodes of each element (8)

for i=1:nelem

k=i*8;
fprintf(fid,'\t \t \t \t %i \n',k);

end

fprintf(fid,'\t \t \t \t </DataArray>\n');

fprintf(fid,'\t  \t  \t  \t  <DataArray  type="UInt8"    Name="types"
NumberOfComponents="1" format="ascii">\n');

%%Elements type (12=hexahedral)

for i=1:nelem

fprintf(fid,'\t \t \t \t %i \n',12);

end
```

```
fprintf(fid,'\t \t \t \t </DataArray>\n');
fprintf(fid,'\t \t \t </Cells>\n');


fprintf(fid,'\t      \t      \t      <CellData      Vectors="Velocity"
Scalars="RVelocity">\n');
fprintf(fid,'\t  \t  \t  \t  <DataArray  type="Float32"  Name="Velocity"
NumberOfComponents="3" format="ascii">\n');

%%Fluid velocity

for i=1:nelem

p=i*3+1;
fprintf(fid,'\t \t \t \t %E %E %E\n',data(p,3),data(p,4),data(p,5));

end

fprintf(fid,'\t \t \t \t </DataArray>\n');
fprintf(fid,'\t  \t  \t  \t  <DataArray  type="Float32"  Name="Pressure"
NumberOfComponents="1" format="ascii">\n');

%%Fluid pressure

for i=1:nelem

p=i*3+1;
fprintf(fid,'\t \t \t \t %E \n',data(p,2));

end

fprintf(fid,'\t \t \t \t </DataArray>\n');

%%Porosity

fprintf(fid,'\t  \t  \t  \t  <DataArray  type="Float32"  Name="porosity"
NumberOfComponents="1" format="ascii">\n');

for i=1:nelem

fprintf(fid,'\t \t \t \t %E\n',pfc(i+1,1));

end

fprintf(fid,'\t \t \t \t </DataArray>\n');


fprintf(fid,'\t  \t  \t  \t  <DataArray  type="Float32"  Name="bforce"
NumberOfComponents="3" format="ascii">\n');

%%Body force

for i=1:nelem

fprintf(fid,'\t \t \t \t %E %E %E\n',pfc(i+1,2),pfc(i+1,3),pfc(i+1,4));

end
```

```
fprintf(fid,'\t \t \t \t </DataArray>\n');


fprintf(fid,'\t \t \t </CellData>\n');
fprintf(fid,'\t \t </Piece>\n');
fprintf(fid,'\t </UnstructuredGrid>\n');
fprintf(fid,'</VTKFile>\n');

fclose('all');
```

Appendix E – Simulations to calibrate FIELD1 and FIELD3

The simulations performed to calibrate all the FIELD1 (Table E.1) and FIELD3 (Table E.2). 'atc' represents the axial compressive tests and 'tri' the triaxial tests.

Table E.1. Iterations to adjust FIELD1 macroscopic mechanical values

	Ec (GPa)	knks	S (MPa)	lambda	Young Modulus (GpPa)	ucs (MPa)	Poisson's ratio
act1	55	0,90	26	1	33,69	3,77	
act2	50	0,90	26	1	30,49	3,83	
act3	30	0,90	26	1	17,75	3,88	
act4	10	0,90	26	1	7,00	4,78	
act5	20	0,90	26	1	14,96	4,92	
act6	15	0,90	26	1	11,36	4,82	
act7	15	0,90	25	1	11,35	4,61	
act8	15	0,90	15	1	11,16	2,74	
act9	15	0,90	20	1	11,31	3,81	
act10	15	0,90	17	1	11,22	3,21	
tri10	15	0,90	17	1	11,31	3,28	0,4893
tri11	15	0,50	17	1	16,23	3,11	0,4193
tri12	15	0,10	17	1	33,49	2,67	0,1805
tri13	5	0,10	17	1	10,82	2,63	0,1821
tri14	5	0,20	17	1	8,41	2,90	0,2839
tri15	5	0,50	17	1	5,39	3,20	0,4189
tri16	5	1,00	17	1	3,54	3,50	0,4989
tri17	5	1,50	17	1	3,53	3,10	0,4877
tri18	5	2,00	17	1	2,05	3,37	0,5800
act13	5	0,10	17	1	11,24	2,52	
act19	5	0,10	25	1	11,36	3,56	
act20	5	0,10	23	1	11,33	3,31	
act21	5	0,10	22	1	11,32	3,19	
tri21	5	0,10	22	1	10,83	3,18	0,1916
tri22	5	0,20	22	1	8,42	3,68	0,2996
tri23	5	0,50	22	1	5,37	4,02	0,4377
tri24	5	1,00	22	1	3,55	4,49	0,5260
tri25	5	1,50	22	1	2,70	4,39	0,5594
tri26	5	2,00	22	1	2,03	4,29	0,6088
tri27	5	2,50	22	1	1,61	4,30	0,6253
tri28	5	3,00	22	1	1,32	4,28	0,6244
tri29	5	3,50	22	1	1,13	3,95	0,6377
tri30	5	4,00	22	1	0,99	4,07	0,6385
tri31	5	5,00	22	1	0,78	3,97	0,6507
tri32	5	6,00	22	1	0,65	4,11	0,6578
tri33	5	8,00	22	1	0,52	4,05	0,6495
tri34	5	0,05	22	1	13,09	3,02	0,1037
tri35	4	0,05	22	1	11,08	3,33	0,1073
act35	4	0,05	22	1	11,58	2,80	
act36	4	0,05	25	1	11,61	3,20	
act37	4	0,05	25	1	9,99	3,11	
act38	4	0,05	25	1	10,68	3,20	
tri38	4	0,05	25	1	10,19	3,40	0,1118

Table E.2. Iterations to adjust FIELD3 macroscopic mechanical values.

	Ec (GPa)	knks	S (MPa)	lambda	Young Modulus (GPa)	ucs (MPa)	Poisson's ratio
act1	84	1,1	550	1	9,25	33,35	
act2	84	1,1	600	1	9,26	37,01	
act3	84	1,1	1000	1	9,41	74,18	
act4	90	1,1	1000	1	11,41	72,64	
act5	120	1,1	1000	1	15,39	73,53	
act6	120	1,1	900	1	15,34	67,02	
act7	120	1,1	950	1	15,37	70,51	
act8	120	1,1	940	1	15,36	69,94	
tri8	120	1,1	940	1	16,59	81,37	0,1603
tri9	120	1,2	940	1	15,91	84,80	0,1744
tri10	110	1,2	940	1	15,15	87,29	0,1560
tri11	110	1,3	940	1	14,46	87,44	0,1683
tri12	120	1,3	940	1	15,11	87,35	0,1758
tri13	115	1,3	940	1	14,57	87,68	0,1785
tri14	115	1,2	940	1	15,13	85,05	0,1648
tri15	121	1,3	940	1	15,20	87,37	0,1793
tri16	116	1,2	940	1	15,19	84,04	0,1644
tri17	117	1,2	940	1	15,34	90,11	0,1654
act17	117	1,2	940	1	14,37	70,79	
act18	117	1,2	930	1	14,37	70,22	
act19	118	1,2	930	1	14,42	69,28	
act20	119	1,2	930	1	14,59	70,70	
act21	119	1,2	920	1	14,58	69,60	
tri21	119	1,2	920	1	15,43	83,97	0,1633
tri22	119	1,3	920	1	14,98	85,79	0,1768
act22	119	1,3	920	1	14,02	68,48	
act23	119	1,3	940	1	14,02	69,36	
act24	119	1,3	960	1	14,03	71,15	
act25	119	1,3	950	1	14,03	70,65	
act26	119	1,3	945	1	14,03	70,08	
act27	120	1,3	945	1	13,92	64,74	
act28	120	1,3	950	1	13,92	65,12	
act29	120	1,3	1000	1	13,96	68,61	
act30	120	1,3	1010	1	14,03	76,82	
act31	130	1,3	1000	1	14,80	70,83	
act32	130	1,3	990	1	14,80	71,47	
act33	130	1,3	950	1	14,77	66,96	
act34	130	1,3	970	1	14,79	70,18	
tri34	130	1,3	970	1	15,80	84,94	0,1813
tri35	130	1,2	970	1	16,55	86,13	0,1670
tri36	110	1,2	970	1	14,38	89,59	0,1714
tri37	115	1,2	970	1	14,82	87,16	0,1710
act37	115	1,2	970	1	13,84	76,80	
act38	115	1,2	900	1	13,80	70,36	
act39	120	1,2	900	1	14,49	67,55	
act40	120	1,2	920	1	14,50	68,70	
act41	120	1,2	940	1	14,51	70,31	
tri41	120	1,2	940	1	15,31	80,50	0,1716